The Influence of Collagen-Based Scaffolds on Cardiac Differentiation and Endothelial Growth



Hazal Gezmis

Trinity College

Department of Materials

University of Oxford

A thesis submitted for the degree of *Doctor of Philosophy*

Hilary Term 2023

Acknowledgement

From the moment I started this DPhil 4 years ago to writing these acknowledgements, life has felt like a rollercoaster. Amidst being unable to carry out experiments due to the pandemic and being stuck in Türkiye for months, unable to return to the UK, after which having to work non-stop every single day for two years straight, here I am. I have kept my promise to those I am grateful for and without whom my thesis would not be what it is today.

First and foremost, I would like to thank my supervisors, Prof Jan Czernuszka and Prof Carolyn Carr, for their endless support and advice throughout the years. Even though the road ahead was full of uncertainty, thank you for giving me the freedom to shape my thesis in whichever way I saw fit.

This work would not have been possible without the support from the funding of the Republic of Türkiye, Ministry of National Education. Thank you for this opportunity; I would never have thought I would be doing my DPhil at the University of Oxford.

I also sincerely thank the Biomaterials crew; Dr Sonia Iftekhar, Dr Jim (Yang Xu), Dr Mu-Huan Lee, Dr Sasza Nabilla, and Zhaoying Ma. I have saved the most precious for last; my dear friend Ilayda Karadag. Thank you for walking this path with me in the toughest of times, keeping me sane in all my ups and downs, for the countless scientific discussions we had trying to make sense of our work, the social activities you planned to cheer me up, and most importantly, for being my family far away from home. I could not have done this without you.

Next, a big thank you to my DPAG colleagues: Dr Ujang Purnama for your guidance and eye-opening discussions throughout the *in vitro* work, Mala Gunadasa-Rohling for her sincere help on *in vivo* experiments, and most importantly, my buddy, Marcos Castro-Guarda. Thank you

for the rooftop chats whenever we had time to spare, keeping an eye on my precious cells and helping me with my experiments, even at the most difficult of times.

I would like to express my gratitude to my girlfriends that Oxford gave me: Dr Kay Chong and Dr Amy (Chenzi Xu). We have made the most unforgettable memories together, and I am beyond grateful for our friendship, the time we spent during our intimate dinners and the laughter we shared throughout the years.

To all my beloved friends out there, they know who they are; thank you for bearing with me. Especially to Deniz Ragipoglu, who listened to my complaints for hours in the middle of the night and gave countless support and advice on scientific and non-scientific matters. You are the most “multifunctional” friend I could ever ask for.

I owe a huge thank you to my parents, Zeynep and Nuri Gezmis, for their endless love and encouragement, not only in the past few years but my entire life. Even though you were hundreds of miles away, you never stopped believing in me, and without you, I would not be the person I am today. Of course, my one and only little brother, Taha Can Gezmis, deserves a thank you for filling my absence in the house and taking care of our parents.

Finally, my heartfelt gratitude goes to my loving husband, Attila Gokce, whose love, support, faith, sacrifices, and understanding gave me the strength to make it through these gruelling years and to achieve my goals. I hope I have made you proud, even though I have kept you waiting for so long. I love you endlessly.

Abstract

Myocardial infarction is the leading cause of death worldwide due to insufficient long-term treatments or the unavailability of suitable donors. To make clinically appropriate therapy for cardiac patients, cardiac tissue engineering focuses on designing 3D constructs that compositionally and mechanically reflect native cardiac tissue by providing better cellular interactions. However, the complexity and the abundance of cell load in the cardiac tissue complicate the developing process.

This thesis reports novel composite scaffolds containing collagen type I, fibrillar elastin gel (FEG) and hyaluronic acid (HA) and their applications *in vitro* and *in vivo*. Highly porous (>97%) scaffolds with various ratios of collagen and FEG were fabricated by lyophilisation, and HA was infiltrated into these structures. The effect of chemically crosslinking and accompanying HA infiltration was also studied. Mechanical testing results showed a strong correlation between scaffold stiffness and the concentration of FEG and the improvement of mechanical properties by HA infiltration in the hydrated state. Despite crosslinking, comparable tensile properties were achieved between the collagen-FEG composites and native porcine heart tissue.

The HA-infiltrated scaffolds were tested *in vitro* using a novel approach enabling the culture and differentiation of human induced pluripotent stem cells (hiPSC) to cardiomyocytes (hiPS-CM) in 3D. The studies with the alamarBlue assay indicated that these scaffolds were favourable to culture hiPSCs and that there was no significant difference between scaffold types in terms of proliferation. The scaffolds were also studied to evaluate the endothelial growth potential of human umbilical vein endothelial cells (HUVEC) using alamarBlue and phalloidin-DAPI staining, showing that these cells proliferated better in collagen-based scaffolds (C100) compared to collagen-FEG composites, which suggests that collagen is a crucial regulator to support endothelialisation. The successful differentiation of hiPS-CMs in

3D was shown in gene expression level by cardiac-specific (MYL7, MYH6) markers, although the differentiated cells were found to be an immature form of cardiomyocytes by immunocytochemistry. Collagen-FEG composites significantly enhanced the gene expression of extracellular matrix (ECM)-specific (COL1A1, ELA) markers than that of C100 scaffolds. The increase in the concentration of FEG also increased the endothelial gene expression (CD31, CD105, VEGFR2 and ANG2) when compared to C100.

The last part of the thesis covers the *in vivo* biocompatibility of collagen and collagen-FEG composites at different pre-conditions using histological staining. Non-crosslinked scaffolds significantly had better ECM deposition and cell migration than crosslinked and HA-infiltrated groups. No type of scaffold was encapsulated within the host, and the presence of capillary blood vessels and glycosaminoglycans was also shown in each scaffold type, suggesting that design scaffolds were feasible *in vivo*.

Preface

The research in this thesis was carried out by the author at the Department of Materials and Department of Philosophy, Anatomy and Genetics, University of Oxford, between January 2019 and March 2022, under the supervision of Prof. Jan Czernuszka and Prof. Carolyn Carr.

The content of this thesis is the product of the author's work, and all the assistance in preparing this thesis and resources have been acknowledged. No part/s of this thesis has been submitted or approved for any other degree at this university or elsewhere.

The author was supported by a DPhil studentship from the Republic of Türkiye, Ministry of Education.

Parts of this thesis were presented at an international conference:

- **Gezmis H.,** Czernuszka J., Carr C. Hyaluronic acid infiltrated collagen type I+ elastin scaffolds for myocardial repair, Recent Advances in Myocardial Tissue Engineering, Tissue Engineering and Regenerative Medicine International Society Asia-Pacific Conference 2022 (TERMIS AP-2022), (Abstract: S-S34-0222), ICC Jeju Island, South Korea, October 5-8, 2022. (Oral Presentation)

Table of Contents

Acknowledgement ii
Abstract iv
Preface vi
Abbreviations xii
1. LITERATURE REVIEW 2
1.1. Introduction 2
1.2. The Structure of Myocardium 2
1.3. Cardiovascular Diseases 5
1.4. Cell Therapies in Cardiac Tissue Engineering 5
1.4.1. Stem Cell-Derived Cardiomyocytes 6
1.4.1.1. Adult Stem Cells 6
1.4.1.2. Pluripotent Stem Cells 7
1.5. Cardiac Patches for Tissue Engineering 8
1.5.1. Decellularised Tissue 9
1.5.2. Cell Sheet 10
1.5.3. Fibrous Scaffold 10
1.5.4. Hydrogel 11
1.5.5. Porous Scaffold 11
1.6. Biomaterials in Cardiac Tissue Engineering 12
1.6.1. Type I Collagen 12
1.6.2. Elastin 15
1.6.3. Hyaluronic Acid 17
1.6.4. Composites 18
1.7. In Vivo Applications in Cardiac Tissue Engineering 19
1.8. Angiogenesis 19
1.8.1. Importance in Cardiac Regeneration 19
1.8.2. In Vitro Evaluation of Angiogenesis 21
1.8.2.1. Human Umbilical Vein Endothelial Cells 21
1.8.3. In Vivo Evaluation of Angiogenesis 22
1.8.3.1. Sponge Implant Model 22
1.8.3.2. Matrigel Plug Assay 23
1.8.3.3. Dorsal Air Sac Model 23
1.9. Aim 23
References 26

2. HISTOLOGICAL AND MECHANICAL CHARACTERISATION OF PORCINE CARDIAC TISSUE 57
2.1. Introduction 57
2.2. Materials and Methods 58
2.2.1. Dissection of Porcine Hearts 58
2.2.2. Cryo-sectioning 59
2.2.3. Histology Staining 59
2.2.3.1. Haematoxylin and Eosin 60
2.2.3.2. Elastica van Gieson 60
2.2.3.3. Alcian Blue 61
2.2.4. Compression and Tensile Testing 61
2.3. Results 63
2.3.1. Histological Evaluation of Porcine Heart 63
2.3.2. Compression Testing 65
2.3.3. Tensile Testing 67
2.4. Discussion 68
2.5. Summary 73
References 74
3. SCAFFOLD FABRICATION AND CHARACTERISATION 79
3.1. Introduction 79
3.2. Materials and Methods 79
3.2.1. Fabrication and Crosslinking 79
3.2.1.1. Collagen-Based Scaffolds 80
3.2.1.2. Production of Fibrillar Elastin Gel (FEG) 81
3.2.1.3. Collagen-FEG Composite Scaffolds 82
3.2.1.4. Crosslinking 83
3.2.1.5. Hyaluronic Acid-Infiltrated Scaffolds 84
3.2.2. Scanning Electron Microscopy 85
3.2.3. Fourier Transform Infrared Spectroscopy 87
3.2.4. Swelling 88
3.2.5. Degradation 89
3.2.5.1. Non-Enzymatic Degradation 89
3.2.5.2. Enzymatic Degradation 90
3.2.6. Compression and Tensile Testing 91
3.2.7. Three-Point Bending 91

3.2.8. Self-Deflection 92
3.3. Results 94
3.3.1. Scaffold Fabrication, Crosslinking and HA Infiltration 94
3.3.2. SEM 94
3.3.3. FT-IR 101
3.3.4. Swelling 110
3.3.5. Degradation 114
***3.3.5.1. Non-Enzymatic Degradation* 114**
***3.3.5.2. Enzymatic Degradation* 116**
3.3.6. Compression and Tensile Testing 119
3.3.7. Three-Point Bending 125
3.3.8. Self-Deflection 126
3.4. Discussion 127
3.4.1. Scaffold Fabrication 127
3.4.2. Crosslinking and HA Infiltration 129
3.4.3. Swelling 131
3.4.4. Degradation Characteristics 135
3.4.5. Compression and Tensile Properties 137
3.4.6. Bending Properties 142
3.5. Summary 144
References 146
4. IN VITRO EVALUATION OF SCAFFOLDS 154
4.1. Introduction 154
4.2. Materials and Methods 154
4.2.1. Cell Culture and Maintenance 154
***4.2.1.1. Human Induced Pluripotent Stem Cells* 154**
***4.2.1.2. Human Umbilical Vein Endothelial Cells* 156**
4.2.2. Scaffold Preparation 157
***4.2.2.1. Scaffold Sterilisation* 157**
***4.2.2.2. Vitronectin Coating* 158**
4.2.3. Cell Seeding on Scaffolds 158
***4.2.3.1. hiPSCs Culture* 158**
***4.2.3.2. HUVECs Culture* 159**
4.2.4. Cell Viability and Proliferation 160
4.2.5. Cardiomyocyte Differentiation 161

4.2.6. Angiogenesis Induction 162
4.2.7. Real-Time Polymerase Chain Reaction 162
4.2.7.1. mRNA Extraction 162
4.2.7.2. cDNA Conversion 164
4.2.7.3. Primer Validation and Annealing Temperature 164
4.2.7.4. RT-PCR Quantification 165
4.2.7.5. Pluripotency 166
4.2.8. Cell Imaging 166
4.2.8.1. Fixation 166
4.2.8.1.1. Glutaraldehyde Fixation 166
4.2.8.1.2. Formaldehyde Fixation 167
4.2.8.2. SEM 167
4.2.8.3. Phalloidin-DAPI 168
4.2.8.4. Immunocytochemistry 169
4.2.9. Mechanical Testing 169
4.2.9.1. Tensile Testing 169
4.2.9.2. Self-Deflection 170
4.3. Results 170
4.3.1. hiPSC Maintenance and Differentiation 170
4.3.2. hiPSC Behaviour on Scaffolds 172
4.3.3. Pluripotency 176
4.3.4. Cardiomyocyte Differentiation 177
4.3.5. ECM Production 182
4.3.6. Mechanical Testing 182
4.3.7. HUVEC Behaviour on Scaffolds 184
4.3.8. Gene Expression for HUVEC 190
4.4. Discussion 190
4.4.1. hiPSC Viability and Proliferation 190
4.4.2. Change in Pluripotency 193
4.4.3. Cardiac Differentiation 194
4.4.4. ECM Production 195
4.4.5. Mechanical Properties 196
4.4.6. Support for Endothelisation 197
4.5. Summary 200
References 202

5. SCAFFOLD IMPLANTATION 207
5.1. Introduction 207
5.2. Materials and Methods 207
5.2.1. Scaffold Preparation and Sterilisation 207
5.2.2. Animals and Surgery 207
5.2.3. Animal Care and Tissue Fixation 209
5.2.4. Paraffin Embedding and Sectioning 209
5.2.5. Histology Staining 210
5.2.6. Light Microscopy Imaging 210
5.3. Results 211
5.3.1. Animal Care and Surgery 211
5.3.2. ECM Deposition and Cell Migration 212
5.3.3. Elastica van Gieson 221
5.3.4. Alcian Blue 226
5.4. Discussion 231
5.5. Summary 234
References 236
6. THESIS SUMMARY AND FUTURE WORK 240
6.1. Thesis Summary 240
6.2. Future Work 242
APPENDICES 244

Abbreviations

2D	Two dimensional
3D	Three dimensional
AB	Alcian Blue
ADH	Adipic dihydrazide
ADSC	Adipose-derived stem cell
ANG2	Angiopoietin- 2
BBE	Bovine brain extract
BM-MSC	Bone marrow mesenchymal stem cell
BSA	Bovine serum albumin
C100	Collagen 100% scaffold
C90E10	Collagen 90% + Elastin 10% scaffold
C80E20	Collagen 80% + Elastin 20% scaffold
C75E25	Collagen 75% + Elastin 25% scaffold
CCR7	C-C chemokine receptor type 7
CD31	Platelet endothelial cell adhesion molecule
CD45	Protein tyrosine phosphatase receptor type C
CD68	Cluster of Differentiation 68
CD206	Mannose receptor
cDNA	Complementary DNA
CM	Cardiomyocyte
CTE	Cardiac tissue engineering
CVD	Cardiovascular diseases
DAPI	4′,6-diamidino-2-phenylindole
DM	Differentiation media
DMEM	Dulbecco's Modified Eagle Media
DMSO	Dimethyl sulfoxide
DNA	Deoxyribonucleic acid
dNTP	Deoxynucleotide triphosphate
DPBS	Dulbecco's phosphate-buffered saline
E	Young's modulus
EBM	Endothelial Basal Medium
EBP	Elastin binding protein

EC	Endothelial cell
ECFC/OEC	Endothelial colony forming cell/Outgrowth endothelial cell
ECM	Extracellular matrix
EDC	1-(3-Dimethylaminopropyl)-3-ethyl carbodiimide hydrochloride
EDV	End-diastolic volume
EF	Ejection fraction
EGM-2	Endothelial Cell Growth Medium-2
EHT	Engineered heart tissue
ELP	Elastin-like polypeptides
EPC	Endothelial progenitor cell
ESC	Embryonic stem cell
ESC-CM	Embryonic stem cell-derived cardiomyocyte
EVG	Elastica van Gieson
FBS	Foetal bovine serum
FEG	Fibrillar elastin gel
FS	Fractional shortening
FT-IR	Fourier transform infrared
GAG	Glycosaminoglycans
GFR Matrigel	Growth factor reduced Matrigel
HA	Hyaluronic acid/hyaluronan
H&E	Haematoxylin and Eosin
HEPES	4-(2-hydroxyethyl)-1-piperazineethanesulfonic acid
HEPES-BSS	HEPES Buffered Saline
hESC	Human embryonic stem cell
HF	Heart failure
hiPSC	Human induced pluripotent stem cell
hiPSC-CM	Human induced pluripotent stem cell-derived cardiomyocyte
HKG	Housekeeping gene
HUVEC	Human umbilical vein endothelial cell
ICC	Immunocytochemistry
IHC	Immunohistochemistry
IM	Induction media
KDR	Vascular endothelial growth factor receptor 2

LCST	Lower critical solution temperature
LV	Left ventricle
MI	Myocardial infarction
MYH6	Myosin heavy chain 6
MLC2v	Ventricular myosin light chain 2
MYL7	Myosin light chain 7
mRNA	Messenger RNA
MSC	Mesenchymal stem cell
NHS	N-hydroxysuccinimide
NMR	Nuclear magnetic resonance
PBS	Phosphate buffer saline
PFA	Paraformaldehyde
REDOX	Oxidation-reduction
RGD	Arg-Gly-Asp
RNA	Ribonucleic acid
ROCK	Rho-associated protein kinase
RPMI	Roswell Park Memorial Institute 1640
RT-PCR	Real-time polymerase chain reaction
SDF-1	Stromal cell-derived factor-1
SEM	Scanning electron microscopy
SMC	Smooth muscle cell
TCPS	Tissue culture polystyrene
TNBS	2,4,6-trinitro-benzenesulfonic acid
TNNT2	Cardiac troponin T
TNS	Trypsin neutralizing solution
TRITC	Tetramethylrhodamine B isothiocyanate
VEGF	Vascular endothelial growth factor
VEGFR	Vascular endothelial growth factor receptor
VPGVG	Valine-Proline-Glycine-Valine-Glycine
VTN	Vitronectin

To my late uncle Kemal Devran



LITERATURE REVIEW

1. LITERATURE REVIEW

1.1. Introduction

Coronary artery diseases are the single leading cause of death worldwide, causing myocardial infarction (MI) that results in permanent non-contractile scar tissue formation and hence the heart becomes challenging to repair because of its complexity. While heart transplants are routinely done, there is a worldwide shortage of donors, and the transplants typically last for ~5 years (1). Since Langer and Vacanti introduced the concept of "tissue engineering" in the 90s (2), it has been adapted to many fields. Designing biocompatible and bioactive tissue-like constructs for use as scaffolds with tissue engineering has been a fundamental goal of cardiac tissue engineering (CTE) for over 25 years.

Nonetheless, some significant difficulties still need to be overcome. Understanding the composition and the working mechanism of native tissue and cellular interactions are the first steps to developing a better approach. Therefore, this chapter aims to understand how the mechanical properties interact with the microstructure, the essential roles of composition, and their effect on cellular interactions and new vascular network formation in cardiac recovery. Regarding a convenient cell source, differentiation protocols and well-matched matrix design can, in principle, make a clinically relevant therapy for cardiac patients. The following sections will highlight the fundamentals and challenges of this promising field and summarise the proposed study.

1.2. The Structure of Myocardium

The heart's highly complex structure and function undertake critical bodily tasks. A mammalian heart contains four chambers with two atria and two ventricles. While the right atria is responsible for receiving venous blood and delivering it to the right ventricle to be transmitted to the lung (pulmonary circulation), the oxygenated blood returns to the left atria and is distributed to the whole body from the left ventricle via the aorta (systemic circulation)

(3). Blood circulation through the body requires higher blood pressure and more robust muscle contraction; thus, the ventricle wall is thicker than the atria, which only pump blood into the ventricles. The wall thickness can vary depending on various factors, including age, gender and workload. The wall becomes thicker on each contraction due to the activated muscles increasing the systolic blood pressure (Figure 1.1). Anatomically, both are based on three layers: epicardium, myocardium, and endocardium (Figure 1.2). The epicardium, the outer layer, consists of an epithelial cell layer, fibro-elastic connective tissue, adipose tissue, and nerves and coronary vessels (4). The myocardium, the main muscle layer, comprises cardiac muscle fibres that bind to the heart's collagen-based connective tissue. The inner layer, the endocardium, contains endothelial cells and connective tissue. Altogether, they maintain the contractility of the heart.

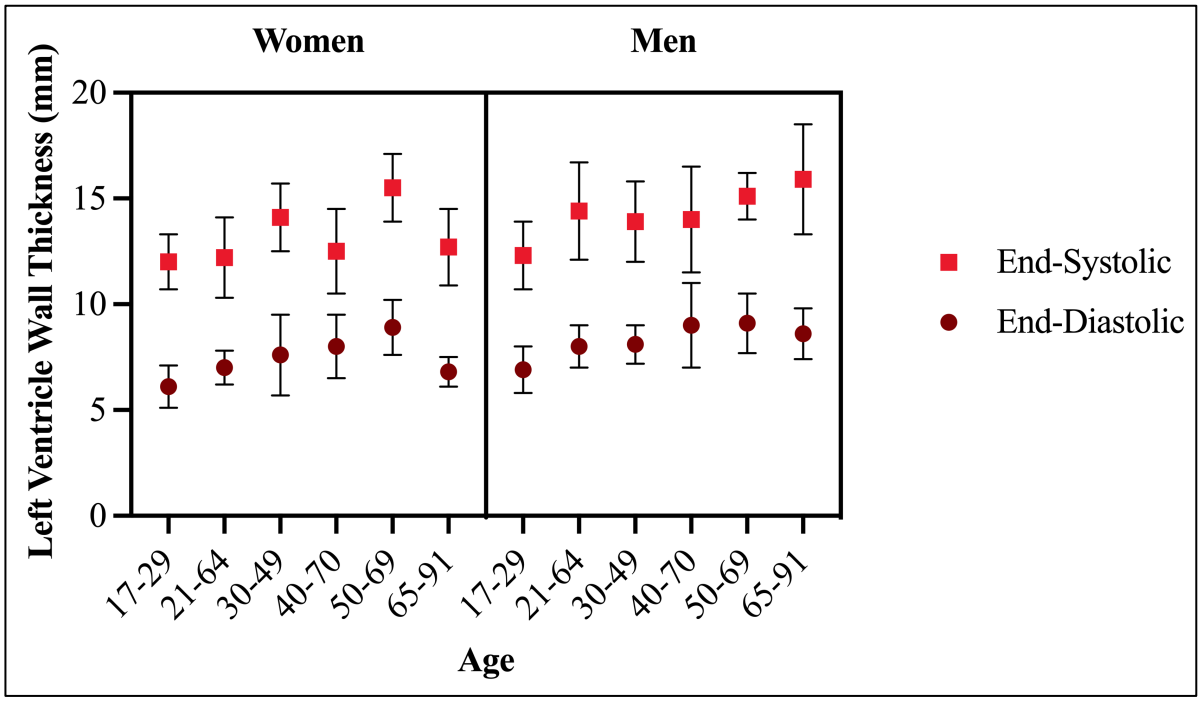


Figure 1.1. The summary of existing studies compares left ventricular wall thickness at diastole and systole. No significant relation between wall thickness and age or gender. Data represent Mean±SD and are revised from (5-7).

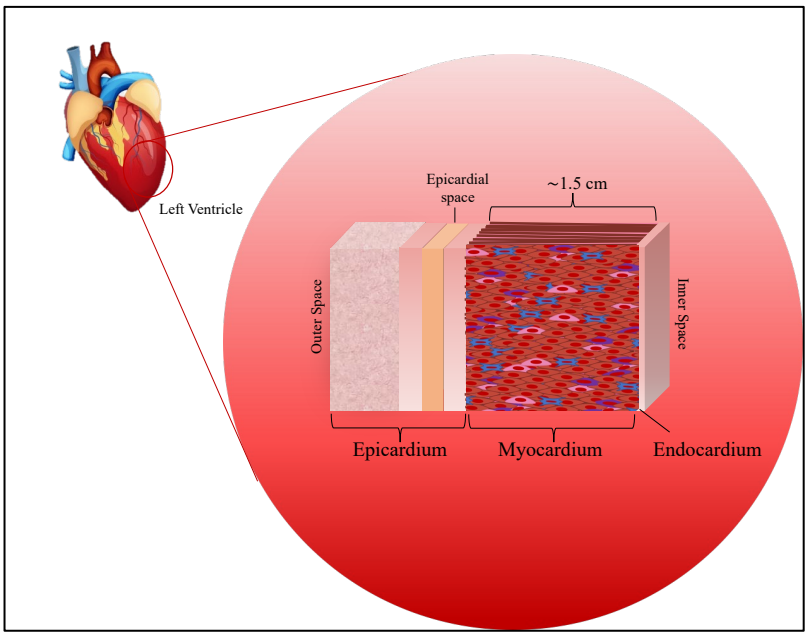


Figure 1.2. Anatomy of a heart wall.

The myocardium comprises cardiac muscle cells called cardiomyocytes (CMs). Cardiomyocytes account for ~40% of the total cell number but occupy about ~90% of the volume of the adult mammalian heart (8-11). The remaining non-myocyte population mainly consists of endothelial cells (ECs) (~50%) and cardiac fibroblasts (~10%), with a minority of hematopoietic-derived cells and smooth muscle cells (SMCs) (12). The cardiac fibroblast is essential for producing the extracellular matrix (ECM) components and transmitting mechanical force through the cytoskeleton (13, 14). The cardiac ECM is a collagen-dense matrix, predominantly type I and III (I/III ratio is 0.3-0.6), with a basal lamina, connective tissue, proteoglycans, glycosaminoglycans (GAGs), and biologically active molecules (9, 15-17). Fibrillar collagen supports muscle fibres and bundles whose orientation provides an appropriate structure for myocyte contraction. These contractile myocytes can be distinguishable from skeletal muscle cells via their centrally localised nucleus within a fibre (6) and become binucleated as they mature (18). Cardiomyocytes are highly oriented cells that attach linearly on either side of intercalated discs. This attachment provides fibre constructs of

various lengths (19). The heart is regarded as one of the least regenerative organs (20) since CMs have a minimal tendency to renew (~45% of total renewal in a lifespan) (21).

1.3. Cardiovascular Diseases

Cardiovascular diseases (CVD) are the leading cause of death, killing ~19 million people in 2020, with a rise of 18.71% since 2010, making death from cardiovascular disease more probable than cancer (22). Reperfusion therapy, whether with thrombolytic agents or rapid angioplasty, is the priority for individuals with MI, yet it is time-dependent as it is insufficient to repair scar tissue once formed (23, 24). Physiologically, MI leads to an inflammatory response which incites the removal of dead cells by macrophages. Subsequently, the over-proliferation of cardiac fibroblasts and ECs brings about scar tissue formation, which limits cardiac muscle contractility and causes dilatation and remodelling (25). Due to inadequate muscle reconstruction, the heart cannot restore its full function, resulting in heart failure (HF) (26). Whereas treating minor injuries with cell transplantation is possible, more advanced therapies are still needed for larger malformations. The ultimate envisioned method is whole heart transplantation; however, its application is limited by the scarcity of suitable donors. Moreover, the survival of patients can be challenging because of the need for immunosuppressants and possible immune rejection (27). Heart-related diseases are also a socio-economic burden for industrialised countries, such as the USA, where those cost $378 billion only between 2017 and 2018 (22). Therefore, relatively cheaper approaches should be considered.

1.4. Cell Therapies in Cardiac Tissue Engineering

Cell-mediated therapies offer great potential to repair damaged tissue by direct injection or tissue-engineered constructs. These have been under investigation to reintegrate the physiologic functions of injured tissues (20). Cardiac tissue engineering focuses on promoting cardiac function with the combination of various scaffolds, cell sources, and biochemical

stimuli. To provide support for damaged myocardium, several approaches have been studied (28-30). No matter which tissue engineering approaches are used, the cell source has been critical, especially for the feasibility of translation to the clinic. Today, scientists have a consensus that the ideal cell should be autologous or immunologically tolerant, abundant, and phenotypically have cardiac tissue-like properties (31, 32). Many types of cells have been used for this purpose, and these have been reviewed extensively elsewhere (33). Early work investigated the potential of bone marrow-derived cells and skeletal myoblasts (32, 34, 35). When Menasché *et al.* injected skeletal myoblasts into a patient's post-infarction scar, cells efficiently enhanced the cardiac contractile functions to reform the myocardium (36). However, myoblasts do not form gap junctions that couple newly formed tissue to the recipient's myocardium, increasing the risk of arrhythmia (37, 38). Bone marrow-derived cells showed some potential to improve cardiac function, but they did not form cardiomyocytes, and the benefit was deemed to be a paracrine effect (39). Considering the need to replace CMs lost from the ventricle wall, CMs from alternative sources have been chosen for CTE in the early studies and were grafted to promote cardiac repair *in vivo* (40-42). A study showed that newly formed intercalated discs connected the cells and host tissue without causing immune rejection (40). Leor *et al*. demonstrated that foetal rat CMs seeded on an alginate-based scaffold could facilitate angiogenesis and ease pathological remodelling without changing the contractility (43). Yet, the use of such cells in the clinic is limited due to the need for an extensive number of cells (~10^9) that cannot be obtained by biopsy (27).

1.4.1. Stem Cell-Derived Cardiomyocytes

1.4.1.1.Adult Stem Cells

Mesenchymal stem cells (MSCs) are adult stem cells with limited differentiation capacity into various lineages (44-46). These multiple source-derived cells have been used in numerous clinical trials, including those in CTE (47). The first clinical trial of MI patients (MAGNUM)

showed that combining a collagen scaffold with bone marrow MSCs was feasible and safe (34). Today, it is reported that 56 MSC-based studies have been completed, and 61 are planned or in progress for the treatment of cardiovascular diseases (35). Although their use is prevalent and practical, the low viability of cells in ischemic lesions has been an obstacle to long-term therapeutic applications (20, 46). Cardiac mesenchymal cells, such as cardiosphere-derived cells, are heart-derived stem cells which show multilineage potential and clonogenicity (48). Their transplantation was safe and supported cardiac regeneration and function in rats (49, 50), though contradicting results are available (51). Studies also show no significant improvement in cardiac function in clinical trials (52, 53).

1.4.1.2.Pluripotent Stem Cells

Considering the large number of cells needed to replace CMs in infarcted tissue, pluripotent stem cells are the most likely cell source (54). Embryonic stem cells (ESCs) derived from the inner cell mass of blastocysts have pluripotency that gives rise to nearly all cell types (55), and these cells have been utilised in various applications, including cardiac regeneration (56-62). The first engineered graft using mouse ESC-derived CMs was introduced in 2006 (57). The study showing immature native tissue-like function and structure in the engineered myocardium was initially promising. Soon after, Caspi *et al*. used human ESC-CMs with a combination of non-myocytes to regenerate vascularised myocardium (58). This application resulted in increased viability and maturation of CMs. Nevertheless, using ESCs in clinical studies has been an issue due to ethical controversies and the need for immune suppression.

After having been introduced by Yamanaka *et al*. in 2006 (63), induced pluripotent stem cells (iPSCs) have been adapted to many fields employing their similarity to ESCs without ethical concern, diversity in terms of differentiated cells, patient-specific use, and the applicability to many disease models (64, 65). This somatic reprogramming approach is critical in cardiac tissue engineering because native cardiomyocytes are hard to obtain and do not proliferate *in*

vitro. The number of cells required to replenish damaged areas of the myocardium is 1-10x10^8 cells cm^{-3} (9, 26, 66, 67).

The first engineered heart muscles with human stem cell-derived cardiomyocytes were formed by combining CMs (iPSC or ESC-derived) and nonmyocytes in collagen scaffolds (68). Constructs with both cell types had comparable physiological properties, even when transplanted *in vivo*, and they promoted capillary-like structures with blood perfusion. Moreover, a 3D-printed construct on which iPSCs differentiated into multiple cell lineages has improved the function and recovery of both murine (69) and swine (70) animal models. Even though iPSC technology can provide new alternatives (71-84), the retroviral vectors in the process with a risk of tumorigenicity as well as chromosomal abnormalities may hinder their use in medicine (15, 32, 85), yet less damaging vectors are now being used in many cases (86). Though, most existing protocols are costly and slow. Efficient large-scale protocols for deriving iPSCs are still needed to secure the feasibility of tissue engineering (21, 87, 88).

1.5. Cardiac Patches for Tissue Engineering

Cardiac patches are tissue replicas engineered in the laboratory to provide physical, chemical, and biological functions, matching that of the native myocardium for alleviating injury and accelerating regeneration (89). Early work on cell-populated matrix production by Eschenhagen *et al.* used collagen-based hydrogels *in vitro* (90). Li *et al.* were the first to implant a cardiac patch of porous collagen scaffold with CMs onto rats; however, the study did not conclude any improvements in structure and function (41). In 2000, for the first time, Leor *et al.* declared a functional advancement in 3D porous scaffold-grafted rat myocardium (43). Then, Zimmerman *et al.* showed the possible use of neonatal rat CMs seeded in collagen. Matrigel to produce heart tissue, and this work has coined the term “engineered heart tissue (EHT)” to the field (91). Today, it is well known that an ideal patch should resemble a native tissue-like structure, improve function over various scar sizes and time scales, and actively

associate with host tissue without triggering tumorigenesis (9, 26, 32, 92-95). Hence, the manufacturing of cardiac patches has been used by other researchers, with various modifications in terms of cell source or scaffold structure (96-100). The cells initiate elasticity at the cellular level by anchoring and pulling on their surroundings (101). Such mechanisms rely on myocyte contractility and transcellular adhesions, such as integrins and cadherins, to deliver forces to substrates. Cells not only apply stress but also respond to substrate stiffness through their cytoskeleton organisation. The surface stiffness can regulate the adhesion structures, cytoskeleton arrangement, cell motility and contractility, and differentiation. For instance, while stress fibres and focal adhesions predominantly cause isomeric contraction on a stiff glassy surface, substrates with an $E \sim 10$ kPa can promote actomyosin striation. Therefore, an appropriate substrate for functional cells should be determined for a functional heart patch. Previous studies used decellularised tissues, cell sheets, foams, fibre meshes, and gels for 3D cardiac patches.

1.5.1. Decellularised Tissue

One of the current challenges in cardiac patches is to design a scaffold in an optimum thickness with an appropriate vascular network (102). Therefore, patches derived from physically, chemically, or enzymatically decellularised tissues of cadavers or non-human organisms are preferable to meet this requirement. Decellularised scaffolds have a native capillary bed in a 3D construct that allows cells to be seeded, proliferate or migrate for repair (103, 104). Also, the tissue matrix comprises natural biomaterials such as collagen and fibrinogen, which can be used for scaffold manufacturing and matching the host heart. A study showed that CMs and ECs could populate decellularised whole heart tissue in rat hearts (105). Cardiac improvement using decellularised ECM matrix was also demonstrated *in vitro* (106) and *in vivo* (107). Clinically, FDA-approved materials obtained by decellularising porcine small intestinal

submucosa matrix were implanted into 11 patients with MI (108), where the matrix did not cause any long-term complications and was safe to treat myocardium.

1.5.2. Cell Sheet

Another method to produce a cardiac patch is the cell sheet technology which is based on plating cells on temperature-sensitive polymer-coated dishes, which allows a confluent cell sheet to dissociate from the dish without damage to the sheet when the temperature is reduced (109-112). Using this approach, studies have provided large-scale vascularised sheets that could be used as advanced cardiac patches (113, 114). Another method for cell sheet engineering was developed by Itabashi *et al.* using polymerised fibrin-coated dishes (115). To date, several modifications have been adapted to the leading technology with numerous cell types, such as stem cell-derived cells (75, 116-121), progenitor cells (111), neonatal cardiomyocytes (113-115, 122-124), skeletal myoblasts (125, 126), or their combinations (119, 127-129). Human iPSC-derived cardiomyocytes (hiPSC-CMs) sheets were also shown to promote left ventricle remodelling, angiogenesis, and contractility after transplantation (73). With an appropriate vascular network, it is possible to maintain cell sheets within the body for the long term (130).

1.5.3. Fibrous Scaffold

Electrospinning can fabricate a wide range of fibrous mats, which uses an electrical charge to stream a polymer solution from a syringe to the collector (131). This technology has been adapted to several studies with different polymeric compositions to regenerate heart muscle (77, 132-140). Khademhosseini and his colleagues observed that fibrous scaffolds featuring elastomeric, biodegradable, and tuneable properties could modulate cell behaviour since they are produced at different weight ratios that can change chemical composition, stiffness, and topography (135). However, electrospinning is usually dependent on synthetic polymers; therefore, a pre-formed fibre scaffold may result in a higher stiffness than needed in a dynamic

matrix of the human myocardium, which is 10-15 kPa (104, 141). Furthermore, it is still challenging to produce a fibrous scaffold with a proper thickness that mimics native cardiac tissue.

1.5.4. Hydrogel

Hydrogel technology is a sophisticated bottom-up approach as these materials are scaffold-free and invasively injectable through a catheter (104). It is based on a gelatinous natural material (collagen, fibrin, alginate, Matrigel, etc.), a template to cast, and a cross-linker (87, 142). The cells are entrapped in the material, a template subsequently gives the desired shape to the gel, and a crosslinker fixes the formed structure. The method was developed in the 1980s, but its adaptation to CTE was led in 1997 by Eschenhagen and Zimmermann. (90). Following this pioneering work, the method has been embraced by main groups, using collagen type I or fibrin gel to entrap CMs (31, 67, 91, 143-145). It allows the production of higher active force and flexibility to various shapes and sizes, resulting in similar mechanical properties to those in heart tissue, and biocompatibility. However, it is not mechanically stable, which makes it hard to control *in vivo* (87). Nonetheless, the methodology is still applied in numerous studies (61, 146-149), and recently, patient-specific ECM-derived hydrogel has become more popular for tissue implants (150-152). A clinical trial using collagen-based EHT is now underway (153).

1.5.5. Porous Scaffold

Porous scaffolds are preferable for cardiac scaffolds since they are easily manufactured with large pore size, allowing cells to migrate and infiltrate through voids (32, 87, 154). Lyophilisation (155-157), salt leaching (10, 158), or more complex methods (159-161) can be chosen for fabrication with a wide range of materials such as most commonly collagen (41, 162, 163), alginate (155, 164, 165) or various synthetic polymers (10, 166-168). One study is fascinating due to its accordion-like honeycomb structure based on poly(glycerol sebacate) (160). These well-oriented porous structures resembled native myocardium due to their

anisotropic mechanical properties (tensile modulus 57 kPA or 195 kPA at the cross- or preferred directions, respectively). Porous scaffolds possess interconnected pores that facilitate cell-to-cell communication and provide gaps for neovascularisation (154). Large pores (>200 μm) allow deep penetration of large vessels into the scaffold, while small voids (<200 μm) induce small vessels at higher density (169). However, if the scaffold is thicker than the clinically relevant size (0.5 cm), these interconnected pores are insufficient to allow nutrients and oxygen to perfuse inside the matrix, resulting in the death of cells in the centre. Combining foam with a designed capillary structure may eliminate this problem (158).

1.6. Biomaterials in Cardiac Tissue Engineering

1.6.1. Type I Collagen

Accounting for 25% of all protein mass in humans, collagen is the most abundant and non-elastic fibrillar protein within the body (170). It has an extensive protein family encoded by 20 different collagen genes. Its abundance in ECM dominantly controls the biological and biomechanical properties that the myocardium needs (26, 102, 154). Therefore, it is the most common type of biomaterial used in scaffold construction for cardiac regeneration (136, 171-177). Researchers prefer collagen-based scaffolds as Arg-Gly-Asp (RGD) peptide sequences of collagen bind to integrins on the surface of cardiomyocytes, and provide adhesion and mechanotransduction (172). It has been shown that collagen could support neovascularisation and inhibit apoptosis of CMs without causing inflammation (176).

Collagen type I comprises two α-1 and one α-2 chains, and each chain has a left-handed helix with recurring Glycine-X-Y motifs (Figure 1.3) (178). While glycine comprises 1/3 of all amino acids in collagen, the rest (X and Y) can be any type of amino acids, most commonly proline (28%) and hydroxyproline (38%), respectively (179). The ubiquity of collagen results in the formation of a ladder of recurring N-H(Gly)•O=C(X/Y) hydrogen bonds within the triple helix (180-185). Both proline and hydroxyproline at different positions change the stability of

the collagen triple helix. The rigidity of collagen fibrils can be reduced by hydrating the fibrils or increased by crosslinking (185, 186).

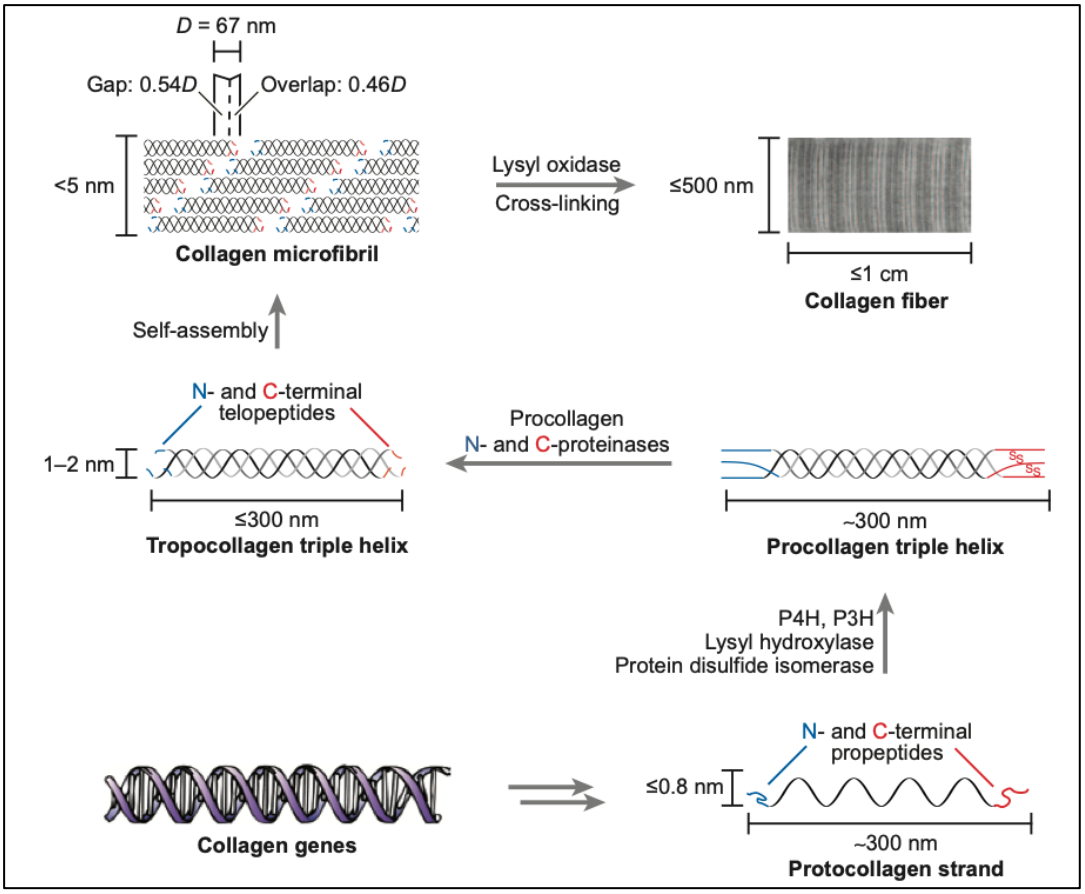


Figure 1.3. Chemical synthesis of collagen fibre. Several sequences of Gly-X-Y form the α-chain, and three of them fold to create a triple helix structure. Many of those helix clusters produce collagen microfibrils followed by collagen fibre composed of fibrils. Taken from (185).

Until 2010, 28 types of collagens had been identified by their different functions and structures (187, 188), and it is well known that collagens type I and III are the principal forms of collagen in the heart (177, 189, 190). The heart also includes collagen type IV within the basement membrane, which links CMs to the ECM (191). Type I collagen is the most abundant structural protein in the cardiac ECM, providing mechanical strength, resilience, and cell-cell interactions (26, 190, 192, 193). It covers approximately 80% of total collagen in the rat or non-human primate myocardium (194); hence it has been used in many tissue-engineering studies, as shown in Table 1.1 (136, 176, 195-206). Collagen type I consists of two identical α-1(I) chains

and one α-2(I) chain (207), whereas collagen type III has three identical α-1(III) chains (208). Type III represents about 11% of total collagen in the non-human primate myocardium (189) and is strongly related to type I. Although animal studies showed that collagen type I is the most abundant, studies in the human heart show that collagen type III is more prevalent (17). Most collagen is insoluble, but enzymes can solubilise it without changing its form (208).

Table 1.1. Selected studies based on the collagen type I derived cardiac patch.

Scaffold	Cell Source(s)	MI Model	Outcome	Ref.
Porous	BM-MSCs	Rat	No inflammatory response, angiogenesis ↑, cell engraftment ↑	(195)
Hydrogel	VSMCs	Rat	Angiogenesis ↑, vessel and capillary density ↑, macrophages population ↑	(196)
	-	Rat	Angiogenesis ↑, LV remodelling ↓, infarct size ↓	(197)
	HUCBCs	Mice	EDV ↓, EF ↑, LV wall thickness ↓, infarct size ↓	(198)
	ECs BM-MSCs	Rat	Cell migration, recruitment and population ↑, vessel density ↑, angiogenesis ↑	(199)
	BM-CACs	Mouse	LVEF ↑, FS ↑, cardiac perfusion ↑, infarcted area ↓, cell engraftment ↑, vascular density ↑,	(200)
Film	BM-MSCs	Mouse	Vessel density ↑, cell population ↑, cardiac regeneration ↑	(201)
	BM-MSCs	Rat	Infarcted area ↓, LVEF ↑, angiogenesis ↑, LV thickness ↑, LV dilatation ↓, infarcted segment perfusion ↑	(202)
	Cardiac Cells	Rat	Electrophysiological properties ↑, infarct size ↓	(203)
	-	Mice	Scar size ↓, angiogenesis ↑, cell migration ↑, EF ↑, FS ↑, LV internal diameter ↓, LV wall thickness↑	(136)
	-	Mice	No inflammation, cardiac deterioration ↑, when applied immediately after MI efficiency ↑	(176)
	ADSCs ESC-CPs	Rat	LVEF ↑, Scar size ↓, angiogenesis ↑	(204)
Sheet	ADSCs	Rat	Non-crosslinked scaffold > cross-linked scaffold	(205)
	ADSCs	Rat	Cell engraftment ↑, LVEF ↑, stiffness↓, cardiac remodelling ↓, angiogenesis ↑	(206)
		Pig	LVEF ↑, EDV ↓, scar size ↓, angiogenesis ↑	

ADSCs: Adipose-derived stem cells; BM-MSCs: Bone marrow mesenchymal stem cells; ECs: Endothelial cells; EDV: End-diastolic volume; EF: Ejection fraction; ESC-CPs: Embryonic stem cell-derived cardiovascular

progenitors; FS: Fractional shortening; HUCBCs: Human umbilical cord blood mononuclear cells; LV: Left ventricular; VSMCs: Vascular smooth muscle cells.

It is possible to change collagen characteristics by manipulating the number of crosslinks and incorporating glycoproteins or proteoglycans. For instance, the hardening of damaged myocardium results in an elastic modulus of 35-70 kPa, which is stiffer (209) than that of a typical heart wall, whose elastic modulus is around 18 kPa in rats (210). It has been suggested that moulding of collagen type I by a plastic mould compression method could optimise the stiffness of the scaffold and ultimately improve cardiac function (136). Combining collagen with other biomaterials may also change its mechanical properties (139, 211).

1.6.2. Elastin

During systolic contraction, heart ventricles transmit blood to the vessels that, in turn, contract to convey venous blood back to the heart again (25). This continuous, reversible contraction and relaxation is supported by elastin within ECM. Since the heart beats 3 x 10^8 times over 10 years, and the native adult mammalian heart has Young's modulus of ~20 kPa (relaxation) to 200-500 kPa (contraction), it is a challenge to design a flexible material meeting the mechanical properties of the myocardium (25, 161, 212).

Elastin is a versatile fibrous protein that forms elastic fibres and microfibrils (213, 214). Tropoelastin, the soluble precursor of elastin, weighs approximately 60 kDa and is encoded by a single gene that is well-conserved in vertebrates (214-216). In elastogenesis, monomeric tropoelastin molecules undergo self-assembly, called coacervation, followed by alignment and crosslinking, respectively, and then deposit on pre-structured microfibrils to form elastic fibres (Figure 1.4) (213-217). These relatively loose and irregular polypeptide sequences are covalently anchored to become a rubbery elastic fibre mesh (170).

While elastin has similarities to collagen regarding its richness in glycine and proline, the molecule is poor in hydroxyproline (4, 215). Since glycine residues locate randomly within the molecule, random coiling of fibres is possible, allowing the elastic fibres to slide over each other or stretch to about 150% of their original length without fracture (3). Moreover, the extensive lysine-derived crosslinks and the wealth of randomly distributed glycine-valine-proline domains make elastin extremely hydrophobic (4, 214, 215, 218). Crosslinks between elastin molecules are mainly controlled by either one of two tetra-functional amino acids that are unique to elastin: desmosine and isodesmosine (4).

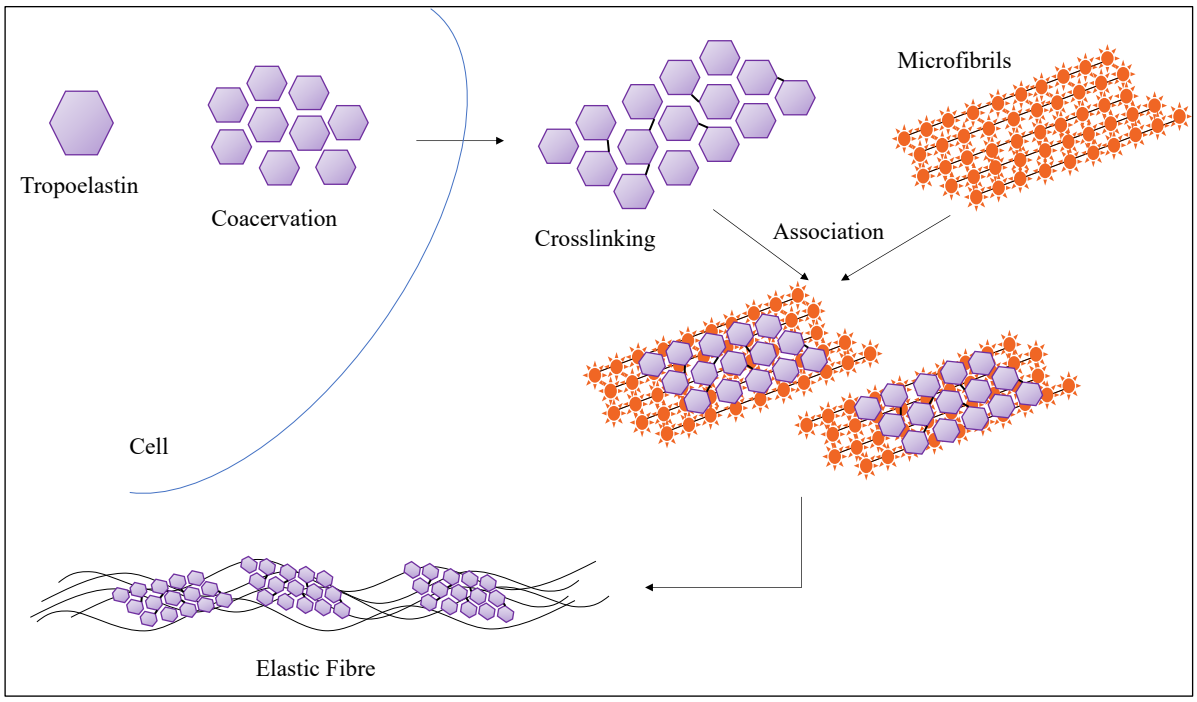


Figure 1.4. Elastogenesis in intracellular space. Monomeric tropoelastin molecules self-assemble so-called coacervation, then align and bond to each other. Crosslinked elastin deposits on pre-formed microfibrils and covalently anchors to form elastic fibre mesh.

Synthesis and assembly of elastic fibres occur during early development until adolescence, such that an organism lacks elastin production in adulthood (216). It is estimated that the turnover of each produced elastin molecule could be around 80 years (219), and the loss of elastic function comes with several conditions, including ageing, aortic aneurysm, and MI (213, 216, 220, 221). Until now, different approaches have been used to understand the importance of the elastin (222-225), although the tightly bound structure makes it hard to manipulate as a

biomaterial source. Researchers have focused on identifying an equivalent to elastin and combining it with other synthetic or natural polymers (226). To date, tropoelastin has been used in hydrogels (227-229) or electrospun fibres (230, 231). Liu *et al.* suggested that including elastin in electrospun fibres could effectively preserve or promote myocardium function following MI (232). Although elastic fibres clearly play a critical role in cardiac morphology and regulate its function (231), there has been relatively little research in this area.

1.6.3. Hyaluronic Acid

GAGs are composed of polysaccharide chains with recurring amino acid and sugar group sequences. Most GAGs within ECM of the native heart are hyaluronic acid (HA), also known as hyaluronan (188, 193, 233). HA is the only non-sulphated GAG that has β-GlcNAc-(1,3)-β-GlcA-(1,4)- repeats (Figure 1.5) (234).

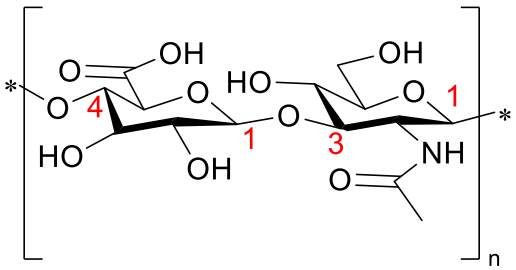


Figure 1.5. General chemical structure of HA. Adapted from (233).

The synthesis of HA occurs in the cell membrane under the control of three different enzymes (188). It can be up to 2 μm long and resides in the pericellular matrix. It is 500 times more viscous than water (234) and contributes to the hydration of the environment needed for cell proliferation and movement (188). The carboxylic acid and hydroxyl groups can modify HA, affecting viscosity, biocompatibility, and functionality (233, 235).

The key role of HA in regulating cell behaviour and fate has been demonstrated in many studies (154, 236-238), reporting enhanced regeneration (139, 156, 239-241) and increased ECM deposition (242). Furthermore, *in vivo* studies concluded that injectable HA hydrogels could enhance heart wall thickness when the compression modulus was relatively high (~43 kPa),

which could be better for reducing myocardial stress (243). As contracting CMs exhibited greater mechanical force on a stiffer surface than that of native myocardium (244), the mechanical features of HA may be useful to tailor this during regeneration (148).

1.6.4. Composites

The complexity of ECM architecture bestows harmony in cardiac tissue that needs to contract and relax constantly. Therefore, the mechanical and functional properties of different types of ECM could be combined to provide a comparable, complex structure (15, 245). Daamen *et al.* developed a porous collagen-elastin-GAG composite in several ratios (246). When collagen was the major component, higher tensile strength ranging from ~350 kPa to ~700 kPa was observed, while the addition of elastin and GAGs enhanced the elasticity (0.78 MPa) and water intake capacity (~29 times more than water), respectively. An electrospun fibre mesh formed from gelatine-collagen and tropoelastin was obtained by Li *et al.* (230) and demonstrated that a fibrous scaffold could be used for cell attachment and proliferation. Moreover, the reduced stiffness of collagen in combination with insoluble elastin was noted as an inducer of contraction (247). It was also shown that the collagen-elastin composition improved new tissue formation and promoted function in infarcted hearts (221). A composite of a porous collagen-HA hybrid scaffold increased water absorption and enhanced significant vascularisation capacity *in vivo* (156). Alternatively, isolated collagen-HA was blended with a synthetic polymer to increase stability (139). *In vitro* vessel formation was statistically augmented in the composite micro-fibrous scaffold, compared with the synthetic scaffold alone, and the newly formed vessels were longer. Although many others exist, a trihybrid scaffold of collagen-elastin-HA has not been observed for a cardiac patch.

1.7. In Vivo Applications in Cardiac Tissue Engineering

The first *in vivo* trials of a construct aimed to see whether cells could survive in the heart and preserve contractile function. To answer these, designed structures were transplanted into the different areas of infarcted hearts (41, 143, 248), and there have been many advanced and detailed applications improving cardiac function (69, 70, 151, 152, 212, 249-251). Zimmermann *et al.* first showed that neonatal rat myocytes in EHT survived *in vivo*, and neovascularisation was observed in the presence of immune suppression (67, 91, 143). The Eschenhagen group also demonstrated that the EHT containing hiPSC-CMs could augment cardiac repair when transplanted onto guinea pig hearts (79). A long-term animal study noted that human hiPSC-CMs transplantation onto swine hearts as a cell sheet improved left ventricle remodelling, neovascularisation and contractility, and the cells were still detectable even in the 8^{th} week post-surgery (73).

Although studies are still promising (252, 253), several question marks should be resolved, such as how efficient neovascularisation is, what the survival rate of the transplanted cells is, how well the construct mimics the recipient's myocardium in terms of functionality, and how beneficial this tissue equivalent is (66).

1.8. Angiogenesis

1.8.1. Importance in Cardiac Regeneration

To design compact constructs with reasonable thickness, ideally, a cardiac-like construct should be ~1.5 cm thick with a cell density of $>10^8/cm^3$ (25, 27, 32). However, this requires a high demand for oxygen and nutrient supply throughout the construct so that the cells can survive (32, 104, 254, 255). Therefore, a major roadblock to the survival of such architecture is the lack of an adequate perfusion system once transplanted *in vivo,* as the cells on the scaffold cannot keep alive if there is no vascular network (27). The capillary network arises from vascularisation that occurs by either vasculogenesis or angiogenesis. While vasculogenesis

describes *de novo* blood vessel formation, angiogenesis corresponds to the sprouting of pre-existing vessels to form new capillaries (Figure 1.6) (256, 257) (170). Vascularity is stimulated by the complex interactions among ECs, SMCs, pericytes and fibroblasts, and angiogenic proteins such as cytokines and growth factors (vascular endothelial growth factor (VEGF), Angiopoietin-1 and 2, etc.) (11, 257-259). Native myocardium has capillaries distanced at ~20 µm from each other (260, 261). Without an adequate capillary network, the cells can stay viable on a scaffold of less than 200 µm thick, which does not reflect the standards of the myocardium (262). To achieve the vasculature, numerous techniques have been tested to date, including pre-vascularisation (58, 134, 147, 212, 263), direct cell transplantation (76, 114, 248) or growth factor delivery (138, 149, 163).

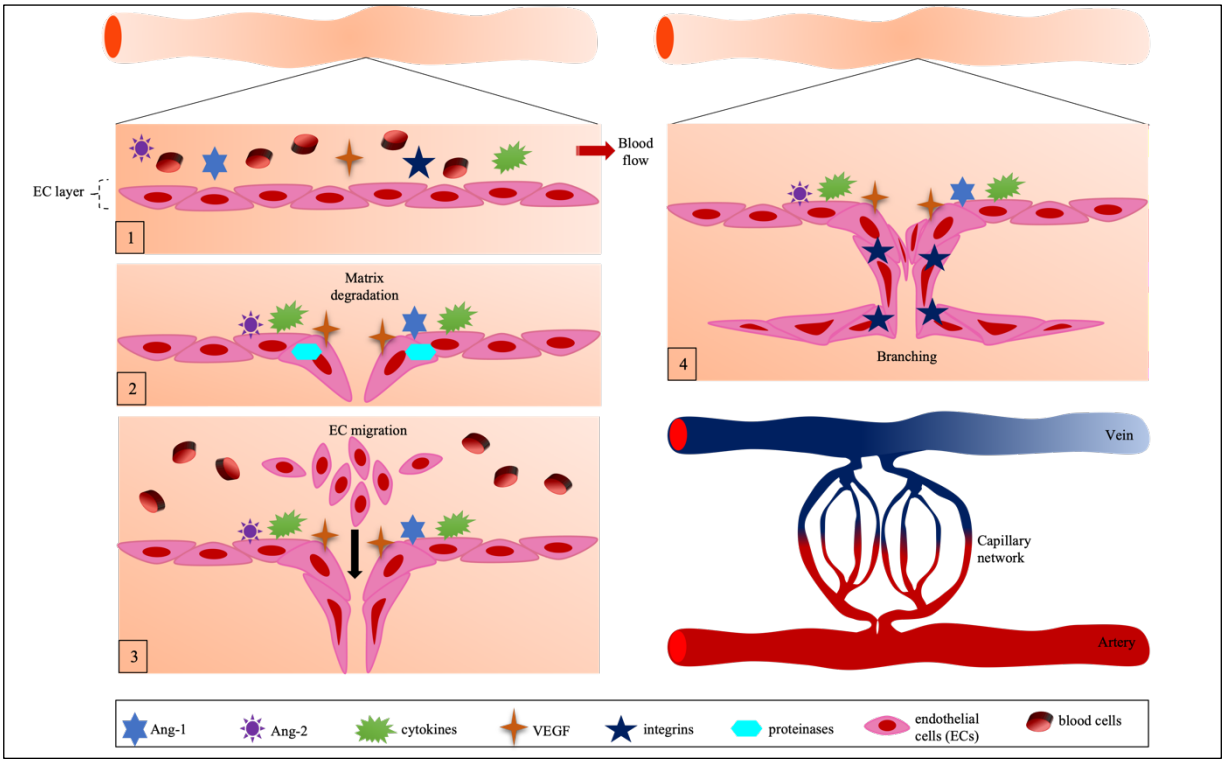


Figure 1.6. The development of new capillaries from existing vessels. (1) New blood vessel formation is controlled by cytokines, integrins and some crucial proteins such as VEGF, Ang-1 and -2 by binding to receptors on ECs. (2) Binding activates matrix metalloproteinases which degrades the basement membrane. (3) This induces endothelial cell proliferation and migration into the degraded area. (4) Integrins expressed by ECs maintain the adhesion of elongated cells to the ECM to form a tube-like structure. Angiopoietins stabilize the capillary network throughout the sprout.

The Radisic group designed an organ-on-a-chip with an engineered capillary network that supported perfusion, vascularisation, cell assembly, and anastomosis (212). It is also possible to use an avascular cardiac patch and allow vascularisation *in vivo.* Shadrin *et al*. demonstrated that a clinically relevant-sized cardio patch induced maturation of hiPSC-CMs, neovascularisation, and maintained electrical coupling and calcium handling without causing arrhythmia (95). Pieper *et al*. used crosslinkers for a scaffold of collagen type I and GAGs which enhanced vasculature and reduced macrophage migration to the region after the transplantation (264). Additionally, Feiner *et al*. developed an electronic mesh cardiac patch based on gelatine and poly(caprolactone), which could monitor electrical activities, drug release, and cell contraction (137). The chip-embedded construct controlled stromal cell-derived factor-1 (SDF-1) release, a chemoattractant for neovascularisation *in vivo.*

1.8.2. In Vitro Evaluation of Angiogenesis

1.8.2.1.Human Umbilical Vein Endothelial Cells

ECs from a variety of sources have been used for *in vitro* models of biomaterials; however, human umbilical vein endothelial cells (HUVECs) are by far the most popular model (Table 1.2) as they provide information about normal EC behaviour and how ECs react to different stimuli or treatment with pro- and anti-angiogenic agents (265). They are isolated from the umbilical vein of the umbilical cord where there are no ethical concerns because the cord is discarded biological waste after the child's birth. HUVECs were first reported as a primary cell source in 1963 (266), later characterised (267), and have been widely utilised for angiogenesis, inflammation, atherosclerosis etc., ever since.

Numerous reasons make HUVECs so valuable in CTE, one of which is that they can easily form spheroids and be co-cultured in 3D constructs with other cell types. This enables their use to understand cellular interactions in advanced 3D models or *in vivo* animal models, by providing a vasculature body. Today, they can be either isolated as a primary culture or

commercially purchased from various companies accompanied by endothelial-specific growth media, supplements, and coating agents to form vessel sprouts. (268). However, using them for pre-vascularisation in clinics is still challenging due to the possibility of immunogenicity and the impracticality of auto-transplantation.

Table 1.2. The summary of publications on biomaterials where different human EC types were used. *

EC Type		Number of Articles	First Report (year)
Macro-vascular EC	HAEC	30	2005
	HCAEC	19	1985
	HPAEC	18	2002
	HUVEC	1321	1991
Micro-vascular EC	HDMEC	33	2002
	HPMEC	15	2001
	HBMEC	14	2007
Circulating EC	EPC	201	2001
	ECFC/OEC	39	2006
EC lines	HMEC-1	29	1994
	Ea.Hy926	54	1992

*Adapted from (265) and updated. A PubMed search was performed on November 16, 2022, using the keywords 'abbreviated cell type' or 'abbreviated cell type+s' linked to the keyword 'biomaterial' by AND as a Boolean function.
Abbreviations: EPC, endothelial progenitor cell; ECFC/OEC, endothelial colony forming cell/outgrowth endothelial cell; HAEC, human aortic endothelial cell; HCAEC, human coronary artery endothelial cell; HPAEC, human pulmonary artery endothelial cell; HUVEC, human umbilical vein endothelial cell; HDMEC, human dermal microvasculature endothelial cell; HPMEC, human pulmonary microvasculature endothelial cell; HBMEC, human brain microvasculature endothelial cell.

1.8.3. In Vivo Evaluation of Angiogenesis

Various *in vivo* assays have been developed throughout the years as they assess the complexity of the vascular network developing in the transplanted material.

1.8.3.1.Sponge Implant Model

Sponge implants are ideal for studying angiogenesis because they enable scientists to characterise some essential proteins and their role in neovascularisation (269, 270). Different synthetic materials can be used to obtain gel-like foams, which have uniform pore size and interconnective porosity and are chemically resistant and biocompatible (270). The sponge can be easily sterilised and then inserted into the animal model subcutaneously (269). New vessel

formation can be quantified by immunohistochemistry (IHC), the evaluation of blood/ haemoglobin content of the sponge or using radioactive tracers in the blood (271).

1.8.3.2.Matrigel Plug Assay

The Matrigel plug assay has been used to test *in vivo* pro- and anti-angiogenic activity of different components in animal models. Matrigel originated from a C57BL/6 mouse tumour, consists of laminin-111, collagen IV, heparan sulfate proteoglycans, and different growth factors, and offers a better resemblance of the natural environment to study any angiogenic reaction (271). The assay is reliable at different concentrations, easy to reproduce quantitively, and relatively fast (272, 273). It enables the test reagent(s) to be trapped in the gel and injected into the host animal subcutaneously. The liquid gel then forms a plug which allows the slow release of the reagents. The plugs are then discarded, and the tissue is assessed for neovascularisation (272).

1.8.3.3.Dorsal Air Sac Model

This model was designed for the *in vivo* evaluation of substance(s) to inhibit tumour angiogenesis (271). It includes a ring covered with filters (0.45 mm pore size) on both sides of a chamber filled with tumorigenic cells, which is implanted in the dorsal air sac of a mouse. Following removing the chamber, the angiogenic effect can be calculated by counting new vessels at the ring site. It is relatively easy to perform yet, requires competence, as the chamber layer needs to be carefully placed to eliminate false results.

1.9. Aim

Cardiac tissue engineering is a versatile branch of science that has the potential to save millions suffering from heart diseases. Despite major advances, engineering a spontaneously beating cardiac patch with a relevant size is still challenging, and many obstacles must be overcome. First, an appropriate cell source must be determined and obtained in an abundant number for clinical applications. Second, a biomimetic scaffold that overcomes mechanical challenges

such as mechanical load, elasticity and electrical stimulation should be designed to promote incorporation into the host tissue and efficient vascularisation.

This proposed study aimed to fabricate a composite porous scaffold of collagen type I, elastin, and HA on which hiPSC-CMs and HUVECs could be cultured. To encourage native capillary-like network formation throughout the scaffold *in vivo*, the scaffolds were designed with a parallel aligned channel system. This should enhance oxygen and nutrient delivery *in vivo* and also increase cell migration and proliferation *in vitro* prior to implantation. The artificial ECM structure composed of collagen type I would provide tensile strength that is essential to overcome the mechanical stresses (tension, shear, pressure) (274) and cell attachment encouraged by the RGD peptide domains that mediate cell adhesion and migration (275). Collagen and elastin would combine the structural strength and elasticity due to the high entropy of polypeptides. Elastic fibres would contact the cells in the surrounding environment, which mitigates mechanical stress arising from cell motility (276). Elastin composition might also provide a more consistent stretching ability for CMs. Since flexibility could only be maintained in a hydrated environment (277), combining the basal scaffold with HA was reasonable. Figure 1.7 summarises the design of this work. The outcomes of this thesis are discussed in the following chapters:

Chapter 2 summarizes the histological and mechanical characterisation of porcine cardiac tissue to determine the optimum mechanical properties to be translated into the scaffold design.

Chapter 3 explores how to fabricate different scaffold composites and characterise scaffold microstructure quantitatively and qualitatively to achieve the best design *in vitro* and *in vivo.*

Chapter 4 characterises hiPSC proliferation, differentiation of CMs, and HUVECs behaviour on composite scaffolds quantitatively and qualitatively.

Chapter 5 evaluates *in vivo* biocompatibility of acellular scaffolds in rats.

Chapter 6 summarizes the thesis work and gives future directions.

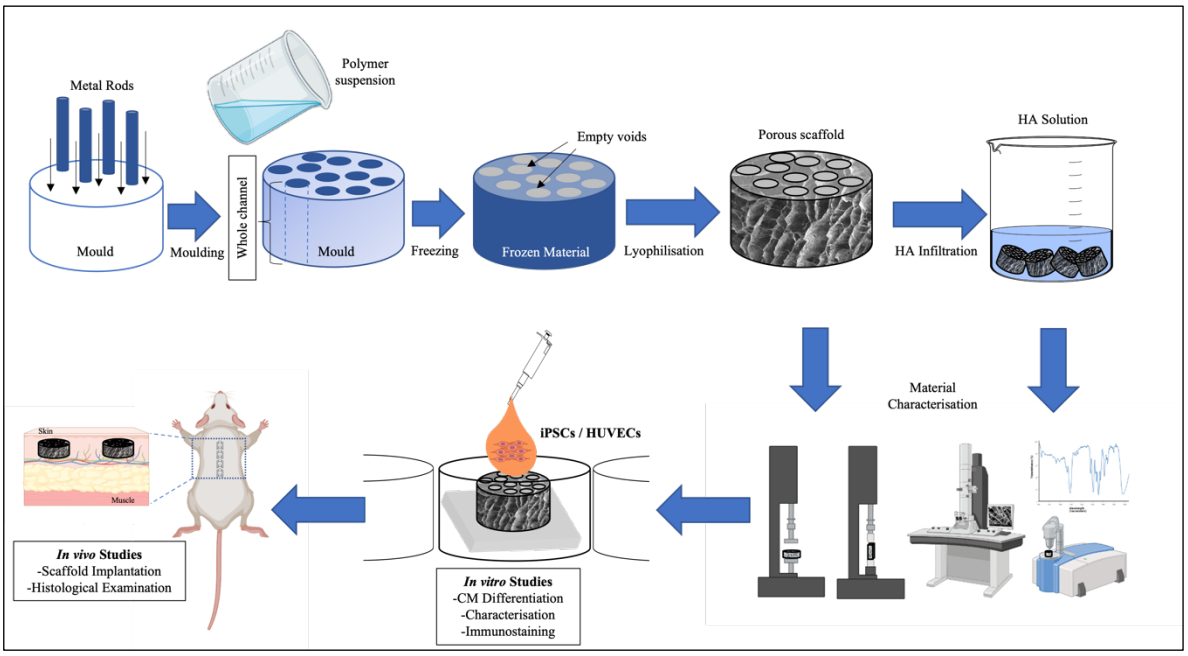


Figure 1.7. Summary of the thesis study. Composite scaffolds of collagen type I with/without elastin were fabricated by lyophilisation, and HA was infiltrated into the composites, respectively. The materials with different composition ratios were then characterised mechanically. The scaffolds were assessed for cell differentiation and behaviour *in vitro*. Histological examination was performed following the implantation of acellular scaffolds subcutaneously.

References

1. Simmonds LO, Nkechi; Rushton, Sally. Annual Report on Cardiothoracic Organ Transplantation 2021/22 NHS: Blood and Transplant: NHS England; 2022 [updated 2022. Available from: https://nhsbtdbe.blob.core.windows.net/umbraco-assets-corp/27816/nhsbt-annual-report-on-cardiothoracic-organ-transplantation-202122.pdf.

2. Langer R, Vacanti JP. Tissue engineering. Science. 1993;260(5110):920-6.

3. Gartner LP. Textbook of histology e-book: Elsevier Health Sciences; 2020.

4. Pawlina W, Ross MH. Histology: a text and atlas: with correlated cell and molecular biology: Lippincott Williams & Wilkins; 2018.

5. Nikitin NP, Loh PH, de Silva R, Witte KK, Lukaschuk EI, Parker A, et al. Left ventricular morphology, global and longitudinal function in normal older individuals: a cardiac magnetic resonance study. Int J Cardiol. 2006;108(1):76-83.

6. Sjogren AL. Left ventricular wall thickness determined by ultrasound in 100 subjects without heart disease. Chest. 1971;60(4):341-6.

7. Stolzmann P, Scheffel H, Leschka S, Schertler T, Frauenfelder T, Kaufmann PA, et al. Reference values for quantitative left ventricular and left atrial measurements in cardiac computed tomography. Eur Radiol. 2008;18(8):1625-34.

8. Banerjee I, Fuseler JW, Price RL, Borg TK, Baudino TA. Determination of cell types and numbers during cardiac development in the neonatal and adult rat and mouse. Am J Physiol Heart Circ Physiol. 2007;293(3):H1883-91.

9. Radisic M, Park H, Gerecht S, Cannizzaro C, Langer R, Vunjak-Novakovic G. Biomimetic approach to cardiac tissue engineering. Philos Trans R Soc Lond B Biol Sci. 2007;362(1484):1357-68.

10. Lesman A, Gepstein L, Levenberg S. Vascularization shaping the heart. Ann N Y Acad Sci. 2010;1188:46-51.

11. Patra C, Boccaccini AR, Engel FB. Vascularisation for cardiac tissue engineering: the extracellular matrix. Thromb Haemost. 2015;113(3):532-47.

12. Pinto AR, Ilinykh A, Ivey MJ, Kuwabara JT, D'Antoni ML, Debuque R, et al. Revisiting Cardiac Cellular Composition. Circ Res. 2016;118(3):400-9.

13. Ivey MJ, Tallquist MD. Defining the Cardiac Fibroblast. Circ J. 2016;80(11):2269-76.

14. Sussman MA, McCulloch A, Borg TK. Dance band on the Titanic: biomechanical signaling in cardiac hypertrophy. Circ Res. 2002;91(10):888-98.

15. Lanza R, Langer R, Vacanti JP, Atala A. Principles of tissue engineering: Academic press; 2020.

16. Weber KT. Cardiac interstitium in health and disease: the fibrillar collagen network. J Am Coll Cardiol. 1989;13(7):1637-52.

17. Wittig C, Szulcek R. Extracellular Matrix Protein Ratios in the Human Heart and Vessels: How to Distinguish Pathological From Physiological Changes? Frontiers in Physiology. 2021;12.

18. Paradis AN, Gay MS, Zhang L. Binucleation of cardiomyocytes: the transition from a proliferative to a terminally differentiated state. Drug Discov Today. 2014;19(5):602-9.

19. Parker KK, Ingber DE. Extracellular matrix, mechanotransduction and structural hierarchies in heart tissue engineering. Philos Trans R Soc Lond B Biol Sci. 2007;362(1484):1267-79.

20. Zhang J, Zhu W, Radisic M, Vunjak-Novakovic G. Can We Engineer a Human Cardiac Patch for Therapy? Circ Res. 2018;123(2):244-65.

21. Laflamme MA, Murry CE. Heart regeneration. Nature. 2011;473(7347):326-35.

22. Tsao CW, Aday AW, Almarzooq ZI, Alonso A, Beaton AZ, Bittencourt MS, et al. Heart Disease and Stroke Statistics-2022 Update: A Report From the American Heart Association. Circulation. 2022;145(8):e153-e639.

23. Barron HV, Bowlby LJ, Breen T, Rogers WJ, Canto JG, Zhang Y, et al. Use of reperfusion therapy for acute myocardial infarction in the United States: data from the National Registry of Myocardial Infarction 2. Circulation. 1998;97(12):1150-6.

24. Schömig A, Mehilli J, Antoniucci D, Ndrepepa G, Markwardt C, Di Pede F, et al. Mechanical Reperfusion in Patients With Acute Myocardial Infarction Presenting More Than 12 Hours From Symptom OnsetA Randomized Controlled Trial. JAMA. 2005;293(23):2865-72.

25. Atala A, Lanza R, Mikos T, Nerem R. Principles of regenerative medicine: Academic press; 2018.

26. Huang K, Hu S, Cheng K. A New Era of Cardiac Cell Therapy: Opportunities and Challenges. Adv Healthc Mater. 2019;8(2):e1801011.

27. Huang NF, Serpooshan V, Morris VB, Sayed N, Pardon G, Abilez OJ, et al. Big bottlenecks in cardiovascular tissue engineering. Commun Biol. 2018;1:199.

28. Hecker L, Birla RK. Engineering the heart piece by piece: state of the art in cardiac tissue engineering. Regen Med. 2007;2(2):125-44.

29. Rane AA, Christman KL. Biomaterials for the treatment of myocardial infarction: a 5-year update. J Am Coll Cardiol. 2011;58(25):2615-29.

30. Mantakaki A, Fakoya AOJ, Sharifpanah F. Recent advances and challenges on application of tissue engineering for treatment of congenital heart disease. PeerJ. 2018;6:e5805.

31. Zimmermann WH, Melnychenko I, Eschenhagen T. Engineered heart tissue for regeneration of diseased hearts. Biomaterials. 2004;25(9):1639-47.

32. Vunjak-Novakovic G, Tandon N, Godier A, Maidhof R, Marsano A, Martens TP, et al. Challenges in cardiac tissue engineering. Tissue Eng Part B Rev. 2010;16(2):169-87.

33. Kishino Y, Fukuda K. Unlocking the Pragmatic Potential of Regenerative Therapies in Heart Failure with Next-Generation Treatments. Biomedicines. 2023;11(3).

34. Chachques JC, Trainini JC, Lago N, Cortes-Morichetti M, Schussler O, Carpentier A. Myocardial Assistance by Grafting a New Bioartificial Upgraded Myocardium (MAGNUM trial): clinical feasibility study. Ann Thorac Surg. 2008;85(3):901-8.

35. Health NIo. U.S. National Library of Medicine; 2022 [updated 11/18/2022. Available from: https://clinicaltrials.gov/ct2/results?term=mesenchymal+stem+cells&cond=Cardiovascular+Diseases&Search=Apply&age_v=&gndr=&type=&rslt=.

36. Menasche P, Hagege AA, Scorsin M, Pouzet B, Desnos M, Duboc D, et al. Myoblast transplantation for heart failure. Lancet. 2001;357(9252):279-80.

37. Leobon B, Garcin I, Menasche P, Vilquin JT, Audinat E, Charpak S. Myoblasts transplanted into rat infarcted myocardium are functionally isolated from their host. Proc Natl Acad Sci U S A. 2003;100(13):7808-11.

38. Menasche P, Alfieri O, Janssens S, McKenna W, Reichenspurner H, Trinquart L, et al. The Myoblast Autologous Grafting in Ischemic Cardiomyopathy (MAGIC) trial: first randomized placebo-controlled study of myoblast transplantation. Circulation. 2008;117(9):1189-200.

39. Mabotuwana NS, Rech L, Lim J, Hardy SA, Murtha LA, Rainer PP, et al. Paracrine Factors Released by Stem Cells of Mesenchymal Origin and their Effects in Cardiovascular Disease: A Systematic Review of Pre-clinical Studies. Stem Cell Rev Rep. 2022;18(8):2606-28.

40. Soonpaa MH, Koh GY, Klug MG, Field LJ. Formation of nascent intercalated disks between grafted fetal cardiomyocytes and host myocardium. Science. 1994;264(5155):98-101.

41. Li RK, Jia ZQ, Weisel RD, Mickle DA, Choi A, Yau TM. Survival and function of bioengineered cardiac grafts. Circulation. 1999;100(19 Suppl):II63-9.

42. Li RK, Yau TM, Weisel RD, Mickle DA, Sakai T, Choi A, et al. Construction of a bioengineered cardiac graft. J Thorac Cardiovasc Surg. 2000;119(2):368-75.

43. Leor J, Aboulafia-Etzion S, Dar A, Shapiro L, Barbash IM, Battler A, et al. Bioengineered cardiac grafts: A new approach to repair the infarcted myocardium? Circulation. 2000;102(19 Suppl 3):III56-61.

44. Pittenger MF, Mackay AM, Beck SC, Jaiswal RK, Douglas R, Mosca JD, et al. Multilineage potential of adult human mesenchymal stem cells. Science. 1999;284(5411):143-7.

45. Pittenger MF, Martin BJ. Mesenchymal stem cells and their potential as cardiac therapeutics. Circ Res. 2004;95(1):9-20.

46. Ji ST, Kim H, Yun J, Chung JS, Kwon SM. Promising Therapeutic Strategies for Mesenchymal Stem Cell-Based Cardiovascular Regeneration: From Cell Priming to Tissue Engineering. Stem Cells Int. 2017;2017:3945403.

47. Braunwald E. Cell-Based Therapy in Cardiac Regeneration: An Overview. Circ Res. 2018;123(2):132-7.

48. Marbán E. Breakthroughs in cell therapy for heart disease: focus on cardiosphere-derived cells. Mayo Clin Proc. 2014;89(6):850-8.

49. Malliaras K, Li TS, Luthringer D, Terrovitis J, Cheng K, Chakravarty T, et al. Safety and efficacy of allogeneic cell therapy in infarcted rats transplanted with mismatched cardiosphere-derived cells. Circulation. 2012;125(1):100-12.

50. Carr CA, Stuckey DJ, Tan JJ, Tan SC, Gomes RS, Camelliti P, et al. Cardiosphere-derived cells improve function in the infarcted rat heart for at least 16 weeks--an MRI study. PLoS One. 2011;6(10):e25669.

51. Zhao Z-A, Han X, Lei W, Li J, Yang Z, Wu J, et al. Lack of cardiac improvement after cardiosphere-derived cell transplantation in aging mouse hearts. Circulation research. 2018;123(10):e21-e31.

52. Makkar RR, Smith RR, Cheng K, Malliaras K, Thomson LE, Berman D, et al. Intracoronary cardiosphere-derived cells for heart regeneration after myocardial infarction (CADUCEUS): a prospective, randomised phase 1 trial. Lancet. 2012;379(9819):895-904.

53. Malliaras K, Makkar RR, Smith RR, Cheng K, Wu E, Bonow RO, et al. Intracoronary cardiosphere-derived cells after myocardial infarction: evidence of therapeutic regeneration in the final 1-year results of the CADUCEUS trial (CArdiosphere-Derived aUtologous stem CElls to reverse ventricUlar dySfunction). J Am Coll Cardiol. 2014;63(2):110-22.

54. Liau B, Zhang D, Bursac N. Functional cardiac tissue engineering. Regen Med. 2012;7(2):187-206.

55. Evans MJ, Kaufman MH. Establishment in culture of pluripotential cells from mouse embryos. Nature. 1981;292(5819):154-6.

56. Xue T, Cho HC, Akar FG, Tsang SY, Jones SP, Marban E, et al. Functional integration of electrically active cardiac derivatives from genetically engineered human embryonic stem cells with quiescent recipient ventricular cardiomyocytes: insights into the development of cell-based pacemakers. Circulation. 2005;111(1):11-20.

57. Guo XM, Zhao YS, Chang HX, Wang CY, E LL, Zhang XA, et al. Creation of engineered cardiac tissue in vitro from mouse embryonic stem cells. Circulation. 2006;113(18):2229-37.

58. Caspi O, Lesman A, Basevitch Y, Gepstein A, Arbel G, Habib IH, et al. Tissue engineering of vascularized cardiac muscle from human embryonic stem cells. Circ Res. 2007;100(2):263-72.

59. Shimko VF, Claycomb WC. Effect of mechanical loading on three-dimensional cultures of embryonic stem cell-derived cardiomyocytes. Tissue Eng Part A. 2008;14(1):49-58.

60. Yang L, Soonpaa MH, Adler ED, Roepke TK, Kattman SJ, Kennedy M, et al. Human cardiovascular progenitor cells develop from a KDR+ embryonic-stem-cell-derived population. Nature. 2008;453(7194):524-8.

61. Liau B, Christoforou N, Leong KW, Bursac N. Pluripotent stem cell-derived cardiac tissue patch with advanced structure and function. Biomaterials. 2011;32(35):9180-7.

62. Chong JJ, Yang X, Don CW, Minami E, Liu YW, Weyers JJ, et al. Human embryonic-stem-cell-derived cardiomyocytes regenerate non-human primate hearts. Nature. 2014;510(7504):273-7.

63. Takahashi K, Yamanaka S. Induction of pluripotent stem cells from mouse embryonic and adult fibroblast cultures by defined factors. Cell. 2006;126(4):663-76.

64. Takahashi K, Tanabe K, Ohnuki M, Narita M, Ichisaka T, Tomoda K, et al. Induction of pluripotent stem cells from adult human fibroblasts by defined factors. Cell. 2007;131(5):861-72.

65. Takahashi K, Yamanaka S. Induced pluripotent stem cells in medicine and biology. Development. 2013;140(12):2457-61.

66. Eschenhagen T, Zimmermann WH. Engineering myocardial tissue. Circ Res. 2005;97(12):1220-31.

67. Zimmermann WH, Melnychenko I, Wasmeier G, Didie M, Naito H, Nixdorff U, et al. Engineered heart tissue grafts improve systolic and diastolic function in infarcted rat hearts. Nat Med. 2006;12(4):452-8.

68. Tulloch NL, Muskheli V, Razumova MV, Korte FS, Regnier M, Hauch KD, et al. Growth of engineered human myocardium with mechanical loading and vascular coculture. Circ Res. 2011;109(1):47-59.

69. Gao L, Kupfer ME, Jung JP, Yang L, Zhang P, Da Sie Y, et al. Myocardial Tissue Engineering With Cells Derived From Human-Induced Pluripotent Stem Cells and a Native-Like, High-Resolution, 3-Dimensionally Printed Scaffold. Circ Res. 2017;120(8):1318-25.

70. Gao L, Gregorich ZR, Zhu W, Mattapally S, Oduk Y, Lou X, et al. Large Cardiac Muscle Patches Engineered From Human Induced-Pluripotent Stem Cell-Derived Cardiac Cells Improve Recovery From Myocardial Infarction in Swine. Circulation. 2018;137(16):1712-30.

71. Zhang J, Wilson GF, Soerens AG, Koonce CH, Yu J, Palecek SP, et al. Functional cardiomyocytes derived from human induced pluripotent stem cells. Circ Res. 2009;104(4):e30-41.

72. Yan B, Abdelli LS, Singla DK. Transplanted induced pluripotent stem cells improve cardiac function and induce neovascularization in the infarcted hearts of db/db mice. Mol Pharm. 2011;8(5):1602-10.

73. Kawamura M, Miyagawa S, Miki K, Saito A, Fukushima S, Higuchi T, et al. Feasibility, safety, and therapeutic efficacy of human induced pluripotent stem cell-derived cardiomyocyte sheets in a porcine ischemic cardiomyopathy model. Circulation. 2012;126(11 Suppl 1):S29-37.

74. Nam YJ, Song K, Luo X, Daniel E, Lambeth K, West K, et al. Reprogramming of human fibroblasts toward a cardiac fate. Proc Natl Acad Sci U S A. 2013;110(14):5588-93.

75. Kawamura M, Miyagawa S, Fukushima S, Saito A, Miki K, Ito E, et al. Enhanced survival of transplanted human induced pluripotent stem cell-derived cardiomyocytes by the

combination of cell sheets with the pedicled omental flap technique in a porcine heart. Circulation. 2013;128(11 Suppl 1):S87-94.

76. Song G, Li X, Shen Y, Qian L, Kong X, Chen M, et al. Transplantation of iPSc Restores Cardiac Function by Promoting Angiogenesis and Ameliorating Cardiac Remodeling in a Post-infarcted Swine Model. Cell Biochem Biophys. 2015;71(3):1463-73.

77. Chen Y, Zeng D, Ding L, Li XL, Liu XT, Li WJ, et al. Three-dimensional poly-(epsilon-caprolactone) nanofibrous scaffolds directly promote the cardiomyocyte differentiation of murine-induced pluripotent stem cells through Wnt/beta-catenin signaling. BMC Cell Biol. 2015;16:22.

78. Weinberger F, Breckwoldt K, Pecha S, Kelly A, Geertz B, Starbatty J, et al. Cardiac repair in guinea pigs with human engineered heart tissue from induced pluripotent stem cells. Sci Transl Med. 2016;8(363):363ra148.

79. Ruan JL, Tulloch NL, Razumova MV, Saiget M, Muskheli V, Pabon L, et al. Mechanical Stress Conditioning and Electrical Stimulation Promote Contractility and Force Maturation of Induced Pluripotent Stem Cell-Derived Human Cardiac Tissue. Circulation. 2016;134(20):1557-67.

80. Kadota S, Pabon L, Reinecke H, Murry CE. In Vivo Maturation of Human Induced Pluripotent Stem Cell-Derived Cardiomyocytes in Neonatal and Adult Rat Hearts. Stem Cell Reports. 2017;8(2):278-89.

81. Vuorenpaa H, Penttinen K, Heinonen T, Pekkanen-Mattila M, Sarkanen JR, Ylikomi T, et al. Maturation of human pluripotent stem cell derived cardiomyocytes is improved in cardiovascular construct. Cytotechnology. 2017;69(5):785-800.

82. Ong CS, Fukunishi T, Zhang H, Huang CY, Nashed A, Blazeski A, et al. Biomaterial-Free Three-Dimensional Bioprinting of Cardiac Tissue using Human Induced Pluripotent Stem Cell Derived Cardiomyocytes. Sci Rep. 2017;7(1):4566.

83. Lemoine MD, Mannhardt I, Breckwoldt K, Prondzynski M, Flenner F, Ulmer B, et al. Human iPSC-derived cardiomyocytes cultured in 3D engineered heart tissue show physiological upstroke velocity and sodium current density. Sci Rep. 2017;7(1):5464.

84. Schaefer JA, Guzman PA, Riemenschneider SB, Kamp TJ, Tranquillo RT. A cardiac patch from aligned microvessel and cardiomyocyte patches. J Tissue Eng Regen Med. 2018;12(2):546-56.

85. Stevens KR, Murry CE. Human Pluripotent Stem Cell-Derived Engineered Tissues: Clinical Considerations. Cell Stem Cell. 2018;22(3):294-7.

86. Shao L, Wu WS. Gene-delivery systems for iPS cell generation. Expert Opin Biol Ther. 2010;10(2):231-42.

87. Hirt MN, Hansen A, Eschenhagen T. Cardiac tissue engineering: state of the art. Circ Res. 2014;114(2):354-67.

88. Lewandowski J, Kolanowski TJ, Kurpisz M. Techniques for the induction of human pluripotent stem cell differentiation towards cardiomyocytes. J Tissue Eng Regen Med. 2017;11(5):1658-74.

89. Radisic M, Christman KL. Materials science and tissue engineering: repairing the heart. Mayo Clin Proc. 2013;88(8):884-98.

90. Eschenhagen T, Fink C, Remmers U, Scholz H, Wattchow J, Weil J, et al. Three-dimensional reconstitution of embryonic cardiomyocytes in a collagen matrix: a new heart muscle model system. FASEB J. 1997;11(8):683-94.

91. Zimmermann WH, Fink C, Kralisch D, Remmers U, Weil J, Eschenhagen T. Three-dimensional engineered heart tissue from neonatal rat cardiac myocytes. Biotechnol Bioeng. 2000;68(1):106-14.

92. Leor J, Cohen S. Myocardial tissue engineering: creating a muscle patch for a wounded heart. Annals of the New York Academy of Sciences. 2004;1015(1):312-9.

93. Zimmermann WH, Cesnjevar R. Cardiac tissue engineering: implications for pediatric heart surgery. Pediatr Cardiol. 2009;30(5):716-23.

94. Taylor DA, Sampaio LC, Gobin A. Building new hearts: a review of trends in cardiac tissue engineering. Am J Transplant. 2014;14(11):2448-59.

95. Shadrin IY, Allen BW, Qian Y, Jackman CP, Carlson AL, Juhas ME, et al. Cardiopatch platform enables maturation and scale-up of human pluripotent stem cell-derived engineered heart tissues. Nat Commun. 2017;8(1):1825.

96. Radisic M, Euloth M, Yang L, Langer R, Freed LE, Vunjak-Novakovic G. High-density seeding of myocyte cells for cardiac tissue engineering. Biotechnol Bioeng. 2003;82(4):403-14.

97. Radisic M, Park H, Shing H, Consi T, Schoen FJ, Langer R, et al. Functional assembly of engineered myocardium by electrical stimulation of cardiac myocytes cultured on scaffolds. Proc Natl Acad Sci U S A. 2004;101(52):18129-34.

98. Radisic M, Marsano A, Maidhof R, Wang Y, Vunjak-Novakovic G. Cardiac tissue engineering using perfusion bioreactor systems. Nat Protoc. 2008;3(4):719-38.

99. Zhang D, Shadrin IY, Lam J, Xian HQ, Snodgrass HR, Bursac N. Tissue-engineered cardiac patch for advanced functional maturation of human ESC-derived cardiomyocytes. Biomaterials. 2013;34(23):5813-20.

100. Jackman CP, Ganapathi AM, Asfour H, Qian Y, Allen BW, Li Y, et al. Engineered cardiac tissue patch maintains structural and electrical properties after epicardial implantation. Biomaterials. 2018;159:48-58.

101. Discher DE, Janmey P, Wang Y-l. Tissue cells feel and respond to the stiffness of their substrate. Science. 2005;310(5751):1139-43.

102. Zhang J. Engineered Tissue Patch for Cardiac Cell Therapy. Curr Treat Options Cardiovasc Med. 2015;17(8):399.

103. Godier-Furnemont AF, Martens TP, Koeckert MS, Wan L, Parks J, Arai K, et al. Composite scaffold provides a cell delivery platform for cardiovascular repair. Proc Natl Acad Sci U S A. 2011;108(19):7974-9.

104. Li Y, Zhang D. Artificial Cardiac Muscle with or without the Use of Scaffolds. Biomed Res Int. 2017;2017:8473465.

105. Ott HC, Matthiesen TS, Goh SK, Black LD, Kren SM, Netoff TI, et al. Perfusion-decellularized matrix: using nature's platform to engineer a bioartificial heart. Nat Med. 2008;14(2):213-21.

106. French KM, Boopathy AV, DeQuach JA, Chingozha L, Lu H, Christman KL, et al. A naturally derived cardiac extracellular matrix enhances cardiac progenitor cell behavior in vitro. Acta Biomater. 2012;8(12):4357-64.

107. Dai W, Gerczuk P, Zhang Y, Smith L, Kopyov O, Kay GL, et al. Intramyocardial injection of heart tissue-derived extracellular matrix improves postinfarction cardiac function in rats. J Cardiovasc Pharmacol Ther. 2013;18(3):270-9.

108. Yanagawa B, Rao V, Yau TM, Cusimano RJ. Initial experience with intraventricular repair using CorMatrix extracellular matrix. Innovations (Phila). 2013;8(5):348-52.

109. Okano T, Yamada N, Sakai H, Sakurai Y. A novel recovery system for cultured cells using plasma-treated polystyrene dishes grafted with poly(N-isopropylacrylamide). J Biomed Mater Res. 1993;27(10):1243-51.

110. Yamada N, Okano T, Sakai H, Karikusa F, Sawasaki Y, Sakurai Y. Thermo-responsive polymeric surfaces; control of attachment and detachment of cultured cells. Die Makromolekulare Chemie, Rapid Communications. 1990;11(11):571-6.

111. Miyagawa S, Roth M, Saito A, Sawa Y, Kostin S. Tissue-engineered cardiac constructs for cardiac repair. Ann Thorac Surg. 2011;91(1):320-9.

112. Fujita J, Itabashi Y, Seki T, Tohyama S, Tamura Y, Sano M, et al. Myocardial cell sheet therapy and cardiac function. Am J Physiol Heart Circ Physiol. 2012;303(10):H1169-82.

113. Sekiya S, Shimizu T, Yamato M, Kikuchi A, Okano T. Bioengineered cardiac cell sheet grafts have intrinsic angiogenic potential. Biochem Biophys Res Commun. 2006;341(2):573-82.

114. Shimizu T, Sekine H, Yang J, Isoi Y, Yamato M, Kikuchi A, et al. Polysurgery of cell sheet grafts overcomes diffusion limits to produce thick, vascularized myocardial tissues. FASEB J. 2006;20(6):708-10.

115. Itabashi Y, Miyoshi S, Kawaguchi H, Yuasa S, Tanimoto K, Furuta A, et al. A new method for manufacturing cardiac cell sheets using fibrin-coated dishes and its electrophysiological studies by optical mapping. Artif Organs. 2005;29(2):95-103.

116. Miyahara Y, Nagaya N, Kataoka M, Yanagawa B, Tanaka K, Hao H, et al. Monolayered mesenchymal stem cells repair scarred myocardium after myocardial infarction. Nat Med. 2006;12(4):459-65.

117. Zhang D, Huang W, Dai B, Zhao T, Ashraf A, Millard RW, et al. Genetically manipulated progenitor cell sheet with diprotin A improves myocardial function and repair of infarcted hearts. Am J Physiol Heart Circ Physiol. 2010;299(5):H1339-47.

118. Hamdi H, Planat-Benard V, Bel A, Puymirat E, Geha R, Pidial L, et al. Epicardial adipose stem cell sheets results in greater post-infarction survival than intramyocardial injections. Cardiovasc Res. 2011;91(3):483-91.

119. Masumoto H, Matsuo T, Yamamizu K, Uosaki H, Narazaki G, Katayama S, et al. Pluripotent stem cell-engineered cell sheets reassembled with defined cardiovascular populations ameliorate reduction in infarct heart function through cardiomyocyte-mediated neovascularization. Stem Cells. 2012;30(6):1196-205.

120. Matsuura K, Wada M, Shimizu T, Haraguchi Y, Sato F, Sugiyama K, et al. Creation of human cardiac cell sheets using pluripotent stem cells. Biochem Biophys Res Commun. 2012;425(2):321-7.

121. Zakharova L, Mastroeni D, Mutlu N, Molina M, Goldman S, Diethrich E, et al. Transplantation of cardiac progenitor cell sheet onto infarcted heart promotes cardiogenesis and improves function. Cardiovasc Res. 2010;87(1):40-9.

122. Miyagawa S, Sawa Y, Sakakida S, Taketani S, Kondoh H, Memon IA, et al. Tissue cardiomyoplasty using bioengineered contractile cardiomyocyte sheets to repair damaged myocardium: their integration with recipient myocardium. Transplantation. 2005;80(11):1586-95.

123. Furuta A, Miyoshi S, Itabashi Y, Shimizu T, Kira S, Hayakawa K, et al. Pulsatile cardiac tissue grafts using a novel three-dimensional cell sheet manipulation technique functionally integrates with the host heart, in vivo. Circ Res. 2006;98(5):705-12.

124. Haraguchi Y, Shimizu T, Yamato M, Kikuchi A, Okano T. Electrical coupling of cardiomyocyte sheets occurs rapidly via functional gap junction formation. Biomaterials. 2006;27(27):4765-74.

125. Kondoh H, Sawa Y, Miyagawa S, Sakakida-Kitagawa S, Memon IA, Kawaguchi N, et al. Longer preservation of cardiac performance by sheet-shaped myoblast implantation in dilated cardiomyopathic hamsters. Cardiovasc Res. 2006;69(2):466-75.

126. Hoashi T, Matsumiya G, Miyagawa S, Ichikawa H, Ueno T, Ono M, et al. Skeletal myoblast sheet transplantation improves the diastolic function of a pressure-overloaded right heart. J Thorac Cardiovasc Surg. 2009;138(2):460-7.

127. Itabashi Y, Miyoshi S, Yuasa S, Fujita J, Shimizu T, Okano T, et al. Analysis of the electrophysiological properties and arrhythmias in directly contacted skeletal and cardiac muscle cell sheets. Cardiovasc Res. 2005;67(3):561-70.

128. Kobayashi H, Shimizu T, Yamato M, Tono K, Masuda H, Asahara T, et al. Fibroblast sheets co-cultured with endothelial progenitor cells improve cardiac function of infarcted hearts. J Artif Organs. 2008;11(3):141-7.

129. Shudo Y, Cohen JE, Macarthur JW, Atluri P, Hsiao PF, Yang EC, et al. Spatially oriented, temporally sequential smooth muscle cell-endothelial progenitor cell bi-level cell sheet neovascularizes ischemic myocardium. Circulation. 2013;128(11 Suppl 1):S59-68.

130. Sekine H, Shimizu T, Sakaguchi K, Dobashi I, Wada M, Yamato M, et al. In vitro fabrication of functional three-dimensional tissues with perfusable blood vessels. Nat Commun. 2013;4:1399.

131. Murugan R, Ramakrishna S. Design strategies of tissue engineering scaffolds with controlled fiber orientation. Tissue Eng. 2007;13(8):1845-66.

132. Carrier RL, Papadaki M, Rupnick M, Schoen FJ, Bursac N, Langer R, et al. Cardiac tissue engineering: cell seeding, cultivation parameters, and tissue construct characterization. Biotechnol Bioeng. 1999;64(5):580-9.

133. Carrier RL, Rupnick M, Langer R, Schoen FJ, Freed LE, Vunjak-Novakovic G. Perfusion improves tissue architecture of engineered cardiac muscle. Tissue Eng. 2002;8(2):175-88.

134. Kenar H, Kose GT, Hasirci V. Design of a 3D aligned myocardial tissue construct from biodegradable polyesters. J Mater Sci Mater Med. 2010;21(3):989-97.

135. Kharaziha M, Nikkhah M, Shin SR, Annabi N, Masoumi N, Gaharwar AK, et al. PGS:Gelatin nanofibrous scaffolds with tunable mechanical and structural properties for engineering cardiac tissues. Biomaterials. 2013;34(27):6355-66.

136. Serpooshan V, Zhao M, Metzler SA, Wei K, Shah PB, Wang A, et al. The effect of bioengineered acellular collagen patch on cardiac remodeling and ventricular function post myocardial infarction. Biomaterials. 2013;34(36):9048-55.

137. Feiner R, Engel L, Fleischer S, Malki M, Gal I, Shapira A, et al. Engineered hybrid cardiac patches with multifunctional electronics for online monitoring and regulation of tissue function. Nat Mater. 2016;15(6):679-85.

138. Fleischer S, Shapira A, Feiner R, Dvir T. Modular assembly of thick multifunctional cardiac patches. Proc Natl Acad Sci U S A. 2017;114(8):1898-903.

139. Kenar H, Ozdogan CY, Dumlu C, Doger E, Kose GT, Hasirci V. Microfibrous scaffolds from poly(l-lactide-co-epsilon-caprolactone) blended with xeno-free collagen/hyaluronic acid for improvement of vascularization in tissue engineering applications. Mater Sci Eng C Mater Biol Appl. 2019;97:31-44.

140. Walker BW, Lara RP, Yu CH, Sani ES, Kimball W, Joyce S, et al. Engineering a naturally-derived adhesive and conductive cardiopatch. Biomaterials. 2019;207:89-101.

141. Handorf AM, Zhou Y, Halanski MA, Li WJ. Tissue stiffness dictates development, homeostasis, and disease progression. Organogenesis. 2015;11(1):1-15.

142. Ahmed EM. Hydrogel: Preparation, characterization, and applications: A review. J Adv Res. 2015;6(2):105-21.

143. Zimmermann WH, Schneiderbanger K, Schubert P, Didie M, Munzel F, Heubach JF, et al. Tissue engineering of a differentiated cardiac muscle construct. Circ Res. 2002;90(2):223-30.

144. Jabbour RJ, Owen TJ, Pandey P, Reinsch M, Wang B, King O, et al. In vivo grafting of large engineered heart tissue patches for cardiac repair. JCI insight. 2021;6(15).

145. Querdel E, Reinsch M, Castro L, Köse D, Bähr A, Reich S, et al. Human engineered heart tissue patches remuscularize the injured heart in a dose-dependent manner. Circulation. 2021;143(20):1991-2006.

146. Morritt AN, Bortolotto SK, Dilley RJ, Han X, Kompa AR, McCombe D, et al. Cardiac tissue engineering in an in vivo vascularized chamber. Circulation. 2007;115(3):353-60.

147. Madden LR, Mortisen DJ, Sussman EM, Dupras SK, Fugate JA, Cuy JL, et al. Proangiogenic scaffolds as functional templates for cardiac tissue engineering. Proc Natl Acad Sci U S A. 2010;107(34):15211-6.

148. Young JL, Engler AJ. Hydrogels with time-dependent material properties enhance cardiomyocyte differentiation in vitro. Biomaterials. 2011;32(4):1002-9.

149. Chiu LL, Montgomery M, Liang Y, Liu H, Radisic M. Perfusable branching microvessel bed for vascularization of engineered tissues. Proc Natl Acad Sci U S A. 2012;109(50):E3414-23.

150. Bejleri D, Streeter BW, Nachlas ALY, Brown ME, Gaetani R, Christman KL, et al. A Bioprinted Cardiac Patch Composed of Cardiac-Specific Extracellular Matrix and Progenitor Cells for Heart Repair. Adv Healthc Mater. 2018;7(23):e1800672.

151. Edri R, Gal I, Noor N, Harel T, Fleischer S, Adadi N, et al. Personalized Hydrogels for Engineering Diverse Fully Autologous Tissue Implants. Adv Mater. 2019;31(1):e1803895.

152. Noor N, Shapira A, Edri R, Gal I, Wertheim L, Dvir T. 3D printing of personalized thick and perfusable cardiac patches and hearts. Advanced science. 2019;6(11):1900344.

153. Health NIo. Safety and Efficacy of Induced Pluripotent Stem Cell-derived Engineered Human Myocardium as Biological Ventricular Assist Tissue in Terminal Heart Failure (BioVAT-HF) 2023 [Available from: https://clinicaltrials.gov/ct2/show/NCT04396899.

154. Xu Y, Guan J. Biomaterial property-controlled stem cell fates for cardiac regeneration. Bioact Mater. 2016;1(1):18-28.

155. Dvir T, Benishti N, Shachar M, Cohen S. A novel perfusion bioreactor providing a homogenous milieu for tissue regeneration. Tissue Eng. 2006;12(10):2843-52.

156. Perng CK, Wang YJ, Tsi CH, Ma H. In vivo angiogenesis effect of porous collagen scaffold with hyaluronic acid oligosaccharides. J Surg Res. 2011;168(1):9-15.

157. Montgomery M, Ahadian S, Davenport Huyer L, Lo Rito M, Civitarese RA, Vanderlaan RD, et al. Flexible shape-memory scaffold for minimally invasive delivery of functional tissues. Nat Mater. 2017;16(10):1038-46.

158. Radisic M, Deen W, Langer R, Vunjak-Novakovic G. Mathematical model of oxygen distribution in engineered cardiac tissue with parallel channel array perfused with culture medium containing oxygen carriers. Am J Physiol Heart Circ Physiol. 2005;288(3):H1278-89.

159. Sheridan MH, Shea LD, Peters MC, Mooney DJ. Bioabsorbable polymer scaffolds for tissue engineering capable of sustained growth factor delivery. J Control Release. 2000;64(1-3):91-102.

160. Engelmayr GC, Jr., Cheng M, Bettinger CJ, Borenstein JT, Langer R, Freed LE. Accordion-like honeycombs for tissue engineering of cardiac anisotropy. Nat Mater. 2008;7(12):1003-10.

161. Bhana B, Iyer RK, Chen WL, Zhao R, Sider KL, Likhitpanichkul M, et al. Influence of substrate stiffness on the phenotype of heart cells. Biotechnol Bioeng. 2010;105(6):1148-60.

162. Radisic M, Yang L, Boublik J, Cohen RJ, Langer R, Freed LE, et al. Medium perfusion enables engineering of compact and contractile cardiac tissue. Am J Physiol Heart Circ Physiol. 2004;286(2):H507-16.

163. Chiu LL, Radisic M. Scaffolds with covalently immobilized VEGF and Angiopoietin-1 for vascularization of engineered tissues. Biomaterials. 2010;31(2):226-41.

164. Schwarzkopf R, Shachar M, Dvir T, Dayan Y, Holbova R, Leor J, et al. Autospecies and post-myocardial infarction sera enhance the viability, proliferation, and maturation of 3D cardiac cell culture. Tissue Eng. 2006;12(12):3467-75.

165. Dvir T, Kedem A, Ruvinov E, Levy O, Freeman I, Landa N, et al. Prevascularization of cardiac patch on the omentum improves its therapeutic outcome. Proc Natl Acad Sci U S A. 2009;106(35):14990-5.

166. Gao J, Crapo PM, Wang Y. Macroporous elastomeric scaffolds with extensive micropores for soft tissue engineering. Tissue Eng. 2006;12(4):917-25.

167. Radisic M, Park H, Martens TP, Salazar-Lazaro JE, Geng W, Wang Y, et al. Pre-treatment of synthetic elastomeric scaffolds by cardiac fibroblasts improves engineered heart tissue. J Biomed Mater Res A. 2008;86(3):713-24.

168. Sugiura T, Hibino N, Breuer CK, Shinoka T. Tissue-engineered cardiac patch seeded with human induced pluripotent stem cell derived cardiomyocytes promoted the regeneration of host cardiomyocytes in a rat model. J Cardiothorac Surg. 2016;11(1):163.

169. Choi SW, Zhang Y, Macewan MR, Xia Y. Neovascularization in biodegradable inverse opal scaffolds with uniform and precisely controlled pore sizes. Adv Healthc Mater. 2013;2(1):145-54.

170. Alberts B, Bray D, Hopkin K, Johnson AD, Lewis J, Raff M, et al. Essential cell biology: Garland Science; 2015.

171. Kofidis T, Akhyari P, Boublik J, Theodorou P, Martin U, Ruhparwar A, et al. In vitro engineering of heart muscle: artificial myocardial tissue. J Thorac Cardiovasc Surg. 2002;124(1):63-9.

172. Yost MJ, Baicu CF, Stonerock CE, Goodwin RL, Price RL, Davis JM, et al. A novel tubular scaffold for cardiovascular tissue engineering. Tissue Eng. 2004;10(1-2):273-84.

173. Brown DA, MacLellan WR, Laks H, Dunn JC, Wu BM, Beygui RE. Analysis of oxygen transport in a diffusion-limited model of engineered heart tissue. Biotechnol Bioeng. 2007;97(4):962-75.

174. Yamamura N, Sudo R, Ikeda M, Tanishita K. Effects of the mechanical properties of collagen gel on the in vitro formation of microvessel networks by endothelial cells. Tissue Eng. 2007;13(7):1443-53.

175. Tandon N, Marsano A, Maidhof R, Wan L, Park H, Vunjak-Novakovic G. Optimization of electrical stimulation parameters for cardiac tissue engineering. J Tissue Eng Regen Med. 2011;5(6):e115-25.

176. Blackburn NJ, Sofrenovic T, Kuraitis D, Ahmadi A, McNeill B, Deng C, et al. Timing underpins the benefits associated with injectable collagen biomaterial therapy for the treatment of myocardial infarction. Biomaterials. 2015;39:182-92.

177. Nielsen SH, Mouton AJ, DeLeon-Pennell KY, Genovese F, Karsdal M, Lindsey ML. Understanding cardiac extracellular matrix remodeling to develop biomarkers of myocardial infarction outcomes. Matrix Biol. 2019;75-76:43-57.

178. Belbachir K, Noreen R, Gouspillou G, Petibois C. Collagen types analysis and differentiation by FTIR spectroscopy. Anal Bioanal Chem. 2009;395(3):829-37.

179. Rich A, Crick FH. The molecular structure of collagen. J Mol Biol. 1961;3:483-506.

180. Corey RB, Pauling L. Fundamental dimensions of polypeptide chains. Proc R Soc Lond B Biol Sci. 1953;141(902):10-20.

181. Ramachandran GN, Kartha G. Structure of collagen. Nature. 1954;174(4423):269-70.

182. Ramachandran GN, Kartha G. Structure of collagen. Nature. 1955;176(4482):593-5.

183. Ramachandran GN. Structure of collagen. Nature. 1956;177(4511):710-1.

184. Fraser RD, MacRae TP, Miller A. Molecular packing in type I collagen fibrils. J Mol Biol. 1987;193(1):115-25.

185. Shoulders MD, Raines RT. Collagen structure and stability. Annual review of biochemistry. 2009;78:929-58.

186. Ramachandran G, Bansal M, Bhatnagar R. A hypothesis on the role of hydroxyproline in stabilizing collagen structure. Biochimica et Biophysica Acta (BBA)-Protein Structure. 1973;322(1):166-71.

187. Heino J. The collagen family members as cell adhesion proteins. Bioessays. 2007;29(10):1001-10.

188. Lockhart M, Wirrig E, Phelps A, Wessels A. Extracellular matrix and heart development. Birth Defects Res A Clin Mol Teratol. 2011;91(6):535-50.

189. Eghbali M, Weber KT. Collagen and the myocardium: fibrillar structure, biosynthesis and degradation in relation to hypertrophy and its regression. Mol Cell Biochem. 1990;96(1):1-14.

190. Weber KT, Sun Y, Tyagi SC, Cleutjens JP. Collagen network of the myocardium: function, structural remodeling and regulatory mechanisms. J Mol Cell Cardiol. 1994;26(3):279-92.

191. Cleutjens JP. The role of matrix metalloproteinases in heart disease. Cardiovascular research. 1996;32(5):816-21.

192. Ricard-Blum S. The collagen family. Cold Spring Harb Perspect Biol. 2011;3(1):a004978.

193. Domenech M, Polo-Corrales L, Ramirez-Vick JE, Freytes DO. Tissue Engineering Strategies for Myocardial Regeneration: Acellular Versus Cellular Scaffolds? Tissue Eng Part B Rev. 2016;22(6):438-58.

194. de Souza RR. Aging of myocardial collagen. Biogerontology. 2002;3(6):325-35.

195. Xiang Z, Liao R, Kelly MS, Spector M. Collagen-GAG scaffolds grafted onto myocardial infarcts in a rat model: a delivery vehicle for mesenchymal stem cells. Tissue Eng. 2006;12(9):2467-78.

196. Callegari A, Bollini S, Iop L, Chiavegato A, Torregrossa G, Pozzobon M, et al. Neovascularization induced by porous collagen scaffold implanted on intact and cryoinjured rat hearts. Biomaterials. 2007;28(36):5449-61.

197. Gaballa MA, Sunkomat JN, Thai H, Morkin E, Ewy G, Goldman S. Grafting an acellular 3-dimensional collagen scaffold onto a non-transmural infarcted myocardium induces neo-angiogenesis and reduces cardiac remodeling. J Heart Lung Transplant. 2006;25(8):946-54.

198. Cortes-Morichetti M, Frati G, Schussler O, Duong Van Huyen JP, Lauret E, Genovese JA, et al. Association between a cell-seeded collagen matrix and cellular cardiomyoplasty for myocardial support and regeneration. Tissue Eng. 2007;13(11):2681-7.

199. Miyagi Y, Chiu LL, Cimini M, Weisel RD, Radisic M, Li RK. Biodegradable collagen patch with covalently immobilized VEGF for myocardial repair. Biomaterials. 2011;32(5):1280-90.

200. Ahmadi A, McNeill B, Vulesevic B, Kordos M, Mesana L, Thorn S, et al. The role of integrin alpha2 in cell and matrix therapy that improves perfusion, viability and function of infarcted myocardium. Biomaterials. 2014;35(17):4749-58.

201. Shi C, Li Q, Zhao Y, Chen W, Chen B, Xiao Z, et al. Stem-cell-capturing collagen scaffold promotes cardiac tissue regeneration. Biomaterials. 2011;32(10):2508-15.

202. Maureira P, Marie PY, Yu F, Poussier S, Liu Y, Groubatch F, et al. Repairing chronic myocardial infarction with autologous mesenchymal stem cells engineered tissue in rat promotes angiogenesis and limits ventricular remodeling. J Biomed Sci. 2012;19:93.

203. Ruping Q, Kuken B, Huang Y, Sun J, Azhati A. Effection of myocardial cell/collagen compound on ventricular electrophysiology in rats with myocardial infarction. Eur Rev Med Pharmacol Sci. 2016;20(11):2357-62.

204. Hamdi H, Planat-Benard V, Bel A, Neamatalla H, Saccenti L, Calderon D, et al. Long-term functional benefits of epicardial patches as cell carriers. Cell Transplant. 2014;23(1):87-96.

205. Arana M, Pena E, Abizanda G, Cilla M, Ochoa I, Gavira JJ, et al. Preparation and characterization of collagen-based ADSC-carrier sheets for cardiovascular application. Acta Biomater. 2013;9(4):6075-83.

206. Arana M, Gavira JJ, Pena E, Gonzalez A, Abizanda G, Cilla M, et al. Epicardial delivery of collagen patches with adipose-derived stem cells in rat and minipig models of chronic myocardial infarction. Biomaterials. 2014;35(1):143-51.

207. Rabotyagova OS, Cebe P, Kaplan DL. Collagen Structural Hierarchy and Susceptibility to Degradation by Ultraviolet Radiation. Mater Sci Eng C Mater Biol Appl. 2008;28(8):1420-9.

208. Patino MG, Neiders ME, Andreana S, Noble B, Cohen RE. Collagen: an overview. Implant Dent. 2002;11(3):280-5.

209. Engler AJ, Carag-Krieger C, Johnson CP, Raab M, Tang HY, Speicher DW, et al. Embryonic cardiomyocytes beat best on a matrix with heart-like elasticity: scar-like rigidity inhibits beating. J Cell Sci. 2008;121(Pt 22):3794-802.

210. Berry MF, Engler AJ, Woo YJ, Pirolli TJ, Bish LT, Jayasankar V, et al. Mesenchymal stem cell injection after myocardial infarction improves myocardial compliance. Am J Physiol Heart Circ Physiol. 2006;290(6):H2196-203.

211. Rnjak-Kovacina J, Wise SG, Li Z, Maitz PK, Young CJ, Wang Y, et al. Electrospun synthetic human elastin:collagen composite scaffolds for dermal tissue engineering. Acta Biomater. 2012;8(10):3714-22.

212. Zhang B, Montgomery M, Chamberlain MD, Ogawa S, Korolj A, Pahnke A, et al. Biodegradable scaffold with built-in vasculature for organ-on-a-chip engineering and direct surgical anastomosis. Nat Mater. 2016;15(6):669-78.

213. Kielty CM, Sherratt MJ, Shuttleworth CA. Elastic fibres. J Cell Sci. 2002;115(Pt 14):2817-28.

214. Wise SG, Weiss AS. Tropoelastin. Int J Biochem Cell Biol. 2009;41(3):494-7.

215. Mecham R. The extracellular matrix: an overview. 2011.

216. Cocciolone AJ, Hawes JZ, Staiculescu MC, Johnson EO, Murshed M, Wagenseil JE. Elastin, arterial mechanics, and cardiovascular disease. Am J Physiol Heart Circ Physiol. 2018;315(2):H189-H205.

217. Debelle L, Tamburro AM. Elastin: molecular description and function. Int J Biochem Cell Biol. 1999;31(2):261-72.

218. Wise SG, Yeo GC, Hiob MA, Rnjak-Kovacina J, Kaplan DL, Ng MK, et al. Tropoelastin: a versatile, bioactive assembly module. Acta Biomater. 2014;10(4):1532-41.

219. Shapiro SD, Endicott SK, Province MA, Pierce JA, Campbell EJ. Marked longevity of human lung parenchymal elastic fibers deduced from prevalence of D-aspartate and nuclear weapons-related radiocarbon. J Clin Invest. 1991;87(5):1828-34.

220. de Carvalho Filho ET, de Carvalho CA, de Souza RR. Age-related changes in elastic fibers of human heart. Gerontology. 1996;42(4):211-7.

221. Yu Y, Yin G, Bao S, Guo Z. Kinetic alterations of collagen and elastic fibres and their association with cardiac function in acute myocardial infarction. Mol Med Rep. 2018;17(3):3519-26.

222. Mizuno T, Mickle DA, Kiani CG, Li RK. Overexpression of elastin fragments in infarcted myocardium attenuates scar expansion and heart dysfunction. Am J Physiol Heart Circ Physiol. 2005;288(6):H2819-27.

223. Baldock C, Oberhauser AF, Ma L, Lammie D, Siegler V, Mithieux SM, et al. Shape of tropoelastin, the highly extensible protein that controls human tissue elasticity. Proc Natl Acad Sci U S A. 2011;108(11):4322-7.

224. Li L, Qian Y, Jiang C, Lv Y, Liu W, Zhong L, et al. The use of hyaluronan to regulate protein adsorption and cell infiltration in nanofibrous scaffolds. Biomaterials. 2012;33(12):3428-45.

225. Van der Donckt C, Van Herck JL, Schrijvers DM, Vanhoutte G, Verhoye M, Blockx I, et al. Elastin fragmentation in atherosclerotic mice leads to intraplaque neovascularization, plaque rupture, myocardial infarction, stroke, and sudden death. Eur Heart J. 2015;36(17):1049-58.

226. Almine JF, Bax DV, Mithieux SM, Nivison-Smith L, Rnjak J, Waterhouse A, et al. Elastin-based materials. Chem Soc Rev. 2010;39(9):3371-9.

227. Mithieux SM, Tu Y, Korkmaz E, Braet F, Weiss AS. In situ polymerization of tropoelastin in the absence of chemical cross-linking. Biomaterials. 2009;30(4):431-5.

228. Rnjak J, Li Z, Maitz PK, Wise SG, Weiss AS. Primary human dermal fibroblast interactions with open weave three-dimensional scaffolds prepared from synthetic human elastin. Biomaterials. 2009;30(32):6469-77.

229. Annabi N, Mithieux SM, Zorlutuna P, Camci-Unal G, Weiss AS, Khademhosseini A. Engineered cell-laden human protein-based elastomer. Biomaterials. 2013;34(22):5496-505.

230. Li M, Mondrinos MJ, Gandhi MR, Ko FK, Weiss AS, Lelkes PI. Electrospun protein fibers as matrices for tissue engineering. Biomaterials. 2005;26(30):5999-6008.

231. Nivison-Smith L, Rnjak J, Weiss AS. Synthetic human elastin microfibers: stable cross-linked tropoelastin and cell interactive constructs for tissue engineering applications. Acta Biomater. 2010;6(2):354-9.

232. Liu Y, Xu Y, Wang Z, Wen D, Zhang W, Schmull S, et al. Electrospun nanofibrous sheets of collagen/elastin/polycaprolactone improve cardiac repair after myocardial infarction. Am J Transl Res. 2016;8(4):1678-94.

233. Mondschein RJ, Kanitkar A, Williams CB, Verbridge SS, Long TE. Polymer structure-property requirements for stereolithographic 3D printing of soft tissue engineering scaffolds. Biomaterials. 2017;140:170-88.

234. Stick RV, Williams S. Carbohydrates: the essential molecules of life: Elsevier; 2010.

235. Schanté CE, Zuber G, Herlin C, Vandamme TF. Chemical modifications of hyaluronic acid for the synthesis of derivatives for a broad range of biomedical applications. Carbohydrate polymers. 2011;85(3):469-89.

236. Toole BP. Hyaluronan in morphogenesis. J Intern Med. 1997;242(1):35-40.

237. Li SH, Sun Z, Guo L, Han M, Wood MF, Ghosh N, et al. Elastin overexpression by cell-based gene therapy preserves matrix and prevents cardiac dilation. J Cell Mol Med. 2012;16(10):2429-39.

238. Khetan S, Guvendiren M, Legant WR, Cohen DM, Chen CS, Burdick JA. Degradation-mediated cellular traction directs stem cell fate in covalently crosslinked three-dimensional hydrogels. Nat Mater. 2013;12(5):458-65.

239. Yoon SJ, Fang YH, Lim CH, Kim BS, Son HS, Park Y, et al. Regeneration of ischemic heart using hyaluronic acid-based injectable hydrogel. J Biomed Mater Res B Appl Biomater. 2009;91(1):163-71.

240. Chi NH, Yang MC, Chung TW, Chen JY, Chou NK, Wang SS. Cardiac repair achieved by bone marrow mesenchymal stem cells/silk fibroin/hyaluronic acid patches in a rat of myocardial infarction model. Biomaterials. 2012;33(22):5541-51.

241. Abdalla S, Makhoul G, Duong M, Chiu RC, Cecere R. Hyaluronic acid-based hydrogel induces neovascularization and improves cardiac function in a rat model of myocardial infarction. Interact Cardiovasc Thorac Surg. 2013;17(5):767-72.

242. Masters KS, Shah DN, Walker G, Leinwand LA, Anseth KS. Designing scaffolds for valvular interstitial cells: cell adhesion and function on naturally derived materials. J Biomed Mater Res A. 2004;71(1):172-80.

243. Ifkovits JL, Tous E, Minakawa M, Morita M, Robb JD, Koomalsingh KJ, et al. Injectable hydrogel properties influence infarct expansion and extent of postinfarction left ventricular remodeling in an ovine model. Proc Natl Acad Sci U S A. 2010;107(25):11507-12.

244. Jacot JG, McCulloch AD, Omens JH. Substrate stiffness affects the functional maturation of neonatal rat ventricular myocytes. Biophys J. 2008;95(7):3479-87.

245. Akhyari P, Kamiya H, Haverich A, Karck M, Lichtenberg A. Myocardial tissue engineering: the extracellular matrix. Eur J Cardiothorac Surg. 2008;34(2):229-41.

246. Daamen WF, van Moerkerk HT, Hafmans T, Buttafoco L, Poot AA, Veerkamp JH, et al. Preparation and evaluation of molecularly-defined collagen-elastin-glycosaminoglycan scaffolds for tissue engineering. Biomaterials. 2003;24(22):4001-9.

247. Ryan AJ, O'Brien FJ. Insoluble elastin reduces collagen scaffold stiffness, improves viscoelastic properties, and induces a contractile phenotype in smooth muscle cells. Biomaterials. 2015;73:296-307.

248. Shimizu T, Yamato M, Isoi Y, Akutsu T, Setomaru T, Abe K, et al. Fabrication of pulsatile cardiac tissue grafts using a novel 3-dimensional cell sheet manipulation technique and temperature-responsive cell culture surfaces. Circ Res. 2002;90(3):e40.

249. Wendel JS, Ye L, Zhang P, Tranquillo RT, Zhang JJ. Functional consequences of a tissue-engineered myocardial patch for cardiac repair in a rat infarct model. Tissue Eng Part A. 2014;20(7-8):1325-35.

250. Wendel JS, Ye L, Tao R, Zhang J, Zhang J, Kamp TJ, et al. Functional Effects of a Tissue-Engineered Cardiac Patch From Human Induced Pluripotent Stem Cell-Derived Cardiomyocytes in a Rat Infarct Model. Stem Cells Transl Med. 2015;4(11):1324-32.

251. Yang H, Wei L, Liu C, Zhong W, Li B, Chen Y, et al. Engineering human ventricular heart tissue based on macroporous iron oxide scaffolds. Acta Biomater. 2019;88:540-53.

252. Ye L, Chang YH, Xiong Q, Zhang P, Zhang L, Somasundaram P, et al. Cardiac repair in a porcine model of acute myocardial infarction with human induced pluripotent stem cell-derived cardiovascular cells. Cell Stem Cell. 2014;15(6):750-61.

253. Tiburcy M, Hudson JE, Balfanz P, Schlick S, Meyer T, Chang Liao ML, et al. Defined Engineered Human Myocardium With Advanced Maturation for Applications in Heart Failure Modeling and Repair. Circulation. 2017;135(19):1832-47.

254. Montgomery M, Zhang B, Radisic M. Cardiac Tissue Vascularization: From Angiogenesis to Microfluidic Blood Vessels. J Cardiovasc Pharmacol Ther. 2014;19(4):382-93.

255. Huang S, Yang Y, Yang Q, Zhao Q, Ye X. Engineered circulatory scaffolds for building cardiac tissue. J Thorac Dis. 2018;10(Suppl 20):S2312-S28.

256. Carmeliet P. Angiogenesis in life, disease and medicine. Nature. 2005;438(7070):932-6.

257. Laschke MW, Harder Y, Amon M, Martin I, Farhadi J, Ring A, et al. Angiogenesis in tissue engineering: breathing life into constructed tissue substitutes. Tissue Eng. 2006;12(8):2093-104.

258. Risau W. Mechanisms of angiogenesis. Nature. 1997;386(6626):671-4.

259. Yancopoulos GD, Davis S, Gale NW, Rudge JS, Wiegand SJ, Holash J. Vascular-specific growth factors and blood vessel formation. Nature. 2000;407(6801):242-8.

260. Rakusan K, Korecky B. The effect of growth and aging on functional capillary supply of the rat heart. Growth. 1982;46(3):275-81.

261. Rakusan K, Flanagan MF, Geva T, Southern J, Van Praagh R. Morphometry of human coronary capillaries during normal growth and the effect of age in left ventricular pressure-overload hypertrophy. Circulation. 1992;86(1):38-46.

262. Radisic M, Malda J, Epping E, Geng W, Langer R, Vunjak-Novakovic G. Oxygen gradients correlate with cell density and cell viability in engineered cardiac tissue. Biotechnol Bioeng. 2006;93(2):332-43.

263. Stevens KR, Kreutziger KL, Dupras SK, Korte FS, Regnier M, Muskheli V, et al. Physiological function and transplantation of scaffold-free and vascularized human cardiac muscle tissue. Proc Natl Acad Sci U S A. 2009;106(39):16568-73.

264. Pieper JS, van Wachem PB, van Luyn MJA, Brouwer LA, Hafmans T, Veerkamp JH, et al. Attachment of glycosaminoglycans to collagenous matrices modulates the tissue response in rats. Biomaterials. 2000;21(16):1689-99.

265. Hauser S, Jung F, Pietzsch J. Human Endothelial Cell Models in Biomaterial Research. Trends Biotechnol. 2017;35(3):265-77.

266. Maruyama Y. The human endothelial cell in tissue culture. Zeitschrift für Zellforschung und Mikroskopische Anatomie. 1963;60(1):69-79.

267. Jaffe EA, Nachman RL, Becker CG, Minick CR. Culture of human endothelial cells derived from umbilical veins. Identification by morphologic and immunologic criteria. J Clin Invest. 1973;52(11):2745-56.

268. Kocherova I, Bryja A, Mozdziak P, Angelova Volponi A, Dyszkiewicz-Konwinska M, Piotrowska-Kempisty H, et al. Human Umbilical Vein Endothelial Cells (HUVECs) Co-Culture with Osteogenic Cells: From Molecular Communication to Engineering Prevascularised Bone Grafts. J Clin Med. 2019;8(10).

269. AlMalki WH, Shahid I, Mehdi AY, Hafeez MH. Assessment methods for angiogenesis and current approaches for its quantification. Indian J Pharmacol. 2014;46(3):251-6.

270. Andrade SP, Ferreira MA. The Sponge Implant Model of Angiogenesis. Methods Mol Biol. 2016;1430:333-43.

271. Staton CA, Stribbling SM, Tazzyman S, Hughes R, Brown NJ, Lewis CE. Current methods for assaying angiogenesis in vitro and in vivo. International journal of experimental pathology. 2004;85(5):233-48.

272. Kastana P, Zahra FT, Ntenekou D, Katraki-Pavlou S, Beis D, Lionakis MS, et al. Matrigel plug assay for in vivo evaluation of angiogenesis. The Extracellular Matrix: Springer; 2019. p. 219-32.

273. Nowak-Sliwinska P, Alitalo K, Allen E, Anisimov A, Aplin AC, Auerbach R, et al. Consensus guidelines for the use and interpretation of angiogenesis assays. Angiogenesis. 2018;21(3):425-532.

274. Badylak SF, Freytes DO, Gilbert TW. Extracellular matrix as a biological scaffold material: Structure and function. Acta Biomater. 2009;5(1):1-13.

275. Terzi A, Storelli E, Bettini S, Sibillano T, Altamura D, Salvatore L, et al. Effects of processing on structural, mechanical and biological properties of collagen-based substrates for regenerative medicine. Sci Rep. 2018;8(1):1429.

276. Muiznieks LD, Keeley FW. Molecular assembly and mechanical properties of the extracellular matrix: A fibrous protein perspective. Biochim Biophys Acta. 2013;1832(7):866-75.

277. Lillie M, Gosline J. The viscoelastic basis for the tensile strength of elastin. International journal of biological macromolecules. 2002;30(2):119-27.



HISTOLOGICAL AND MECHANICAL CHARACTERISATION OF PORCINE CARDIAC TISSUE

2. HISTOLOGICAL AND MECHANICAL CHARACTERISATION OF PORCINE CARDIAC TISSUE

2.1.Introduction

As discussed in the previous chapter, the heart's complex composition and architecture enables it to serve as a biological pump to supply blood and oxygen to the entire body. The heart contracts with a twisting motion caused by different bands of muscle fibres (1). The sub-epicardium contains a helix of fibres running in a left-handed direction; fibres in the myocardium run circumferentially, whilst those in the sub-endocardium run in a right-handed helix (Figure 2.1).

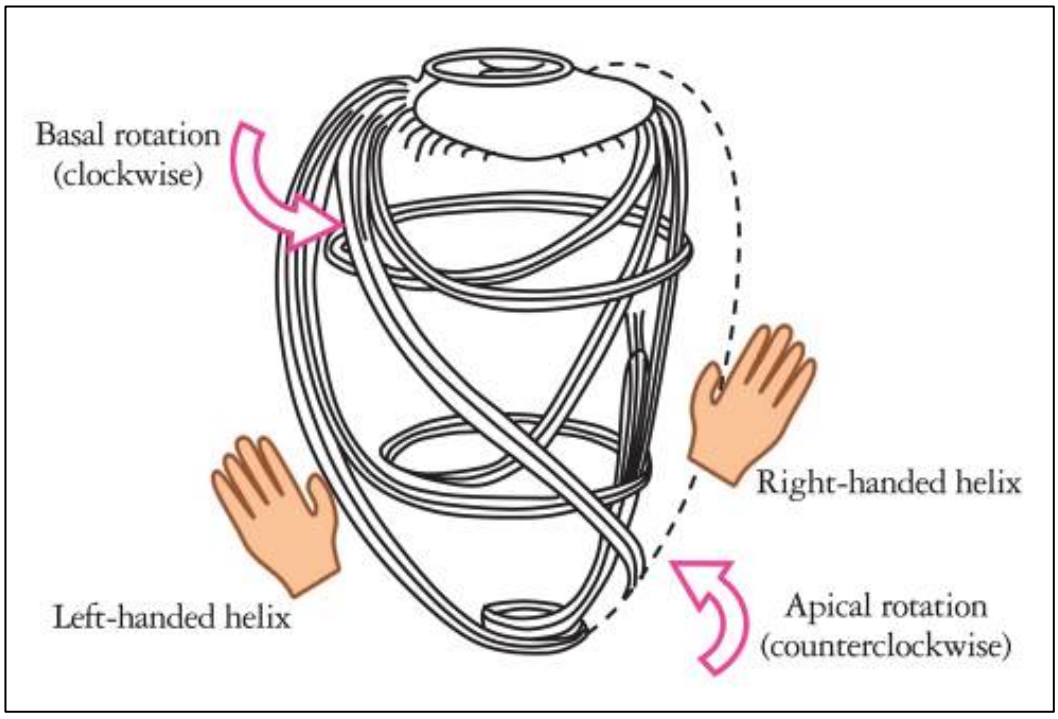


Figure 2.1. Myocardial fibre orientation and direction of rotation (1).

The heart contains different extracellular matrix (ECM) components, but the most predominant is collagen. During deformation, the collagen protects the myocardial fibre from overstretching and failure and assists in relaxing (2, 3). If an infarction occurs, the myocardium is permanently damaged due to massive cell loss, and it is still not clear how the mechanical properties of the infarcted tissue have changed after this event. Therefore, it is necessary to understand the

mechanical properties of a native heart to be able to mimic its features in any new design. As it is difficult to obtain human heart samples, one of the best testing materials for comparison is a porcine heart (4, 5), as this is of a similar size as the human heart and was even used for xenotransplantation (6). The following chapter will evaluate the mechanical and histological properties of porcine myocardium to understand what should be considered in scaffold design.

2.2.Materials and Methods

2.2.1. Dissection of Porcine Hearts

Six porcine hearts, in total, were obtained from juvenile pigs (1-year-old) from a local butcher in Oxford, UK, with samples from three hearts used for each test performed. The hearts had been removed from the sacrificed animals 2-3 days previously and stored at +4°C in a cold room before the collection. Obtained hearts were transported to the research facility at +4°C and rinsed in 300 mL/heart of PBS (0.1 M) (Sigma Aldrich, UK) to discard accumulated blood for 1h at room temperature. The hearts were dissected using a surgical dissection kit, and samples were taken from the left ventricle (L=30 mm, W=20 mm, T=20 mm), as seen in Figure 2.2. The main three layers of the heart were preserved for histology staining. In contrast, samples for mechanical testing were excised from the middle layer of the myocardium, and both the epicardium and endocardium were removed to ensure that only the functional muscle tissue was tested. Because the fibre orientation changes along the layers of the myocardium (7), the mid-myocardial layer of the left ventricle was targeted to reduce the variation.

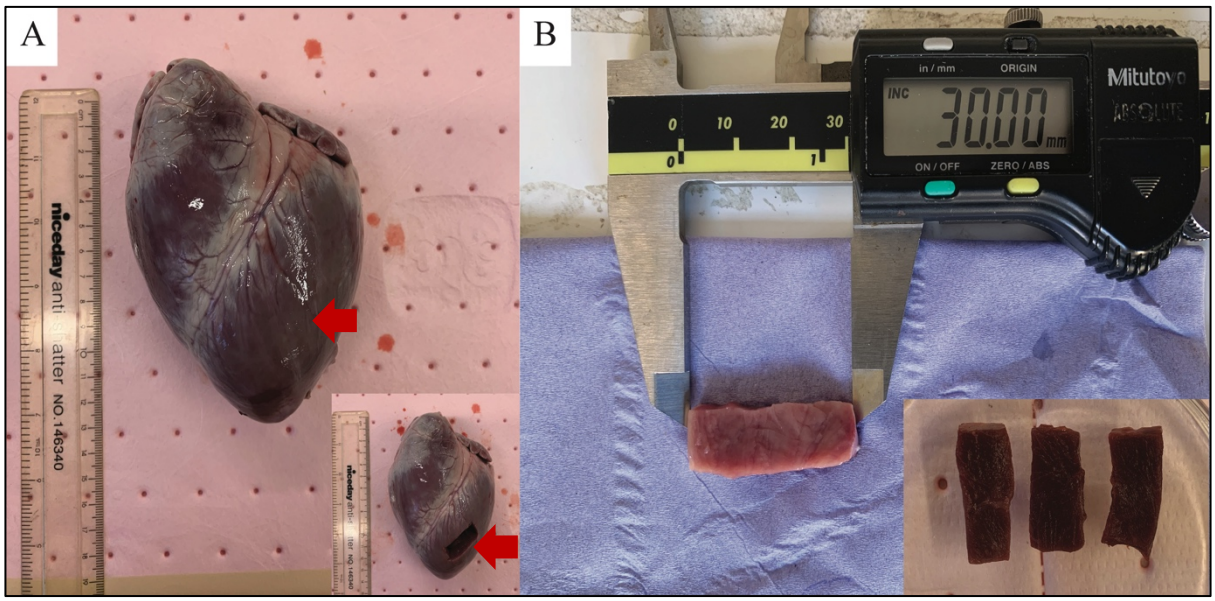


Figure 2.2. The dissection of porcine heart tissue. (A) The red arrows indicate the left ventricular region of the heart where the samples were collected. (B) Initial dimensions for mechanical testing as three samples/heart. (Tensile Test Dimensions: T=4 mm, L=30 mm, W=10 mm; Compression Test Dimensions: L/H/T=10 mm)

2.2.2. Cryo-sectioning

The dissected three-layered samples were then fixed in 10% formalin (Sigma Aldrich, UK) for >1 month. Following fixation, the samples were equilibrated in 30% sucrose (Sigma Aldrich, UK) prepared in DPBS (Gibco, Thermo Fisher, UK) overnight at +4°C. The samples were transferred into weighing boats (Sigma Aldrich, UK) using tweezers and embedded in Tissue-Tek OCT compound (Optimum Cutting Temperature, Sakura Finetek, USA). Samples were frozen at -20°C for at least 48 hrs before sectioning. The tissue blocks were sliced into 14 µm cryo-sections using a cryostat (Bright 5040) at -15°C and mounted on positively charged slides (Superfrost Plus, Thermo Scientific, USA). The tissue blocks were sectioned in a transverse plane. The cross-sections were stored at -80°C before staining. The cryostat was provided by histology lab facilities in the Department of Physiology, Anatomy and Genetics (DPAG).

2.2.3. Histology Staining

Histology staining was performed in the Department of Materials. The brightfield images were taken by either Eclipse Ci upright microscope (Nikon, Japan) or Axio Observer inverted

microscope (Zeiss, Germany), provided by Mommersteeg Group in DPAG, UK and Biomaterial Application and Research Center in ACU, Türkiye, respectively.

2.2.3.1.Haematoxylin and Eosin

Haematoxylin and Eosin (H&E) staining was performed at room temperature unless otherwise stated. The frozen slides were left on the bench for 10 mins to reach room temperature, dried and rinsed with DPBS (Sigma Aldrich, UK) once to remove the OCT. Then the sections were re-hydrated by immersing in absolute, 90, and 70% ethanol (EtOH) solutions and distilled water, respectively, for 3 mins each. The hydrated slides were stained with "haematoxylin solution according to Mayer" (Sigma Aldrich, UK) for 7 mins to counterstain the nuclei. The slides were rinsed in running tap water for 5 mins. They were then stained with the eosin Y solution (1% alcoholic) (Sigma Aldrich, U.K.) for 13 mins and immediately dehydrated with 96% EtOH (2 mins) and absolute EtOH (2 x 1 min). The slides were cleared with Histo-Clear II (National Diagnostics, Scientific Laboratory Supplies, UK), and a non-aqueous mounting agent DPX (Thermo Scientific, UK) or Entellan was used to mount them for imaging.

2.2.3.2.Elastica van Gieson

Elastica van Gieson (EVG) staining kit (Sigma-Aldrich, UK) was used to stain elastic and collagen fibres within the myocardium. The slides were prepared for the hydration steps mentioned in Section 2.2.3.1, and the kit's protocol was followed as instructed. Briefly, the samples were stained for "Elastin according to Weigert-resorcin fuchsin solution" for 10 mins. The sections were then rinsed in running tap water for 1 min. The slides were stained with "Weigert's iron haematoxylin staining solution" for 5 mins. They were again rinsed in running tap water for 1 min. This was followed by staining with "Picrofuchsin solution according to van Gieson" for 2 mins. The samples were immediately dehydrated with 70, 96% and absolute EtOH series for 2 mins each. The slides were cleared with Histo-Clear II and covered with a non-aqueous mounting agent.

2.2.3.3.Alcian Blue

To stain acidic glycosaminoglycans (GAG), including hyaluronic acid (HA), in tissue sections, 1% Alcian Blue (AB) (Merck, Germany) in 3% acetic acid at pH 2.5 was chosen. The slides were prepared for the hydration steps, as mentioned in Section 2.2.3.1. After hydration, samples were stained in AB solution for 15 mins and rinsed well in running tap water for 5 mins. The slides were then rinsed with distilled water once and counterstained with a Neutral red solution (MP Biomedicals, USA) for 1 min. Samples were rapidly dehydrated with 96% and absolute EtOH, respectively, for 2 mins. The slides were cleared with Histo-Clear II for 2 mins and mounted as aforementioned.

2.2.4. Compression and Tensile Testing

Static uniaxial compression and tensile tests were performed to determine the static Young's modulus using an Instron BlueHill Universal System (Instron, USA) connected to a 50 N load cell. Three samples from each of the three hearts were prepared as stated in Section 2.2.1 and immersed in PBS overnight at +4°C.

The size of each test sample was standardised by using a digital calliper, as stated in Figure 2.2. Before compression, samples were cut into ~10 mm cubes (Figure 2.3A). The test was performed in two different orientations, across (longitudinal, X-axis) and along (circumferential, Y-axis) the fibre alignment (Figure 2.3C), using an "unconfined" function with a standard parallel plate at a rate of 0.5 mm min^{-1} until failure. The parallel plates were mounted with epoxy adhesive to prevent slippage. 100 mN of preload was set at a rate of 2 mm min^{-1}. To calculate the stress on the specimen, the constant cross-sectional area was assumed to be true.

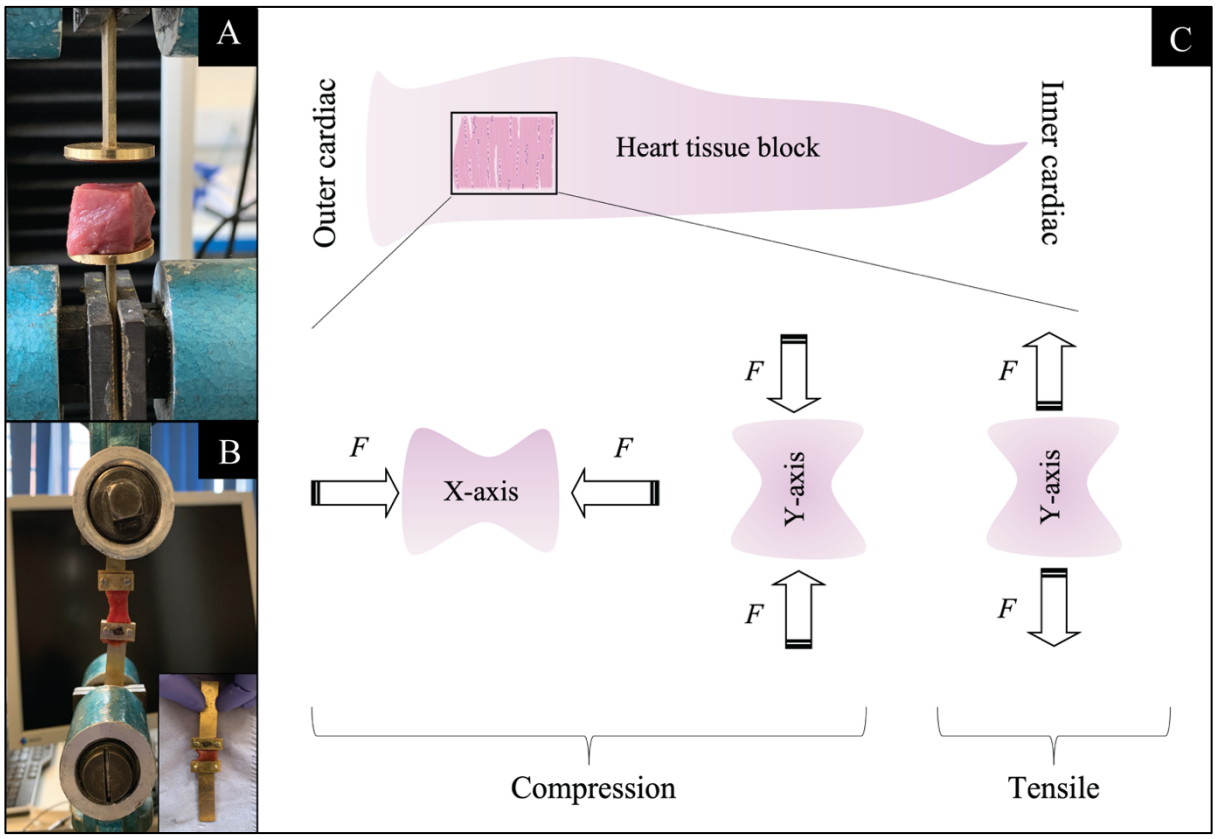


Figure 2.3. The setup for (A) compression and (B) tensile testing of porcine myocardium, and (C) illustration of the cross-sectioned native heart (top) showing the orientation of fibres considered during the sample preparation prior to uniaxial testing (*F*: Force).

For tensile testing, both ends of each sample were dehydrated with 70, 90%, and absolute EtOH gradient series for 2 mins each and mounted with epoxy adhesive to ensure that there was no slippage while testing. Meanwhile, the mid-region was kept in cold PBS to keep it hydrated. The samples were gripped at both ends at a distance of 15 mm with a micrometre adjustment clamp designed by our group members (Figure 2.3B). The testing was performed at 14 mm min^{-1} with no preload until failure. Each sample had a necking region of 20 mm×10 mm (LxW) and a gripping region of 5 mm×10mm with a thickness of 4 mm. Two regions were of interest: the E_L region representing the elastic modulus in the low-strain and the E_H region representing the elastic modulus in the high-strain. A one-way ANOVA followed by Tukey's post-hoc test was used to statistically analyse the data and plot the stress-strain curve.

2.3. Results

2.3.1. Histological Evaluation of Porcine Heart

Histology images were taken from the area where the mechanical test samples were obtained (Figure 2.3A, framed area). Tiles imaging obtained each captured picture frame from single positions in the block sample (Figure 2.4A). Images of porcine heart myocardium indicated that most of the ECM and cellular cytoplasm (Figure 2.4A-C) and that ECM was oriented uniaxially at the different regions of the tissue (red arrows). The elastic fibres were generally seen at the tissue ruptures, shown as black lines, but it was not perfectly clear, possibly due to the abundance of collagen (shown as dark pink in Figure 2.4E). AB staining showed that the acid mucin groups (blue dots) were randomly distributed in the ECM along the axis of collagen fibres (Figure 2.4F&G). The magnification was increased to be able to observe mucin groups better, as seen in an insert in Figure 2.4G.

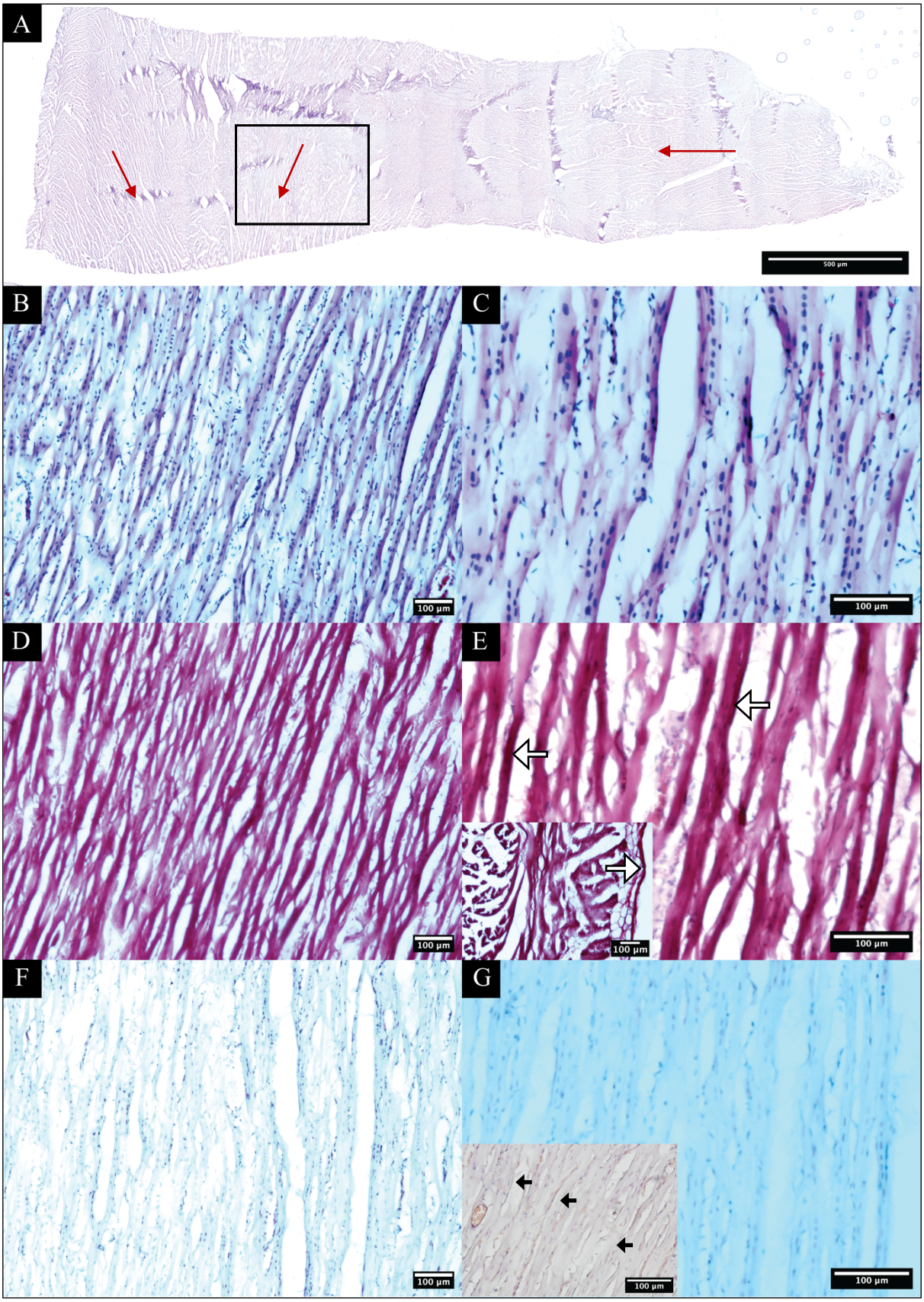


Figure 2.4. Histology images of porcine myocardium. (A) the tiles of the sectioned cardiac tissue. (B and C) H&E-stained sections where cell cytoplasm and nuclei were stained pink and dark blue, respectively. (D and E) and inset from EVG-stained sections. Elastic fibres, collagen and nuclei are shown as black, red/pink and black, respectively. (F and G) and inset

demonstrate AB staining, which dyed acid mucins to blue and nuclei to pink/red. Red, white and black arrows indicate the fibre orientation, elastic fibre, and acidic glycosaminoglycans (GAGs), respectively (Mag.:10X (left), 20X (right) with inset).

2.3.2. Compression Testing

The representative compressive stress-strain curve was obtained for myocardium samples from three different porcine hearts, as seen in Figure 2.5. The compression test was applied in two orientations; in the directions of the sagittal plane (referred to as longitudinal/ X-axis) and in the transverse plane (referred to as circumferential/ Y-axis). Although testing was applied to three samples from the same heart, mechanical properties of the myocardium varied across the whole heart, therefore these samples were treated as biologically different samples. The compressive moduli (E_C) were calculated by taking the slope at the linear region between 5-10% and 15-20% strain for longitudinally and circumferentially orientated samples, respectively. The samples tested on the Y-axis possessed 5 to 10-fold higher elastic modulus than the samples tested on the X-axis. Overall, the E_C was significantly increased when the force axis was changed (Figure 2.6). A J-shaped (non-linear) response was seen for samples, which is common for biological materials.

The orientation of the force applied significantly changed the way the tissue behaved. For instance, the samples compressed longitudinally (X-axis) could not resist the volume change at the beginning, leaving them almost fully compressed at 20% strain at a stress of about 6 kPa (Figure 2.6A). However, the samples compressed circumferentially (Y axis) resisted volume change, with a 5-10% strain at a stress of about 5 kPa (Figure 2.5B). They even showed further resistance to increasing volume change as the sample was compressed more at stress around 45 kPa. These samples could still tolerate compressive stress at around 80 kPa.

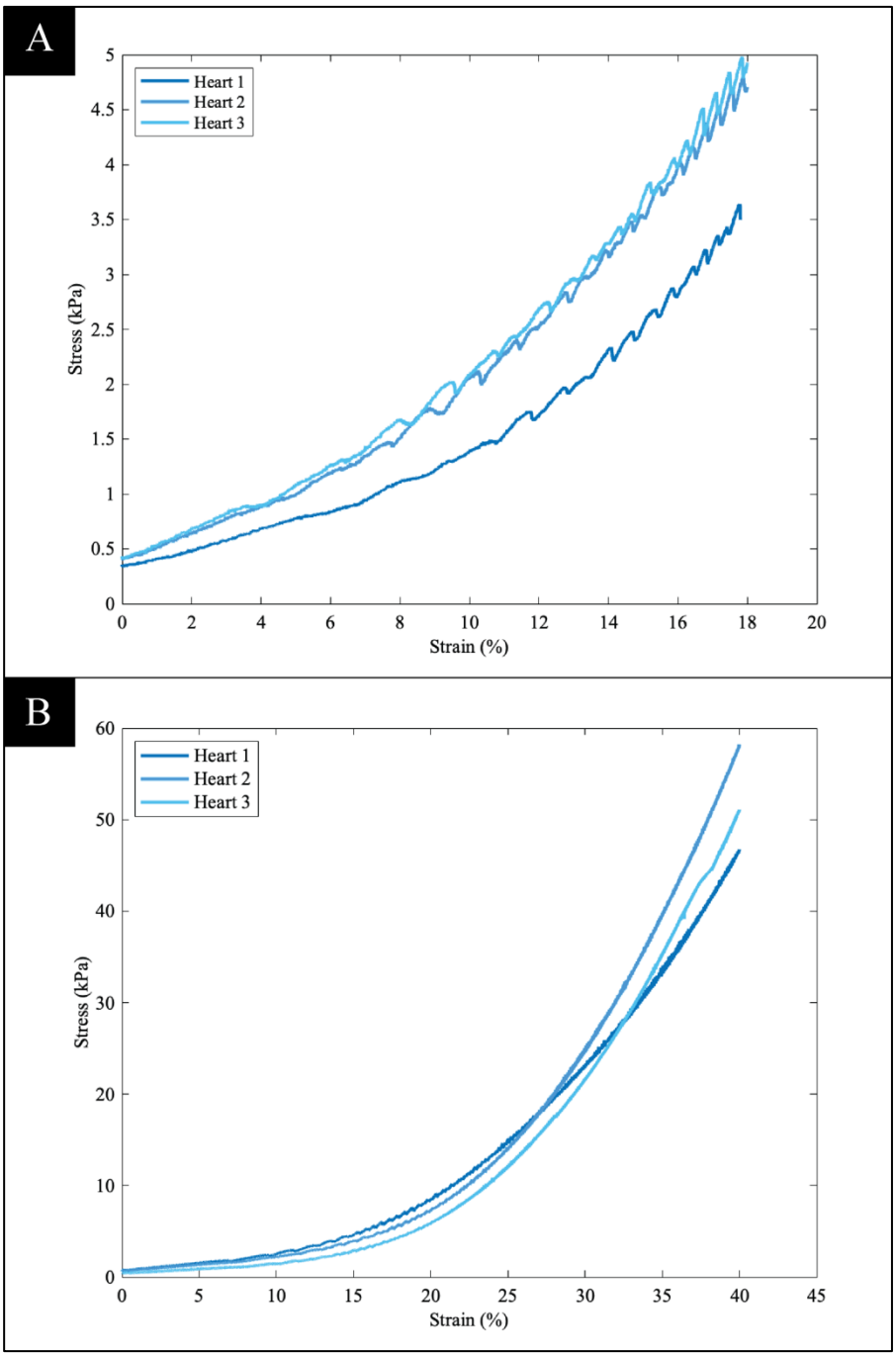


Figure 2.5. The representative stress-strain curve of three porcine heart tissues analysed from (A) the X-axis and (B) the Y-axis under compression. The samples in A were taken from different hearts from those in B.

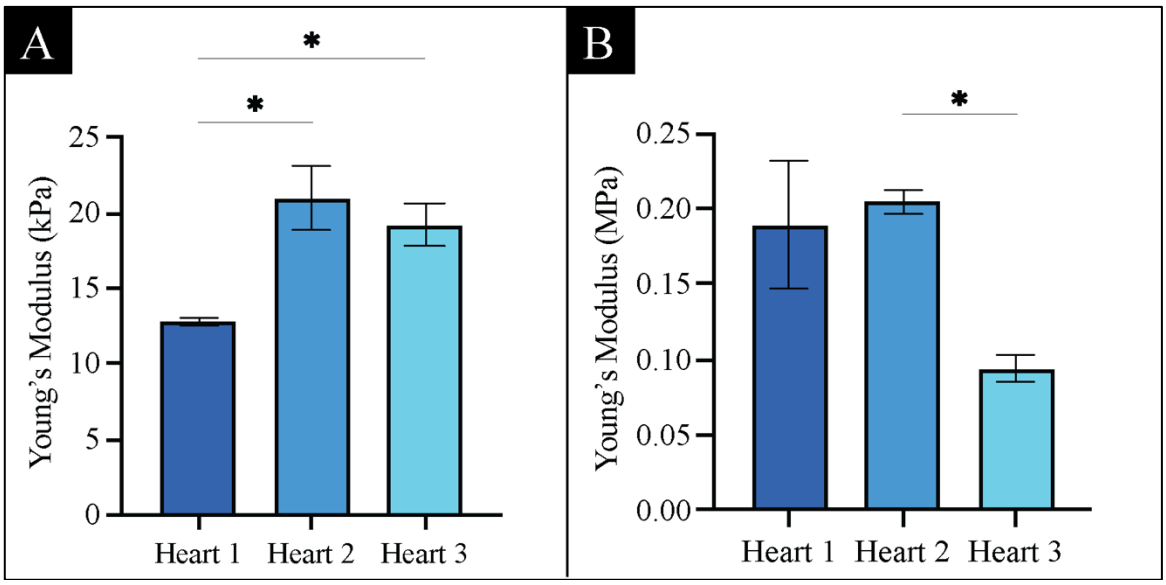


Figure 2.6. The comparison of Young's Modulus for the porcine heart from (A) X-axis and (B) Y-axis under compression. Error bars were included to show the reproducibility of the measurement across multiple samples from the same heart. (N=3, *p<0.05).

2.3.3. Tensile Testing

Representative stress-strain curves for native myocardium samples under tension are shown in Figure 2.7. A small J-curve behaviour was seen for Hearts 2 and 3 but not for 1. Here, two regions of the curve were of interest: The E_L region corresponds to the elastic modulus in the low strain, and the E_H region gives the elastic modulus in the high strain.

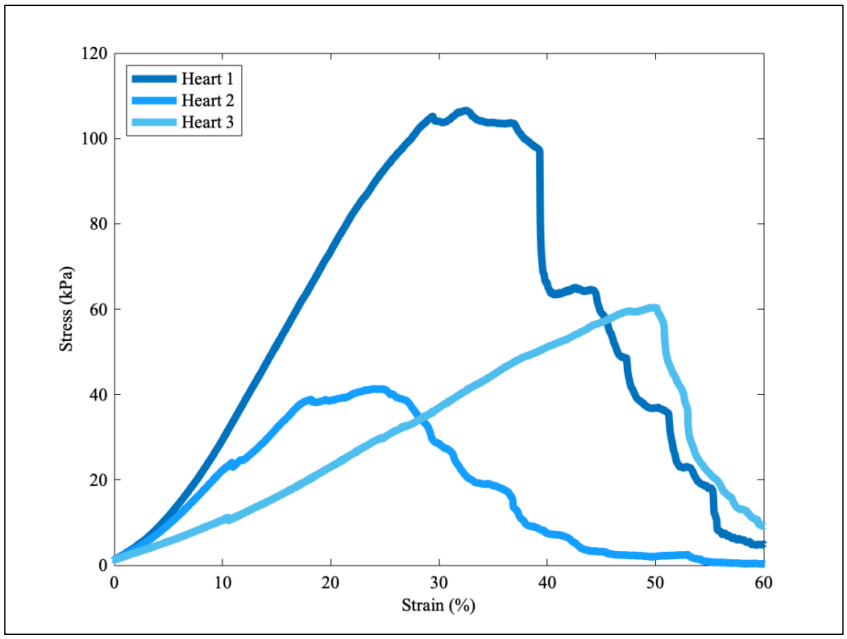


Figure 2.7. Representative stress-strain curve of three porcine heart tissues analysed circumferentially (Y-axis) under tension. (N=3).

The results revealed that the myocardium tended to become stiffer at the higher stretch. Measuring the different beads of the same heart showed that the tensile properties changed across the myocardium (Table 2.1). The overall extensibility and strain-to-failure were 20.69±7.26% and 65.36 ±10.81%, respectively.

Table 2.1. The elastic modulus of porcine heart myocardium samples under tension. E_L: Elastic modulus at low-strain, E_H: Elastic modulus at high-strain, E_T: Tensile modulus. (Mean±SD, *p<0.05).

Young's Modulus (MPa)	E_L	E_H	E_T	p-value
Heart 1	0.13±0.010	0.43±0.071	0.37±0.02	0.0021*
Heart 2	0.03±0.007	0.12±0.002	0.14±0.05	
Heart 3	0.09±0.001	0.16±0.017	0.13±0.02	

2.4. Discussion

It is well established that the myocardium possesses a laminar macrostructure, consisting mainly of cardiomyocytes lying parallel to each other by forming myofibrillar structures (8). Parallel aligned myofibers are connected by endomysial collagen, which, together with other collagen components and elastin, form individual myolamines (layers). The orientation of these layers changes throughout the myocardium. Our samples were cross-sectioned in the circumferential direction, and we could see that the fibre orientation changed across the sample (red arrows in Figure 2.4A). When we focused on a particular area, it was possible to observe collagen along the muscle fibres (Figure 2.4D&E). However, the H&E staining was unsuitable for determining the myofiber structures which may have been clearer with Masson-Trichome staining. Furthermore, EVG staining does not discriminate between collagen type I and III. The ratio between collagen type I and III is about 0.3-0.6 in healthy human left ventricle, whereas the ratio is higher in healthy myocardium of other species such as long-tailed macaques (85% and 11% Col type I and III, respectively), rat (6.41 ratio) or porcine (2.3 ratio) (9). However,

it is not convenient to use collagen type III in medical applications as it is less abundant, and the purification costs much more than collagen type I. Consequently, we decided to exclude collagen type III in our material design.

The traditional H&E staining cannot distinguish elastic fibres; therefore, we utilised the EVG method to identify elastic fibres in cardiac tissue, commonly used for skin, aorta, etc., on formalin-fixed or paraffin-embedded sections (10). In this staining, the elastic fibres will be stained dark blue/black, collagen will be red, and the other cytoplasmic elements will be stained yellow. These images also confirmed that the cardiac ECM is composed predominantly of collagen. The elastic fibres were observed at the ruptured area of ECM but were not seen as a consistent fibre, suggesting that the elastin content of cardiac muscle is relatively low compared with tissue types such as blood vessels (11). The current staining suggested that there may be more in the endo and epicardium (Figure 2.4E inset), which was already reported elsewhere (12). The elastin content of the native porcine myocardium has been reported to be 37.74 μg/mg of tissue (13). Another study found the ratio of collagen and elastin in porcine LV to be 19.48±1.4 (14). It is known that the elastic fibres intertwine with collagen fibres to support elasticity and strength, but they are less likely to form fibre bundles like collagens (11). This may explain why the elastic fibres were not clear in our samples. It is also worth noting that the porcine heart sections were over-stained as frozen sections are usually not optimal for differential histological staining and therefore the extent of collagen staining in the heart may be overestimated. Nevertheless, our data confirmed that elastin is present at a low level and informed decisions about how much and how to blend the elastin content in the material design in the next step.

AB staining was used for detecting acidic polysaccharides (GAGs) in the porcine left ventricle. The GAGs (shown as blue dots/lines) were randomly distributed throughout the ECM. Although total GAG content has been reported to be 4.72 μg/mg of tissue (13), even lower than

the elastin content of the tissue, it has a valuable role in the heart, as described in Chapter 1. HA is the most prevalent GAG in the myocardium and is essential for water retention. The random presence of GAGs shown in our staining is important in determining how they contribute to the material design.

The mechanics of the heart have been the focus of numerous studies over the years. However, myocardial contractile efficiency is not a direct input of its activity but also its passive mechanical properties (15). These properties also outline the extensibility of the chamber size. There are multiple ways to test the mechanical properties of cardiac tissue, including tensile and compression testing, which are particularly important to define the bulk mechanics of a material. Strain can be applied from different directions compared to the direction of CM and ECM orientation in the tissue. As the myocardium has a multiaxial orientation that varies from the epicardium to the endocardium (seen in Figure 2.4A), it is crucial to test along and across the CM/ECM alignment to reveal anisotropic mechanical properties that result from this structure.

Young's modulus of composite structures is thought to be highly related to the fibre orientation angle (16). The *in vivo* circumferential modulus should be higher to redistribute blood during systolic contraction. For this reason, it is important to determine the mechanical properties of the tissue from the centre of the myocardium. As far as possible, the samples were collected from where the fibres seemed to be linear, and the compression test was applied uniaxially in two different orientations: along (compressed from the Y-axis) and across (compressed from the X-axis) the muscle fibre of the tissue. The results showed that the E_C was significantly different between the X and Y axis by increasing ~10-fold (Figure 2.6). This is because the compression was predominantly against the orientation of the collagen fibres for the longitudinal axis (X), whereas the samples compressed along the circumferential axis (Y)

following the alignment of the collagen fibres. In theory, the stiffness becomes the highest value when the load is applied along the fibre direction (0° angle).

As histology staining can confirm, the area where the mechanical test samples were collected was the combination of horizontally aligned muscle and collagen fibres which shortened under the applied load. The study intended to standardise cardiac tissue analysis by examining equivalent-sized samples collected along the same axis (X or Y) and from the mid-wall of the left ventricle, as shown previously (17). Based on here, we assumed that the anisotropic terms should not have a role in the material stress. Regardless of whether the fibres can carry compressive loads, the results show that myofibers surrounded by the ECM can resist compression and contribute to the stress response.

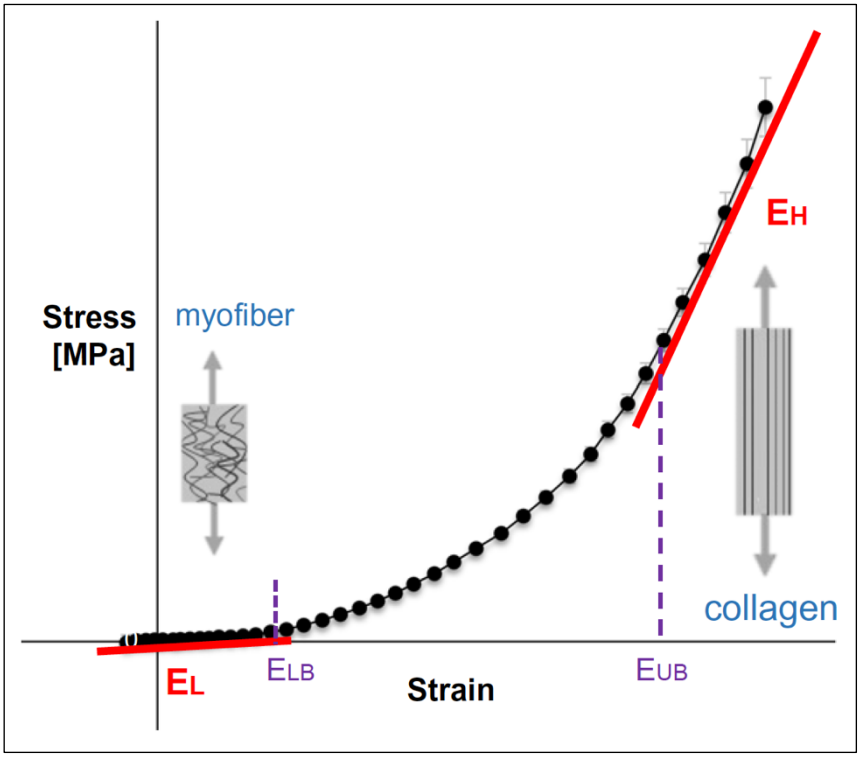


Figure 2.8. Representative J-curve behaviour where the elastic modulus was obtained at low (E_L) and high (E_H) strain. E_{LB} denotes the lower boundary of the exponential transition region; E_{UB} is the upper bound of the exponential transition zone. Modified from (18).

The E_L corresponds to elastic modulus at a low-stress, linear region of the stress-strain curve (Figure 2.8) where the collagen fibres are not yet assembled, and the mechanical properties of the tissue are predominantly determined by the elastic fibres and myofibers. Here the collagen

fibres stretched gradually, resulting in an accumulated stiffening of the tissue. The E_H represents the elastic modulus in the high-tensile region after all collagen fibres have fully straightened (18, 19). This also concludes that the stiffness in the passive cardiac tissue results in myofiber rearrangement and orientation. The alignment of these elastic and collagen fibres normally causes a huge J-curve behaviour for non-organised tissues, such as the skin. Here, the small J-curve behaviour was seen in Figure 2.7, implying that most fibres were already aligned. In the current study, the elasticity of the samples significantly changed from low to high strain, which agrees with the existing literature. Although passive mechanical properties are more compliant and nonlinear, it is also true that the active organ mechanical properties are substantially stiffer and more linear (20). In this study, we particularly tested porcine heart LV myocardium due to its mechanical similarity to the human heart. It was shown that the healthy human myocardium also exhibits nonlinear, highly anisotropic, viscoelastic properties with a stiffer behaviour circumferentially than in the longitudinal axis (21).

Here, it should be noted that the number of samples tested was limited. It was previously emphasised that even replicates of the same or similar loading conditions in a sample often gave coefficients that differed significantly (22). This within-sample variability has been attributed to numerical imbalances in the docking algorithms or to the strain history dependence of the tissue (23). During the sample preparation, it was noted that the size and the free wall thickness of the hearts were substantially different, although we had tried to exclude sex and age differences during selection. Heart 1 exhibited higher stiffness (0.37±0.02) and tensile strength (103.12±1.67 kPa) than Hearts 2 and 3. Previous studies also concluded a considerably low tensile strength (24-26). But this could be due to the source of the sample, and region where being taken, and the dimension of the sample tested as well as the testing conditions. Therefore, to increase the reliability of the current study, the results of Heart 1 will not be used for the mechanical comparison of the native tissue and the scaffolds in Chapter 3.

Techniques such as 3D kinematics, triaxial structural-mechanical analysis, and finite element modelling could provide a more accurate inference of complex 3D coupling behaviour between myofibers and collagen fibres by explaining the numerous complexities of the heart when the structural integrity is well-preserved. A more comprehensive insight into the heart structure will enable us to understand muscle fibre and ECM contribution to the heart's mechanical properties to be able to develop advanced cardiac patches.

2.5. Summary

This chapter presented the histological characterisation of the porcine LV and its mechanical properties obtained by compression and tensile testing methods. Different staining procedures were conducted targeting various ECM components, and the mechanical properties were compared with previous results. The main findings include the following:

- Most of the myocardial ECM was found to be collagen, and the fibre orientation changed throughout the bulk tissue. Visualisation of cardiac elastic fibres was found to be indistinct compared to collagen. AB staining was used to characterise hyaluronan, which is randomly dispersed along the axis of collagen fibres.
- The compression test confirmed that cardiac stiffness is highly related to fibre orientation. When the force was along the fibre direction (circumferential axis), the material became less compressible, assumed to be related to the orientation of the myofibers.
- The tensile test exhibited a small J-curve behaviour due to abundant well-aligned muscle fibres. At low strain lengths, the mechanical properties were assumed to be mainly controlled by elastic fibres, which were dominated by collagen fibres at high strength, yet this could not be proven in this chapter.

References

1. Nakatani S. Left ventricular rotation and twist: why should we learn? J Cardiovasc Ultrasound. 2011;19(1):1-6.

2. Rohmer D, Sitek A, Gullberg GT. Reconstruction and visualization of fiber and laminar structure in the normal human heart from ex vivo diffusion tensor magnetic resonance imaging (DTMRI) data. Invest Radiol. 2007;42(11):777-89.

3. Weber KT, Sun Y, Tyagi SC, Cleutjens JP. Collagen network of the myocardium: function, structural remodeling and regulatory mechanisms. J Mol Cell Cardiol. 1994;26(3):279-92.

4. Crick SJ, Sheppard MN, Ho SY, Gebstein L, Anderson RH. Anatomy of the pig heart: comparisons with normal human cardiac structure. J Anat. 1998;193 (Pt 1)(Pt 1):105-19.

5. Lelovas PP, Kostomitsopoulos NG, Xanthos TT. A comparative anatomic and physiologic overview of the porcine heart. J Am Assoc Lab Anim Sci. 2014;53(5):432-8.

6. Längin M, Mayr T, Reichart B, Michel S, Buchholz S, Guethoff S, et al. Consistent success in life-supporting porcine cardiac xenotransplantation. Nature. 2018;564(7736):430-3.

7. Holzapfel GA, Ogden RW. Constitutive modelling of passive myocardium: a structurally based framework for material characterization. Philos Trans A Math Phys Eng Sci. 2009;367(1902):3445-75.

8. McEvoy E, Holzapfel GA, McGarry P. Compressibility and anisotropy of the ventricular myocardium: experimental analysis and microstructural modeling. Journal of biomechanical engineering. 2018;140(8).

9. Wittig C, Szulcek R. Extracellular Matrix Protein Ratios in the Human Heart and Vessels: How to Distinguish Pathological From Physiological Changes? Frontiers in Physiology. 2021;12.

10. Reddy VB, David O, Spitz DJ, Haber MH. Gattuso's Differential Diagnosis in Surgical Pathology: Elsevier Health Sciences; 2021.

11. Wang K, Meng X, Guo Z. Elastin Structure, Synthesis, Regulatory Mechanism and Relationship With Cardiovascular Diseases. Frontiers in Cell and Developmental Biology. 2021;9.

12. Shi X, Zhang S, Liu Y, Brazile B, Cooley J, Butler JR, et al. Spatial distribution and network morphology of epicardial, endocardial, interstitial, and Purkinje cell-associated elastin fibers in porcine left ventricle. Bioactive Materials. 2023;19:348-59.

13. Wainwright JM, Czajka CA, Patel UB, Freytes DO, Tobita K, Gilbert TW, et al. Preparation of cardiac extracellular matrix from an intact porcine heart. Tissue Eng Part C Methods. 2010;16(3):525-32.

14. Schulte JB, Simionescu A, Simionescu DT. The acellular myocardial flap: a novel extracellular matrix scaffold enriched with patent microvascular networks and biocompatible cell niches. Tissue Engineering Part C: Methods. 2013;19(7):518-30.

15. Knaapen P, Germans T, Knuuti J, Paulus WJ, Dijkmans PA, Allaart CP, et al. Myocardial energetics and efficiency: current status of the noninvasive approach. Circulation. 2007;115(7):918-27.

16. Wang H, Zhou H, Gui L, Ji H, Zhang X. Analysis of effect of fiber orientation on Young's modulus for unidirectional fiber reinforced composites. Composites part B: engineering. 2014;56:733-9.

17. Ramadan S, Paul N, Naguib HE. Standardized static and dynamic evaluation of myocardial tissue properties. Biomedical Materials. 2017;12(2):025013.

18. Jang S, Vanderpool RR, Avazmohammadi R, Lapshin E, Bachman TN, Sacks M, et al. Biomechanical and Hemodynamic Measures of Right Ventricular Diastolic Function: Translating Tissue Biomechanics to Clinical Relevance. J Am Heart Assoc. 2017;6(9).

19. Avazmohammadi R, Hill MR, Simon MA, Zhang W, Sacks MS. A novel constitutive model for passive right ventricular myocardium: evidence for myofiber–collagen fiber mechanical coupling. Biomechanics and modeling in mechanobiology. 2017;16(2):561-81.

20. Liu H, Soares JS, Walmsley J, Li DS, Raut S, Avazmohammadi R, et al. The impact of myocardial compressibility on organ-level simulations of the normal and infarcted heart. Scientific reports. 2021;11(1):1-15.

21. Sommer G, Schwarz M, Kutschera M, Kresnik R, Regitnig P, Schriefl AJ, et al. Biomechanical properties of the human ventricular myocardium. Biomedical Engineering/Biomedizinische Technik. 2013;58(SI-1-Track-D):000010151520134108.

22. Yin FC, Strumpf RK, Chew PH, Zeger SL. Quantification of the mechanical properties of noncontracting canine myocardium under simultaneous biaxial loading. Journal of biomechanics. 1987;20(6):577-89.

23. Fung Y, Fronek K, Patitucci P. Pseudoelasticity of arteries and the choice of its mathematical expression. American Journal of Physiology-Heart and Circulatory Physiology. 1979;237(5):H620-H31.

24. Demer LL, Yin F. Passive biaxial mechanical properties of isolated canine myocardium. The Journal of Physiology. 1983;339(1):615-30.

25. Ghaemi H, Behdinan K, Spence A. In vitro technique in estimation of passive mechanical properties of bovine heart: Part I. Experimental techniques and data. Medical engineering & physics. 2009;31(1):76-82.

26. Przyklenk K, Connelly CM, McLaughlin RJ, Kloner RA, Apstein CS. Effect of myocyte necrosis on strength, strain, and stiffness of isolated myocardial strips. Am Heart J. 1987;114(6):1349-59.



SCAFFOLD FABRICATION AND CHARACTERISATION

3. SCAFFOLD FABRICATION AND CHARACTERISATION

3.1. Introduction

This chapter will cover the fabrication of pure collagen scaffolds, collagen/elastin composite scaffolds, and their hyaluronic acid (HA)-infiltrated composites. The freeze-dry/lyophilisation method was chosen to obtain the interconnective porous scaffolds. The effects of changing the scaffold composition, concentration, processing temperature, and crosslinking density on the scaffold properties will be examined. Specifically, this chapter will study the swelling and degradation characteristics and relevant mechanical properties to understand the scaffold's feasibility in native cardiac tissue.

3.2. Materials and Methods

3.2.1. Fabrication and Crosslinking

Collagen scaffolds and collagen-elastin composites were manufactured, and then HA was incorporated. All scaffold dimensions for each testing method used throughout this thesis are listed in Table 3.1.

Table 3.1. Scaffold dimensions based on the experiment conducted.

Choice of Experiment		Specimen Size
Physicochemical	SEM	40mm x 10mm x 6mm, cross-sectioned to 4 mm in length
	FT-IR	15 mm x 10 mm, sliced transversely to 5 mm in thickness
	Swelling	40mm x 10mm x 6mm
	Degradation	40mm x 10mm x 6mm, cross-sectioned to 10 mm in length
Mechanical	Compression	15 mm x 10 mm
	Tensile	40mm x 10mm x 6mm
	Three-Point Bending	
	Self-Deflection	
Biological	AlamarBlue Assay, RT-PCR, ICC	40mm x 10mm x 6mm, cross-sectioned to 4 mm in length
	In vivo implantation	40mm x 10mm x 6mm, cross-sectioned to 10 mm in length
	Tensile	40mm x 10mm x 6mm
	Self-Deflection	

3.2.1.1.Collagen-Based Scaffolds

Pure collagen suspension (1% w/v) was prepared by mixing collagen type I powder from bovine Achilles tendon (Sigma Aldrich, UK) with deionised water (Scientific Laboratory Supplies, UK). The pH was adjusted to 3.2 by adding glacial Acetic Acid (Fisher Scientific, UK) dropwise. The suspension was then blended using a handheld blender (Voche, UK) for 10 mins in an ice bath and stored at +4°C overnight for extra swelling. The next day, the suspension was centrifuged (Thermo, IEC CL10, UK) at 5000 rcf for 10 mins at room temperature to remove entrapped air bubbles, and the upper layer of the suspension was discarded before moulding. Pure collagen suspension was first moulded either in cylindrical (D:10 mm, H: 15 mm) or rectangular (L: 40 mm, W: 10 mm, T: 6 mm) moulds (Figure 3.1A&C). Then, each mould had round-shape stainless steel wires (1 x 300 mm, cut off 1 x 60 mm) inserted to create channels to increase liquid transition inside the scaffolds (Figure 3.1A-C). The moulds were stored at -20°C overnight and freeze-dried (Christ I-5, Martin Christ, Germany) for ~24 hrs under a vacuum of 0.05 mbar by an Edwards RV2 Two Stage High Vacuum Pump 240V E2M2 (Edwards, UK) (Figure 3.1B&D). The pure 100% collagen scaffolds were named C100.

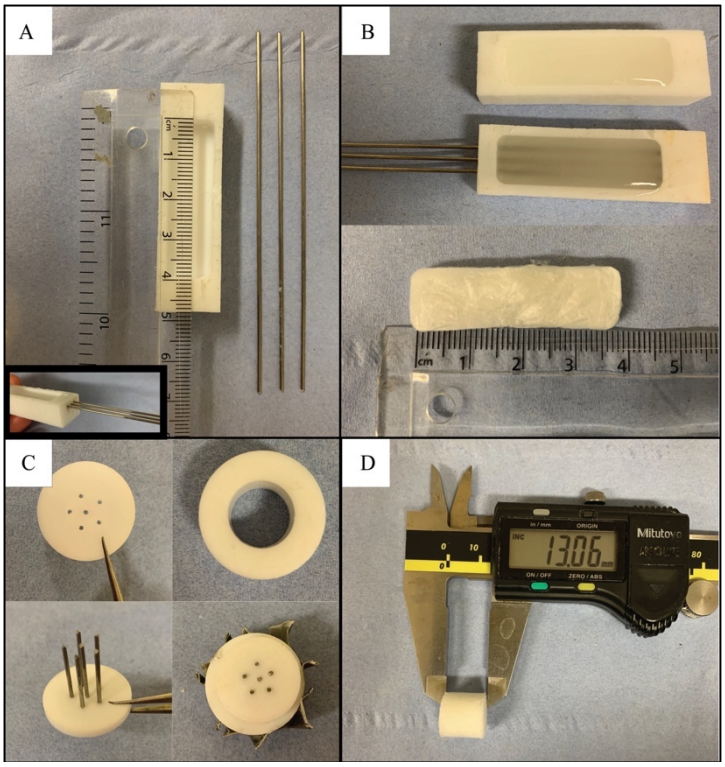


Figure 3.1. Rectangular and cylindrical moulds for scaffold fabrication. (A) shows rectangular (L: 40 mm, W: 10 mm, T: 6 mm) mould and long metallic rods (D: 1 mm, L: 80 mm) were used to fabricate rectangular scaffolds (B), whereas (C) shows cylindrical (D:10 mm, H: 15 mm) mould and short metallic rods (D: 1 mm, L: 20 mm) that were chosen to obtain cylindrical scaffolds (D) based on the testing requirements.

3.2.1.2.Production of Fibrillar Elastin Gel (FEG)

Fibrillar elastin gel (FEG) production was previously optimised by one of the former group members (1). Briefly, 0.25 M of oxalic acid (150 mL) (Sigma Aldrich, UK) was prepared with deionised water by continuously stirring. 1:10 (w/v) of insoluble elastin powder (Sigma Aldrich, UK) was gently mixed with 50 mL of oxalic acid solution to avoid the formation of air bubbles. The suspension was poured into a 100 mL flask (Borosilicate Glass Round Bottom Flask, Socket: 14/23, Sigma Aldrich, UK) with an air condenser (Quickfit™ Borosilicate Glass Liebig Condenser, C1/11/SC, Thermo Fisher Scientific, UK) which was attached to the sink with PVC Reinforced Hose (Department of Materials Stores) secured with hose clips (11-16 mm) to run tap water continuously. The suspension was then heated to 100±2°C using a water bath on a hot stirring plate (Stuart US152 Hot Stirrer, RS Components, UK) at 300 rpm for 70 mins. The setup was sealed with aluminium foil to maintain the temperature at ~100°C. The

system was monitored throughout the experiment using a regular Mercury thermometer (-10°C to +110°C, 176mm, Department of Materials Stores). After 70 mins, the heated flask was transferred to an ice bath (0°C) for 10 mins, and then to a 50 mL centrifuge tube (Polypropylene, Corning® CentriStar™ Cap, Sigma Aldrich, UK) to centrifuge (Heraeus Megafuge 1.0 Centrifuge, Thermo Fisher Scientific, UK) at 5000 rcf for 5 mins to remove the supernatant. The obtained pellet was mixed with 50 mL of fresh oxalic acid, and the process was repeated for three sequential hydrolyses (Figure 3.2). The pellet was purified by rinsing in excess (1:4 v/v) deionised water for 1 hour on the stirrer, centrifuged at 5000 rcf for 5 mins, and stirred for 30 mins in excess deionised water (1:3 v/v). The 30-minute washing was repeated four times, followed by a centrifuge at 5000 rcf for 5 mins each. The final pellet comprised a gel-like substance named FEG which was stored at +4°C overnight for extra swelling and then transferred into Polystyrene anti-static weighing dishes (Sigma Aldrich, UK), frozen overnight at -20°C, and freeze-dried (Christ I-5, Martin Christ, Germany) for 24 hrs. The cooling rate was not controlled. The resulting sponge form of FEG was initially weighed, sealed, and stored at +4°C for further experiments.

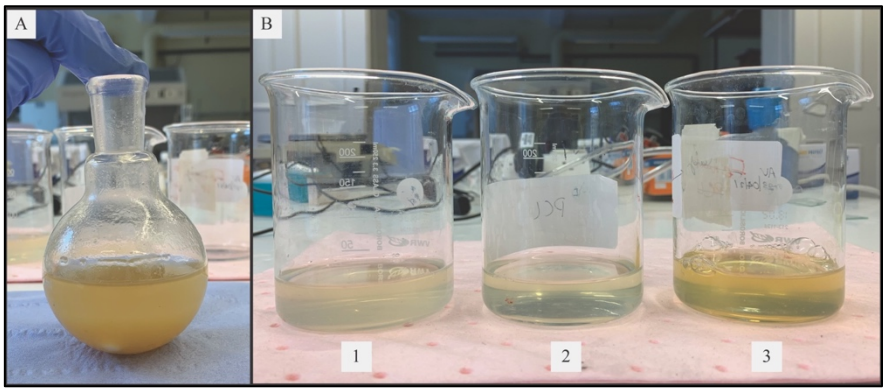


Figure 3.2. The hydrolysis steps of pure elastin production. (A) the final stage of jelly elastin suspension after three hydrolysis steps. (B) the by-products of elastin purification after first (1), second (2), and third (3) hydrolysis.

3.2.1.3. Collagen-FEG Composite Scaffolds

1% (w/v) collagen-FEG suspensions were prepared in deionised water by mixing collagen type I powder from bovine Achilles tendon (Sigma Aldrich, UK) and previously freeze-dried FEG

sponges. The pH was adjusted to 2.7 by adding glacial Acetic Acid (Fisher Scientific, UK) dropwise, as this was within the range for the solubilisation of elastin. The different ratios of collagen-FEG composites, indicated in Table 3.2, were manufactured as described in Section 3.2.1.1 and stored at room temperature in a dark, cool place until further characterisation.

Table 3.2. The desired ratio of Collagen-FEG composite scaffolds (1% w/v).

Composition	Collagen (mg/mL)	FEG (mg/mL)	Abbreviation
90% Collagen-10% FEG	9.0	1.0	C90E10
80% Collagen-20% FEG	8.0	2.0	C80E20
75% Collagen-25% FEG	7.5	2.5	C75E25

3.2.1.4.Crosslinking

After freeze-drying the scaffolds, 1/3 of each design was left non-crosslinked (Non-XL), and the rest of them were chemically crosslinked (XL). A cross-linking solution was prepared by mixing 60 mM of 1-(3-Dimethylaminopropyl)-3-ethyl carbodiimide hydrochloride (EDC) (Fluorochem Ltd, UK) and 30 mM of N-hydroxysuccinimide (NHS) (Sigma Aldrich, UK) in 75% ethanol (prepared from absolute ethanol, Sigma Aldrich, UK). After adjusting the pH to 4.8 by adding 0.2 N of HCl, the scaffolds were immediately added into the crosslinking solution and left on the stirrer for 4 hrs at room temperature. The samples were then rinsed with 1 M NaCl and deionised water (200 mL each) for 2 hrs each. Half of the crosslinked scaffolds were transferred either to weighing dishes (Sigma Aldrich, UK) with excess deionised water to freeze at -20°C overnight before freeze-drying for 24 hrs or into the previously dialysed HA solution for infiltration, as described in the following section. The schematic view of EDC/NHS crosslinking of proteins is given in Figure 3.3.

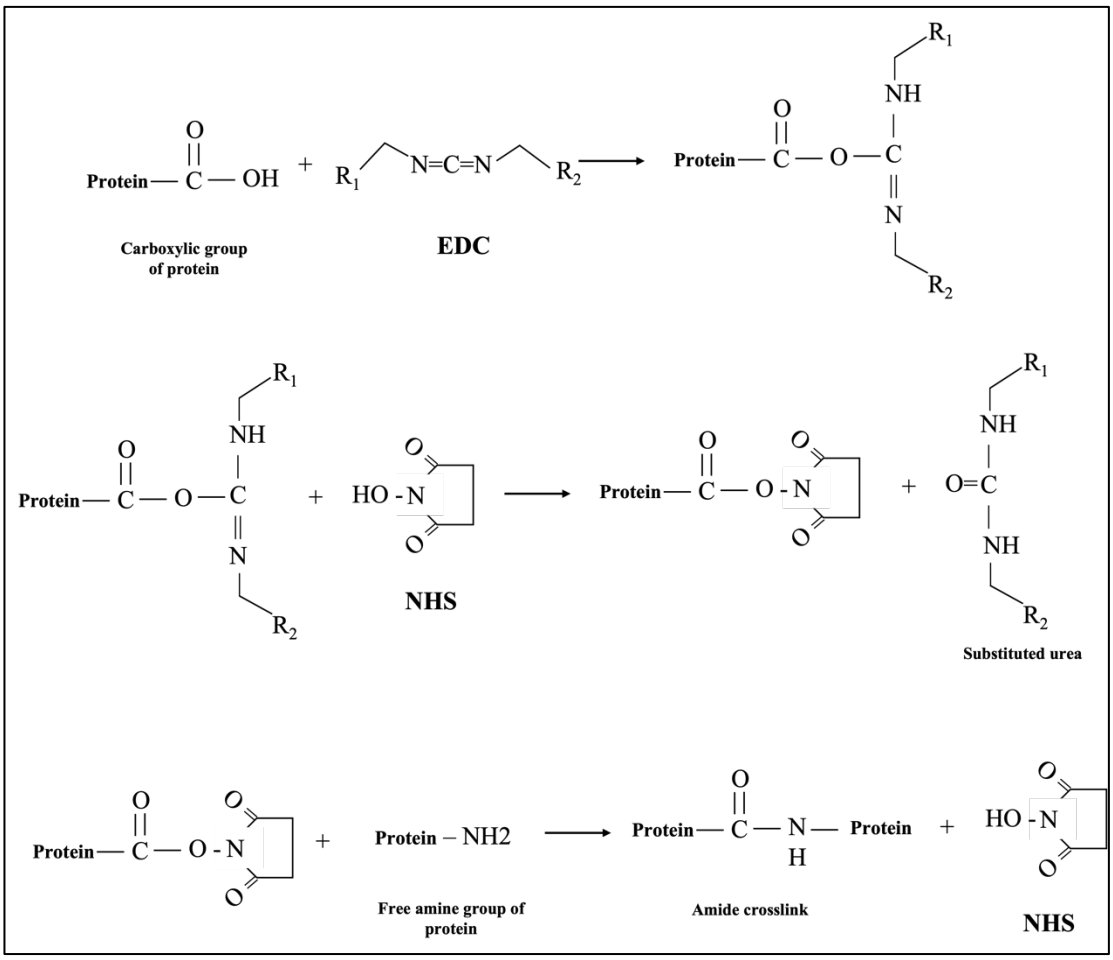


Figure 3.3. EDC/NHS-mediated zero-length crosslinking of proteins (2).

3.2.1.5.Hyaluronic Acid-Infiltrated Scaffolds

HA mixture was prepared as previously described by one of our group members (3). Briefly, 0.2 g of sodium hyaluronate 95% (SHA) ($C_{14}H_{22}NNaO_{11}$, Agros Organics, Thermo Fisher, UK) was dissolved in 50 mL of deionised water (~4 mg/mL) with continuous stirring at room temperature. 30X molar excess of adipic dihydrazide (ADH) (Sigma Aldrich, UK) was added to the mixture to form a clear, viscous solution. The pH was adjusted to 4.75 by adding 0.1N HCl dropwise. The mixture was chemically crosslinked by adding 20 mM of EDC, and the pH was maintained at 4.75. The HA solution was stirred at room temperature for 24 hrs. The reaction was stopped by adding 2 M of NaOH to increase the pH to 7.0-7.4. The solution was transferred to a dialysis tube (Mw cut-off=14,000 g/mol) (Sigma Aldrich, UK) with the help of a syringe and clipped at both ends with double latches. The mixture was then dialysed against

150 mM NaCl solution and the deionised water for 24 hrs each. The dialysed HA solution was transferred into a beaker, and the pre-formed crosslinked scaffolds were placed in the solution to create a secondary network for 24 hrs at room temperature. The HA-infiltrated scaffolds (HA) were rinsed in 1 M NaCl (200 mL) and deionised water for 2 hours, respectively. The scaffolds were placed in the moulds with excess deionised water and stored at -20°C overnight before freeze-drying for 24 hrs. Figure 3.4. shows how HA is functionalised by EDC and ADH.

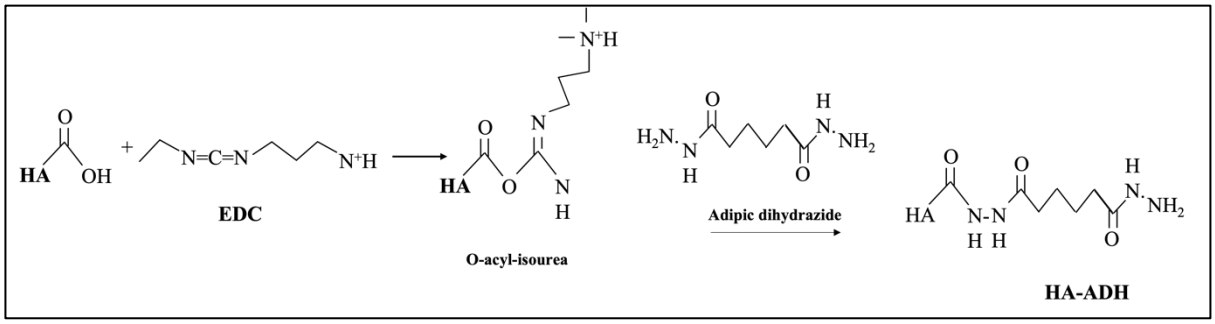


Figure 3.4. HA functionalisation and dihydrazide-bond formation by EDC and ADH (4).

3.2.2. Scanning Electron Microscopy

The channel and micropore structures and the pores' physiochemistry were characterised under scanning electron microscopy (SEM). The freeze-dried rectangular samples were initially incubated in liquid nitrogen for 15 s to preserve the microstructure of the scaffolds. After incubation, the samples were immediately cross-sectioned with a razor blade to 3-4 mm in length, left to air dry and adhered transversely to aluminium stubs (12.5 mm x 6 mm, Agar Scientific, UK) covered with adhesive carbon tabs (12 mm, Agar Scientific, UK).

The samples were sputter coated with platinum using EM ACE600 (Leica Microsystems, Germany) for ~1 min at the sputter rate of 0.10 nm/s at room temperature. The resulting coating thickness was ~6 nm. The Zeiss EVO® MA10 SEM (Zeiss, Germany) was used to image the samples with a vacuum of $1x10^{-5}$-$1x10^{-6}$ mbar. Images were generated using the secondary electron mode at a 20-35 mm working distance. An accelerating voltage of 10 kV was applied using a tungsten source, and a probe current was adjusted to 100 pA. Before imaging, the gun was aligned, and the aperture and astigmatism were corrected manually. Images were taken at

magnifications of 25X-100X. The channel diameter was measured on SEM by assuming they were circular, and the measurement was repeated for 9 different samples to obtain the mean and standard deviation (SD). Both instruments were supplied by the David Cockayne Centre for Electron Microscopy, University of Oxford.

Images were analysed using ImageJ® (National Institutes of Health, USA). The pore size distribution was determined by assuming they were elliptical. The diameters of >100 pores from 12 samples were measured to obtain the mean and SD. The area fraction was used to determine the surface porosity by analysing voids to pore walls and the average pore size was calculated.

The scaffold porosity (P_T) was calculated theoretically by densities using the scaffold's dimensions and the mass before and after the PBS (Sigma Aldrich, UK) immersion (N=5). The dimensions (length, width, and thickness, cm) of all scaffolds were measured using a digital calliper (Mituyoto™, CD-6" CSX, Japan) and the mass (g) was measured using a balance (Analytical Balance, BDH, USA) before PBS immersion. After 24 hrs of PBS incubation, scaffolds were drained on a wire mesh for 1 min and re-weighed, and the dimensions were re-measured. The bulk density (ρ_{Bulk}) and the hydrated scaffolds density (ρ_{wet}) were determined using Equation 3.1.

$$\rho = \frac{mass}{Volume}$$

(Equation 3.1)

The total porosity (P_T) was calculated using Equation 3.2 as follows;

$$P_T = \left(1 - \frac{\rho_{Bulk}}{\rho_{wet}}\right) \times 100$$

(Equation 3.2)

For all analyses, Welch's one-way ANOVA test was used for group comparisons.

3.2.3. Fourier Transform Infrared Spectroscopy

Fourier Transform Infrared (FT-IR) spectroscopy is an analytical technique providing insight into the functional groups of protein structure and the effect of surface properties on protein behaviour. It can be conducted in a solid state compared to other techniques, such as X-ray crystallography or nuclear magnetic resonance (NMR). Using this technique, it is possible to characterise the spectral properties of protein secondary structures and amino acid sequences (5).

In most infrared protein studies, 5 characteristic bands are of particular interest, three of which are known as amide bands. The Amide I band has the strongest absorption of infrared light at between 1600-1700 cm^{-1}. It is the best-known peptide bond vibration resulting from the weak coupling of C=O stretching vibrations with C-N stretching and N-H bending. The amide II band is caused by C-N stretching with N-H in-plane bending at 1500-1600 cm^{-1} wavelength, whereas the Amide III band is formed at 1200-1300 cm^{-1} by a complex mixture of N-H bending and C-N stretching together with C-H and N-H deformation vibrations (6). The combination of EDC-NHS has been widely accepted as a coupling agent that targets a molecule's carboxylic group in an acidic environment and reacts with an amine group of another molecule to form an amide bond (7). An increase in the EDC ratio to the carboxylic groups will result in higher crosslinking density, changing the peaks of any related band group in FT-IR analysis. Therefore, FT-IR was chosen to understand the protein structure of the used materials and the degree of crosslinking of C100 scaffolds, collagen-FEG composites, and HA-infiltrated scaffolds. FT-IR was performed using the Varian Excalibur FTS 3500 Spectrometer at the Oxford Materials Characterisation Services, University of Oxford. Scanning was performed for 3 samples per condition at a wavenumber range of 600-4000 cm^{-1}, with a resolution of 4 cm^{-1} and 64 scans. Second derivatives of the spectra were computed by applying the Savitzky-Golay method with 8 smoothing points in Origin® 2018 (OriginLab Corporation, USA)

software until a good fit was achieved. The signals of products as received were enhanced by the Peak Resolution Enhancement tool using Savitzky–Golay in Origin® 2017. Spectra were normalised to the signal at 2925 cm^{-1} because the crosslinking does not influence this bond, except for FEG-based materials whose spectra were normalised to the signal at 2872 cm^{-1} (8). The relative crosslinking intensity of scaffolds was calculated by the normalisation of amide and ester bonds to the signal at 2925 cm^{-1}. Two-way ANOVA followed by Tukey's post-hoc test was applied to compare the degree of crosslinking among the scaffold types (N=3).

3.2.4. Swelling

The swelling ratio (Q_m) at different temperatures was performed to understand the hydration effect on all freeze-dried scaffolds. The ratio was calculated by comparing the hydrated sample's mass to the original mass of the dry sample, as shown in Equation 3.3. The mass of the dry sample was ~20 mg (Sample dimensions are stated in Table 3.1), and the test was conducted in 0.1 M PBS for 24 hrs either at 20°C or 37°C for 5 different samples per condition. After being immersed in PBS, the samples were drained on a wire mesh for 1 min and re-weighed.

$$Q_m = \frac{mass_{wet} - mass_{dry}}{mass_{dry}}$$

(Equation 3.3)

The theoretical volumetric swelling ratio (Q_v) was also calculated by the relationship between the densities of the polymer (ρ_p) and solvent (ρ_s), as stated in Equation 3.4. The densities of solvent (PBS), collagen and elastin are 1, 1.35 and 1.23 g/cm^3 (9), respectively. Due to the spontaneous infiltration of HA, the HA-infiltrated scaffolds were not included.

$$Q_v = 1 + \frac{\rho_p}{\rho_s}(Q_m)$$

(Equation 3.4)

The polymer-solvent interaction parameter (χ) was calculated by the equation of simplified Flory-Huggings theory using the swelling data where v_{2m} is the volume fraction obtained from the reciprocal Q_v.

$$\chi = \frac{ln(1 - v_{2m}) + v_{2m}}{{v_{2m}}^2}$$

(Equation 3.5)

Q_v data was also obtained experimentally for all scaffold types at 20°C by the change in the volume after solvent absorption compared to the volume of the dry sample, using the following equation:

$$\mathrm{Q_v} = \frac{\mathrm{volume}_{wet} - \mathrm{volume}_{dry}}{\mathrm{volume}_{dry}}$$

(Equation 3.6)

Two-way ANOVA with Tukey's post-hoc test was used for comparisons.

3.2.5. Degradation

3.2.5.1.Non-Enzymatic Degradation

Non-enzymatic degradation was performed for all scaffold types (N=5) by checking the mass change over 3 months. At the beginning of the test, the sample's mass was recorded after being immersed in 0.1 M of PBS with 0.2 mg/mL sodium azide (Sigma Aldrich, UK) overnight in a shaking water bath (Jeio Tech BS-31, Medline Scientific, UK) at 37°C. The hydrated samples were removed from PBS the next day, drained for 1 min on a wire mesh, and the new mass was noted as the original mass at 0 hr ($mass_0$). Each sample was again placed in fresh 0.1 M of PBS with 0.2 mg/mL sodium azide in the shaking water bath at 37°C, and the change in the mass was recorded weekly ($mass_x$) for 12 weeks. The mass loss was calculated at each time point, as indicated in Equation 3.7.

$$\text{Mass Loss (\%)} = \left(\frac{\mathrm{mass_0\text{-}mass_x}}{\mathrm{mass_0}}\right) \times 100$$

(Equation 3.7)

3.2.5.2.Enzymatic Degradation

Enzymatic degradation was studied for all scaffold types (N=5) at 0 hr, 1 hr, 3hrs, 6 hrs, 12 hrs, 24 hrs and 48 hrs. The $mass_0$ was initially recorded as described in Section 3.2.5.1. The hydrated samples were removed from PBS the next day, drained for 1 min on a wire mesh, and the new mass was noted as the original mass at 0 hr ($mass_0$). After this point, different enzyme cocktails were chosen as an incubation solution based on the composition of the scaffold design, as shown in Table 3.3.

Table 3.3. Enzyme cocktails of the related scaffold type.

Scaffold / Enzyme	Non-XL							
	C100	C90E10	C80E20	C75E25	C100	C90E10	C80E20	C75E25
Collagenase (0.05 mg/mL)	+	+	+	+				
Collagenase (0.005 mg/mL)					+			
Elastase (0.005 U/mL)		+	+	+		+	+	+
Scaffold / Enzyme	**XL**				**HA**			
	C100	C90E10	C80E20	C75E25	C100	C90E10	C80E20	C75E25
Collagenase (0.5 mg/mL)	+	+	+	+	+	+	+	+
Elastase (0.5 U/mL)		+	+	+		+	+	+
Hyaluronidase (0.5 mg/mL)					+	+	+	+

Due to the fragile structure of non-crosslinked scaffolds, they were incubated either in 1:10 or 1:100 diluted concentrations of the initial enzyme cocktails. All enzyme cocktails were prepared in PBS with 0.2 mg/ml sodium azide. Collagenase from *Clostridium histolyticum*, elastase from porcine pancreas and hyaluronidase from bovine testes (all from Sigma Aldrich, UK) were used for enzymatic degradation.

The samples were removed from the enzyme cocktail at each timepoint, drained for 1 min on a wire mesh, and the change in the mass was recorded ($mass_x$). Each sample was again placed back in the shaking water bath at 37°C. The mass loss was calculated at each time point, as indicated in Equation 3.7.

3.2.6. Compression and Tensile Testing

Static uniaxial compression and tensile tests were performed to determine the static Young's modulus of scaffolds in the dry and wet state. The tests were performed using an Instron BlueHill Universal System (Instron, USA) for five samples from each group. The system was connected to a 50 N load cell.

The size of scaffolds was stated in Table 3.1 for both testing methods. For dry samples, the compression test was performed as mentioned in Section 2.2.4 and 0.5 N min^{-1} rate was chosen with the same preload parameters for testing. To hydrate samples, scaffolds were immersed in 0.1 M of PBS for 24 hrs at room temperature. The sample's diameters were re-measured and re-recorded. Due to the high elasticity of collagen-FEG composites and sensitivity to any force to apply, non-crosslinked samples were tested at a rate of 5 mN min^{-1} until failure with a 5 mN preload set at a 2 mm min^{-1} rate. For crosslinked and HA-infiltrated scaffolds, the test setup was rearranged at a rate of 50 mN min^{-1} until failure. 25 mN of preload was set at a rate of 2 mm min^{-1}.

A tensile test was performed with the parameters described in Section 2.2.4 for hydrated scaffolds without dehydrating or epoxy adhesive. To hydrate samples, scaffolds were immersed in 0.1 M of PBS for 24 hrs at room temperature. The scaffold dimensions (length, width, and thickness) were re-measured before the test. For both tests, two-way ANOVA followed by Tukey post-hoc was used for statistical analysis.

3.2.7. Three-Point Bending

To evaluate the bending modulus of scaffolds in a dry state, the samples stated in Table 3.1 were tested using an Instron BlueHill Universal System (Instron, USA) for five samples of each group. The set-up was re-designed by Materials Workshop, as shown in Figure 3.5A&B and installed into the system. The test was conducted with a cross-head speed of 0.5 mm min^{-1} using a span of 15 mm, as shown in Figure 3.5C. 50 mN of preload was chosen. A typical

stress-strain curve or three-point bending was obtained from the Instron software. The scaffold's effective bending modulus (E_{bend}) is proportional to the slope of the stress-strain curve. Welch's one-way ANOVA test was used for statistical analysis to compare the bending moduli of each group in the dry state.

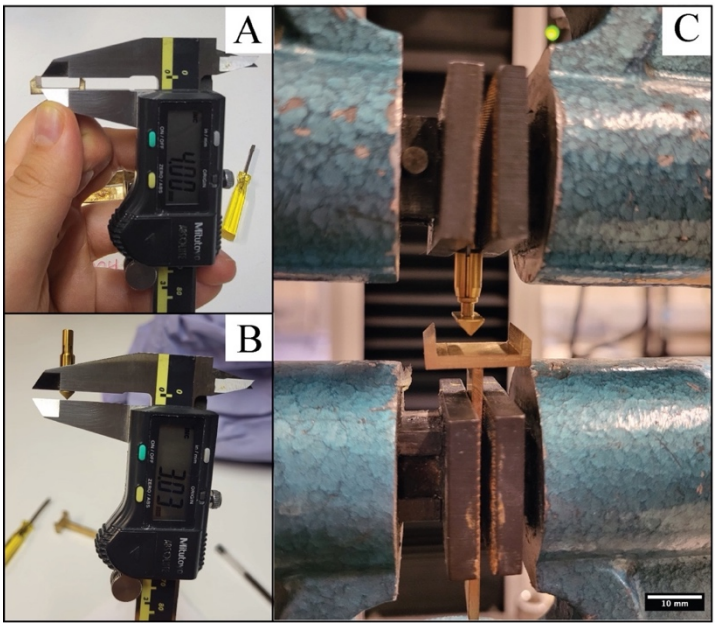


Figure 3.5. The set-up of a three-point bending test designed for the system. (A) shows the height of the two-beam stand while (B) depicts the crosshead (third beam), and (C) when they are installed into the Instron testing machine.

3.2.8. Self-Deflection

As the hydrated scaffolds could not be characterised using our three-point bending test method due to the extremely low load requirement, a previously designed (10) self-deflection method was preferred to test wet samples. The five rectangular scaffolds/groups, stated in Table 3.1, were weighed (Analytical Balance, BDH, USA) in the dry state ($mass_{dry}$) and immersed in 0.1 M PBS for 24 hrs at room temperature. The scaffolds were then placed on a wire mesh for 1 min to drain excessive PBS and re-weighed ($mass_{wet}$). The water uptake ratio (Q_m) was calculated using Equation 3.3. An abrasive material was placed on the edges of the stands to prevent the scaffold from completely falling through. The samples were then placed on the stands with a span of 20 mm and allowed to self-deflect for 2 mins. The schematic view of the

self-deflection set-up is displayed in Figure 3.6. The images were taken by the camera (Canon EOS2000D, Japan) before and after the deflection, where the camera was in a fixed position on another stand. The images were then processed on ImageJ (National Institutes of Health, USA) to calculate the deflection (*D*) of the hydrated scaffolds by using Equation 3.8 where h is the distance between the centre of the span and the lower surface of the deflected scaffolds, and t is the thickness of the scaffold.

$$D = h - \frac{t}{2}$$

(Equation 3.8)

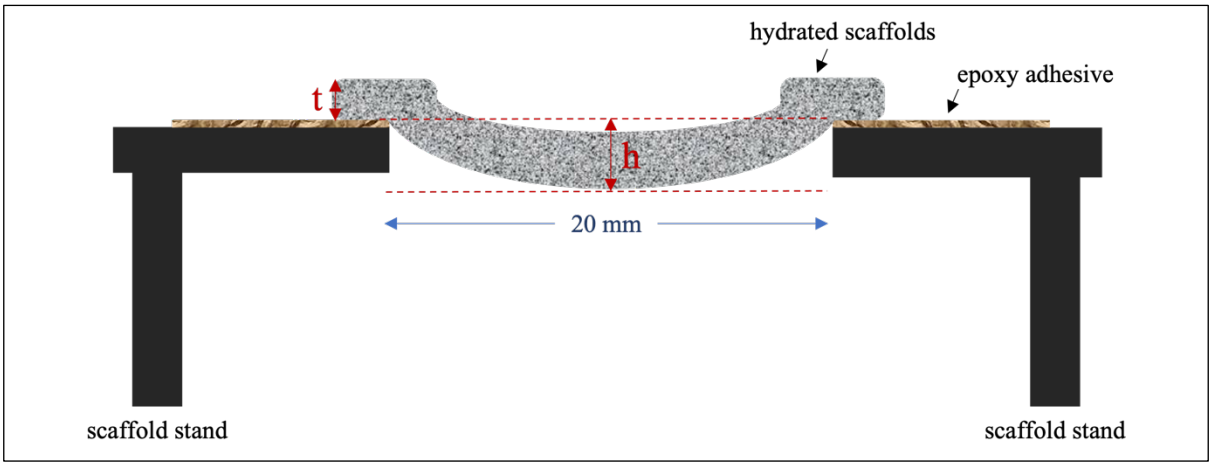


Figure 3.6. Schematic display of self-deflection testing set-up.

Equation 3.9 was used to determine the bending modulus of the scaffold (E_{Bend}) using Q_m as a water uptake ratio, $mass_{dry}$ as the dry mass of the scaffold, g as the gravitational acceleration, l as the span distance, and I as the second moment of inertia. Deflection is assumed to have a linear relationship with load in Equation 3.9 as the equation relies on a simply supported beam with uniformly distributed load (the weight of the absorbed PBS).

$$E_{Bend} = \frac{5ql^4}{384DI} = \frac{5Q_m mass_{dry} gl^3}{384DI}$$

(Equation 3.9)

Statistical analysis was performed using two-way ANOVA followed by Tukey's post-hoc test.

3.3. Results

3.3.1. Scaffold Fabrication, Crosslinking and HA Infiltration

The production protocol of FEG was previously established, as stated (1). The freeze-dried FEG was rehydrated in the current study to create composite scaffolds. For C100 scaffolds, the suspension pH was adjusted to 3.2, whereas the pH of collagen-FEG suspensions was adjusted to 2.7 to rehydrate FEG. pH adjustment was needed to maintain the isoelectric points of both collagen and FEG to generate mixtures that would not cause precipitation or phase separation upon fabrication.

The HA infiltration was first attempted on non-crosslinked composite scaffolds. It was observed that the resulting scaffolds lost their structural integrity after the washing step and dehydration, and freeze-dried scaffolds did not reshape after rehydration (Figure 3.7). They were very distorted and dense, which would affect the feasibility of HA infiltration. Therefore, the pre-crosslinked scaffolds were immediately transferred into the HA solution to create a secondary network without being freeze-dried. The pre-crosslinking helped the scaffold to preserve structural composition and efficient HA infiltration.

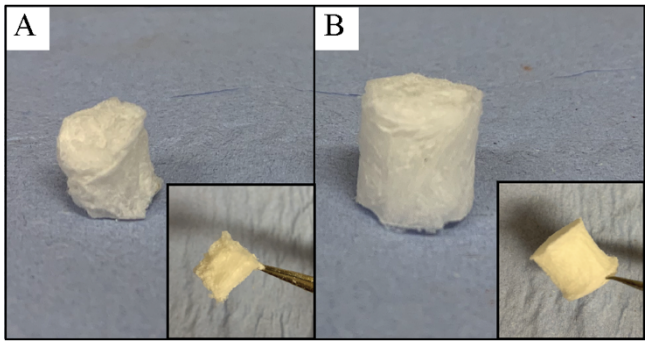


Figure 3.7. HA infiltration into (A) non-crosslinked and (B) crosslinked composite scaffolds. Insets indicate the scaffold morphology after dehydration.

3.3.2. SEM

SEM was performed to understand surface characteristics and porosity distribution. The morphology of pores varied considerably among the scaffold types. Although they were characterised as one elongated big pore containing small, interconnected pores, the 3D

structure made it nearly impossible to identify where the pores started; therefore, they were treated as ellipses during image processing so that the assumptions would not be taken from spherical pores, directly.

Figure 3.8 depicts non-crosslinked scaffolds with various concentrations of FEG to understand the effect of collagen substitution on pore size distribution. It was found that the collagen exchange with FEG encouraged homogenous and circular pores to become more elongated and plate-like as the FEG ratio increased.

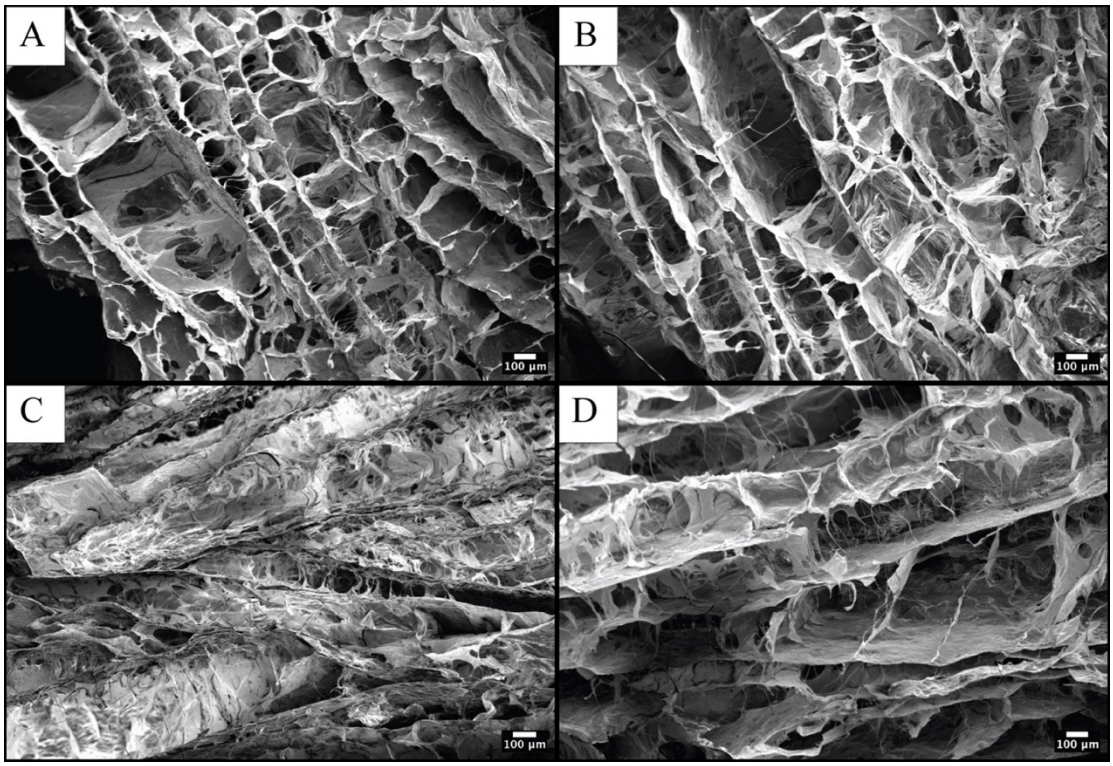


Figure 3.8. SEM images of non-crosslinked (A) C100, (B) C90E10, (C) C80E20, and (D) C75E25 scaffolds (cross-section).

The change in the surface porosity was significantly different among non-crosslinked scaffold types, having 71.59±2.17%, 71.27±1.78%, 68.58±2.38% and 64.80±3.39% porosity for C100, C90E10, C80E20 and C75E25, respectively ($p=0.016$, Figure 3.9A). Additionally, total porosity from relative density supported this decrease, as seen in Table 3.4. A similar difference in area fraction was observed for crosslinked ($p=0.0001$) but not for HA-infiltrated scaffolds, which experienced a slight increase in porosity in collagen-FEG composites ($p=0.55$). The

highest porosity was achieved in crosslinked C100 scaffolds. A supporting fit was also obtained for total porosity analysis for all conditions.

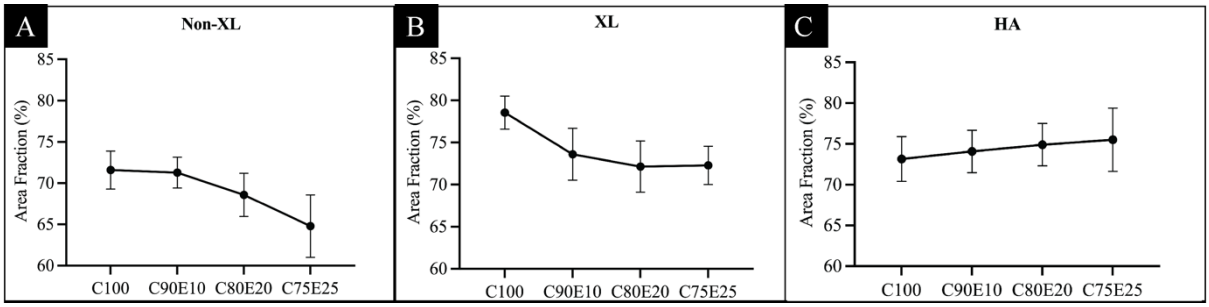


Figure 3.9. Surface porosity change in (A) non-crosslinked, (B) crosslinked, and (C) HA-infiltrated scaffolds (N=12).

Table 3.4. Total porosity (%) from relative density. One way-ANOVA was used to calculate the significant difference between the scaffolds based on the content (column) or condition (row). (Mean±SD, N=5, *p<0.05).

	Non-XL	**XL**	**HA**	**p value**
C100	98.05±0.22	98.12±0.09	97.68±0.17	0.011*
C90E10	97.50±0.25	97.73±0.16	97.57±0.37	0.37
C80E20	97.13±0.50	97.83±0.03	97.22±0.06	0.028*
C75E25	96.86±0.39	97.83±0.08	97.17±0.27	0.02*
p value	0.065	0.017*	0.022*	

The relative pore size was found to range between 50-200 µm for C100 and C90E10, while the pore size of C80E20 and C75E25 composites was mostly found at 20-110 µm with no obtained pores at >150 µm (Figure 3.10). At this range, the average pore size was 65±14 µm, 65±15 µm, 49±20 µm and 48±19 µm, respectively. There was no observation of FEG deposition on the surface of the collagen struts, even at the higher magnifications (data not shown).

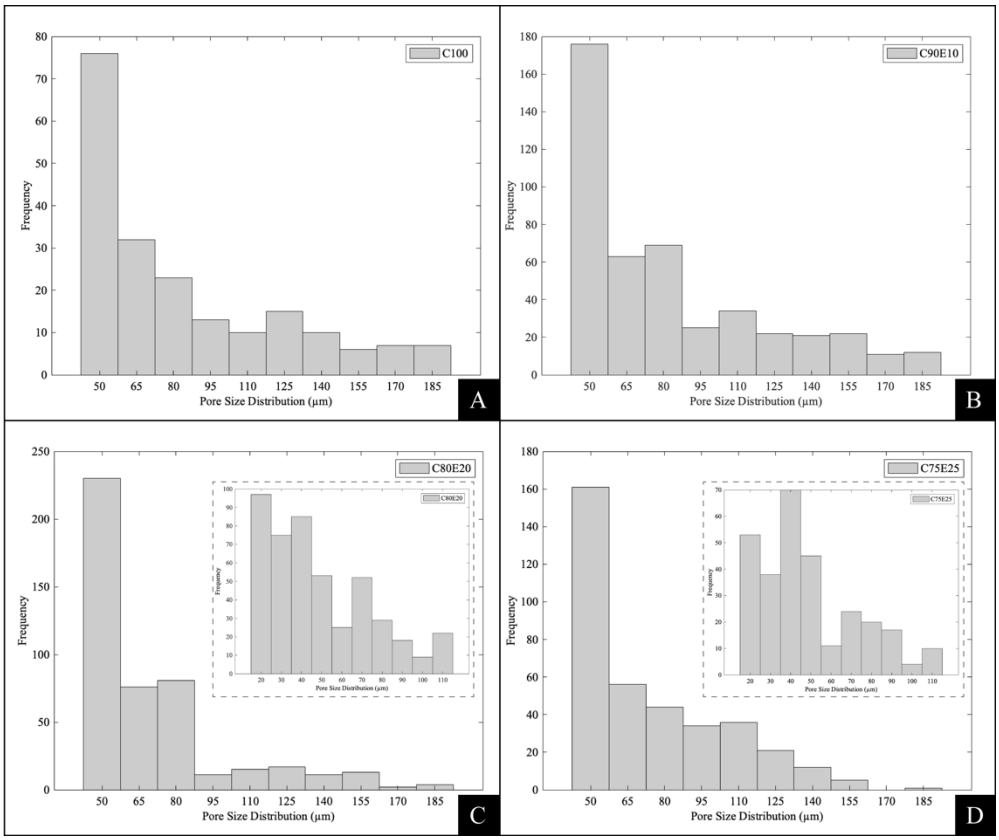


Figure 3.10. Pore size distribution of non-crosslinked (A) C100, (B) C90E10, (C) C80E20, and (D) C75E25 scaffolds.

The crosslinking considerably changed the structural apparency of the pores when the interconnectivity increased as the collagen was substituted with FEG (Figure 3.11). The surface porosity was significantly reduced as the FEG composition increased, showing 78.55±1.86%, 73.60±2.95%, 72.15±2.87% and 72.28±2.04% porosity for C100, C90E10, C80E20 and C75E25, correspondingly (p=0.0001, Figure 3.9B). Although there was no clear difference in the total porosity of collagen-FEG composites (Table 3.4), the substitution of collagen with FEG changed the total porosity of scaffolds significantly (p=0.017). Moreover, it was possible to observe a range in pore size (50-250 µm) of C100 and C90E10 scaffolds, while smaller pores (<100 µm) were mostly obtained in C80E20 and C75E25 scaffolds (Figure 3.12). The average pore size for crosslinked scaffolds was 127±56 µm, 122±53 µm, 61±17 µm, and 62±16 µm for C100, C90E10, C80E20, and C75E25, respectively.

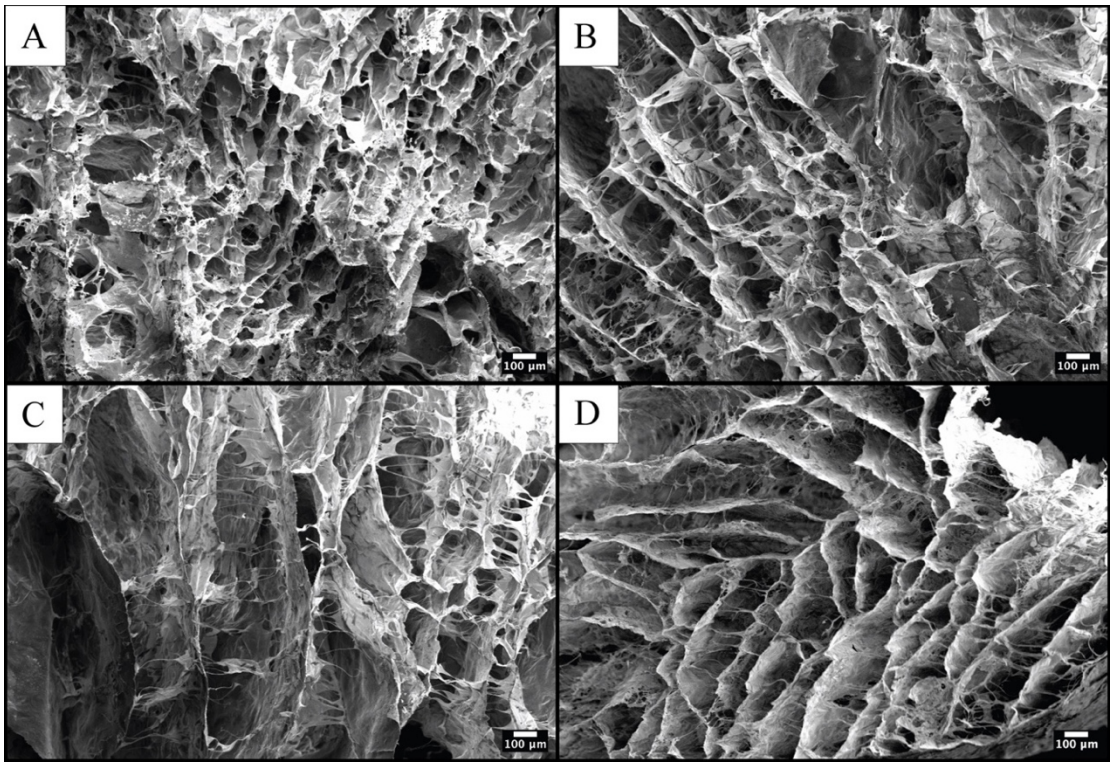


Figure 3.11. SEM images of crosslinked (A) C100, (B) C90E10, (C) C80E20, and (D) C75E25 scaffolds (cross-section).

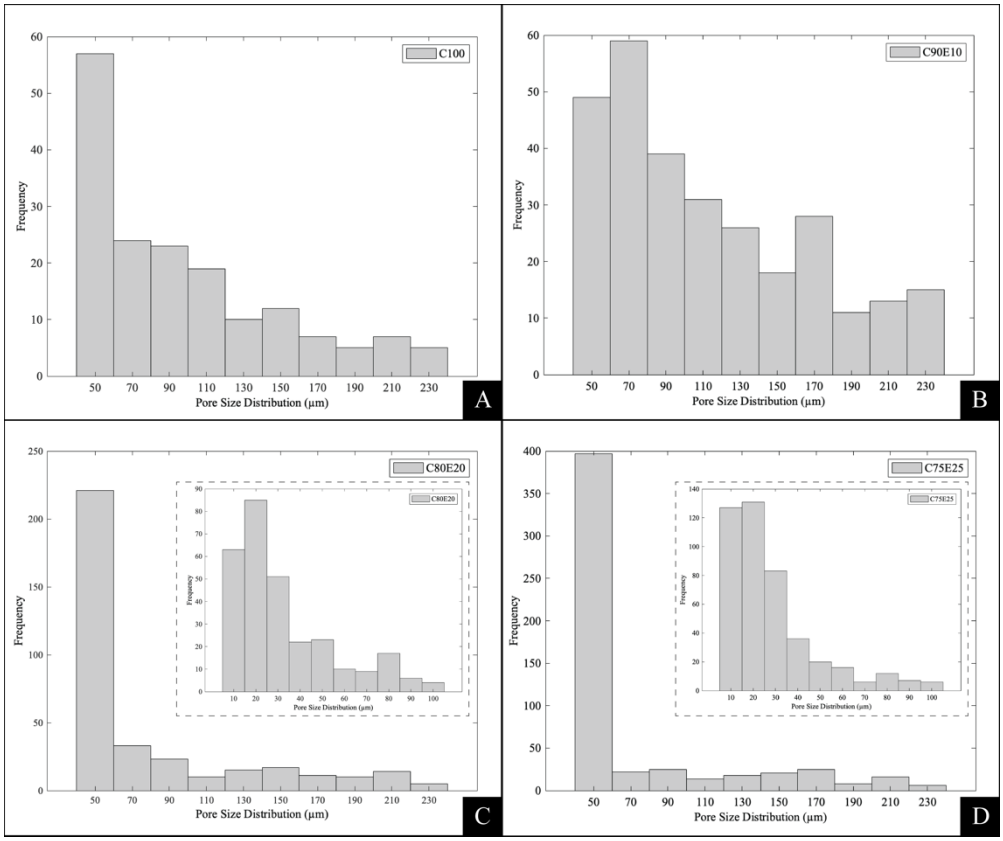


Figure 3.12. Pore size distribution of crosslinked (A) C100, (B) C90E10, (C) C80E20, and (D) C75E25 scaffolds.

The infiltration of HA to the pre-crosslinked scaffolds did not change the microstructure of C100 scaffolds; however, HA seemed to be well-blended with FEG struts following infiltration (Figure 3.13). The interconnected pores became less obvious as the FEG composition increased. The infiltration of HA connected the rods seen in crosslinked scaffolds resulting in more integrated pores, especially in C75E25 scaffolds. This can be seen in the area fraction change among the HA-infiltrated collagen-FEG composites compared to crosslinked ones, which increased by 0.64%, 3.81%, and 4.46% for C90E10, C80E20, and C75E25, respectively. Although the total porosity from relative density analysis obtained a significant difference between HA-infiltrated scaffolds, there was a slight decrease compared to the crosslinked scaffolds, as seen in Table 3.4. The pore size distribution of the scaffolds is presented in Figure 3.14. The average pore size for the HA-infiltrated scaffold was recorded as 92±27 µm, 63±14 µm, 65±15 µm, and 63±14 µm for C100, C90E10, C80E20, and C75E25, respectively.

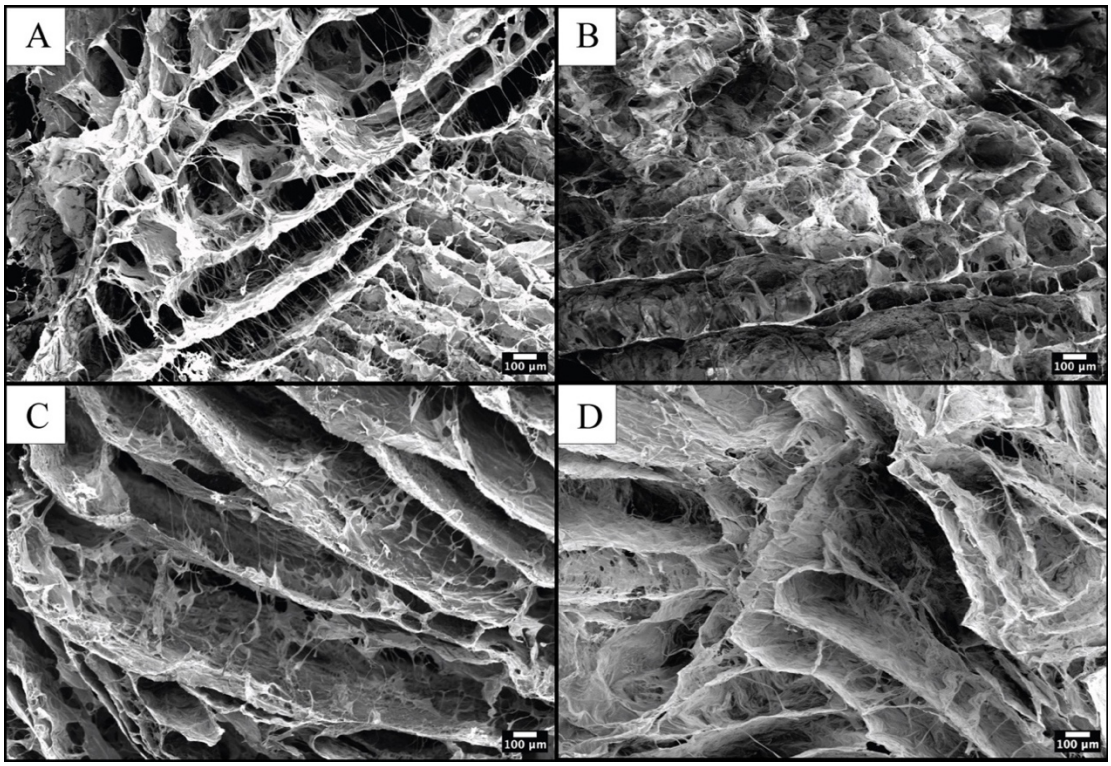


Figure 3.13. SEM images of hyaluronic acid-infiltrated (A) C100, (B) C90E10, (C) C80E20, and (D) C75E25 scaffolds (cross-section).

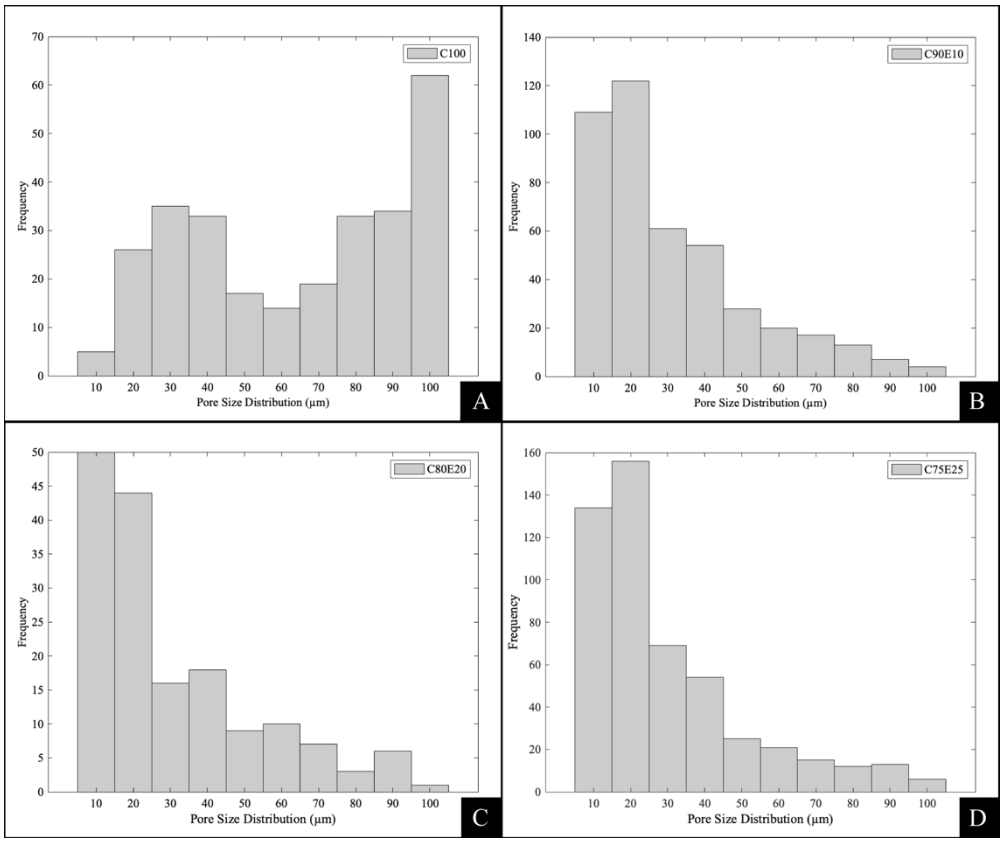


Figure 3.14. Pore size distribution of HA-infiltrated (A) C100, (B) C90E10, (C) C80E20, and (D) C75E25 scaffolds.

The change in the channel diameter was also measured using SEM (Figure 3.15). The results indicated that the average channel diameters of C100 scaffolds were 1.14±0.10 mm, 1.20±0.08 mm and 1.16±0.12 mm for three conditions. Unlike C100 scaffolds, the average channel diameter was relatively lower for collagen-FEG composite scaffolds changing from 1.16±0.10 mm to 1.02±0.11 mm. Overall, change in channel diameter did not differ in all groups, except for crosslinked scaffolds ($p=0.003$), where considerably higher channel diameter was obtained in C100 scaffolds; however, there was no significance between collagen-FEG composites ($p=0.43$). This result showed that crosslinking and HA infiltration did not change the channel size even after the second freeze-dry.

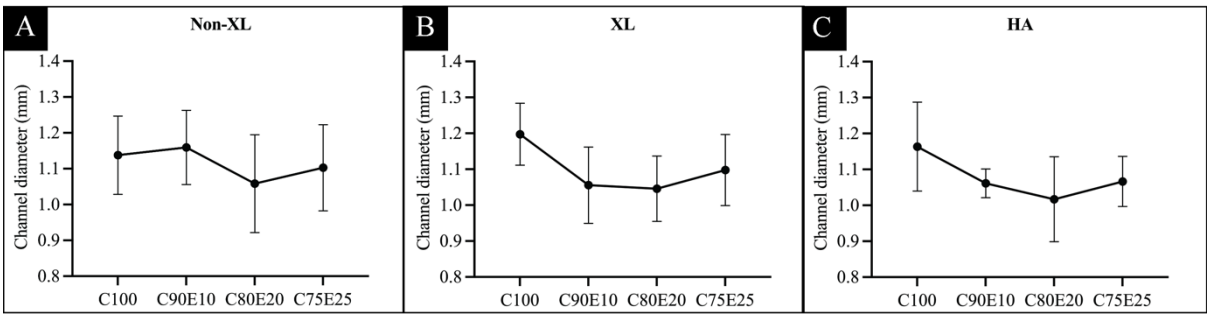


Figure 3.15. Channel diameters change of (A) non-crosslinked, (B) crosslinked, and (C) HA-infiltrated scaffolds (12≤N≤16).

3.3.3. FT-IR

FT-IR was conducted to identify the degree of crosslinking and to understand the effect of crosslinking on scaffold chemistry. All scaffold types and raw materials (as received) were studied.

The absorbance spectra for powder elastin as purchased and refined are shown in Figure 3.16 with their second derivatives. The characteristic peaks of elastin were represented here for all conditions, and the band assignments were categorised in Table 3.5. It was found that Amide A significantly shifted by -11 cm^{-1} and -9 $cm^{-1,}$ and Amide I shifted by 6 cm^{-1} and 7 cm^{-1} after FEG was produced and crosslinked, respectively. Except for these, there was no significant shift between non-crosslinked and crosslinked FEG materials. The second derivative of the Amide I, shown in Table 3.7, indicated no significant shift at 1616-1621 cm^{-1} peaks assigned to the intermolecular β-sheet (weak). In addition, two strong β-sheet peaks at 1628-1637 cm^{-1} were observed, indicating intramolecular β-sheets, with no significant shift either. Higher peak intensity was seen after crosslinking since the Amide I/Amide A ratio was found as 3.23±0.12, 4.09±0.02 and 5.11±0.24 for raw material, non-crosslinked and crosslinked FEG, respectively.

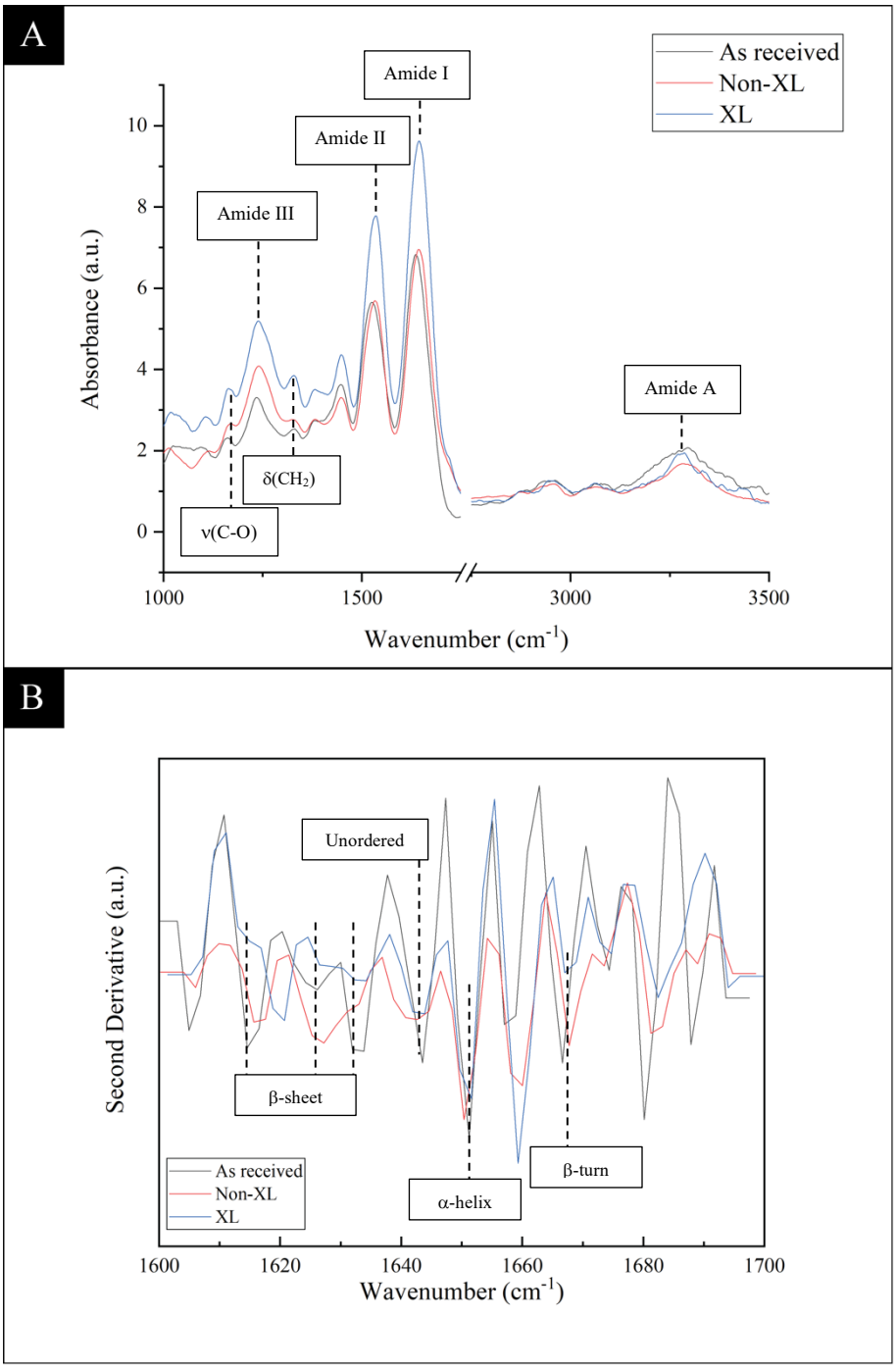


Figure 3.16. (A) FT-IR spectrum of non-crosslinked elastin powder (as received), non-crosslinked and crosslinked FEG scaffolds between 1000-3500 cm^{-1} and (B) the second derivative of these materials between 1600-1700 cm^{-1}.

Table 3.5. Band assignments for FT-IR spectra of FEG at different conditions (11).

Sample	Absorption Band (cm^{-1})					
	Amide A	Amide I	Amide II	δ(CH_2)	Amide III	ν(C-O)
FEG - as received	3296	1637	1526	1329	1234	1161
FEG - Non-XL	3285	1643	1533	1325	1240	1171
FEG - XL	3287	1645	1535	1329	1238	1165

The FT-IR spectra for collagen type I as received, and non-crosslinked, crosslinked and HA-infiltrated C100 scaffolds and second derivative of collagen structure are presented in Figure 3.17. All bands assigned to the protein structure can be seen for all samples and are summarised in Table 3.6. There is a significant shift in Amide I and II after scaffold fabrication, as 10 cm^{-1} and 11 cm^{-1}, respectively. A considerable shift was noted in the $\delta(CH_2)$ band by 14 cm^{-1} after production. There was no significant shift between non-crosslinked and crosslinked C100 scaffolds; however, a higher peak intensity was recorded as 3.23±0.49 and 1.32±0.06 for both Amide and ν(C-O) ester bonds, respectively, which can be seen in Figure 3.22. These peaks directly indicate the crosslinking efficacy of EDC-NHS. A second derivative of protein structure, presented in Table 3.7, revealed a -6 cm^{-1} shift for weak intermolecular β-sheets, which shifted back into the first position after crosslinking. There was no significant shift on any assigned bands, but for crosslinked scaffolds, only one intramolecular β-sheet was noticeable at 1628-1637 cm^{-1}. The ratio of Amide III (1240 cm^{-1}) to δ(C-H) (1456 cm^{-1}) was around 1 for all scaffolds after fabrication, indicating that a triple-helix structure of collagen was preserved (12, 13).

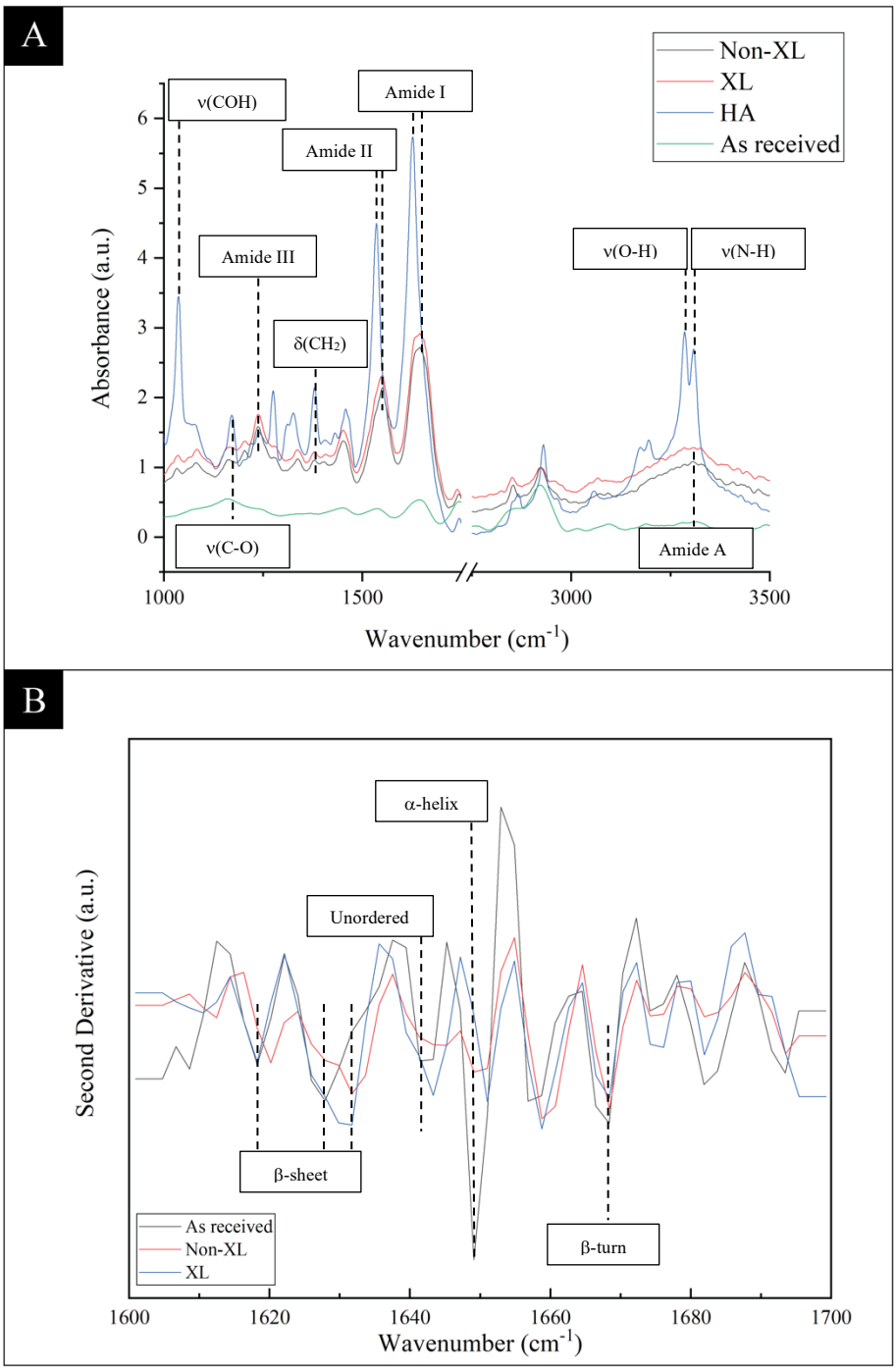


Figure 3.17. (A) FT-IR spectrum of non-crosslinked collagen powder (as received) and non-crosslinked, crosslinked and HA-infiltrated C100 scaffolds, between 1000-3500 cm^{-1} and (B) the second derivative of these materials between 1600-1700 cm^{-1}.

Table 3.6. Band assignments of collagen-based materials by FT-IR at different conditions (5).

Sample	Absorption Band (cm^{-1})								
	ν(N-H)	ν(O-H)	Amide A	Amide I	Amide II	δ(CH_2)	Amide III	ν(C-O)	ν(COH)
Collagen - as received	-	-	3287	1635	1539	1323	1240	1159	-
C100 - N-XL	3306	-	3285	1645	1550	1337	1238	1163	-
C100 - XL	3310	-	3285	1645	1551	1337	1238	1165	-
C100 - HA	3308	3285	-	1628	1535	1327	1240	1171	1038

Table 3.7. Secondary structure assignment of Amide I components in FEG and Collagen type I by FT-IR at different conditions (14, 15).

Sample	2nd Derivative of Amide I					
	β-sheet (weak)	β-sheet (strong)	β-sheet (strong)	Random coil	α-helix	β-turns
FEG - as received	1616	1628	1634	1645	1653	1668
FEG Non-XL	1618	1628	1634	1641	1651	1668
FEG XL	1618	1628	1632	1643	1651	1668
C100 - as received	1622	1630	1638	1649	1653	1668
C100 Non-XL	1616	1632	1638	1645	1655	1668
C100 XL	1622	1630	-	1647	1655	1668

Figure 3.18 shows the FT-IR spectra of HA at a different stages of fabrication. Here, characteristic bands of HA structure were presented, and it can be seen that the twin peaks at N-H and O-H stretching vibrations directly indicated the HA crosslinking. Table 3.8 summarises all the assigned bands for HA-based materials. There was a significant shift for C=O stretching vibration by 13 cm^{-1} after producing HA. There was no clear peak at sodium hyaluronan powder's N-H bending and C-N stretching vibrations. Following ADC and EDC introduction, these peaks became detectable, and crosslinking did not change band location for any specific peak range, except for COH stretching vibration, which shifted by -6 cm^{-1} after crosslinking.

The HA infiltration to C100 scaffolds resulted in a significant shift in various peaks of interest for the protein structure (Table 3.6). A significant shift occurred for Amide I, II, CH_2 bending and C-O stretching vibrations by -17, -16, -10 and 6 cm^{-1}, respectively, after HA infiltration and prolonged crosslinking. There were also twin peak appearances of O-H and N-H stretching

vibrations that correspond to HA crosslinking directly. The effect of prolonged crosslinking with HA was shown in Figure 3.22, where 1.9 and 1.3-fold higher peak intensity was observed for Amide and ester bonds, correspondingly in C100 HA-infiltrated scaffolds compared to crosslinked ones.

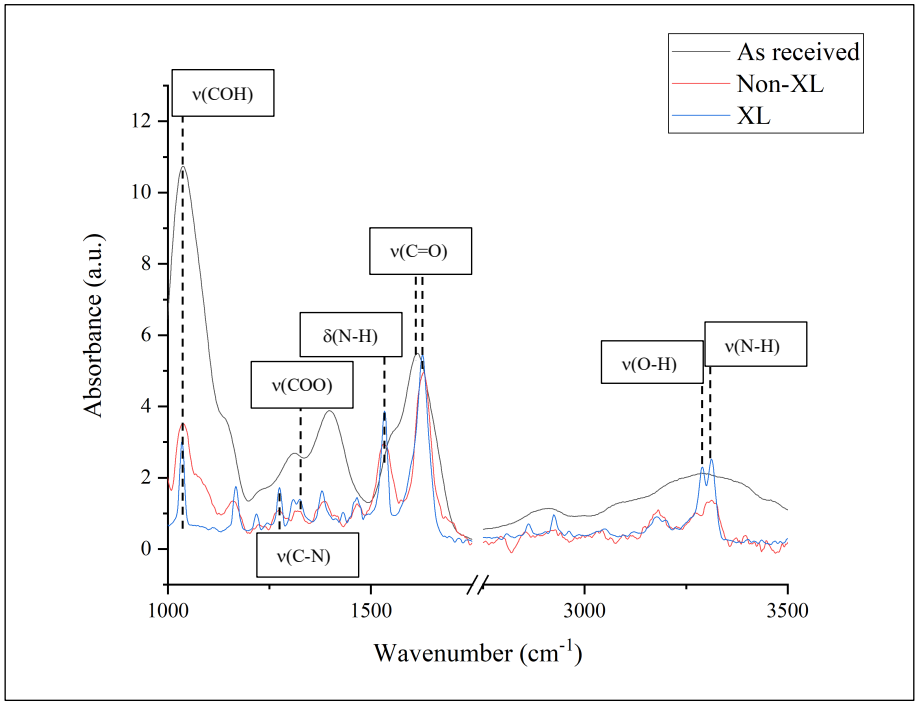


Figure 3.18. (A) FT-IR spectrum of non-crosslinked SHA powder (as received), non-crosslinked (ADH & EDC) and prolonged crosslinked HA scaffolds between 1000-3500 cm^{-1}.

Table 3.8. Band assignment for FT-IR spectra of hyaluronic acid-based materials at different conditions.

Sample	Absorption Band (cm^{-1})						
	ν(N-H)	ν(O-H)	ν(C=O)	δ(N-H)	ν(COO-)	ν(C-N)	ν(COH)
HA - as received	-	3289	1616	-	1398	-	1036
HA - Non-XL	3312	3289	1629	1531	1466	1273	1040
HA - XL	3312	3290	1628	1533	1466	1275	1034

The spectra of FT-IR were also presented for C90E10, C80E20 and C75E25 composite scaffolds in Figure 3.19-21. All assigned bands of protein structure and the efficient HA crosslinking were indicated in these figures and summarised in Table 3.9. There was no significant shift between non-crosslinked and crosslinked C90E10 and C80E20 scaffolds. However, for C75E25 composite scaffolds, Amide I and II considerably shifted by 8 cm^{-1} and

6 cm^{-1}, respectively. In addition, 11 cm^{-1} of a shift was noticed for the Amide A band after crosslinking C75E25 composites. A series of striking shifts was obtained for all scaffold types after HA infiltration alongside prolonged crosslinking. The Amide I, II and $\delta(CH_2)$ peaks shifted by -19 cm^{-1}, -16 cm^{-1} and 40 cm^{-1}, respectively, in HA-infiltrated C90E10 scaffolds and by -14, -14, and 40 cm^{-1} in C80E20 HA infiltrated scaffolds. A significant shift by -12 cm^{-1} recorded at 1153 cm^{-1} corresponded to C-O stretching vibration. Amide I, II, III, and CH_2 bending vibrations of C75E25 HA scaffolds shifted by -19, -18, 6 and 42 cm^{-1}, respectively. The twin peak at 3280-3330 cm^{-1} region seen for all HA-infiltrated composites could confirm the prolonged crosslinking of HA with ADH and EDC. The relative peak intensity of Amide I in C90E10 composites was 2.91±0.24 after crosslinking and increased by 1.92-fold following HA infiltration, as presented in Figure 3.22. Meanwhile, post-crosslinking ester bond intensity was obtained as 1.08±0.09, which increased to 1.56±0.11 after the contribution of HA. Compared to non-crosslinked C80E20 scaffolds, Amide I absorbance was 1.15- and 2.32-fold higher in crosslinked and HA-infiltrated scaffolds, respectively. It was detected as high as 1.15-fold in crosslinked and 1.37-fold in HA-infiltrated C80E20 scaffolds for ester crosslinking. The same trend can be seen in C75E25 composites, as the Amide I absorbance intensified by 3.32±0.17 and 4.47±0.04 after crosslinking and HA-infiltration, respectively. 1.29- and 1.49-fold higher ester absorbance was found in crosslinked and HA-infiltrated C75E25 scaffolds, correspondingly compared to non-crosslinked ones. All comparisons were statistically significant for all scaffold types.

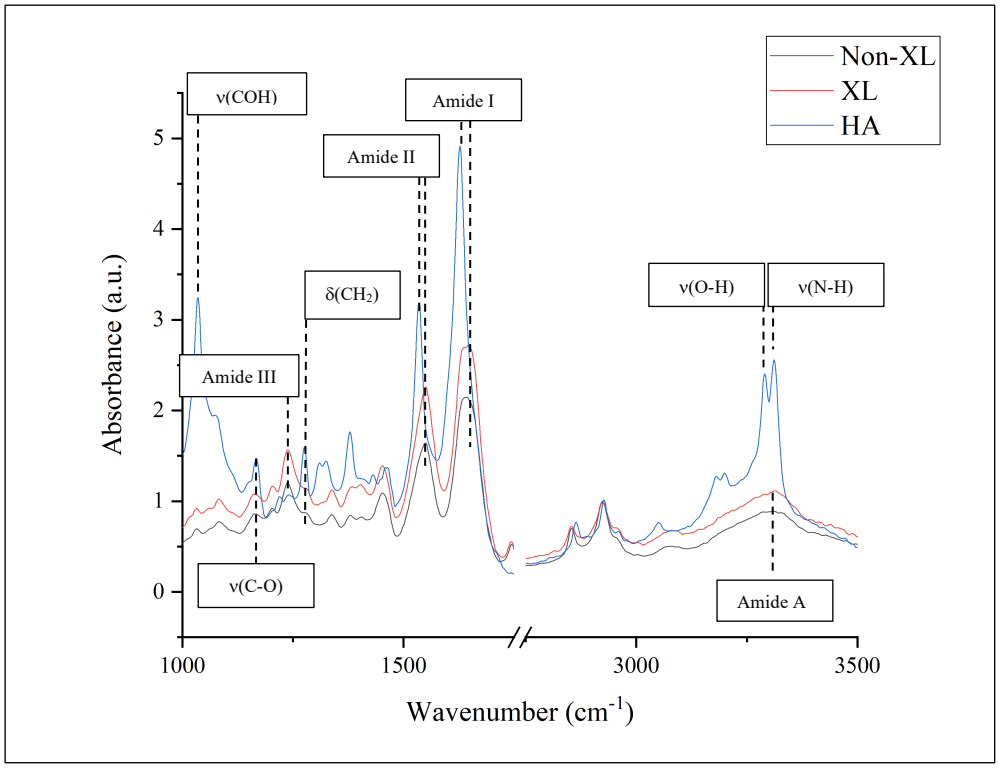


Figure 3.19. FT-IR spectrum of (A) non-crosslinked, crosslinked, and HA-infiltrated C90E10 scaffolds, between 1000-3500 cm^{-1}.

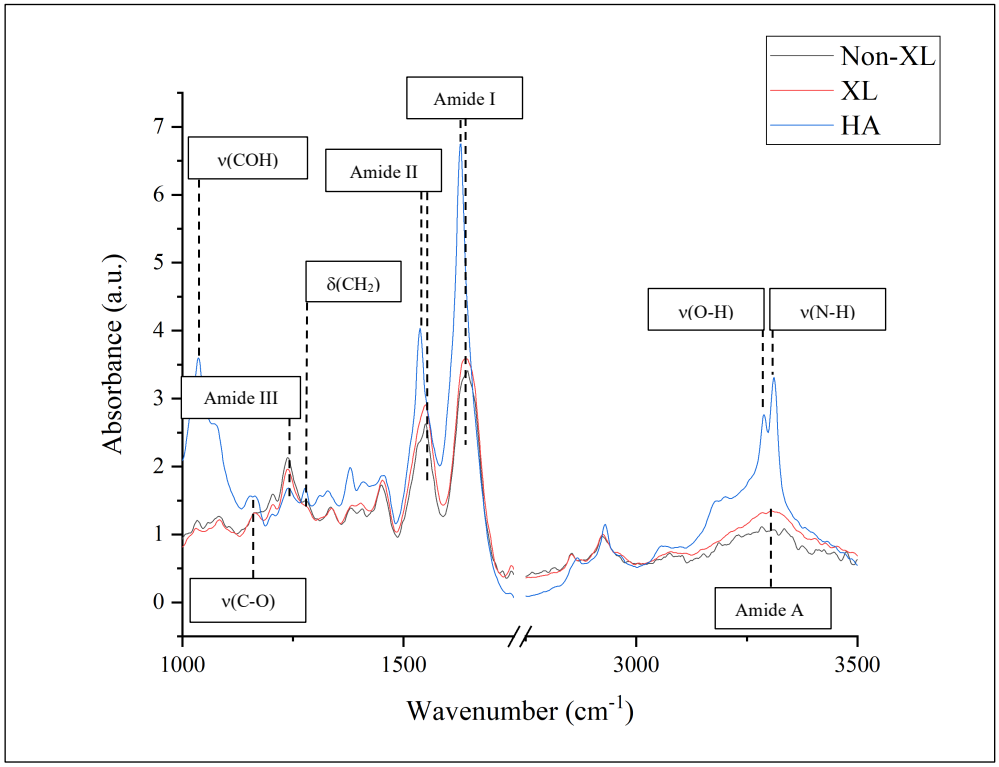


Figure 3.20. FT-IR spectrum of (A) non-crosslinked, crosslinked, and HA-infiltrated C80E20 scaffolds, between 1000-3500 cm^{-1}.

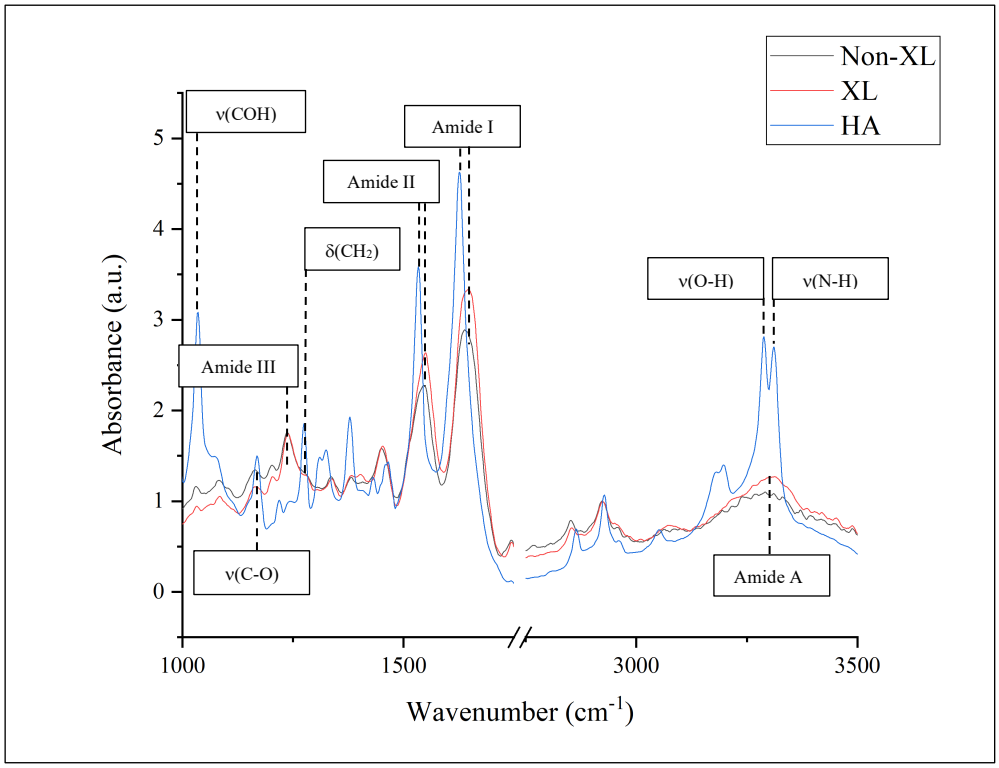


Figure 3.21. FT-IR spectrum of (A) non-crosslinked, crosslinked, and HA-infiltrated C75E25 scaffolds, between 1000-3500 cm^{-1}.

Table 3.9. Band assignments for FT-IR spectra of C90E10, C80E20 and C75E25 scaffolds at different conditions.

Sample	Absorption Band (cm^{-1})								
	ν(N-H)	ν(O-H)	Amide A	Amide I	Amide II	δ(CH_2)	Amide III	ν(C-O)	ν(COH)
C90E10									
Non-XL	3308	-	3286	1645	1551	1339	1238	1165	-
XL	3311	-	3287	1647	1551	1339	1238	1163	-
HA	3312	3291	-	1628	1535	1379	1242	1166	1035
C80E20									
Non-XL	3310	-	3283	1645	1551	1335	1238	1163	-
XL	3310	-	3279	1643	1551	1339	1238	1165	-
HA	3312	3289	-	1629	1537	1379	1240	1153	1035
C75E25									
Non-XL	3311	-	3291	1639	1545	1337	1236	1165	-
XL	3314	-	3302	1647	1551	1337	1238	1165	-
HA	3310	3289	-	1628	1533	1379	1244	1168	1035

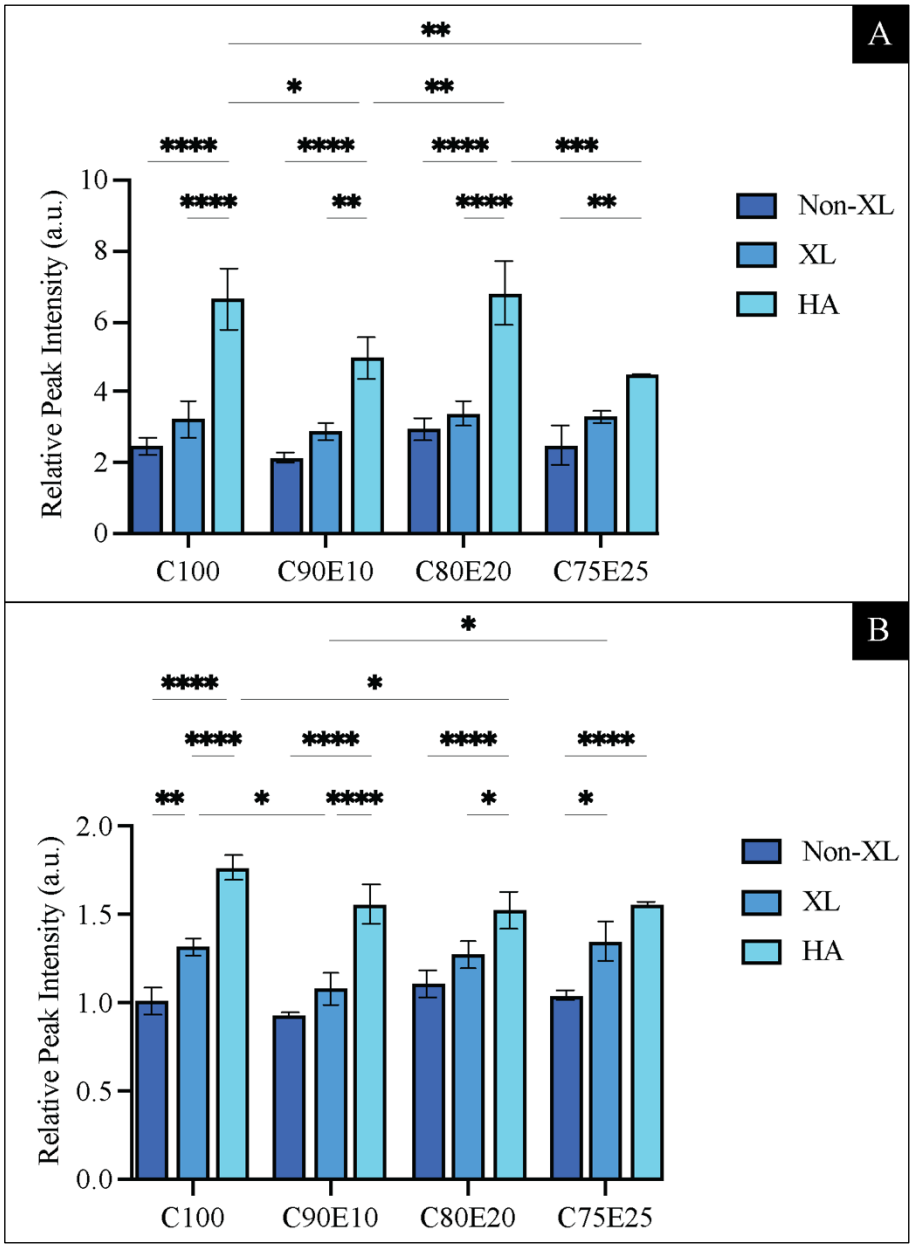


Figure 3.22. The relative crosslink intensity change based on (A) Amide I and (B) ν(C-O) ester bond. Two-way ANOVA followed by Tukey post-hoc test was used. (Mean±SD, *p<0.05, **p<0.01, ***p<0.001, ****p<0.0001, N=3).

3.3.4. Swelling

Figure 3.23 shows the change in the swelling ratio of C100, C90E10, C80E20 and C75E25 scaffolds tested with PBS at 20°C and 37°C. The scaffold's solvent absorption ratio varied based on composition, physicochemical structure, and temperature. No significant difference was found in non-crosslinked scaffolds, regardless of content and temperature.

The crosslinking increased the amount of solvent absorbed significantly to 51.43±2.67, 44.03±1.20, 41.38±1.36 and 35.10±1.02 at 20°C, for C100, C90E10, C80E20 and C75E25 scaffolds, respectively; although it decreased as the FEG content increased. The solvent absorption increased by 3.8-, 3.5-, 2.8- and 2.3-fold for C100, C90E10, C80E20, and C75E25 HA-infiltrated scaffolds, respectively, compared to the non-crosslinked group. Yet, it was not significantly different from that in the crosslinked scaffolds, except for C80E20 scaffolds, which was unexpected as the HA is known to increase the solvent uptake ratio normally. The swelling ratio of HA-scaffolds also decreased as the FEG content increased, where the solvent absorbed decreased significantly from 5099±144 to 3316±207%.

When the temperature was 37°C, C100-HA scaffolds absorbed the most solvent by 5611±221%, where the swelling ratio increased by 11.8% in C100-HA scaffolds compared to the crosslinked scaffolds ($p<0.001$). Although a similar increase was observed in the C90E10 group ($p<0.01$), there was no significant difference between crosslinked and HA-infiltrated groups of C80E20 and C75E25 scaffolds. A decrease in solvent absorption was seen again as more collagen was replaced with FEG. C90E10 and C80E20 scaffolds absorbed more PBS, which increased by 3.4-fold after crosslinking compared to non-crosslinked scaffolds. Following HA infiltration, a slight increase could still be seen as ~3.7-fold for both scaffolds. However, C75E25 scaffolds experienced an increase of 2.7- and 3-fold after crosslinking and HA-infiltration, respectively.

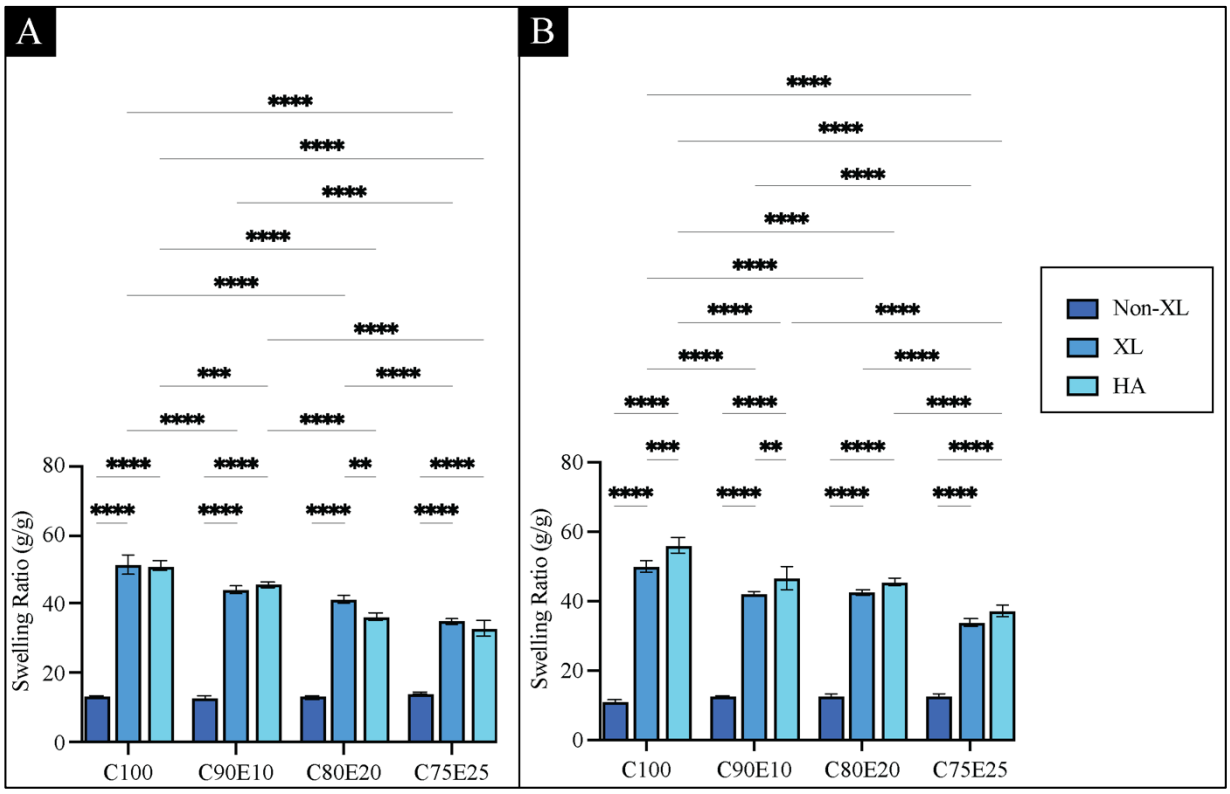


Figure 3.23. The change in solvent absorption for non-crosslinked, crosslinked, and hyaluronic acid-infiltrated scaffolds at (A) 20°C and (B) 37°C. Two-way ANOVA followed by Tukey post-hoc test was used. (**p<0.01, ***p<0.001, ****p<0.0001, N=5).

The theoretical volume fractions and polymer-solvent interaction parameters were determined for non-crosslinked and crosslinked scaffolds at 20°C, as seen in Table 3.10. It was found that the volume fraction significantly reduced after crosslinking, with a fold change of between 2.4-3.7 as collagen content increased. At 37°C, a significant change was noticed only for C100 non-crosslinked scaffolds compared to other non-crosslinked groups, shown in Table 3.11, but it was not noticeable after crosslinking.

The polymer-solvent interaction parameter (χ) was calculated to understand the miscibility of polymers with the solvent, which ranged between -0.518 to -0.520 and -0.505 to -0.507 for non-crosslinked and crosslinked scaffolds, respectively. No significant change was recorded when the temperature was 37°C, except for C100 non-crosslinked group, with a slight decrease compared to all scaffold types.

Table 3.10. The summary of volume fractions (ϕ) and polymer-solvent interaction parameters (χ) for scaffolds in PBS at 20ºC.

20ºC	ϕ		χ	
Scaffold	Non-XL	XL	Non-XL	XL
C100	0.0525	0.0142	-0.518	-0.505
C90E10	0.0582	0.0171	-0.520	-0.506
C80E20	0.0576	0.0184	-0.520	-0.506
C75E25	0.0536	0.0218	-0.519	-0.507

Table 3.11. The summary of volume fractions (ϕ) and polymer-solvent interaction parameters (χ) for scaffolds in PBS at 37ºC.

37ºC	ϕ		χ	
Scaffold	Non-XL	XL	Non-XL	XL
C100	0.0728	0.0149	-0.526	-0.505
C90E10	0.0572	0.0178	-0.520	-0.506
C80E20	0.0571	0.0182	-0.520	-0.506
C75E25	0.0554	0.0226	-0.519	-0.508

The occurrence of shrinkage or swelling resulting in scaffolds after PBS immersion for 24 hrs was determined experimentally at 20ºC and summarised in Table 3.12. It can be seen that shrinkage occurred in non-crosslinked scaffolds, but the scaffolds swelled after crosslinking and HA infiltration. Non-crosslinked scaffolds shrunk by 51.4-70.3%, with a decrease in shrinkage as the FEG content increased. After crosslinking, the presence of FEG in C80E20 and C75E25 scaffolds caused volumetric shrinkage, with the C75E25 group shrinking by 15.73%. After HA infiltration, all scaffolds swelled by ~20% compared to their dry volume.

Table 3.12. The experimental volumetric shrinkage (%) and swelling (%) of non-crosslinked, crosslinked, and HA-infiltrated scaffolds after PBS absorption at 20ºC. One-way ANOVA was performed for different conditions within the same scaffold content. The negative values indicate volumetric shrinkage, whereas positive values show volumetric swelling. (Mean±SD, *p<0.001, **p<0.0001, N=5.)

Scaffold	Non-XL	XL	HA	p value
C100	-70.31±4.9	3.05±2.7	18.87±5.4	<0.0001**
C90E10	-64.29±3.7	2.73±1.3	20.19±6.2	<0.0001**
C80E20	-64.03±9.1	-10.34±6.5	23.87±4.8	<0.0001**
C75E25	-51.43±4.9	-15.73±7.7	19.96±1.0	0.0003*

3.3.5. Degradation

3.3.5.1.Non-Enzymatic Degradation

The non-enzymatic degradation profile of all scaffolds is presented in Figure 3.24. It was found that the substitution of collagen with FEG resulted in faster degradation for non-crosslinked scaffolds. The same profile could also be seen for crosslinked scaffolds; however, for HA-infiltrated scaffolds, the presence of FEG caused slower degradation. In the first week, non-crosslinked, crosslinked, and HA-infiltrated C100 scaffolds considerably degraded less than other groups by losing 13.3%, 5.73% and 14.81% of their original mass, correspondingly. In comparison, non-crosslinked, crosslinked, and HA-infiltrated C75E25 scaffolds significantly degraded more than other groups by losing 18.95%, 13.4% and 19.72% of their initial mass, respectively. The same trend was seen after week 2, but the degradation of C75E25 slowed down, whereas C100 degradation increased over 12 weeks such that, in the end, no significant difference was found between the scaffolds. At week 12, 8.54±0.53%, 6.22±1.43%, 8.83±1.21% and 9.51±1.12% of mass for C100, C90E10, C80E20 and C75E25 non-crosslinked scaffolds remained respectively. After crosslinking, the remaining mass of C100, C90E10, C80E20 and C75E25 scaffolds was 4.44±0.39%, 3.81±0.14%, 5.89±0.26%, and 5.35±0.65% of their initial mass, whereas it was 4.04±0.55%, 4.56±0.45%, 6.65±0.74%, and 6.78±0.76% after HA infiltration, respectively.

Overall, initially, non-crosslinked scaffolds seemed more resistant to degradation over time than crosslinked and HA-infiltrated versions. When FEG was introduced; unfortunately, neither crosslinking nor the infiltration of HA alongside prolonged crosslinking slowed down the degradation rate of these scaffolds without any enzymatic activity.

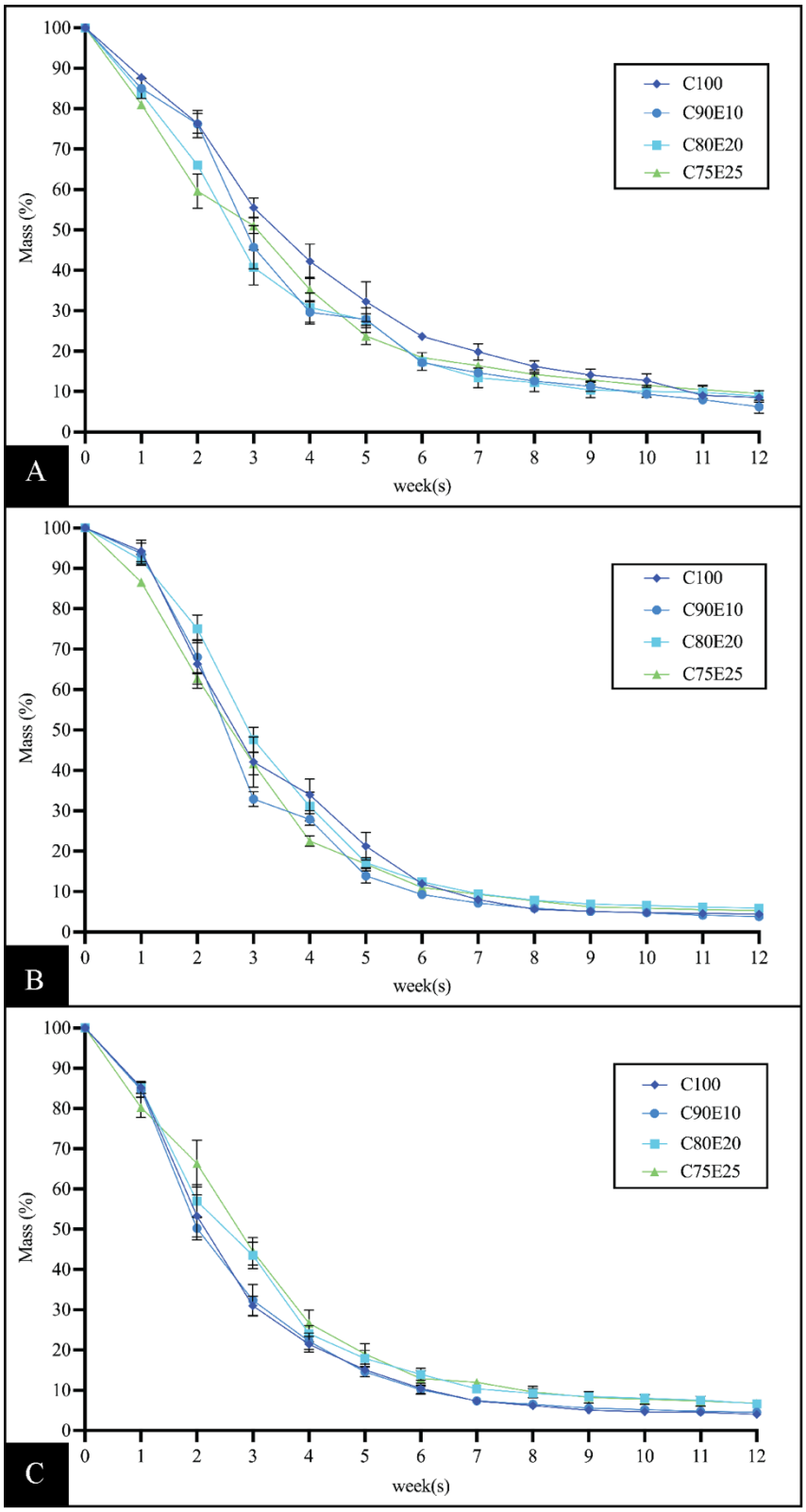


Figure 3.24. Non-enzymatic degradation of (A) non-crosslinked, (B) crosslinked, and (C) hyaluronic acid-infiltrated scaffolds for 12 weeks. (No error bar appeared for certain points on the graphs where the error bar is shorter than the size of the symbol used.)

3.3.5.2.Enzymatic Degradation

The enzymatic degradation profile of non-crosslinked C100 and collagen-FEG composite scaffolds is presented in Figure 3.25. The C100 scaffolds were degraded by collagenase only, whereas collagen-FEG composite scaffolds were degraded either by elastase or elastase+collagenase enzyme cocktail. The results revealed that when collagenase was introduced, C100 non-crosslinked scaffolds lost 41.76±4.3% of their mass in the first hour (Figure 3.25A). Due to the decrease in the substrate, the degradation rate slowed, yet there was no detectable scaffold structure nor fibre to weigh by 12 hrs.

Figure 3.25B shows the degradation rate of non-crosslinked collagen-FEG composites by elastase for 48 hrs. The results indicated that the mass loss of C90E10, C80E20, and C75E25 scaffolds was 9.81±3.8%, 34.33±4.71%, and 16.48±2.34% after 1 hr, respectively. The degradation of C80E20 scaffolds was much faster than the other two, but this difference disappeared after 6 hrs. By the end of 48 hrs, the remaining mass was 9.75±0.7%, 18.09±2.77% and 17.23±2.49% of the original mass of C90E10, C80E20, and C75E25, correspondingly.

The degradation of non-crosslinked collagen-FEG composite scaffolds by both collagenase and elastase was presented in Figure 3.25C. This was experimented to understand the proportional contribution of both enzymes to the degradation rate. It was seen that the enzyme cocktail degraded the scaffolds faster than elastase alone only, as two enzymes in the cocktail attacked the different regions of the protein structure in scaffolds. C80E20 and C75E25 scaffolds degraded in the first 3 hrs, whereas C90E20 scaffolds could withstand until 12 hrs. Since there is more collagen peptide structure to attack, collagen appeared to be degraded initially slowly but then completely by collagenase, and elastase played a more direct role in collagen-FEG composite scaffold degradation.

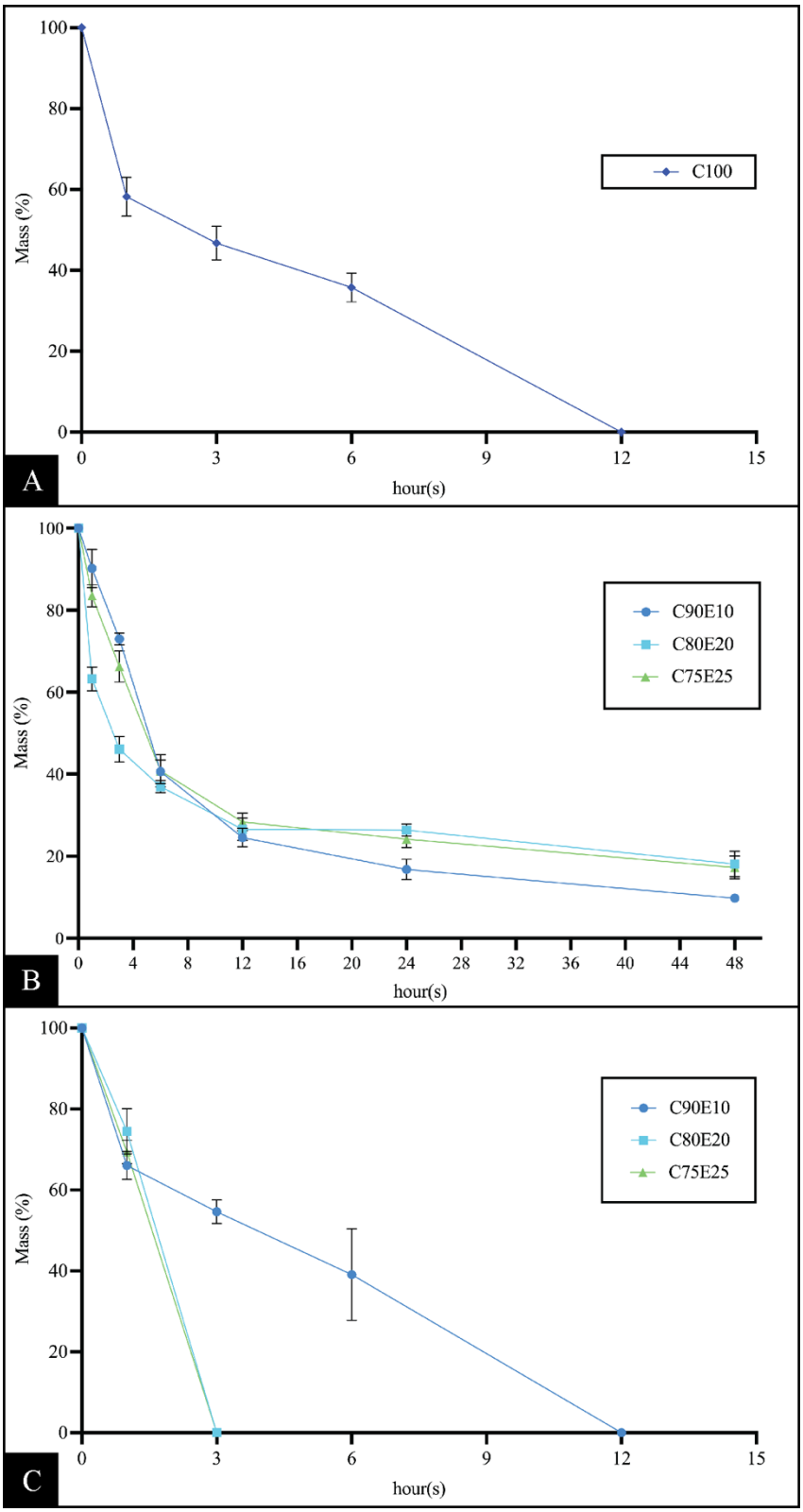


Figure 3.25. Enzymatic degradation of non-crosslinked scaffolds with (A) collagenase only, (B) elastase only, and (C) both enzymes.

The collagenase and elastase-controlled degradation profile of crosslinked scaffolds is presented in Figure 3.26A. While C100 scaffolds were degraded by 0.5 mg/mL collagenase only, collagen-FEG composite scaffolds were degraded by 0.5 mg/mL collagenase and 0.5 U/mL elastase. Although collagen-FEG composite scaffolds experienced a similar degradation rate with no significant difference, C100 crosslinked scaffolds underwent the highest mass loss, losing 82.25±0.43% of the original mass ($p<0.0001$). After 48 hrs of degradation, the remaining mass compared to the initial mass was 30.73±1.75%, 29.2±2.56% and 26.38±2.24% for C90E10, C80E20 and C75E25, respectively ($p=0.99$).

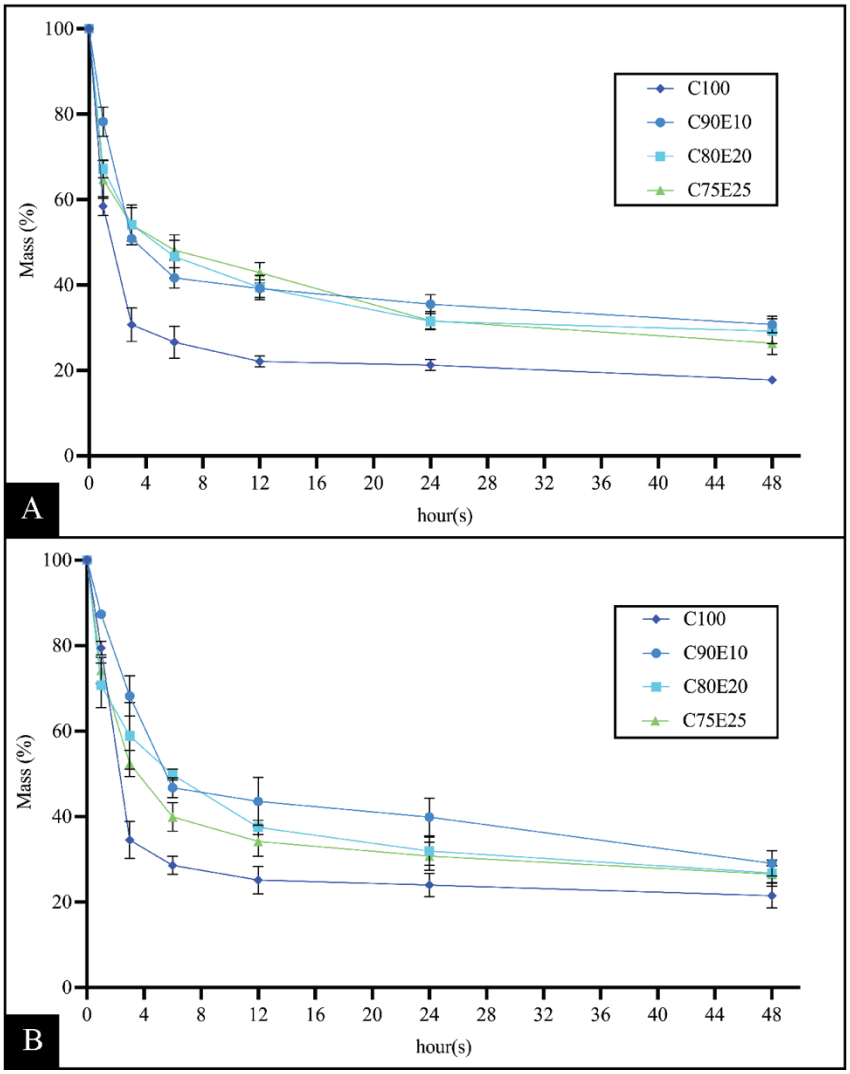


Figure 3.26. Enzymatic degradation of (A) crosslinked and (B) hyaluronic acid-infiltrated scaffolds for 48 hours.

Enzymatic degradation of HA-infiltrated scaffolds for 48 hours is shown in Figure 3.26B. The enzyme cocktail consisted of collagenase and hyaluronidase for C100 scaffolds, whereas an enzyme cocktail of collagenase, elastase, and hyaluronidase degraded collagen-FEG composite scaffolds. As with the crosslinked scaffolds, no significant difference in the mass loss after 48 hrs was obtained between collagen-FEG composites (p=0.56). However, the degradation rate of C75E25 scaffolds was faster than C90E10 and C80E20 over 12 hrs, losing 65.81±3% of the original mass. The fastest degradation rate was seen in the C100 scaffolds, losing 65.48±3.88% of its mass in 3 hrs. Even though the rate was slow after this point, the remaining mass was 21.48±2.49% of the original mass after 48 hrs, which was the biggest loss of the experimental group (p=0.041).

Table 3.13 compared the remaining mass of crosslinked and HA-infiltrated scaffolds after 48 hrs of enzymatic activity. No significant difference was found when comparing cross-linked and HA-infiltered composites; however, collagen-FEG composite scaffolds could withstand enzymatic reactions better than C100 scaffolds in both cases.

Table 3.13. The comparison of enzymatic degradation profile between crosslinked and hyaluronic acid-infiltrated composites after 48 hrs. (Mean±SD, *p<0.05)

Sample	Mass remaining (%) after 48 hrs		
	XL	HA	p value
C100	17.29±0.43	21.48±2.49	0.079
C90E10	30.73±1.75	29.04±2.41	0.442
C80E20	30.00±2.56	26.78±2.50	0.330
C75E25	26.38±2.24	26.52±1.61	0.937
p value (C100 vs collagen-FEG composites)	0.006*	0.041*	

3.3.6. Compression and Tensile Testing

Compressive stress-strain profiles of C100 and collagen-FEG composite scaffolds are presented in Figure 3.27 for non-crosslinked, crosslinked, and HA-infiltrated conditions. The compressive modulus (E_C, kPa) was measured by taking the gradient at the linear region between 5-20% strain and summarised in Table 3.14. An S-curve response was seen for all

scaffold types in a dry state. The crosslinked scaffolds exhibited significantly higher E_C than non-crosslinked scaffolds in all groups. However, the HA-infiltration significantly reduced the elastic modulus to the value of non-crosslinked scaffolds, and no considerable difference was found between both groups. Although the HA-infiltrated group was exposed to a prolonged crosslinking process, the structural contribution of HA significantly changed the compressive properties of these scaffolds. Focusing on the HA-infiltrated scaffolds, the E_C decreased as the FEG proportion of the material increased; nonetheless, this was not found statistically significant ($p=0.33$). The lowest E_C value was observed in HA-infiltrated C75E25 scaffolds as 15.55±1.50 kPa.

When comparing dry scaffolds to those in a wet state under compression, as indicated in Figure 3.28, it was found that all scaffolds exhibited ~10-fold lower compressive modulus than dry scaffolds, except for C100 crosslinked scaffolds having ~5-fold lower E_C. It was also noticed that the testing machine was not sensitive enough to test the scaffolds at high strain; therefore, the E_C was obtained by measuring the gradient of the linear region up to 5% strain. The non-crosslinked and HA-infiltrated scaffolds displayed very similar compressive moduli; the only significant difference occurred between the E_C values of C100 and C75E25 non-crosslinked scaffolds. Both C100 and C90E10 experienced significantly higher E_C after crosslinking, 4.56±0.33 kPa and 2.14±0.07 kPa, respectively. The higher stiffness appeared to be compensated after HA infiltration for both scaffold types.

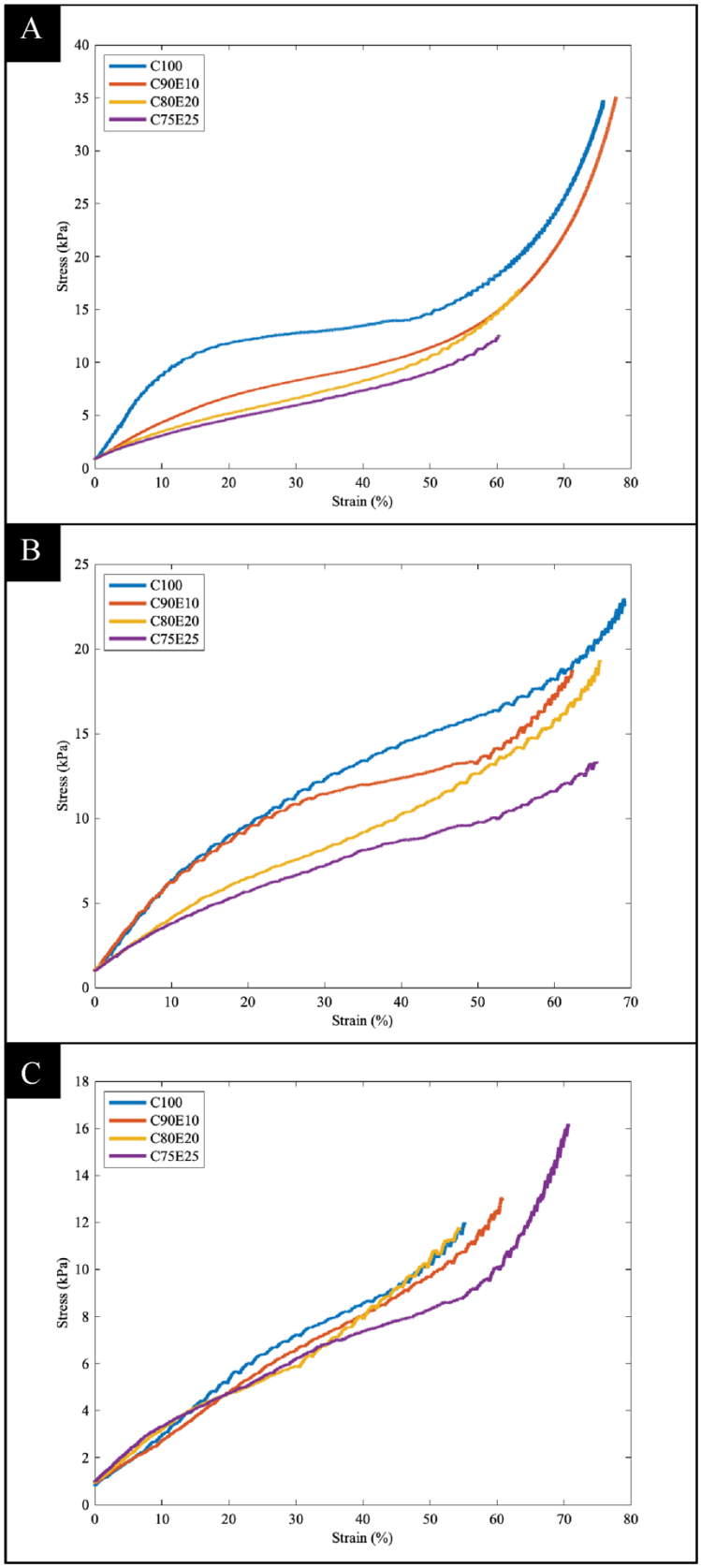


Figure 3.27. Representative stress-strain profile of (A) non-crosslinked, (B) crosslinked, and (C) HA-infiltrated C100, C90E10, C80E20 and C75E25 scaffolds at dry state under compression.

Table 3.14. The summary of Young's modulus of all scaffold types in the dry state. One-way ANOVA was used to compare different conditions within the same scaffold content. T-test was performed for dual comparisons. (Mean±SD, *p<0.05).

Compressive Modulus (kPa)	Non-XL	XL	HA	p value (Non-XL vs HA)	p value (XL vs HA)
C100	23.29±0.20	29.77±2.39	21.73±3.80	0.724	0.005*
C90E10	17.69±1.41	31.34±0.38	20.66±3.70	0.326	0.004*
C80E20	17.22±2.32	22.86±1.73	16.17±2.75	0.863	0.009*
C75E25	17.59±1.28	21.82±3.20	15.33±1.50	0.638	0.024*
p value	0.042*	0.041*	0.33		

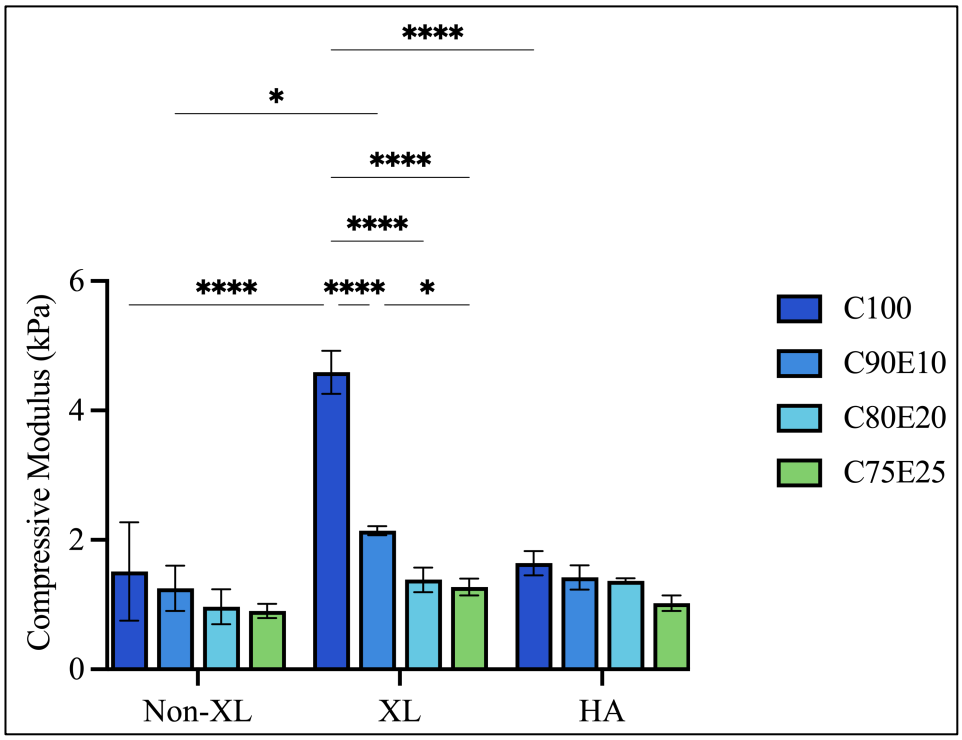


Figure 3.28. The Young's modulus of all scaffold types at wet state under compression. Two-way ANOVA with Tukey's post-hoc was used for comparison (*p<0.05; ****p<0.0001).

The representative tensile stress-strain curves of all scaffold types in the wet state are shown in Figure 3.29. and related E_T values obtained at low strain between 5-10% strain are presented in Table 3.15. This was quite challenging as the low strain region of collagen-FEG composites was not distinguishable due to both an increase in FEG content and the HA-infiltration. The increase in the FEG content also decreased the elastic modulus under tension, and the strain-to-failure significantly went up to 100.28%, 27.31% and 24.94% in non-crosslinked, crosslinked, and HA-infiltrated C75E25 scaffolds, respectively. C75E25 scaffolds exhibited

the lowest E_T values for all conditions and were found statistically significant in crosslinked and HA-infiltrated group comparison. In contrast, C100 scaffolds displayed higher stiffness, nearly doubled after crosslinking, and E_T became 0.30±0.029 MPa in the HA-infiltrated group as the crosslinked was prolonged. When the tensile modulus of scaffolds was compared to the E_T of the native porcine heart (taken from Section 2.3.3), a significant difference was only seen in C100 HA-infiltrated scaffolds (Table 3.15), meaning that the tensile properties of designed materials are mostly compatible to the passive heart tensile mechanics.

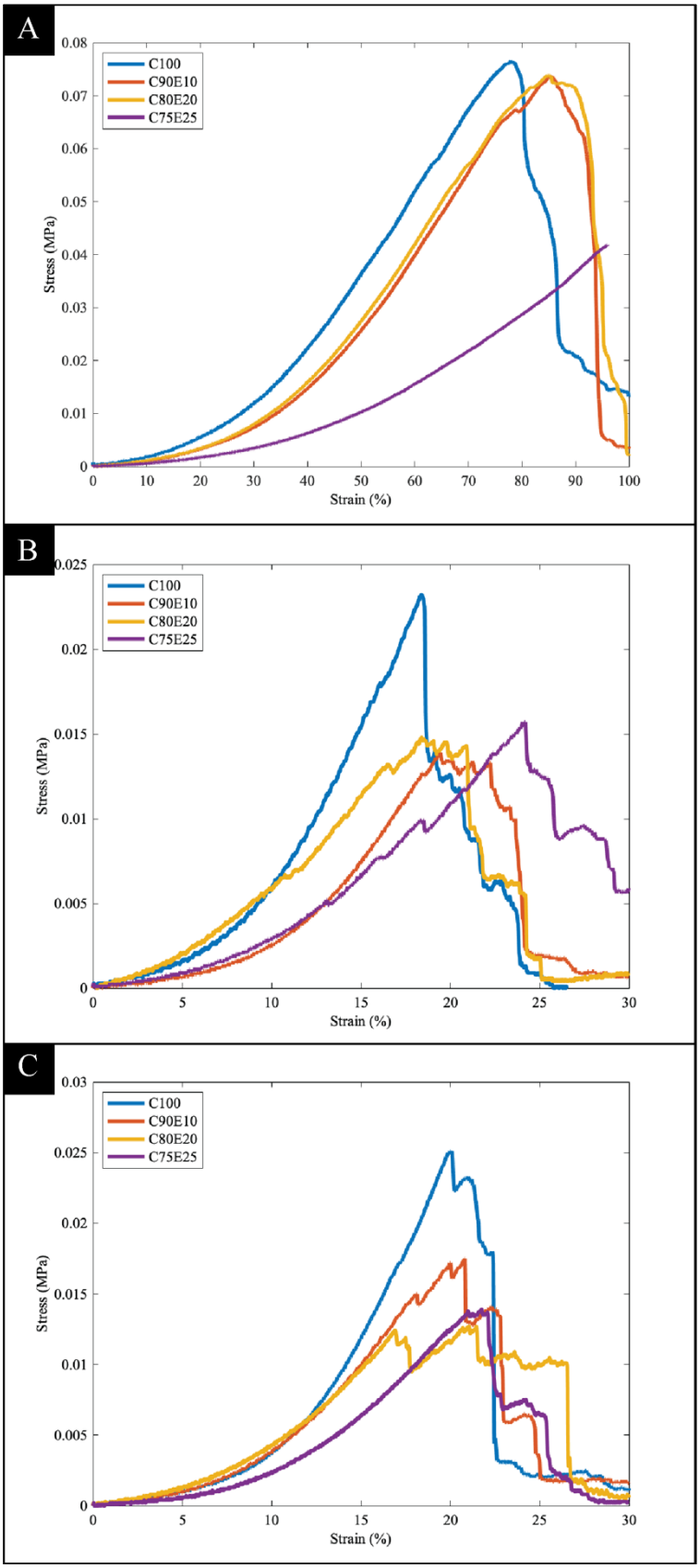


Figure 3.29. Representative stress-strain response of (A) non-crosslinked, (B) crosslinked, and (C) HA-infiltrated C100, C90E10, C80E20 and C75E25 scaffolds under tension.

Table 3.15. The summary of Young's modulus of all scaffold types and comparison with the native porcine heart under tension. Two-way ANOVA with Tukey post-hoc was used for statistics. (Mean±SD, *p<0.05).

Tensile Modulus (MPa)	Non-XL	XL	HA	p value
C100	0.16±0.024	0.27±0.009	0.30±0.029	0.011*
C90E10	0.15±0.012	0.15±0.008	0.17±0.011	0.194
C80E20	0.15±0.036	0.15±0.017	0.15±0.005	0.990
C75E25	0.11±0.019	0.11±0.011	0.13±0.018	0.194
p value	0.077	0.0002*	0.0005*	
Porcine Heart		0.13±0.004		
p value (vs C100)	0.981	0.067	0.0003*	
p value (vs C90E10)	0.4	0.393	0.118	
p value (vs C80E20)	0.551	0.369	0.307	
p value (vs C75E25)	0.238	0.344	0.911	

3.3.7. Three-Point Bending

Three-point bending test was conducted to characterise the bending properties of each scaffold type in the dry state (Figure 3.30). Both crosslinking and HA infiltration significantly increased the E_{Bend} compared to non-crosslinked scaffolds. For C100 and C90E10 scaffolds, the infiltration of HA considerably reduced the E_{Bend} by ~1.5 and ~1.8-fold, respectively. The highest bending modulus was obtained in the C80E20 crosslinked group at 7.07±0.89 kPa; however, this was reduced to 5.71±0.36 kPa after HA infiltration, although it was not significant. The lowest elastic modulus was seen in C75E25 non-crosslinked group as 2.08±0.10 kPa, but the scaffolds became stiffer following crosslinking (~2.75-fold) and HA infiltration (~3-fold).

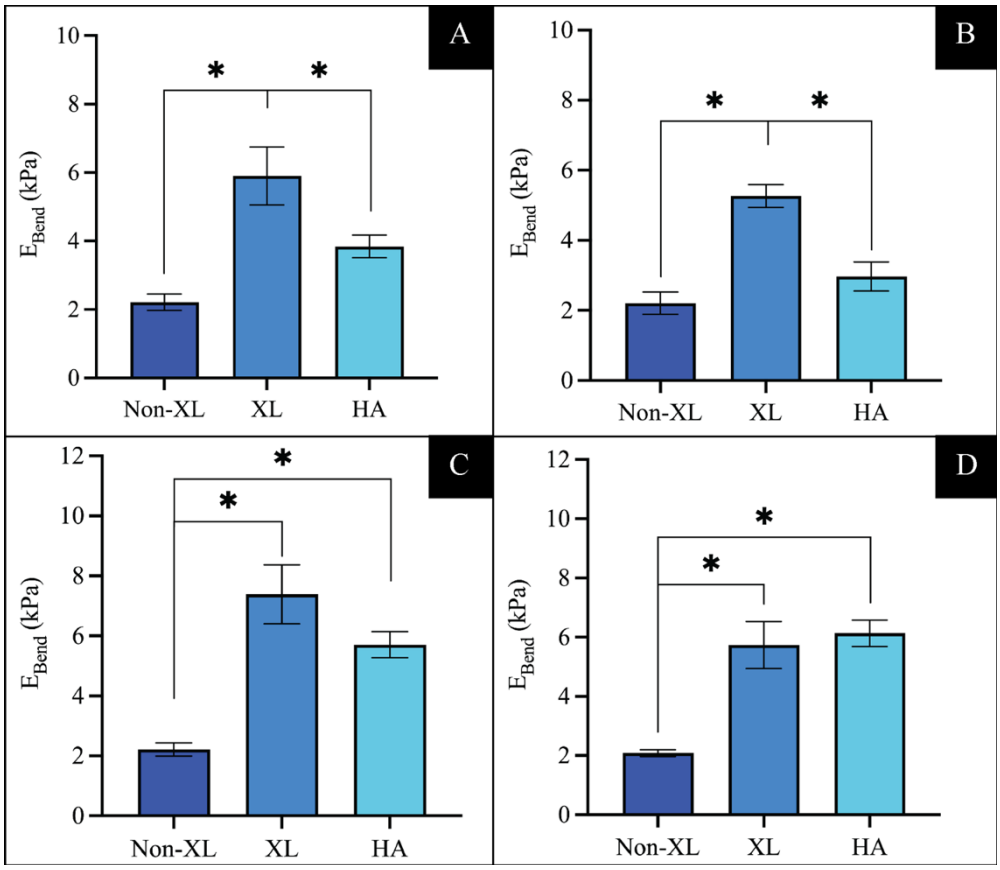


Figure 3.30. Bending modulus (E_{Bend}) of (A) C100, (B) C90E10, (C) C80E20, and (D) C75E25 scaffolds at dry state. One-way ANOVA was used for statistical analysis. (N=5, *p<0.05).

3.3.8. Self-Deflection

A self-deflection test analysed the bending characteristics of hydrated scaffolds, as the three-point bending test would not be suitable for these samples (Figure 3.31) It was found that crosslinked scaffolds were significantly stiffer than non-crosslinked and HA-infiltrated scaffolds, except for C100 scaffolds, where there was no clear change in bending properties between crosslinked and HA-infiltrated groups. C90E10, C80E20 and C75E25 scaffolds became stiffer, with a 6, 1.8 and 2.1-fold increase in E_{Bend} after crosslinking. Although the crosslinking caused stiffness in collagen-FEG composite scaffolds, the infiltration of HA significantly reduced the bending modulus to the level of non-crosslinked scaffolds ($p>0.05$ for all). The E_{Bend} in C7525 HA infiltrated scaffolds was 2.77±0.82 kPa compared to C100, C90E10, and C80E20 HA scaffolds, as their bending modulus was found as 12.63±1.41,

4.69±1.28 and 4.68±0.88 kPa, respectively. This result implies that the increased FEG content contributes more to bending properties in a hydrated state.

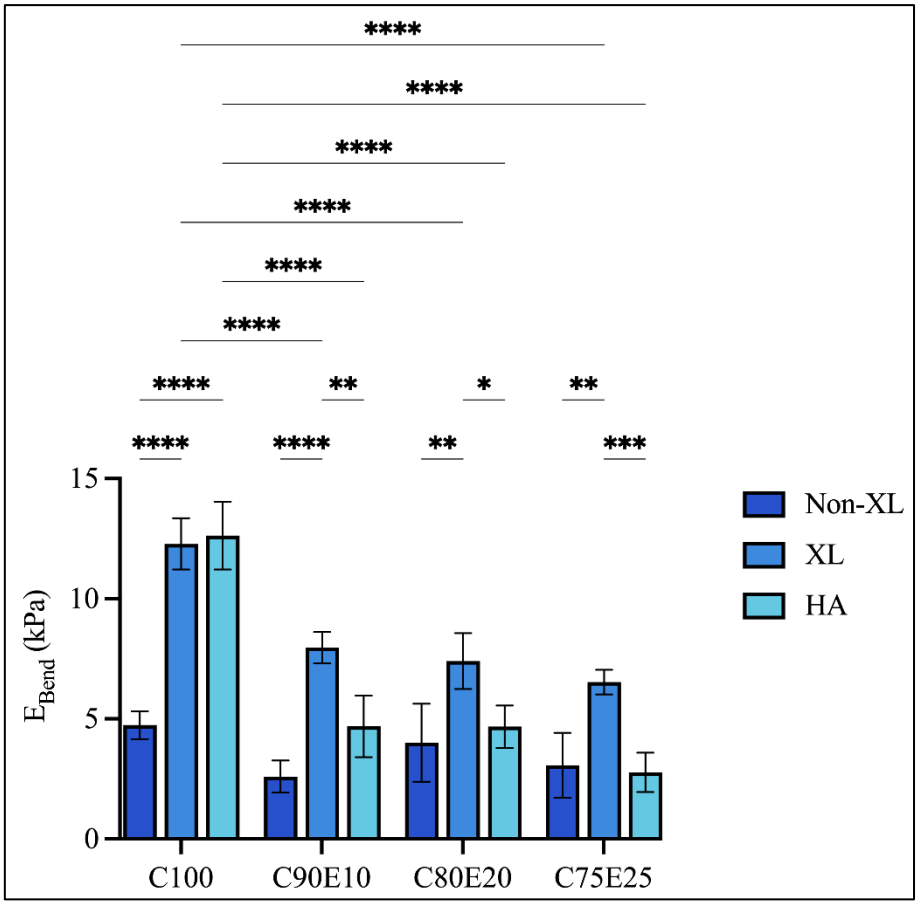


Figure 3.31. The bending modulus comparison of scaffold types in the hydrated state. Two-way ANOVA with Tukey post-hoc was used for statistical analysis. (N≥5, *p<0.05, **p<0.01, ***p<0.001, ****p<0.0001).

3.4. Discussion

3.4.1. Scaffold Fabrication

Collagen, an essential component of the ECM, is required as both a load-bearing element and a moderator of biological responses. Despite being widely used in tissue engineering, this biomaterial often does not meet the mechanical requirements of the cardiovascular environment, frequently due to collagen's propensity to creep over time (16). The strategy of combining collagen with other biomaterials has been widely accepted to improve the strength of the scaffolds while retaining biological activity. Elastin is a major ECM protein in the vasculature as it controls blood flow by sufficiently storing elastic-strain energy. This protein's

high extensibility and resilience, and low stiffness may allow it to mimic the mechanical properties of native cardiovascular tissue. Ideally, the presence of elastin in porous collagen scaffolds would alter the mechanical and biological responses. Therefore, we used collagen type I and FEG to obtain porous scaffolds in this study. Because of collagen denaturation in alkaline conditions and insolubility of elastin at higher pH, collagen and collagen-FEG suspensions were prepared in acidic conditions (pH 3.2 or 2.7, respectively). These proteins swell in acetic acid solution because the pH is lower than their isoelectric point(s) (pI) (for collagen 7.8 (17, 18), and for FEG ~5.6 (1, 19)). When pH<pI, it increases the number of positive charges caused by the ionisation of amino acid residues in protein(s), resulting in electrostatic repulsion. This increase in polymer-solvent interactions following ionisation ultimately increases the protein's water uptake. Successful suspensions were obtained based on the difference between the pH and pI of both proteins.

Scaffold design has been one of the major components of tissue engineering by controlling the physicochemical properties of the scaffold to achieve new tissue structure. Optimisation of the pore structure, including the interconnectivity and high porosity, facilitates cell seeding and spatial cell distribution. The pore structure also shapes the matrix permeability by affecting nutrient diffusion and the disposal of waste products (20). The pore size should be large enough to support cell migration and small enough to permit cell attachment. Here, we used the freeze-drying (lyophilisation) method to fabricate porous scaffolds by controlling both temperature and pressure. This method is highly advantageous as it employs only water upon freezing as a porogen and has been widely studied for collagen-based scaffolds (20-22). However, the use of freeze-drying has not been used for fabricating elastin-based scaffolds previously as the molecular interaction with the solvent is quite poor for elastin. In this study, a relatively high freezing temperature (-20°C) and a slow rate of cooling were chosen to obtain a wide range of different pore sizes with smaller interconnective pores. Here, Figures 3.6, 3.9 and 3.11 show

the SEM images of non-crosslinked, crosslinked and HA-infiltrated scaffolds, respectively. More homogeneous and circular pores were seen in the C100 scaffolds without crosslinkers, while the pores became longer, smaller, and slab-like as the FEG ratio increased. This has been hypothesised to be caused by an increase in mechanical impedance by the FEG molecules, which delays the growth of ice crystals and ultimately results in the formation of narrower pores (1). This could also explain why a significant decrease in porosity was observed after more FEG was added to the composites.

3.4.2. Crosslinking and HA Infiltration

The combination of elastin with collagen has been widely adapted to design composite scaffolds; however, the mechanical properties of the resulting materials have been reported to be relatively low in terms of mechanical strength, stability and resistance to degradation etc. (20, 23). Carbodiimides have been widely used to crosslink collagen-based materials and immobilise other proteins within the matrix. EDC, in particular, is a non-toxic, water-soluble crosslinker that forms amide bonds between carboxylic and amino groups on the protein molecules (20, 24). We found that scaffolds without crosslinking became very gummy and lost their form and proposed that crosslinking with EDC would improve the mechanical properties of collagen-based materials and their resistance to hydrolytic and enzymatic degradation. We used a 2:1 EDC/NHS ratio because it was previously noted to result in the most efficient crosslink density (24). 75% ethanol was also chosen instead of distilled water to increase the crosslinking efficiency. It was found that EDC/NHS crosslinking considerably changed the morphology of the pores with a smaller interconnectivity, average pore size and porosity as the FEG ratio increased. However, total porosity was not significantly different compared to the non-crosslinked parent of the scaffolds (Table 3.4). This could be explained by the fact that any linkage between the carboxylic and amino groups of the proteins turned the pre-existing pores into smaller pores, as seen in SEM images. However, crosslinked samples retained their

structure better, which resulted in higher water-holding ability without affecting the total porosity.

The crosslinking efficiency of the collagen and collagen-FEG composite scaffolds as well as their raw materials, was tested by FT-IR. In the presence of NHS, EDC forms amide bonds with hydroxylysine and amines of lysine residues by activating the carboxyl groups of aspartic acid or glutamic acid residues, resulting in stable structures (25). Therefore, any increase in the absorbance of the corresponding amide bond would be a direct indicator of effective crosslinking. Here we characterised four amide bonds for proteins: Amide I, II, III and A. For elastin's refined version (FEG), all related peaks were detected with a clear increase in the absorbance of Amide I after crosslinking. The amide I band, with characteristic frequencies ranging from 1600 to 1700 cm^{-1}, is primarily associated with a carbonyl group (C=O bond) stretching vibrations along the polypeptide backbone (13). Here, the amide I band, linked to the protein's secondary structure, showed no significant shift in elastin's inter- and intramolecular β-sheets, meaning that the structural integrity of the elastin was preserved after crosslinking. β-turns observed in the secondary structure of the elastin are found to be important as they arise from the repetition of the amino acid sequence of valine-proline-glycine-valine-glycine (VPGVG), which determines for the elasticity of the elastin molecule (Urry's model) (26). Large-amplitude/low-frequency vibrations are possible with these valine-glycine sequences. Reduced amplitudes of these vibrations induce a significant decrease in the entropy of the segment, causing a driving force for a return to the relaxed state, which characterises the protein's elastic behaviour.

Amide bands were also obtained for C100 scaffolds by FT-IR, with no clear shift after crosslinking, but higher peak intensity for both Amide and ν(C-O) ester bond, indicating the crosslinking efficiency of EDC-NHS. The Amide III/δ(C-H) ratio also proved that the triple-helix collagen structure was maintained. For those collagen-FEG composite scaffolds, a slight

shift is typically seen when functional groups of biopolymers form hydrogen bonds with one another.

An intuitive approach to designing collagen-based composites is to supplement the matrix with other extracellular matrix components found in native tissues. HA has been known to support cell migration within biomaterials by its high water-uptake capacity and show high swelling characteristics in biological fluids (27, 28). It has been widely studied with the combination of collagen-like proteins and other GAGs to optimise the mechanical features of scaffolds (3, 20, 24, 27). In this study, pre-formed collagen and collagen-FEG composite scaffolds were HA-infiltrated upon crosslinking because the non-crosslinked scaffolds could not incorporate the HA and preserve their shape. D-glucuronic acid and N-acetyl-D-glucosamine are constituents of the HA. Due to the abundance of hydroxyl groups here, HA can easily create hydrogen bonds and potentially bind water (29). These strong hydrogen bonds within HA possibly caused shrinkage while filling the pores in this study (Figure 3.7), which can be seen as a slight reduction in the total porosity of all scaffolds. In addition, prolonged crosslinking with HA had some effects on the chemical structure of the scaffolds. HA-infiltration was also confirmed by the presence of twin-peak at (N-H) and (O-H) stretching vibrations for all scaffolds, along with changes at (CH_2) bending of Amide I and II. While Amide I vibration reflects C=O stretching at peptide bonds, Amide II mostly corresponds to N-H bending vibrations (30). These alterations are mainly due to the presence of characteristic groups of HA. Major differences in the positions of the main peaks of collagen and FEG observed after HA infiltration may result from interactions between polymers when hydrogen bonding between them is involved.

3.4.3. Swelling

The swelling behaviour of collagen scaffolds and collagen-FEG composites was examined in PBS both at 20°C and 37°C (Figure 3.23). The swelling ratio revealed how scaffolds interacted with a physiological solvent such as PBS, where they absorbed the solvent and grew larger

when submerged. Following 24 hrs of solvent absorption, no disintegration was observed for any scaffold types, implying that collagen and FEG intrinsic molecules are inherently crosslinked. Although there was no clear change among non-crosslinked scaffolds, the presence of FEG significantly reduced the scaffold's solvent uptake capacity by 32% and 34% compared to C100 scaffolds after crosslinking and HA infiltration, respectively. This implies that the solvent absorption was weaker for elastin compared to collagen due to the hydrophobic nature of elastin (31). Because elastin is known to have lower critical solution temperature (LCST) due to an imbalance hydrophilic–hydrophobic interactions between the polymer and solvent (32). Upon an increase in temperature, hydrophobic parts of a polymer chain can aggregate and lower the surface area that is accessible to solvents, which pulls the non-contracting network segments. The entropy gain for the solvent molecules is what propels the contraction. Highly ordered water molecules surround hydrophobic segments, but as the temperature rises, this order is broken, allowing the hydrophobic segments to associate and fold. When the entropy gain from the released water molecules outweighs the enthalpy gain from water attaching to the polymer, the contraction is subsequently generated. The current study showed a reduction in the solvent absorbed by non-crosslinked scaffolds as temperature increased; however, this was only significant for C100 scaffolds. No clear difference occurred among non-crosslinked composites could be due to the scaffolds' weak structural stability, which resulted in fast solvent loss during 1 min drainage on mesh before weighing. The effect of crosslinking on water uptake was less obvious on composites compared to C100 scaffolds, implying that collagen contracted more within composites as FEG's hydrophobicity overpowered collagen's ability to support its structure. The hydrophobic segments of FEG again caused less solvent to be absorbed, yet this was still significantly higher than those reported elastin-based crosslinked scaffolds (33, 34).

To predict how cell culture medium may be absorbed during culture and how the scaffold may behave *in vivo*, it is crucial to understand how hydrated the scaffolds are. Since crosslinking occurs between amino and carboxylic acid groups, which are involved in water binding, it is known to lower the material's hydrophilic characteristics (amino and carboxylic acid groups) (35). The polarity of the scaffold material and the development of crosslinks between macromolecular components have opposing effects on the hydrophilicity of a scaffold composition (20). The presence of HA in scaffolds is anticipated to increase the polarity of the polymer composition, favourably affecting its swelling. However, when EDC/NHS crosslinkers are present, HA should create ester-type linkages between its carboxylic groups and the amino and/or hydroxyl groups of collagens (16). This increased degree of crosslinking by HA infiltration may cause a reduction in the swelling capacity, which could explain why no clear change in solvent uptake ratio was observed after HA introduction to the scaffolds. In addition, swelling was increased by HA infiltration in all scaffolds. Considering the impact of crosslinking on shrinkage, both crosslinking and the presence of HA significantly improved the scaffold's durability.

Next, the polymer-solvent interaction was analysed by using swelling data. Phase separation of biopolymers occurs in many biopolymer mixes because the entropic contribution is frequently greater than that of enthalpy (36). Two-phase separation processes can be seen depending on the affinity of the various biopolymers to the solvent in this situation. The first one, also known as segregative phase separation or thermodynamic incompatibility, is frequently seen. It manifests as a net repulsion between the biopolymers when the Flory-Huggins interaction parameter (χ) is positive. In contrast, χ , found below zero in the current study, is related to the associative phase separation, the second phase separation phenomenon which happens because the interactions between the two biopolymers are favourable. This occurs when the polymers have opposite charges, for example, at a pH slightly below the

protein's pI. Here, a complexation process occurs, which results in either the aggregative phase separation or the production of soluble complexes. A rich solvent phase containing only very small amounts of biopolymer(s) and a rich biopolymer(s) phase that forms the so-called coacervate are the two coexisting phases in an associative phase separation (37). Here, it is believed that the negative χ reflects the production of a soluble complex with minor coacervates of both polymers. The mixture was stored in the fridge overnight to achieve maximum compatibility at a pH of 2.7-3.2, below both proteins' pI, which would prolong the interaction between polymers overnight at low temperatures. As a result, the current binary polymer blend has improved the dispersion and interfacial adhesion between the two components in a less phase-separated polymer mixture. Therefore, the interaction between collagen and FEG during scaffold fabrication is proposed to be that shown in Figure 3.32, where fibrillar elastin peptide struts form an equilibrium physical network phase with local bridging of these peptides by collagen fibres. Higher elastin concentrations had a uniform distribution, with the elastic fibres mostly enclosed within the collagen struts. Their interaction was later stabilised by chemically crosslinking using EDC/NHS. The current study did not focus on the post-crosslink chemical interactions between these two components. One theory about the crosslink affinity is that the FEG is less sensitive to being crosslinked by EDC/NHS compared to collagen, as less solvent absorption was observed after crosslinking when more collagens were replaced with FEG. The crosslink density observed by FT-IR data (Figure 3.22B) also supported this theory as the ratio of ester bonds was 1.3, 1.16 and 1.15 for C100, C90E10 and C80E20 crosslinked scaffolds, respectively, compared to the non-crosslinked group, but increased to 1.28 for the C75E25 group, nearly as much as C100, suggesting that the higher concentration of FEG was more efficient to be crosslinked by EDC, because EDC could not pick up small quantities of FEG. Although FEG consists of fewer amine and carboxyl groups, it is unclear whether chemical bounding occurred between collagen and FEG polymers

or FEG only crosslinks to itself. Further analysis for the quantification of amide and ester bounds such as 2,4,6-trinitro-benzenesulfonic acid (TNBS) (34) or nuclear magnetic resonance (NMR) spectroscopy would give a better insight into intra- and intermolecular interactions.

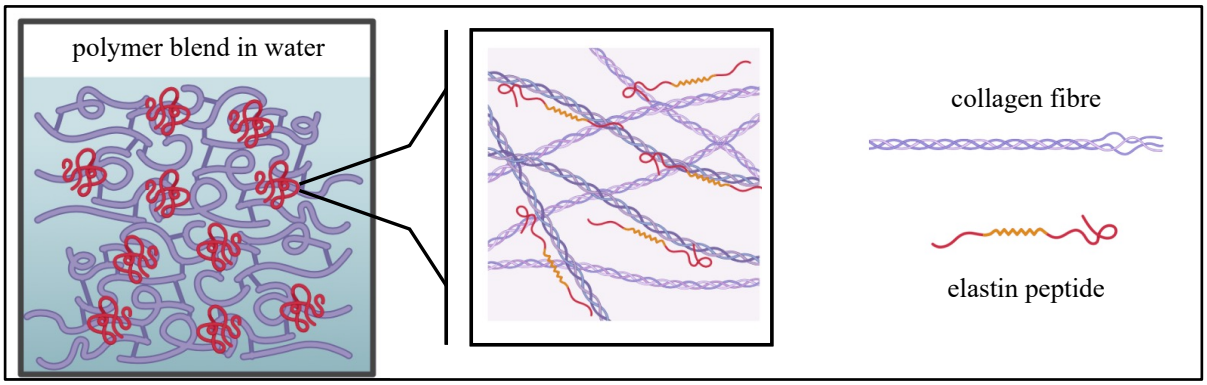


Figure 3.32. Representative collagen-FEG interaction in water during scaffold fabrication.

3.4.4. Degradation Characteristics

The long-term degradation profile is important to understand the stability of scaffolds during tissue replacement. Here, non-enzymatic biodegradation in physiological conditions was studied for 3 months, which has been reported as sufficient to support new tissue formation (22, 38, 39). The results showed that the majority of scaffolds degraded in the first half of the experiment, and less than 10% of scaffolds remained intact in PBS for over 3-5 weeks. The degradation characteristics of the scaffolds can also be improved by both crosslinking and HA-infiltration, as they regulate biodegradation by increasing the interaction with water. This could be explained by the water-polymer interactions (40). When water penetrates the polymer body, it causes swelling and starts the production of oligomers and monomers by water-induced hydrolysis. It has been observed that the scaffold's weight would drop as oligomers and monomers leach out. In addition, water can attack functional groups such as carbonate groups and ester groups formed from ester crosslinking by EDC. Another reason for the faster degradation rate for these scaffolds could be the good accessibility of functionalised groups offering better surface interaction (39).

Enzymatic degradation was also studied in the presence of collagenase, elastase, and hyaluronidase. The results indicated that non-crosslinked scaffolds showed less stability against enzymatic reactions and disintegrated after an hour of degradation, implying that bulk degradation occurred when both water and enzyme could enter the whole polymer bulk, resulting in hydrolysis throughout the entire matrix, as enzymes would be more efficient in the lack of extra crosslinkers. In particular, the oligomers and carboxyl end groups at the scaffold surface can easily disperse into the media in non-crosslinked scaffolds. If this dispersion is fast, it can lead to adverse tissue reactions and inflammation after implantation. The biostability of the scaffolds to enzymatic degradation increased after crosslinking, and relatively slower dispersion of the scaffolds was seen. However, even without crosslinkers, collagen-FEG composite scaffolds showed better stability against enzymatic reactions. Collagen is broken down by collagenase through internal and external degradation (25). Collagenase binds to the triple helix structure on the collagen surface as part of the external breakdown process and then attaches to the inside of collagen fibres to carry out internal degradation following the destruction of the triple helix structure. The fast destruction of these helical structures in C100 scaffolds compared to the collagen-FEG composites could be due to the hydrophobic region of the FEG decreasing the interaction with water. However, structural stability was achieved by the introduction of crosslinking; the significant mass loss was only observed in the first 4 hrs of the enzymatic reaction, leaving the scaffolds intact after 48 hrs.

Interestingly, HA-infiltrated scaffolds did not degrade faster than the crosslinked scaffolds. This could be because crosslinkers in the HA-infiltrated scaffolds, which provide stability during proteolytic catalysis, making the crosslinking more dominant than the presence of HA. Yet, collagen fibres were still easily attacked by collagenase compared to FEG being attacked by elastase as collagen was more interactive with the surrounding solvent.

3.4.5. Compression and Tensile Properties

Previous investigations into the mechanical stiffness, strength, and stability of scaffolds against degradation have demonstrated that these qualities were increased by crosslinking (34, 41-43). That was seen in our study although both HA infiltration and the presence of FEG resulted in a scaffold with reduced compressive strength and stiffness.

The S-shape compressive stress-strain curves of all dry scaffolds (Figure 3.27) are related to the three regions of rubbery-like materials: the toe (elastic), the linear (collapse plateau) and the failure (densification). However, this changed to J-curve behaviour when scaffolds were hydrated, which is common for biological materials (Figure 3.29). The construct matrix's composition affects the shape of the curves, represented by the extension of each of the three areas. C100 scaffolds often featured a short toe region in the low strain range. In contrast, the toe regions of the collagen-FEG and collagen-FEG-HA composites were significantly longer and extended to high strains of up to 50% and 60%, respectively. According to calculations, Young's modulus of collagen is roughly 4 GPa and it exhibits elastic behaviour over an elongation range of 2.5–4% (44). Molecular dynamics and optical tweezers have shown that entropic elasticity brought on by molecular ordering governs the mechanics for small deformations, but for greater deformations, energetic elasticity takes over. This transition is brought on by the deformation of covalent bonds in the protein backbone and the stretching and breaking of intramolecular interactions, including hydrogen bonds. In contrast, elastic fibres have a Young's modulus that spans 300 to 600 kPa, with a maximum extension of 100 to 220%. According to the random chain model, elastin functions similarly to a classic rubber, where the polymers are kinetically free and highly entropic. Stretching provides the restorative force for recoil by organising the links and reducing the system's overall entropy. In this study, the results indicated that the combination of collagen with FEG balanced the relationship of both materials’ mechanics in a way to be used in tissue engineering applications.

The shape of the stress-strain curve was shown to be independent of the crosslinker, while the linear region's extension and modulus varied with the crosslinker and HA infiltration. The linear region of hydrated scaffolds was hard to identify as the machine was unable to detect the sample and assumed to be the fact of immediate strut buckling and collapse simultaneously. The compressive modulus of the scaffolds was within the range of the reported elastic modulus regardless of pre-conditioning (Table 3.16); it is worth noting that the E_C was significantly lower for hydrated scaffolds, which was not comparable to native myocardium (Section 2.3.2). It is known that the hydrophilic materials show decreased mechanical strength than the scaffolds containing more hydrophobic regions (45). A particular study showed a decrease in stiffness after hydration, which was most likely brought on by weakening hydrogen bonds within the collagen's molecular structure, as seen by stiffness results (5–10 kPa for the dry and 0.5–1 kPa for the hydrated forms) (46). This 10-fold decrease in compression modulus following interaction with water is also consistent with the current study.

Table 3.16. Reported studies based on the compressive strength of collagen-based scaffolds. ELP: Elastin-like polypeptides. HA: Hyaluronic acid. [a]dry samples, [b]hydrated samples, [n.r.]not reported.

Sample	E_C (kPa)	REF
Collagen-FEG (1% w/v) + HA	15.33-31.34[a]	present work
Collagen-FEG (1% w/v) +HA	0.9-2.14[b]	present work
Collagen-FEG (1% w/v)	1.6-2.6[b]	(1)
Collagen-Elastin	0.25-0.32[n.r.]	(16)
Collagen-HA	4.26-6.23[b]	(20)
Collagen	2.9[b]	(34)
Collagen-Elastin	10.2-13.2[a]	(47)
Collagen-HA	0.4[b]	(48)
Collagen	4580-4710[a]	(49)
Collagen-ELP	9.83-16.55[b]	(50)

The E_C of crosslinked scaffolds was higher than both non-crosslinked and HA-infiltrated scaffolds. The physical presence of the crosslink normally draws the fibres together and can

lead to further pore size reduction, creating a denser structure and ultimately increasing mechanical stiffness (34). However, the current study overcame the increased mechanical stiffness by adding FEG, as the affinity of FEG to crosslinking is lower than that of collagen fibres (Section 3.4.3). Mechanically, FEG decreased the scaffold compressive specific moduli significantly in a concentration dependant manner. The contribution of HA was the greatest for C100 scaffolds under wet conditions, reducing the stiffness by ~2.5-fold. This decrease became less obvious as more FEG was introduced. As previously explained, HA would provide a potential attachment site (amino and carboxylic acid groups) for water while HA covalently attached to collagen. However, the hydrophobic FEG units may interfere with these water attachment sites and hinder interaction with collagen fibres. The decrease in water uptake with an increase in the content of FEG supports this conclusion.

The literature dictates that the mechanical properties of a scaffold should be the same if the relative density remains constant (51). The scaffolds' modulus and strength decreased when tested in compression versus tension, even though E_T and E_C were in the same order of magnitude. Although the collagen structure's fibres align and offer additional strength when stretched, they are likely weaker in compression, where strut buckling and pore collapse are more likely to occur as failure mechanisms. Similar to prior studies, these porous structures are less resistant to compressive deformation than tensile deformation (34, 52). This study incorporated FEG into the scaffold matrix to increase the scaffold extensibility and strain-to-failure. Due to the modulus difference between collagen and elastin ($E_{collagen}>E_{elastin}$), the mechanical properties of the result materials vary significantly with changes in the polymer ratio. This study found that the higher the FEG content, the more extensible the scaffold becomes, reaching ~100% of strain-to-failure without crosslinker. However, the strain-to-failure of scaffolds was significantly reduced to 25% by crosslinking, which is not comparable to the experiments on native porcine cardiac tissue which showed that the strain-to-failure

could go up to 65.36 ±10.81% (Section 2.3.3) (23). However, the ordered crosslinked collagen network is necessary for the strong strain-limiting qualities to be present. This network cannot be crosslinked successfully without a strong crosslinking agent such as EDC. In comparison to a loosely crosslinked mesh structure, the highly crosslinked collagen mesh structure maintains a "normal" conformation and offers increased resistance to extrusion and durability when a load is applied. It should be noted that all of these materials were crosslinked with EDC/NHS, as this is necessary for stability in cell culture conditions.

The E_T of scaffolds with higher FEG content agreed with the E_T of porcine heart samples. It is worth noting that the elastic modulus of adult human myocardium ranges around 10-20 kPa to 200-500 kPa during diastole and systole, respectively (53). Even after months or years of healing, scars have been shown to exhibit stiffness values of more than 55 kPa during diastole (~10-fold higher than healthy) (54). Not only systolic pressure but also the relative thickness of the tissue affects these mechanics. Hence, the direct comparison would also be deceptive considering the difference in structural density of these constructs (scaffolds being porous and less dense, whereas the ECM is populated with cells and denser). In a particular study, the 10% contribution of elastin to a collagen-based porous scaffold resulted in a 22% lower tensile modulus (23). For our scaffold, 10% substitution with FEG caused 6% less stiff material, which was significantly improved even after crosslinking (44.4%) and HA infiltration (43%) compared to collagen-based scaffolds. The improvement was more distinct as more collagen was substituted with FEG. Although it is difficult to obtain the natural tissue's full mechanics, the scaffolds' stress features have become more compatible with the literature after the introduction of the FEG (55-57).

We previously explained the lengthening relationship between collagen and elastic fibres at different strains (Section 2.4). The tensile properties of collagen-FEG composites closely matched those of myocardium (Table 3.15), which shows the regions of low strain and high

strain that correlate to the extension of FEG and collagen, respectively. This relation is represented in Figure 3.33. At low strain, the elastic fibres predominately influence the mechanical properties of the tissue, and the collagen fibres have not yet assembled. When under low tension, constrained FEG molecules expand as a force is applied. Since FEG is present in the scaffold as coiled or folded fibres that stretch following the application of stress, this contracted form can be linked to the higher extensibility of FEG compared to collagen. Only when there is little strain is the FEG in charge of accommodating the force; once there is full extension, the collagen fibres take over.

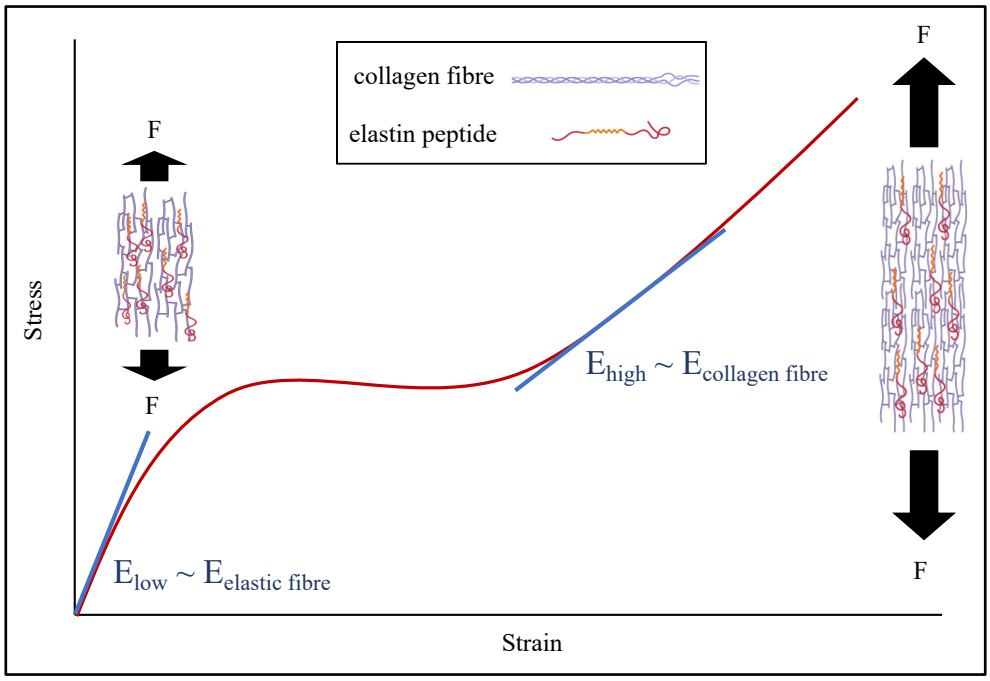


Figure 3.33. The schematic view of elastic and collagen fibre behaviour within composite scaffolds under tension. Both the FEG and collagen fibres are first relaxed and folded. The FEG fibres unfold initially when the force (F) is applied at low stresses (E_{low}) (5-10%); as more force is applied at higher strain (E_{high}), the FEG's breaking point is achieved, and the force is then transmitted to the collagen fibres, which expand until the sample fractures.

Overall, the compressive and tensile properties of designed scaffolds were within the range of previously designed materials yet still quite far from mimicking the native cardiac tissue. The composition of collagen and FEG significantly improved the scaffold mechanics and strengthened with the contribution of crosslinker and HA. This could be further evaluated by *in vitro* and *in vivo* work as a denser ECM content would reflect the native tissue features better.

3.4.6. Bending Properties

According to earlier chapters, the heart muscle possesses a multicomponent hybrid microstructure and anisotropic mechanical properties. Numerous research teams have examined the mechanical characteristics of the myocardium; however, the data is very inconsistent because of biological variability and a lack of consistency in the testing procedures (8). Aside from compressive and tensile, the bending properties are important, as they would provide more information about the structural flexibility of the materials. Here, a three-point bending test in the dry state studied scaffolds' bending properties. The results emphasised the contribution of HA to the composite since HA considerably reduced the E_{Bend} by 1.2 to 1.8-fold when up to 20% of collagen was replaced with FEG. However, HA infiltration did not decrease the E_{Bend} for 25% of FEG-introduced scaffolds. This was unexpected because C75E25 scaffolds exhibited the lowest compressive and tensile moduli. The fact that the current experiment was carried out in dry conditions may have affected this result. Studies have indicated that HA chains may still absorb a significant amount of water even in the crosslinked state, demonstrating their very hydrophilic nature (24). The secondary network created by HA infiltration was highly packed within collagen or collagen-FEG networks, and the hydration of the scaffolds may easily cause the HA network to stretch out and contribute more to the mechanical strength. When scaffolds were hydrated, as expected, HA infiltration contributed to the bending properties more, reducing the E_{Bend} to the level of non-crosslinked scaffolds, suggesting that the hydrophilic nature of HA probably dominates the structural components in the wet state. This also implies that the HA network favourably reduces the stiffening effect of crosslinking.

Normally, during flexure testing, the scaffold will be bent with one side under tension and the other in compression. Therefore, the effective bending modulus, $E_{Bend,}$ should fall between E_T and E_C. Here, the bending modulus of scaffolds was within the range between E_T and E_C, where

E_T was significantly larger than E_C, which implies that the E_C should have a greater impact on the value of E_{Bend} and the neutral axis in bending would be toward the tensile surface. The scaffold's compressive area progressively reaches the linear elastic strain after the initial slope. It begins to enter the second deformation stage, which causes a fall in the compressive region's modulus and, as a result, a reduction in the effective bending modulus. Another striking point of the current study was that the more FEG was present, the higher the flexibility was; even 10% of FEG significantly decreased the wet bending modulus by 1.5-2.7-fold, depending on the presence of crosslinking and/or HA. When force was applied at the centre, collagen took the role of tensile stress in C100 scaffolds. It was anticipated to have a larger membrane force and a higher effective bending modulus. In addition, as FEG replaced more collagen molecules in composites, this would substantially lower the E_C, lowering the bending modulus.

The flexure modulus has been studied in several studies. A model describing the bending of a single collagen fibre like a rod revealed that bending modulus could change from 1.0 GPa to 3.9 GPa, and crosslinking with EDC did not significantly affect its bending properties (58). Another important finding was that hydrated collagen fibrils had moduli in the MPa range, whereas dehydrated collagen fibrils often have moduli in the GPa range (59). In contrast, Young's moduli of 0.90 and 0.79 MPa were found in a study comparing fibrillin-rich and fibrillin-free elastin fibres. The statistical difference between the two groups was insignificant, indicating that scaffolding microfibrils have little effect on the mechanical characteristics of individual elastic fibres (60). These studies were mainly conducted by atomic force microscopy (AFM) nanoindentation, as a manual three-point bending test is not ideal for soft tissues, especially in wet conditions. A study found a value of 3.69 kPa using AFM indentation to characterise bending moduli of collagen-chitosan scaffolds (61). It is not surprising to see such a big difference in bending properties from a single fibre to scaffold as these parameters are highly correlated with the length and diameter of the sample (62), orientation (63), and being

a single fibre or a bundle. One thing is certain; while collagen exhibits higher bending modulus, the presence of elastin would increase its flexibility which is in good agreement with the current study. The present work also fits with the previous work of the group's members (1, 3); however, a direct comparison would again not be possible as the current scaffold combination is quite novel.

3.5. Summary

This chapter focused on fabricating collagen scaffolds or collagen-FEG-based composites with the incorporation of HA via crosslinking. Both SEM and FT-IR examined the microstructural and physicochemical properties upon processing. The swelling and degradation characteristics were of interest for structural integrity. The chapter also aimed to investigate the biocompatibility of designed scaffolds to native tissue in terms of mechanical properties. The main findings are:

- The successful fabrication of collagen-FEG composites and their HA-infiltrated versions with high porosities (>97%), was achieved and confirmed by FT-IR. The physical embedding of FEG fibres in collagen, which formed the dominant structure for all compositions, was revealed by microstructural analysis. Additionally, it was found that an increase in FEG content resulted in a decrease in solvent uptake, indicating that FEG dominates the swelling features of composites in a concentration-dependent manner.
- A better polymer-solvent interaction was accomplished by prolonged mixing at lower temperatures and pH, below the isoelectric point of both collagen and FEG. However, the lower affinity of FEG to be crosslinked with EDC/NHS possibly caused physical crosslinking between collagen and FEG. Degradation analysis showed that this physical interaction was still strong enough to maintain the structural integrity of composites within physiological conditions over time.

- Incorporating FEG and HA infiltration significantly shaped the mechanical properties of composite scaffolds. When force was applied, the compressive and tensile properties were mainly dominated by the FEG component, while the HA highly influenced the bending properties after sufficient hydration.

References

1. Iftekhar S. Isolation of Fibrillar Elastin Gel (FEG) and its application in heart valve tissue engineering: University of Oxford; 2020.

2. Yang C. Enhanced physicochemical properties of collagen by using EDC/NHS-crosslinking. Bulletin of Materials Science. 2012;35(5):913-8.

3. Nazir R. Development and characterization of collagen type I and hyaluronic acid (HA) based interlaced scaffolds for tissue engineered heart valves (TEHVS): University of Oxford; 2017.

4. Schanté CE, Zuber G, Herlin C, Vandamme TF. Chemical modifications of hyaluronic acid for the synthesis of derivatives for a broad range of biomedical applications. Carbohydrate polymers. 2011;85(3):469-89.

5. Stani C, Vaccari L, Mitri E, Birarda G. FTIR investigation of the secondary structure of type I collagen: New insight into the amide III band. Spectrochimica Acta Part A: Molecular and Biomolecular Spectroscopy. 2020;229:118006.

6. Glassford SE, Byrne B, Kazarian SG. Recent applications of ATR FTIR spectroscopy and imaging to proteins. Biochim Biophys Acta. 2013;1834(12):2849-58.

7. Nam K, Kimura T, Kishida A. Controlling coupling reaction of EDC and NHS for preparation of collagen gels using ethanol/water co-solvents. Macromol Biosci. 2008;8(1):32-7.

8. Everaerts F, Torrianni M, Hendriks M, Feijen J. Biomechanical properties of carbodiimide crosslinked collagen: influence of the formation of ester crosslinks. Journal of Biomedical Materials Research Part A: An Official Journal of The Society for Biomaterials, The Japanese Society for Biomaterials, and The Australian Society for Biomaterials and the Korean Society for Biomaterials. 2008;85(2):547-55.

9. Palombo F, Winlove CP, Edginton RS, Green E, Stone N, Caponi S, et al. Biomechanics of fibrous proteins of the extracellular matrix studied by Brillouin scattering. Journal of The Royal Society Interface. 2014;11(101):20140739.

10. Chen Q. Collagen-based scaffolds for heart valve tissue engineering: University of Oxford; 2013.

11. Popescu MC, Vasile C, Craciunescu O. Structural analysis of some soluble elastins by means of FT-IR and 2D IR correlation spectroscopy. Biopolymers. 2010;93(12):1072-84.

12. Liu H, Li D, Guo S. Studies on collagen from the skin of channel catfish (Ictalurus punctaus). Food Chemistry. 2007;101(2):621-5.

13. Zhang J, Duan R, Huang L, Song Y, Regenstein JM. Characterisation of acid-soluble and pepsin-solubilised collagen from jellyfish (Cyanea nozakii Kishinouye). Food Chemistry. 2014;150:22-6.

14. Hu X, Kaplan D, Cebe P. Determining beta-sheet crystallinity in fibrous proteins by thermal analysis and infrared spectroscopy. Macromolecules. 2006;39(18):6161-70.

15. Sadat A, Joye IJ. Peak fitting applied to fourier transform infrared and raman spectroscopic analysis of proteins. Applied Sciences. 2020;10(17):5918.

16. Ryan AJ, O'Brien FJ. Insoluble elastin reduces collagen scaffold stiffness, improves viscoelastic properties, and induces a contractile phenotype in smooth muscle cells. Biomaterials. 2015;73:296-307.

17. Highberger JH. The isoelectric point of collagen. Journal of the American Chemical Society. 1939;61(9):2302-3.

18. Morozova S, Muthukumar M. Electrostatic effects in collagen fibril formation. The Journal of chemical physics. 2018;149(16):163333.

19. Stein WH, Miller Jr EG. The composition of elastin. Journal of Biological Chemistry. 1938;125(2):599-614.

20. Davidenko N, Campbell J, Thian E, Watson C, Cameron R. Collagen–hyaluronic acid scaffolds for adipose tissue engineering. Acta biomaterialia. 2010;6(10):3957-68.

21. Koivurinta J, Hämäläinen E, Kellomäki M. The effect of cross-linking time on a porous freeze-dried collagen scaffold using 1-ethyl-3-(3-dimethylaminopropyl) carbodiimide as a cross-linker. Journal of Applied Biomaterials and Biomechanics. 2008;6(2):89-94.

22. Daamen W, Nillesen S, Hafmans T, Veerkamp J, Van Luyn M, Van Kuppevelt T. Tissue response of defined collagen–elastin scaffolds in young and adult rats with special attention to calcification. Biomaterials. 2005;26(1):81-92.

23. Minardi S, Taraballi F, Wang X, Cabrera FJ, Van Eps JL, Robbins AB, et al. Biomimetic collagen/elastin meshes for ventral hernia repair in a rat model. Acta biomaterialia. 2017;50:165-77.

24. Nazir R, Bruyneel A, Carr C, Czernuszka J. Collagen type I and hyaluronic acid based hybrid scaffolds for heart valve tissue engineering. Biopolymers. 2019;110(8):e23278.

25. Jiang Y-H, Lou Y-Y, Li T-H, Liu B-Z, Chen K, Zhang D, et al. Cross-linking methods of type I collagen-based scaffolds for cartilage tissue engineering. American Journal of Translational Research. 2022;14(2):1146.

26. Gonzalez de Torre I, Alonso M, Rodriguez-Cabello J-C. Elastin-based materials: promising candidates for cardiac tissue regeneration. Frontiers in Bioengineering and Biotechnology. 2020;8:657.

27. Lin Y-C, Tan F-j, Marra KG, Jan S-S, Liu D-C. Synthesis and characterization of collagen/hyaluronan/chitosan composite sponges for potential biomedical applications. Acta Biomaterialia. 2009;5(7):2591-600.

28. Shabafrooz V, Mozafari M, Köhler GA, Assefa S, Vashaee D, Tayebi L. The effect of hyaluronic acid on biofunctionality of gelatin–collagen intestine tissue engineering scaffolds. Journal of Biomedical Materials Research Part A. 2014;102(9):3130-9.

29. Gadomska M, Musiał K, Bełdowski P, Sionkowska A. New Materials Based on Molecular Interaction between Hyaluronic Acid and Bovine Albumin. Molecules. 2022;27(15):4956.

30. Chatterley AS, Laity P, Holland C, Weidner T, Woutersen S, Giubertoni G. Broadband Multidimensional Spectroscopy Identifies the Amide II Vibrations in Silkworm Films. Molecules. 2022;27(19):6275.

31. Sawadkar P, Mandakhbayar N, Patel KD, Buitrago JO, Kim TH, Rajasekar P, et al. Three dimensional porous scaffolds derived from collagen, elastin and fibrin proteins orchestrate adipose tissue regeneration. Journal of tissue engineering. 2021;12:20417314211019238.

32. Wilharm N, Fischer T, Hayn A, Mayr SG. Structural Breakdown of Collagen Type I Elastin Blend Polymerization. Polymers. 2022;14(20):4434.

33. Palumbo FS, Pitarresi G, Fiorica C, Rigogliuso S, Ghersi G, Giammona G. Chemical hydrogels based on a hyaluronic acid-graft-α-elastin derivative as potential scaffolds for tissue engineering. Materials Science and Engineering: C. 2013;33(5):2541-9.

34. Grover CN, Cameron RE, Best SM. Investigating the morphological, mechanical and degradation properties of scaffolds comprising collagen, gelatin and elastin for use in soft tissue engineering. Journal of the mechanical behavior of biomedical materials. 2012;10:62-74.

35. Charulatha V, Rajaram A. Influence of different crosslinking treatments on the physical properties of collagen membranes. Biomaterials. 2003;24(5):759-67.

36. Doublier J-L, Garnier C, Renard D, Sanchez C. Protein–polysaccharide interactions. Current opinion in Colloid & interface Science. 2000;5(3-4):202-14.

37. Schmitt C, Sanchez C, Desobry-Banon S, Hardy J. Structure and technofunctional properties of protein-polysaccharide complexes: a review. Critical reviews in food science and nutrition. 1998;38(8):689-753.

38. Chan EC, Kuo S-M, Kong AM, Morrison WA, Dusting GJ, Mitchell GM, et al. Three dimensional collagen scaffold promotes intrinsic vascularisation for tissue engineering applications. PloS one. 2016;11(2):e0149799.

39. Lam CX, Hutmacher DW, Schantz JT, Woodruff MA, Teoh SH. Evaluation of polycaprolactone scaffold degradation for 6 months in vitro and in vivo. Journal of Biomedical Materials Research Part A: An Official Journal of The Society for Biomaterials, The Japanese Society for Biomaterials, and The Australian Society for Biomaterials and the Korean Society for Biomaterials. 2009;90(3):906-19.

40. Zhang H, Zhou L, Zhang W. Control of scaffold degradation in tissue engineering: a review. Tissue Engineering Part B: Reviews. 2014;20(5):492-502.

41. Chiu LL, Radisic M, Vunjak-Novakovic G. Bioactive scaffolds for engineering vascularized cardiac tissues. Macromolecular bioscience. 2010;10(11):1286-301.

42. Madhavan K, Belchenko D, Motta A, Tan W. Evaluation of composition and crosslinking effects on collagen-based composite constructs. Acta biomaterialia. 2010;6(4):1413-22.

43. Chiu LL, Radisic M. Scaffolds with covalently immobilized VEGF and Angiopoietin-1 for vascularization of engineered tissues. Biomaterials. 2010;31(2):226-41.

44. Miranda-Nieves D, Chaikof EL. Collagen and elastin biomaterials for the fabrication of engineered living tissues. ACS Biomaterials Science & Engineering. 2017;3(5):694-711.

45. Wang X, Li Q, Hu X, Ma L, You C, Zheng Y, et al. Fabrication and characterization of poly (l-lactide-co-glycolide) knitted mesh-reinforced collagen–chitosan hybrid scaffolds for dermal tissue engineering. Journal of the mechanical behavior of biomedical materials. 2012;8:204-15.

46. Varley M, Neelakantan S, Clyne T, Dean J, Brooks R, Markaki A. Cell structure, stiffness and permeability of freeze-dried collagen scaffolds in dry and hydrated states. Acta biomaterialia. 2016;33:166-75.

47. Chen Q, Bruyneel A, Clarke K, Carr C, Czernuszka J. Collagen-based scaffolds for potential application of heart valve tissue engineering. J Tissue Sci Eng. 2012;11(003):1-6.

48. Gleeson J, Plunkett N, O'Brien F. Addition of hydroxyapatite improves stiffness, interconnectivity and osteogenic potential of a highly porous collagen-based scaffold for bone tissue regeneration. Eur Cell Mater. 2010;20(218):30.

49. Elango J, Zhang J, Bao B, Palaniyandi K, Wang S, Wenhui W, et al. Rheological, biocompatibility and osteogenesis assessment of fish collagen scaffold for bone tissue engineering. International Journal of Biological Macromolecules. 2016;91:51-9.

50. Pal P, Nguyen QC, Benton AH, Marquart ME, Janorkar AV. Drug-loaded elastin-like polypeptide–collagen hydrogels with high modulus for bone tissue engineering. Macromolecular bioscience. 2019;19(9):1900142.

51. Harley BA, Leung JH, Silva EC, Gibson LJ. Mechanical characterization of collagen-glycosaminoglycan scaffolds. Acta Biomater. 2007;3(4):463-74.

52. Huang Y, Onyeri S, Siewe M, Moshfeghian A, Madihally SV. In vitro characterization of chitosan–gelatin scaffolds for tissue engineering. Biomaterials. 2005;26(36):7616-27.

53. Huyer LD, Montgomery M, Zhao Y, Xiao Y, Conant G, Korolj A, et al. Biomaterial based cardiac tissue engineering and its applications. Biomed Mater. 2015;10(3):034004.

54. Emig R, Zgierski-Johnston CM, Timmermann V, Taberner AJ, Nash MP, Kohl P, et al. Passive myocardial mechanical properties: meaning, measurement, models. Biophys Rev. 2021;13(5):587-610.

55. Bax DV, Smalley HE, Farndale RW, Best SM, Cameron RE. Cellular response to collagen-elastin composite materials. Acta biomaterialia. 2019;86:158-70.

56. Daamen WF, van Moerkerk HT, Hafmans T, Buttafoco L, Poot AA, Veerkamp JH, et al. Preparation and evaluation of molecularly-defined collagen-elastin-glycosaminoglycan scaffolds for tissue engineering. Biomaterials. 2003;24(22):4001-9.

57. Kumar VA, Caves JM, Haller CA, Dai E, Liu L, Grainger S, et al. Acellular vascular grafts generated from collagen and elastin analogs. Acta biomaterialia. 2013;9(9):8067-74.

58. Yang L, Van der Werf KO, Fitié CF, Bennink ML, Dijkstra PJ, Feijen J. Mechanical properties of native and cross-linked type I collagen fibrils. Biophysical journal. 2008;94(6):2204-11.

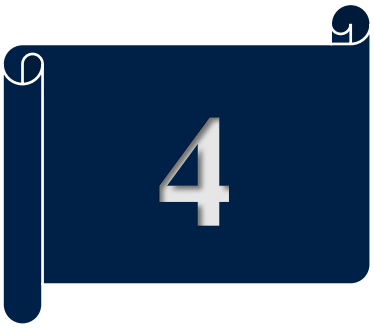
59. Gachon E, Mesquida P. Mechanical properties of collagen fibrils determined by buckling analysis. Acta Biomaterialia. 2022;149:60-8.

60. Koenders MM, Yang L, Wismans RG, van der Werf KO, Reinhardt DP, Daamen W, et al. Microscale mechanical properties of single elastic fibers: the role of fibrillin–microfibrils. Biomaterials. 2009;30(13):2425-32.

61. Zhu Y, Dong Z, Wejinya UC, Jin S, Ye K. Determination of mechanical properties of soft tissue scaffolds by atomic force microscopy nanoindentation. Journal of biomechanics. 2011;44(13):2356-61.

62. Wenger MP, Bozec L, Horton MA, Mesquida P. Mechanical properties of collagen fibrils. Biophysical journal. 2007;93(4):1255-63.

63. Wang J, Yuan B, Han RP. Modulus of elasticity of randomly and aligned polymeric scaffolds with fiber size dependency. Journal of the mechanical behavior of biomedical materials. 2018;77:314-20.



IN VITRO EVALUATION OF SCAFFOLDS

4. IN VITRO EVALUATION OF SCAFFOLDS

4.1. Introduction

The following chapter will focus on the feasibility of the designed scaffolds *in vitro* to see their contribution to human induced pluripotent stem cells (hiPSCs) maintenance, proliferation, and differentiation into cardiomyocytes (hiPSC-CMs), the endothelial cell (EC) proliferation and support towards vascularisation. As hyaluronic acid (HA)-infiltrated scaffolds showed the best match of mechanical properties with the native tissue, the *in vitro* analysis was only made upon these scaffold types. The cell viability, distribution, and proliferation were assessed using the alamarBlue™ colourimetry assay, scanning electron microscopy (SEM) and Phalloidin-DAPI staining. The change in pluripotency due to a prolonged culture period was analysed using real-time polymerase chain reaction (RT-PCR). RT-PCR and immunocytochemistry (ICC) were utilised to determine the differentiation to CMs. RT-PCR presented the inherent production of extracellular matrix (ECM) gene expression in both cell types. The change in the mechanical properties in the presence of cells was also studied using tensile and self-deflection tests.

4.2. Materials and Methods

4.2.1. Cell Culture and Maintenance

4.2.1.1.Human Induced Pluripotent Stem Cells

IMR90 and M180 were two cell lines used in *in vitro* tests. IMR90, which originated from Dr James Thomson (WiCell, University of Wisconsin), was kindly donated by Prof Sian Harding of Imperial College London. Human lung fibroblasts isolated from the lung tissue of a 16-week-old female Caucasian foetus were used to create the IMR90 iPS cell line using viral transduction of Yamanaka factors (1). M180 cell line was made up of human iPSCs produced by reprogramming adult human myoblasts utilising Yamanaka technology and an ecotropic retrovirus and was provided by Emmanuelle Massourides (CECS/I-STEM, France) according

to a Material Transfer Agreement (MTA). While IMR90 were used throughout *in vitro* studies, M180 was used only to determine pluripotency due to long-term scaffold maintenance.

For cell culture, hiPSCs were expanded and cultivated under the lab's standard operating procedure. Before the cell culture, T25 flasks or 6-well plates were coated with Matrigel® Growth Factor Reduced (GFR) Basement Membrane Matrix (Corning, UK) prepared in Dulbeccos's Modified Eagle Medium: Nutrient Mixture F12 (DMEM/F-12, 1X) basal media (Gibco, Life Technologies Ltd., UK) as 1:100 ratio and incubated in 5% CO_2 incubator at 37ºC for one hr at least. Coated plates could be maintained at 37ºC for about 2 weeks, and the coating solution could be reused up to 3 times. Once thawed, GFR Matrigel® Matrix (LDEV-free) was aliquoted in sterile centrifuge tubes and stored at -20ºC until further use. The cells were expanded on GFR Matrigel-coated plates with feeder-free TeSR™-E8™ basal media containing TeSR™-E8™ supplement (25X) (both from Stem Cell Technologies, Canada) and 1X penicillin-streptomycin (Gibco, UK).

After being taken out of the cryovial in liquid nitrogen, the cells were put in a 37°C water bath for ~2 mins, allowing most ice to melt. The dimethyl sulfoxide (DMSO) in the cryopreservation solution was immediately diluted by adding 10 mL warm TeSR™-E8™ complete media to a 15 mL falcon tube (Corning, UK) with the cells. Centrifugation (Heraeus Megafuge 8R, Thermo Scientific, UK) was used to collect the pellet for 4 mins at 1500 rpm. To increase the viability of the cells, the supernatant was removed, and the pellet was resuspended in TeSR™-E8™ complete medium with 10 µM ROCK inhibitor, Y-27632 (Tocris Bioscience, UK). ~1 million cells/well in a total volume of 2 mL were added to each well and left for 10 mins at room temperature to adhere. The culture cells were regularly checked for viability and any occurrence of contamination.

When the hiPSCs attained a confluency of 95%, they were either passaged or banked. After the media had been discarded, the plates were rinsed with Dulbecco's Phosphate Buffered

Saline (DPBS, Sigma Aldrich, UK). Enzyme-free ReLeSR (Stem Cell Technologies, Canada) was used to dissociate the cells after adding 1 mL to each well of a 6-well plate or 2 mL/T25 flask for 1 min at room temperature. Then, most of the ReLeSR was removed from the flask, leaving a thin layer. The cells were incubated in a 37°C incubator (5% CO_2) for an additional 4-5 mins. TeSR™-E8™ was used to strip the plates twice, after which cells and medium were collected in a 50 mL falcon tube (Corning, UK). The cells were then replated onto the flasks or plates (~$5x10^5$ cells/well of 6-well plates, ~$1x10^6$ cells/T25 flask) and left for adherence for 10 mins in the hood.

For cell banking, the cells were dissociated, as described above. Following centrifugation, the pellet was resuspended in Cryostor CS10 media containing 10% DMSO (Stem Cell Technologies, UK) and quickly transferred into cryovials as 1 million cells/1mL/vial to be stored in Mr Frosty Freezing Container (Thermo Fischer Scientific, UK) at -80°C up to two days before being placed into liquid nitrogen.

4.2.1.2.Human Umbilical Vein Endothelial Cells

The human umbilical vein endothelial cell (HUVEC) line (Passage 0) (HUVECs in EGM™-Plus, single donor, to 500.000 cells/mL, LOT: 00291) was purchased from Lonza (USA). Upon purchasing, the vial was stored in liquid nitrogen until thawing. EGM™-Plus media was prepared to culture the cells by mixing EBM™-Plus Basal Medium and EGM™-Plus SingleQuots Kit (both from Lonza, USA) containing L-glutamine, Foetal Bovine Serum (FBS), ascorbic acid, rhEGF, hydrocortisone, heparin hemisuccinate, bovine brain extract (BBE), gentamicin sulphate and amphotericin-B. Once everything was mixed, the bottle was sealed with aluminium foil to keep in the dark and stored at a +4°C fridge. Subculture reagents of Trypsin/EDTA, HEPES Buffered Saline (HEPES-BSS) and Trypsin Neutralizing Solution (TNS) were also purchased from Lonza and aliquoted as 10 mL/falcon tube to be stored at -20°C.

To culture the cells, EGM™-Plus media were added into T25 or T75 flasks as 5 mL or 10 mL, respectively and incubated at 37°C for at least 30 mins. The cryovial was kept in the 37°C water bath for ~1 min under close watch. The cell suspension was immediately mixed and dispensed into the flasks. The media was renewed after 16-24 hrs and every other day afterwards. Once confluent, the media was discarded, and the flask was rinsed with 5-8 mL of HEPES-BSS. The cells were incubated with 2-5 mL of Trypsin-EDTA in the CO_2 incubator for 4 mins. The flasks were carefully tapped to encourage detachment and neutralised with 5-8 mL of TNS at room temperature. The suspension was then collected into a 50 mL falcon tube, and the flask was washed off with HEPES-BSS once again. The pellet was obtained by centrifugation at 200xg for 5 mins and resuspended either with EGM™-Plus media to culture or with freezing media containing 10% FBS (Gibco, UK) and DMSO (ChemCruz™, Santa Cruz Biotechnology, USA) in EGM™-Plus media for banking. The banking cells were stored in Mr Frosty's freezing container at -80°C and transferred to the liquid nitrogen the next day.

4.2.2. Scaffold Preparation

4.2.2.1.Scaffold Sterilisation

C100, C90E10, C80E20 and C75E25 HA-infiltrated scaffolds were used for *in vitro* studies as they were found to be mechanically the best variation of all conditions. The rectangular scaffolds were cut cross-sectionally in 3-4 mm, which was big enough to be placed in a 24-well plate. Polystyrene (PS) plaques were cut in discs (D=10 mm) to eliminate solution/cell suspension loss during cell seeding. Before sterilisation, forceps were heated at >200°C for 2 hrs using a mini high-temperature dry steriliser (JVSURF, UK). While PS plaques were incubated in absolute EtOH for two days, the scaffolds were transferred into separate absolute EtOH containers and stored at +4°C for 24 hrs (two washes lasting 6 hrs and one wash for 12 hrs consecutively, ensuring the EtOH was refreshed). After this point, everything was assumed to be sterilised.

4.2.2.2. Vitronectin Coating

To increase the affinity of hiPSCs to scaffolds, vitronectin (VTN) was preferred as the coating agent. It is a xeno-free cell culture matrix, an alternative to Matrigel, to promote adhesion of the cells to the scaffolds (2). The method was also applied to those HUVEC-seeded scaffolds to see the potential influence of the coating on these cell types and the possibility of co-culture. After EtOH sterilisation, the PS plaques were first transferred to the sterile petri dishes (Corning, UK) to evaporate EtOH. The dry plaques were then placed onto the 24-well plates as required. The scaffolds were also put into sterile petri dishes, rinsed with DPBS three times, and transferred onto the PS plaques, as shown in Figure 4.1. The excess DPBS was discarded by pipetting, and scaffolds were coated with 10 µg/mL vitronectin XF™ (Stem Cell Technologies, Canada) freshly prepared in CellAdhere™ Dilution Buffer (Stem Cell Technologies, Canada) as 100 µl/scaffold. After coating, the samples were incubated in a CO_2 incubator for 24 hrs. The scaffold preparation for cell seeding is presented in Figure 4.1.

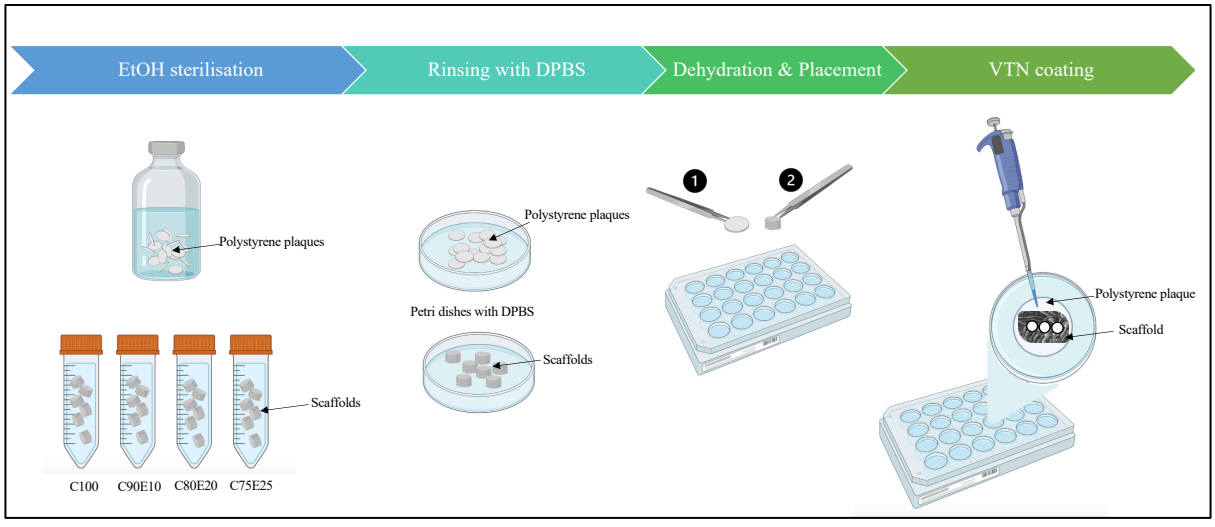


Figure 4.1. The process of scaffold and plaque sterilisation for cell seeding.

4.2.3. Cell Seeding on Scaffolds

4.2.3.1. hiPSCs Culture

After the scaffolds were sterilised and subsequently coated with VTN, the excess VTN was removed from the scaffolds, which were left for partial air drying under laminar flow.

Meanwhile, confluent IMR90 cells were dissociated for cell seeding on scaffolds. The dissociation was performed per plate because the longer the plate was incubated with ReLeSR, the lower the cell dissociation and viability were. Briefly, the medium was removed, and the culture plate was rinsed with DPBS. The cells were incubated for 1 min with 1mL/well ReLeSR at room temperature then the majority of it was discarded. Following 8 mins of incubation at 37°C, the cells were collected in a 50 mL falcon tube and centrifuged at 100xg for 8 mins. The pellet was resuspended in fresh media to count the cell (1:10 or 1:20 dilution as needed) in an automated cell counter (Countess™, Thermo Fisher Scientific, UK) using cell counting chamber slides. The cells were mixed with 0.4% Trypan Blue solution (Thermo Fisher Scientific, UK). Only live cells with intact membranes can effectively reject the dye; therefore, dead cells with defective membranes become stained. Cell seeding density was optimised as $1x10^6$ cells/scaffold in 50µL and $5x10^5$ cells/well for tissue culture polystyrene (TCPS, positive control). Upon seeding, the plates were left under the hood for cellular attachment for ~30 mins, and 50 µL of fresh TeSR-E8 complete medium was added if needed. The media was completed to 1 mL/well, and the plates were placed in a 37°C incubator. The media was renewed every day.

4.2.3.2.HUVECs Culture

Upon scaffold sterilisation and VTN coating, confluent HUVECs were dissociated as described in Section 4.2.1.2 via trypsinisation. Passage 2 was used for cell seeding to assess cellular viability and induction, followed by RT-PCR and Phalloidin-DAPI. Briefly, dissociated cells were collected in a 50 mL falcon tube and centrifuged at 200xg for 8 mins. The supernatant was removed, and the resuspension was diluted to count the cells in the cell counter using trypan blue. $5x10^5$ cells/scaffold in 50 µL was chosen, while the density of $1x10^5$ cell/TCPS was used for positive control. The cell-seeded scaffolds were incubated at 37°C for 3 hrs to

allow cellular attachment, and the media was completed to 1 mL/well and changed every two days.

4.2.4. Cell Viability and Proliferation

The alamarBlue™ cell viability reagent (Invitrogen, UK) characterised IMR90 and HUVEC adhesion and proliferation. An indicator dye called alamarBlue™ comprises a fluorescent dye, resazurin (dark blue), which is converted to resorufin (magenta) in the mitochondria when cells undergo oxidation-reduction (REDOX) processes (3). The fluorescent intensity of resorufin is proportional to the number of cells and reflects their metabolic activity. A calibration curve of cell number against fluorescent intensity was generated for both IMR90 cells and HUVECs for the quantification of cell number attached to the scaffold during the alamarBlue™. Briefly, the cells were dissociated and counted as described in Sections 4.2.1.1 and 4.2.1.2. The number of cells ranging from $1x10^4$ to $6x10^5$ as triplicates were cultured on a 24-well plate for 5 hrs, and the appropriate complete media supplemented with 10% alamarBlue™ was added onto it. After incubating the plate at 37°C for 3 hrs at dark, the supernatant was pipetted into an aluminium foil-covered transparent 96-well plate with a clear bottom (Greiner Ltd, UK). At 544/590 nm wavelengths, fluorescence was measured using a FLUOstar Omega plate reader (BMG Labtech Ltd, UK). The number of viable cells in each well and corresponding fluorescence read were graphed to obtain a linear trendline, which produced a slope to be used in cell quantification.

Cell behaviour on scaffolds was then determined by alamarBlue™. 16 hrs after cell seeding with the densities, aforementioned, the attachment was evaluated on Day 1 (D1) and proliferation was measured repeatedly on D3, D7, D14 and D21 for IMR90 cells and on D4 and D7 for HUVECs. At each time point, the scaffolds (2 acellular controls and 4 cellular samples) were rinsed with DPBS once and transferred into a new 24-well plate. Either fresh TeSR™-E8™ for IMR90 or EGM™-Plus for HUVECs supplemented with 10% alamarBlue™ was added to a new plate, and samples were incubated in media-alamarBlue™ solution at 37°C

for 3 hrs in the dark. After incubation, the supernatant was pipetted into 96-well plate and measured using the plate reader, as mentioned above. The number of cells in the specific well was calculated by the fluorescence of the cellular scaffold (F_{sample}) compared to the acellular scaffold ($F_{control}$) using the slope from the calibration curve as follows:

$$Cell\ Number = \left(F_{sample} - F_{control} \right) \times Slope$$

(Equation 4.1)

A two-way ANOVA with Tukey's post-hoc test was used for statistical analysis.

4.2.5. Cardiomyocyte Differentiation

hiPSCs differentiation to cardiomyocyte (hiPSC-CM) was induced directly on scaffolds after hiPSCs had been maintained on these constructs for 21 days. The differentiation protocol was previously established in Carr Group from DPAG (4) with the addition of 1X penicillin-streptomycin into each differentiation media (DM) to minimise infection. Briefly, when confluent, the media was changed to Roswell Park Memorial Institute (RPMI) 1640 supplemented with 1% B27 Minus Insulin (both Gibco, UK), containing 6 μM CHIR99201 (Tocris Bioscience, UK) on Differentiation Day 0 (DD0). The media was then changed to RPMI 1640 containing 1% B27 Minus Insulin with no additional factors on DD2. On DD3, the media was renewed to fresh RPMI with 1% B27 Minus Insulin with the addition of 2.5 μM Wnt-C59 (Tocris Bioscience, UK). Two days later, the medium was changed again to RPMI with 1% B27 Minus Insulin with no additional factors, and the media was renewed every two days. The glucose depletion was applied on DD11 and DD13 by changing the media to RPMI 1640 without glucose (Gibco, UK), containing 1% B27 minus insulin. On DD15, the medium was changed again to RPMI with 1% B27 Supplement (Gibco, U.K.). By DD17, differentiated cells were either fixed for imaging or messenger ribonucleic acid (mRNA) extraction. The differentiation process upon long-term proliferation was schematised in Figure 4.2.

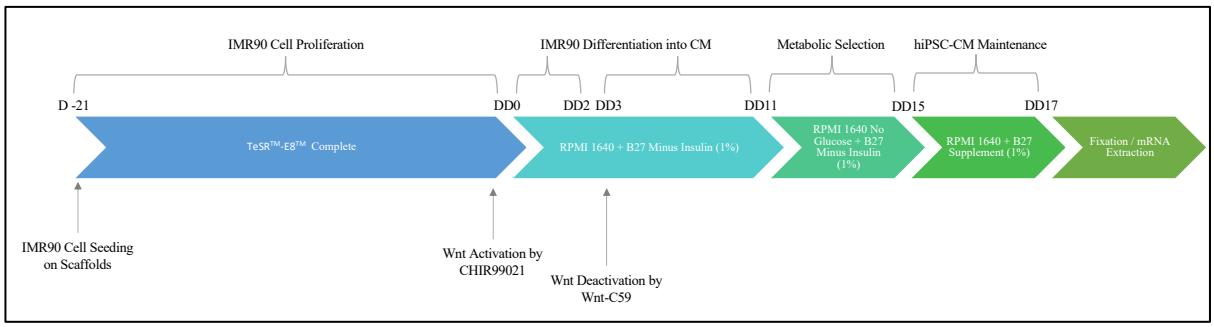


Figure 4.2. The timeline of hiPSCs (IMR90) differentiation into cardiomyocytes.

4.2.6. Angiogenesis Induction

HUVECs were seeded onto the pre-coated scaffolds as stated in Section 4.2.3.2 and cultured for 7 days before induction. At this point, half of the batch was maintained in EGM™-Plus media for 24 hrs. On D7, the other half of the batch was rinsed with DPBS twice, and the EGM™-Plus media was changed to Endothelial Cell Growth Medium-2 (EGM-2) containing SingleQuots™ Supplements and Growth Factors (Lonza, USA) to induce rapid endothelial growth and angiogenesis. The cells were incubated with the induction media (IM) at 37°C for 24 hrs. The induced cells were either fixed or mRNA-extracted by methods explained in the following sections.

4.2.7. Real-Time Polymerase Chain Reaction

4.2.7.1.mRNA Extraction

A positive control group of monolayer cells (TCPS) on DD17 of differentiation were dissociated as above, and mRNA was extracted from the pellet of cells. For scaffolds, a minimum of two samples were taken at a time to maximise the quantity of mRNA isolated on DD17. Each had its own control scaffold group maintained in TeSR™-E8™ complete media only throughout the culture period. TCPS was exposed to 1 mL of TRIzol™ reagent (Invitrogen, UK) for ~1 min via pipetting directly on a culture plate and then collected into an RNase-free microcentrifuge tube (Eppendorf, UK) to be kept in an ice bucket. TRIzol™ reagent was used to isolate high-quality total RNA, as extracting nucleic acids from scaffolds was challenging. The duplicate samples (N=3) were transferred into the same RNase-free microcentrifuge tube

containing 500 µL of TRIzol™, and the samples were disintegrated into fragments using a sterile micro-pestle (Eppendorf, UK). The samples were centrifuged at 12000xg for 4 mins to remove the scaffold residues. The supernatant was collected into a sterile 15 mL falcon tube, and 500 µL of TRIzol™ was added to the pellet again. The centrifugation was repeated to collect the supernatant, which was then transferred to the same falcon tube. The samples were left on the ice while other samples were similarly disintegrated. Prior to RNA extraction, the work surface was disinfected with RNaseZAP™ (Sigma Aldrich, UK). After this point, all sample supernatant was handled with the RNeasy® Mini Kit (Qiagen, UK) to extract mRNA according to the manufacturer's protocol. Briefly, 700 µL of absolute EtOH was added to the supernatant and agitated slowly. Up to 700 µL of the suspension was transferred into an RNeasy spin column placed in a 2 mL collection tube and centrifuged for 15 s at 10000xg. The flow-through solution was discarded, and the left-over supernatant was transferred to the column, followed by the centrifugation in the same manner. The spin column membrane was then rinsed with 700 µL of Buffer RW1 and centrifuged at 10000xg for 15 s. After discarding the flow-through, the column membrane was rinsed with 500 µL of Buffer RPE twice, followed by centrifugation at 10000xg for 15 s and 2 mins, respectively. The collection tube was renewed, and the column membrane was centrifuged at 14000xg for 1 min to dehydrate the membrane. The column was then transferred onto an RNase-free microcentrifuge tube, and 30 µL of RNase-free water (Thermo Fisher, UK) was added directly onto the membrane. The tubes were centrifuged at 10000xg for 1 min to elute total RNA, which was then stored at -80°C until reverse transcription.

The amount and quality of mRNA were determined by NanoDrop UV spectrometry (NanoDrop™ Lite, Thermo Fisher Scientific, UK). Before reading, mRNA samples were vortexed for 10 s using the Vortex-Genie 2 (Scientific Industries Inc., USA). RNase-free water

was utilised as a blank control. The mRNA having an A_{260}/A_{280} ratio at 1.9-2.1 and a concentration of >100 ng/µL was used for complementary DNA (cDNA) conversion.

4.2.7.2.cDNA Conversion

RNA was converted into cDNA using the High-Capacity cDNA Reverse Transcription Kit (Life Technologies, UK). The materials added to each well are listed in Table 4.1, as the total volume of the reaction was 20 µL/well. The solution was incubated for 10 mins at 25°C, 120 mins at 37°C, and 5 mins at 85°C, respectively, in a SensoQuest Basic Thermal Labcycler gradient (SensoQuest GeneFlow, UK). cDNA samples were removed from +4°C then stored at -20°C. Before the RT-PCR, all cDNA samples were diluted to a working concentration of 5 ng/µL.

Table 4.1. The material list for cDNA conversion of mRNA samples.

Ingredient	Volume (µL)/reaction
10X RT Buffer	2
25X dNTP Mix	0.8
10X RT Random Primers	2
MultiScribe Reverse Transcriptase	1
Nuclease-free water	4.2
RNA sample	10
Total volume	20

4.2.7.3.Primer Validation and Annealing Temperature

The primers listed in Appendix D were purchased from Sigma-Aldrich, UK and validated using RT-PCR. The validation was critical to determine the primer's annealing temperature during gene expression analysis. The purchased primers were diluted to a working concentration of 6 mM by using nuclease-free water. The reaction mix was prepared by adding 6 µL of master mix (PowerSYBR® Green PCR Master Mix, Applied Biosystems, UK) and 0.5 µL of each primer (forward and reverse) for each well. The serial dilution of cDNA (5 ng/µL, from monolayer cells) was prepared as 1:1, 1:10, 1:100 and 1:1000 using nuclease-free water. The reaction mixture and 3 µL of diluted cDNA were loaded onto the 96-well qPCR plate

(MicroAmp™ Fast, Applied Biosystems, China). The plate was sealed using a MicroAmp™ Optical Adhesive Film (Applied Biosystems, UK) before being centrifuged for 4 mins at 4400 rpm to collect the reaction mixture at the bottom of the plate. The StepOnePlus™ Real-Time PCR System (Applied Biosystems, UK) was then used to run the plate. A two-step cycle with a total of 40 cycles was employed for the reaction. The stage conditions were as follows: holding at 95°C for 600 s, cycling at 95/60°C for 15 s, and an annealing/extension at various temperatures for 30 s. The validated annealing temperatures of each primer are also listed in Appendix D.

4.2.7.4.RT-PCR Quantification

The RT-PCR was carried out using StepOnePlus™ Real-Time PCR System, as mentioned above, to determine changes in the gene expression regarding differentiation and ECM production. The list of primers is given in Appendix D. SYBR Green was again used as a detection method for the reaction. The cDNA (5 ng/µL), primers and SYBR Green were mixed using the recipe in Section 4.2.7.3 and distributed as a total of 10 µL/well to the 96-well qPCR plate. The plate was sealed with adhesive film to prevent evaporation and centrifuged at 4400 rpm for 4 minutes to sink the mixture to the bottom. A two-step cycle was conducted at a specific annealing temperature validated for each primer.

The Ct Livak method was used to determine the relative mRNA expression, plotting the data as $2^{-\Delta\Delta C_T}$. Comparing the experimental group to the control group (TCPS) served as the basis for the analysis. The cycle threshold (C_T) was determined to be the number of cycles needed for a sample's fluorescent signal to outperform the background signal. A housekeeping gene (β-ACTIN or UBC) was used to normalise the mRNA expression where the C_T of each target gene (TG) was normalised twice: once against the housekeeping gene (HKG) and once against the control group. The calculations were made as follows:

1) Calculate the average of C_T(TG) and C_T(HKG)

2) Calculate ΔC_T: $\Delta C_T = C_T(TG) - C_T(HKG)$

3) Calculate $\Delta\Delta C_T$: $\Delta\Delta C_T = \Delta C_T$ (experimental group) $- \Delta C_T$ (control group)

4) Calculate the relative fold change: $2^{-\Delta\Delta C_T}$

Two-way ANOVA followed by Tukey's post-hoc test was applied for statistics between the scaffold types cultured with or without DM/IM.

4.2.7.5.Pluripotency

To check variations arising from any long-term culture effect on pluripotency, RT-PCR was conducted based on the genes OCT4 and NANOG, common pluripotency markers of hiPSCs. This experiment was conducted on IMR90 and M180 cell lines to compare cell line-specific variations during long-term maintenance. The cells were populated on 6-well plates until confluency, as described in Section 4.2.1.1. They were then cultured on VTN-coated scaffolds (Section 4.2.3.1) for either 7 or 21 days. At each time point, the culture was terminated and RT-PCR was performed, as stated in Section 4.2.7.4.

4.2.8. Cell Imaging

4.2.8.1.Fixation

4.2.8.1.1. Glutaraldehyde Fixation

Glutaraldehyde fixation was chosen for imaging by SEM since its effectiveness as a fixative for stabilising surfaces and intracellular structures for SEM research was previously proposed at the cellular level before the use of freeze-substitution (5). A 2.5% glutaraldehyde fixation solution was prepared using 25% stock glutaraldehyde solution (TAAB Laboratories Equipment Ltd., UK) and 0.1 M cacodylate buffer. The cacodylate buffer was also prepared by mixing sodium cacodylate trihydrate (Sigma-Aldrich, UK) and distilled water at a pH of 7.4, adjusted by 1 N HCl. The glutaraldehyde fixative solution was later filtered using a 0.22 µm membrane filter (Millipore, UK) and stored at -80°C until further use.

The hiPSC-seeded scaffolds were fixed on D7 and D21 to assess cell behaviour and proliferation using SEM. HUVEC-seeded scaffolds were also fixed with glutaraldehyde to compare the effect of induction on cell behaviour (the cells without induction on D7 and with induction on D8). Briefly, the cellular scaffolds were rinsed with 0.1 M cacodylate buffer twice after removing the media. 2.5% glutaraldehyde fixation solution was added to wells for 2 hrs at room temperature. The scaffolds were washed with 0.1 M cacodylate buffer and distilled water three times and once, respectively, and kept in distilled water and stored in a -80°C freezer overnight. The frozen samples were then freeze-dried, as mentioned in Section 3.2.1.1.

4.2.8.1.2. Formaldehyde Fixation

The IMR90 cells and HUVECs cultured on VTN-coated coverslips (VWR, UK) and scaffolds with or without induction were fixed with 4% paraformaldehyde (PFA, Thermo Fisher Scientific, UK) for confocal microscopy imaging. Upon culturing, the cells were rinsed with PBS containing Mg^{++} and Ca^{++} (Sigma Aldrich, UK) three times. The cells on scaffolds and coverslips were then fixed in 4% PFA solution for 1 hr and 30 mins, respectively, at room temperature and washed with DPBS twice. The samples were stored in DPBS at +4°C until the staining procedure.

4.2.8.2.SEM

SEM was utilised to image cell attachment on scaffolds previously fixed with 2.5% glutaraldehyde and freeze-dried. As mentioned in Section 3.2.2, the stubs mounted on scaffolds were transversely attached. Using Leica EM ACE600 for 1 minute at a rate of 0.10 nm/s at room temperature, the samples were sputter coated, which resulted in an 8 nm coating thickness. Under a certain vacuum, the materials were imaged using the Zeiss EVO MA10. The secondary electron mode was then used to create images at a working distance of 10 mm. A tungsten source was used to apply an accelerating voltage of 5 kV, and a probe current of

100 pA was set. After adjustments, images were captured at 100X, 200X and 500X magnifications.

4.2.8.3.Phalloidin-DAPI

Phalloidin-DAPI staining was performed on HUVECs to analyse the morphology of actin filaments and nuclei arrangement, which regulate cell fate. Phalloidin is a heptapeptide toxin that binds selectively to filamentous-actin (F-actin) (6). Fluorescent derivatives of phalloidin can be used to examine cellular F-actin through fluorescence microscopy. The blue-fluorescent DNA stain DAPI (4′,6-diamidino-2-phenylindole) exhibits a 20-fold increase in fluorescence when it binds to AT sections of double-stranded DNA (7). It is frequently used as a nuclear counterstain at an excitation of 405 nm wavelength in fluorescence microscopy. Here, tetramethylrhodamine B isothiocyanate (TRITC)-conjugated phalloidin (Sigma-Aldrich, UK) and DAPI (Thermo Fisher Scientific, UK) were used as staining dyes. First, the PFA-fixed cells were treated with 0.1% Triton®X-100 (MP Biomedicals, UK) prepared in DPBS for 5 mins at room temperature. Followed by rinsing with DPBS three times, 1% bovine serum albumin (BSA) (Sigma-Aldrich, UK) prepared in DPBS was added to samples and incubated at 37°C for 30 mins. The samples were then washed with 0.1% BSA in DPBS once, and 500 µL of Phalloidin (1:200, prepared in 0.1% BSA) was applied for 2 hrs at 37°C. After rinsing three times with DPBS at 5 mins intervals, the samples were treated with DAPI (1:5000, prepared in DPBS) for 10 mins at room temperature. They were washed with DPBS three times again and kept in DPBS in the dark during imaging. The imaging was performed using Olympus Fluoview FV1200 Biological Confocal Laser Scanning Microscope (Olympus, Japan) at the Dunn School of Pathology, University of Oxford. The images were then processed using ImageJ.

4.2.8.4.Immunocytochemistry

Immunostaining was carried out for IMR90 and hiPSC-CMs cultured on both coverslip and scaffolds at room temperature unless it states otherwise. Fixed cells were incubated in 100 mM Glycine (in DPBS, Sigma Aldrich, UK) for 15 mins to saturate the reactive PFA groups. Following washing three times in DPBS at 5 mins intervals, the samples were permeabilised in 0.5% Triton®X-100 (in DPBS) for 10 mins. They were then rinsed with DPBS three times and treated with blocking solution (1% BSA prepared in 0.05% Triton®X-100) for 1 hr. The samples were incubated with the primary antibody in a blocking solution overnight at +4°C dark room.

Upon rinsing with DPBS, the samples were treated with secondary antibody in a blocking solution for 1 hr and rinsed again. Nuclei were counterstained with DAPI (1:5000 in DPBS) for 10 mins at room temperature and then washed with DPBS. While monolayer cells were mounted with 1:1 DPBS: Glycerol under glass coverslips, the scaffolds were kept in DPBS and stored at the dark, +4°C. The imaging was conducted using the confocal microscope, and images were processed on ImageJ.

The list of antibodies and related working concentrations of this study can be found in Appendix E.

4.2.9. Mechanical Testing

4.2.9.1.Tensile Testing

A tensile test was performed on hiPSC-CM-cultured scaffolds (N=5) where the rectangular scaffolds (as stated in Table 3.1) were seeded as described in Sections 4.2.3.1 and 4.2.5. The scaffolds were coated with VTN (1.2 mL/scaffold) for 48 hrs, and the cell seeding density was $6x10^6$ cells/scaffold in 500 µL. The samples were kept in RPMI with a 1% B27 supplement and washed with DPBS twice before testing. The wet tensile testing was applied using Autograph AGS-X (Shimadzu Corp., Japan) in the Department of Materials. A testing rate of

14 mm min^{-1} until failure was used after a 100 mN preload set at a 2 mm min^{-1} rate. E_T values were obtained at low strains up to 5%. Statistical comparison was made between cellular and acellular scaffolds using a two-way ANOVA with Tukey's post-hoc test upon plotting a stress-strain curve.

4.2.9.2.Self-Deflection

The self-deflection was performed on hiPSC-CM-cultured rectangular scaffolds, as mentioned in Section 3.2.8. Upon sterilisation and VTN coating, samples were carefully labelled and weighed to record the dry mass. The samples were prepared as described above and maintained in RPMI with a 1% B27 supplement prior to the test. The images were then processed, and the deflection was calculated using Equation 3.9.

4.3. Results

4.3.1. hiPSC Maintenance and Differentiation

hiPSCs were grown on Matrigel-coated 6-well plates using TeSR™-E8™ complete medium (Figure 4.3A-C) until they reached confluency before differentiation. The ROCK inhibitor was used to stabilise cells being plated after thawing but was not necessary when passaging from confluence because the enzyme-free procedure with ReLeSR formed cells in clusters (Figure 4.3A), and this had a substantially greater survival rate. Previously in plot studies, some cells were discovered to spontaneously develop a branching cell at the edges within the flask. Therefore, the current method was optimised for more delicate cell dissociation. Instead of flasks, it was much simpler to cultivate the cells in open plates, like 6-well plates, but extra caution was required because this raised the risk of contamination.

Various factors, including the handling of the cell culture, cell dissociation, and culture duration, influenced the success of differentiation. Additionally, the outcome of the differentiation process was influenced by the confluence of the cells. The differentiation process took place after 90-95% confluency (Figure 4.3C). If cells were cultured too densely

(100% confluent for a couple of days), they detached from the plates. However, when cells were cultured at less than 90% confluence, the differentiation was also inefficient, and no contraction on DD7-17 was observed. This shows the importance of choosing the best confluence before beginning the differentiation process, which requires experience with these cells. As shown in Figure 4.3, hiPSCs were differentiated using a modified version of the GiWi procedure created by Lian *et al.* (8, 9) and Burridge *et al.* (10, 11) and optimised in DPAG by Dr Ujang Purnama. The Wnt pathway was activated and inhibited as part of the differentiation protocol utilising the small molecules CHIR99021 and Wnt-C59, respectively. The differentiating cells cluster together and leave debris on other parts of the well (Figure 4.3D) after Wnt-pathway activation started on DD2. The Wnt-pathway was inactivated on DD3, resulting in no evident cell death by DD5 (Figure 4.3E). After this point, roughly on DD7-9, the cells forming a muscle-like structure connected one to another started to contract and continued to contract then onwards, prior to dissociation on DD17 (Figure 4.3F). The differentiated cells were dissociated to see the change in morphology which the cells became more elongated and branched (Figure 4.3G) and showed increased cell size with time in culture (Figure 4.3H-I).

The same maintenance and differentiation protocol was optimised for 3D culture to show the effect of scaffolds' composition on cell behaviour and differentiation.

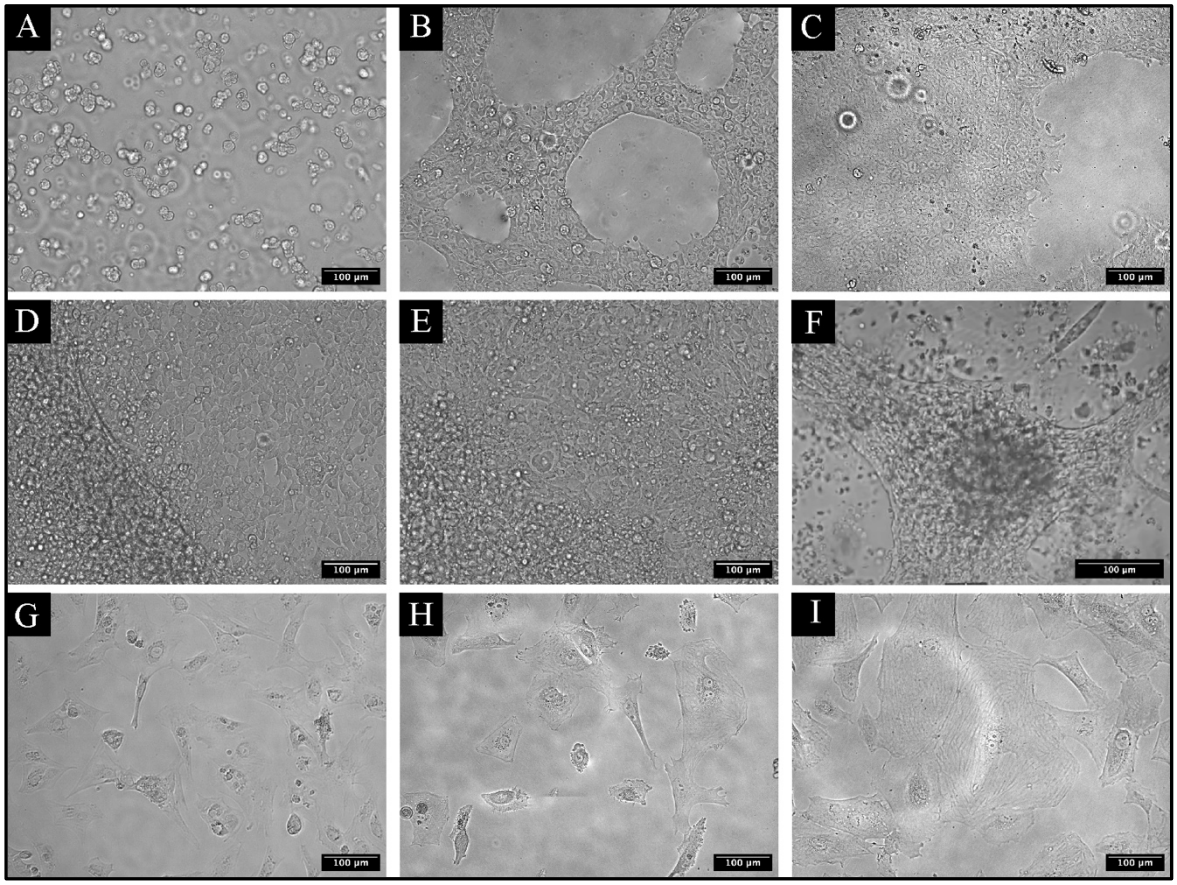


Figure 4.3. hiPSC maintenance and differentiation into cardiomyocytes under brightfield microscopy. (A) IMR90 cells after dissociation. (B) IMR90 cells 3 days after dissociation. (C) The confluent IMR90 before differentiation starts. hiPSCs differentiation into cardiomyocytes on days (D) 3 and (E) 5. (F) The iPSC-CM cells on day 17 with contraction. The dissociation of differentiated cells on days (G) 1, (H) 3 and (I) 7. Scale Bar: 100 µm.

4.3.2. hiPSC Behaviour on Scaffolds

A non-invasive alamarBlue™ assay assessed hiPSC cell viability on scaffolds. The amount of resazurin (dark blue) converted to resorufin (magenta) in the mitochondria will indicate cell proliferation. The calibration curve was plotted to quantify the viability of these cells on the scaffold, shown in Figure 4.4. The slope was used to quantify the cell number corresponding to specific fluorescence at that time.

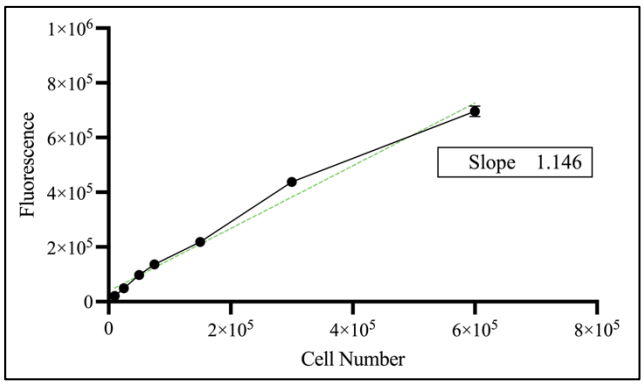


Figure 4.4. The calibration curve graph assessed by alamarBlue™ for the IMR90 cell line.

Optimisation of cell seeding density and the benefit of pre-coating scaffolds was studied using the alamarBlue assay, as given in Figure 4.5. Cells were seeded and allowed to attach for 16 hrs before the addition of alamarBlue. This time point was chosen to allow cells to become attached and viable but with limited time for proliferation. The cell adherence when seeded as a monolayer on dishes coated with Matrigel (~100%) was significantly higher than on those coated with VTN (~80%). The cells attached to the monolayer more than they did on scaffolds, regardless of coating agents. The attachment on coating-free scaffolds was inefficient compared to coated scaffolds. A doubled cell seeding number significantly improved the initial adherent cell number, increasing by ~2-fold. This was still considerably lower than those Matrigel-coated scaffolds, although they contained half the number of cells. However, Matrigel was not found to be ideal for studying the effect of scaffold content on cell behaviour as it contains various growth factors that may overshadow scaffolds' benefits.

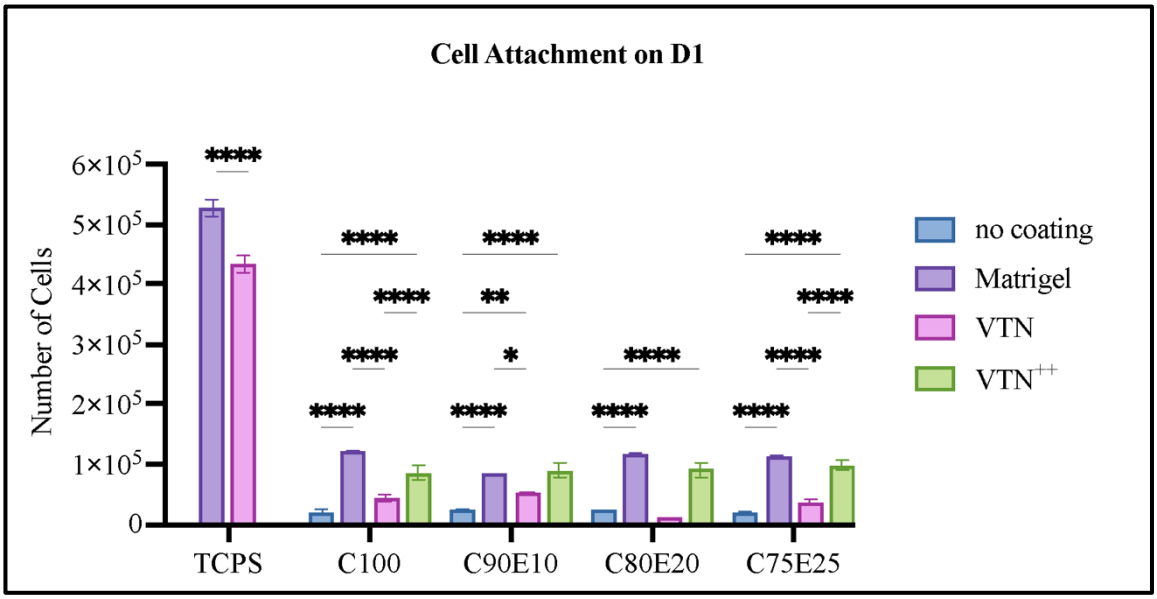


Figure 4.5. Cell adherence comparison on a monolayer (TCPS) and scaffolds conditioned by no coating, coating with Matrigel and VTN. The initial cell number was $5x10^5$ cells/well/scaffold. $^{++}$ indicates the cell seeding number was doubled. Two-way ANOVA with Tukey's post-hoc test was used. $^{*}p<0.05$, $^{**}p<0.01$, $^{***}p<0.001$, $^{****}p<0.0001$ (N=3).

Figure 4.6 indicates the hiPSCs proliferation on TCPS and scaffolds. The initial cell density was adjusted as $5x10^5$ cells/well and $1x10^6$ cells/scaffold for TCPS and scaffolds, respectively. This was mainly due to the unavailability of enough space to grow on the culture plate for TCPS samples and the low adherence to scaffolds at lower densities. ~80% of the cells could attach the VTN-coated plates successfully. However, after D3, they reached confluence, started to die on D14, and eventually detached from the plate. In contrast, the cell-seeded scaffolds showed cell proliferation throughout the experiment, although the initial cell density was low (5.7-7.4%). All scaffolds experienced a similar trend showing low cellular attachment on D1, an adaptation on D3-7 and exponential growth up to D21. The highest average cell number on D21 was C75E25, with 243,737±13,596 cells/scaffold. Unfortunately, the converted resorufin could not be cleared efficiently from the scaffolds without harming the cells within the scaffolds during pipetting. Nevertheless, the data show similar rates of proliferation on the scaffolds.

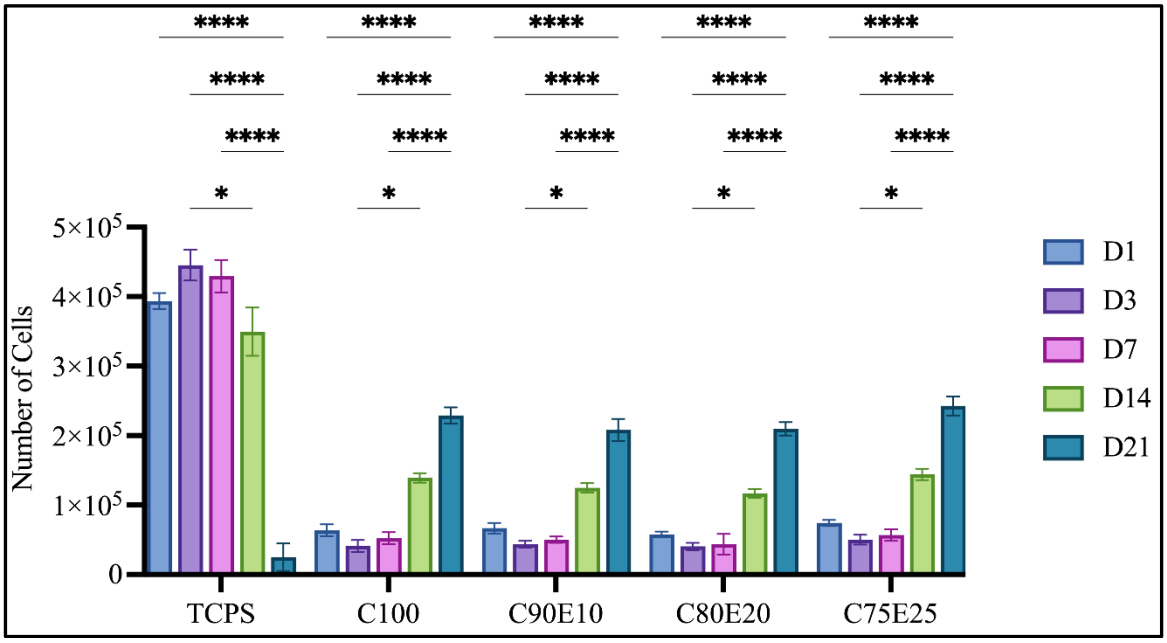


Figure 4.6. AlamarBlue cell viability analysis of IMR90 cultured on a monolayer (TCPS), C100, C90E10, C80E20 and C75E25 scaffolds for 1, 3, 7, 14 and 21 days. (The statistics of TCPS to any scaffold on the same day ($p<0.0001$) were not shown in the graph). Two-way ANOVA with Tukey's post-hoc test was used. $^{*}p<0.05$, ****$p<0.0001$ (N=4).

The cell morphology was imaged by SEM in the absence and presence of VTN, as presented in Figure 4.7. After D7, cell attachment could be seen on all scaffolds but with fewer cells on the VTN-free scaffolds compared to VTN-coated scaffolds. Substantial cell growth was observed on D21, covering all the imaged surfaces, especially on collagen-FEG composite scaffolds. The cell proliferation became more distinguishable as the FEG content increased. Due to the noticeable cell coverage on the scaffold surface on D21, it was hoped that this level of confluency was sufficient to start the differentiation process.

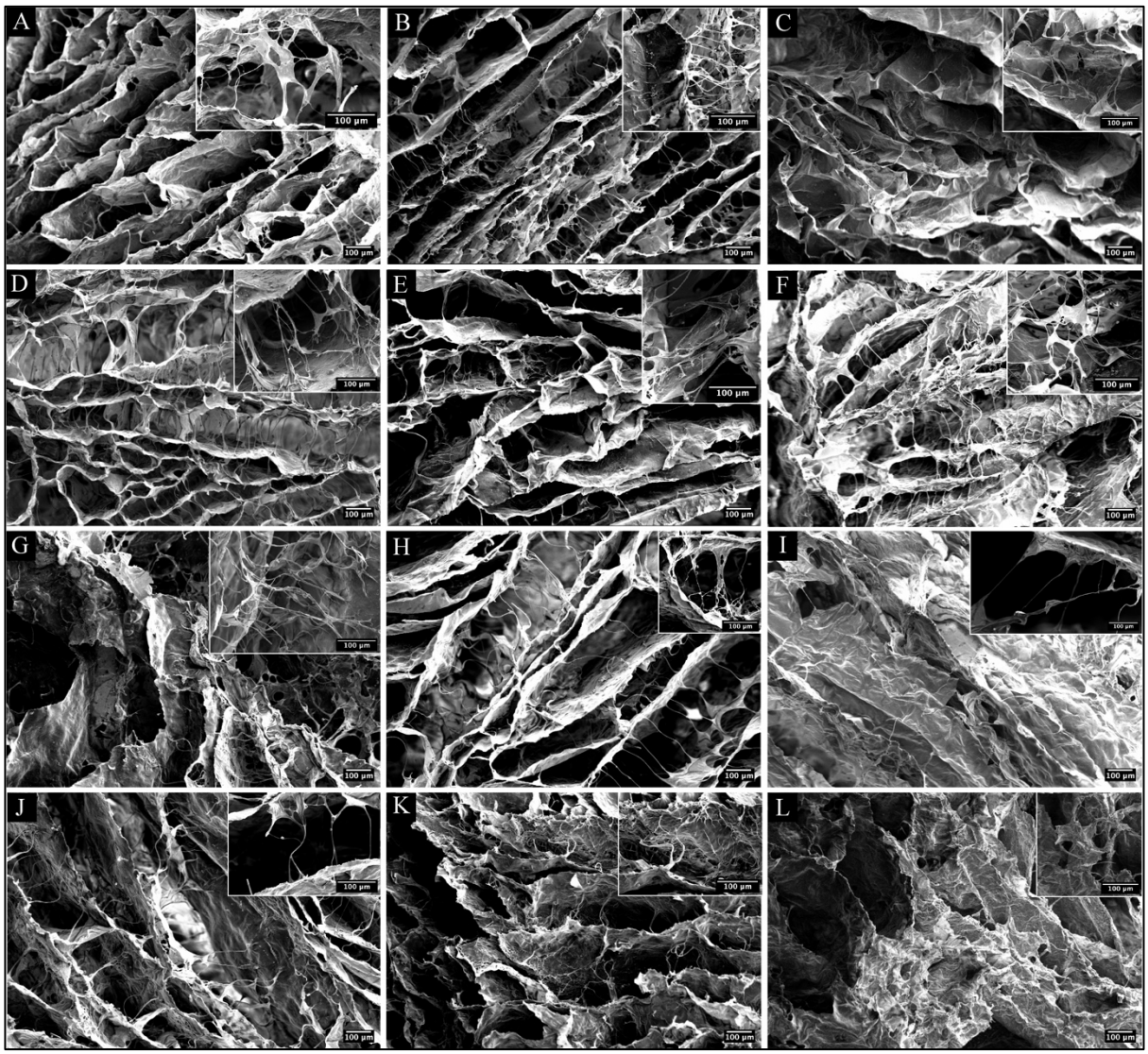


Figure 4.7. SEM imaging of iPSCs on C100 (A-C), C90E10 (D-F), C80E20 (G-I), and C75E25 (J-L) cultured without VTN coating for 7 days (left), with VTN coating for 7 days (middle) and 21 days (right). Scale Bar: 100 µm.

4.3.3. Pluripotency

The impact of prolonged hiPSC culture within the scaffold on pluripotency was studied by RT-PCR using two primers: OCT4 and NANOG. The analysis was conducted for both IMR90 and M180 cell lines at two-time points for comparison and presented in Figure 4.8. Interestingly, not only was the expression an antagonist at different time points, but both cell lines simultaneously experienced opposite expressions of the related gene. The OCT4 expression reduced by 2.6, 2.3, 2.8 and 4-fold on IMR90-seeded C100, C90E10, C80E20 and C75E25 scaffolds, respectively (Figure 4.8A). For IMR90, NANOG upregulated on D21 for all

scaffolds except for C75E25 and significantly downregulated as the FEG content increased (Figure 4.8B). No significance was observed for M180-seeded scaffolds regarding OCT4 expression (Figure 4.8C). However, NANOG upregulation was observed as the FEG content increased on D7 and dramatically downregulated on D21, reducing by 1.8, 1.7, 1.9 and 2.5-fold for C100, C90E10, C80E20 and C75E25 scaffolds, respectively (Figure 4.8D).

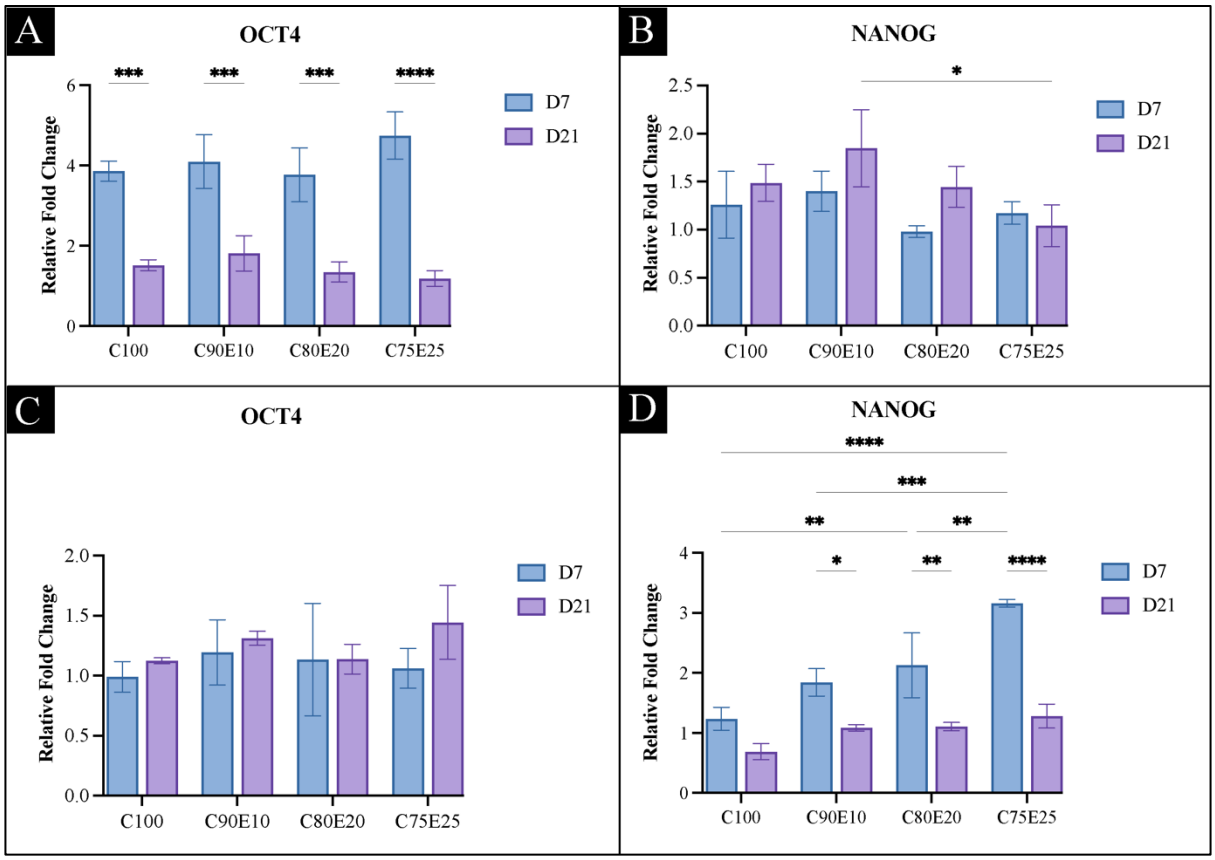


Figure 4.8. OCT4 and NANOG expression on (A-B) IMR90 and (C-D) M180 cell lines cultured on scaffolds for 7 and 21 days. Two-way ANOVA with Tukey's post-hoc test was used for multiple comparisons. *p<0.05, **p<0.01, ***p<0.001, ****p<0.0001. Data represented the Mean±SD and was normalised to TCPS (N=3).

4.3.4. Cardiomyocyte Differentiation

The cardiomyocyte differentiation on various scaffold types cultured with or without DM was examined by RT-PCR and ICC. The RT-PCR was used to determine the change in the expression of cardiac and ECM primers. Figure 4.9 presents the difference in the myosin light chain-2 atrial isoform (MYL7), α-myosin heavy chain (MYH6), and troponin T2 (TNNT2) expression of hiPSC-cultured scaffolds with or without DM (DM). The data from the cells on

3D constructs were normalised to the data obtained from monolayers cultured without DM. When the differentiation was induced by DM, a significantly higher gene expression was seen on MYL7 and MYH6 compared to those cultured without DM. However, these genes were less expressed in 3D compared to 2D. When no DM was present, MYL7 expression was upregulated for the cells cultured on C75E25 by 3.4, 4.7 and 2.7-fold compared to C100, C90E10, and C80E20, respectively, only significant to C80E20. However, C80E20 scaffolds had significantly higher MYL7 expression than other scaffolds when DM was used. MYH6 expression did not change among scaffolds with no DM. But it significantly upregulated in collagen-FEG composite scaffolds compared to C100. Although TNNT2 expressed similarly on 2D and 3D cells, it was significantly reduced by more FEG being substituted in the scaffold when no DM was present.

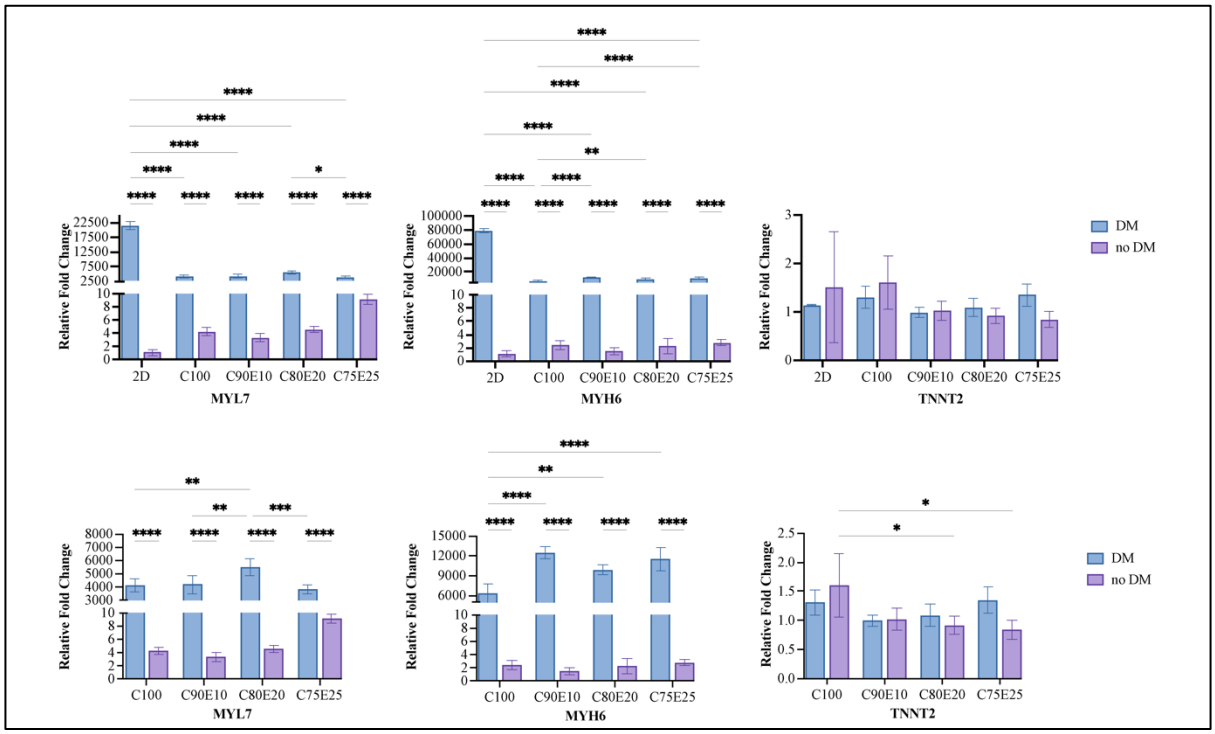


Figure 4.9. Cardiac-related gene expression on iPSCs-cultured scaffolds with and without differentiation media (DM). The figures above include the comparison of 2D and scaffolds, while the ones below demonstrate the gene expression changes between scaffolds. Two-way ANOVA with Tukey's post-hoc was used for comparison. Data represented the Mean±SD and was normalised to monolayer cells (TCPS) cultured in the same condition. *p<0.05, **p<0.01 (N=3).

Cardiac cell differentiation was also studied by ICC using sarcomeric α-actinin and cardiac troponin-T antibodies in confocal microscopy. The images seen in Figure 4.10 represent the cells cultured without DM and fixed after 38 days. As the FEG has autofluorescence, the laser gain of the microscopy was adjusted using negative control, which was stained only by a secondary antibody for each antibody type. The 3D structure also hardened the imaging of actinin structure at higher magnification; therefore, images were taken at 10X to show a general view of expression, if any. In confocal images, cells were observed in all samples, further confirming the successful adhesion of cells throughout the culture period.

The immunofluorescence showed that the cells were mostly mononucleated, suggesting these were immature; unfortunately, the 3-dimensional structure made it difficult to evaluate this situation comprehensively. The cells on C100 scaffolds expressed sarcomeric α-actinin; however, most were clumpy and observed locally (Figure 4.10A). No excitation was obtained on the cells from C90E10 scaffolds, even though the cells were spotted everywhere (Figure 4.10C). The sarcomeric α-actinin expression was seen on C80E20 (Figure 4.10E) and C75E25 (Figure 4.10G) with no clump observation. Regarding cardiac troponin-T protein expression, it was clear that the cells within collagen-FEG composite scaffolds (Figure 4.10D, F&H) exhibited higher expression than those of C100 scaffolds (Figure 4.10B).

The ICC images for cells on scaffold cultured in DM were provided in Figure 4.11. The sarcomeric α-actinin protein expression decreased as more collagen was substituted with FEG. Although abundant cells were detected in the C75E25 specimen, no apparent excitation was observed regarding sarcomeric α-actinin. In contrast, cardiac troponin-T expression increased by more substitution of FEG in the construct at the protein level.

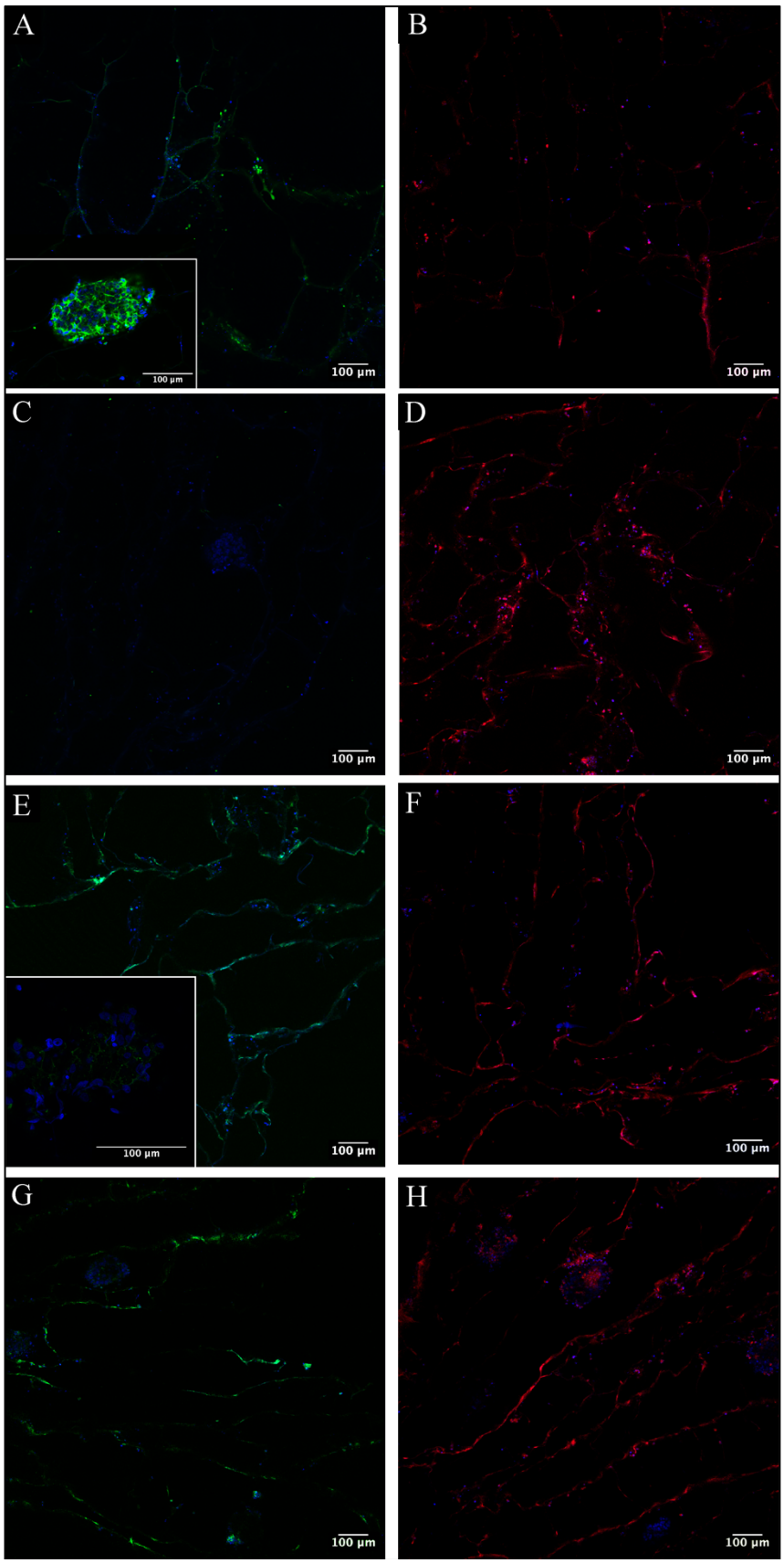


Figure 4.10. Immunocytochemistry of iPSCs-seeded (A-B) C100, (C-D) C90E10, (E-F) C80E20 and (G-H) C75E25 scaffolds showing sarcomeric α-actinin and cardiac troponin-T without DM. Green: sarcomeric α-actinin, red: cardiac troponin-T, and blue: DAPI.

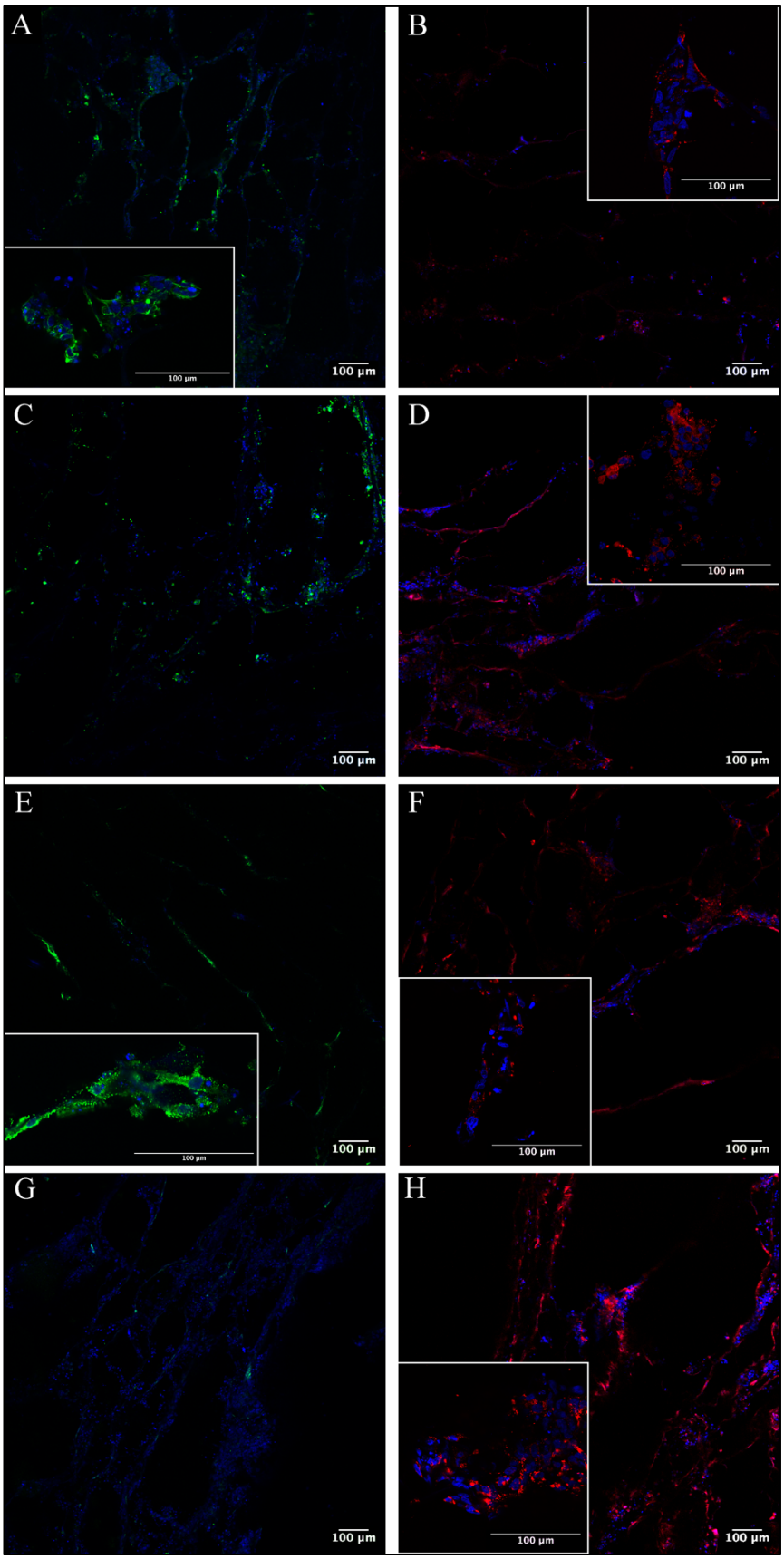


Figure 4.11. Immunocytochemistry of iPSCs-seeded (A-B) C100, (C-D) C90E10, (E-F) C80E20 and (G-H) C75E25 scaffolds showing sarcomeric α-actinin and cardiac troponin-T with DM. Green: sarcomeric α-actinin, red: cardiac troponin-T, and blue: DAPI.

4.3.5. ECM Production

The production of ECM-related proteins by iPSCs on each scaffold was determined by RT-PCR, as seen in Figure 4.12. The genes of interest were: COL1A1 (collagen type I-specific), ELA (elastin-specific) and HAS-2 (hyaluronic acid-specific). COL1A1 expression was significantly upregulated by ~3-fold for C100 when DM was introduced. Surprisingly, a ~4-fold increase in this gene expression was also observed in C75E25 scaffolds with DM. As expected, ELA was upregulated by the presence of FEG in the construct, with almost 6 times higher expression in the cells of C75E25 compared to C100 without DM. However, its expression did not change among scaffolds with DM. HAS-2 significantly upregulated more in C100, C90E10, C80E20, and C75E25 scaffolds by 13, 25, 23 and 16-fold, respectively, when DM was used.

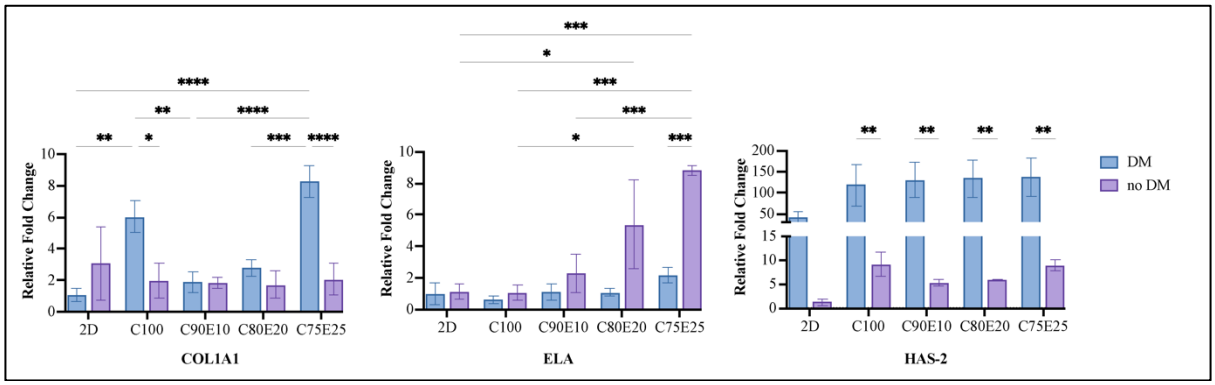


Figure 4.12. ECM-related gene expression on hiPSCs-cultured scaffolds with and without DM. Two-way ANOVA followed by Tukey's post-hoc test was used for comparison. Data represented the Mean±SD and was normalised to monolayer cells (TCPS) cultured without differentiation media. *p<0.05, **p<0.01, ***p<0.001, ****p<0.0001 (N=3).

4.3.6. Mechanical Testing

The change in mechanical properties of cellular scaffolds was assessed by tensile and self-deflection testing (Figure 4.13), and the data are presented in Figure 4.14. As scaffolds comprised HA, the acellular HA-infiltrated scaffolds were used for dual comparison in tensile testing.

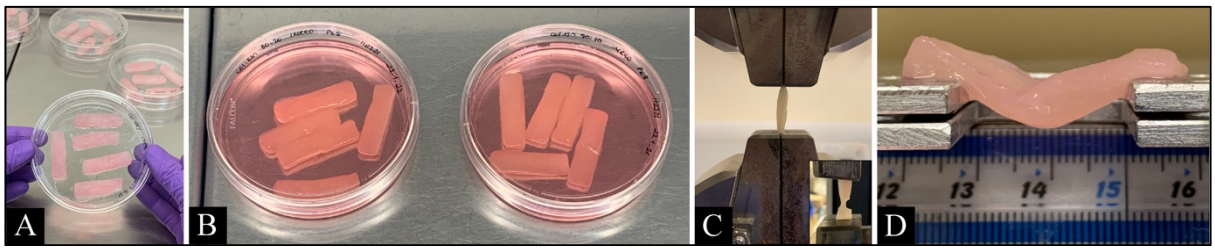


Figure 4.13. The process of mechanical testing on cellular scaffolds. (A) hiPSC seeding and adherence on C100, C90E10, C80E20 and C75E25 HA-infiltrated scaffolds. (B) hiPSC culture and differentiation for 38 days. (C) tensile testing on samples showing failure at the high strain (inset). (D) a sample was left to self-deflect on the system for 2 mins.

The existence of cells in the structure made the scaffolds significantly stiffer than acellular ones for the composites (Figure 4.14A&B). Compared to acellular controls, 1.75, 1.32 and 1.92-fold increase in stiffness was found for C90E10, C80E20 and C75E25 scaffolds, respectively. Strangely, a 1.34-fold decrease in tensile modulus was obtained in the cellular C100 scaffold. Deflection analysis revealed that the bending modulus has significantly reduced as more collagen was replaced with FEG (Figure 4.14C); 25% substitution resulted in almost 3 times less stiff structure when cells were present.

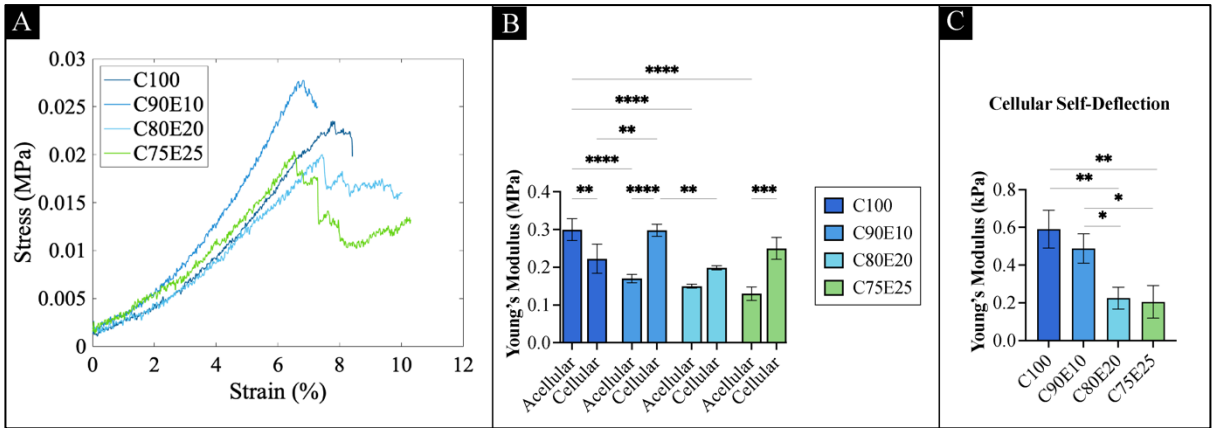


Figure 4.14. Mechanical testing of iPSC-CMs cultured on C100, C90E10, C80E20 and C75E25 HA-infiltrated scaffolds. (A) representative stress-strain curve of cellular scaffolds under tension. (B) E_T comparison between acellular and hiPSC-CMs-seeded scaffolds. (C) self-deflection testing on hiPSC-CMs-seeded scaffolds. Two-way and one-way ANOVA with Tukey's post-hoc was used for (B) and (C), respectively. Data represent the Mean±SD, *p<0.05, **p<0.01, ***p<0.001, ****p<0.0001 (N=3).

Scaffold's strain-to-failure was significantly reduced by 48.5% for C100 cellular scaffolds compared to acellular. This was less significant in collagen-FEG composites with a 41.1-43%

change. Table 4.2 gives the comparative strain-to-failure of cellular scaffolds to acellular HA scaffolds.

Table 4.2. Comparative strain-to-failure of cellular and acellular scaffolds. An unpaired t-test followed by Welch's correction was conducted for dual comparison. Mean±SD (N=5), *p<0.01, **p<0.001.

	Strain-to-Failure (%)		p value
Scaffold Type	**Acellular**	**Cellular**	
C100	17.63±1.19	9.07±0.85	0.0021*
C90E10	20.82±1.02	11.84±1.95	0.0013*
C80E20	21.89±1.23	12.89±1.09	0.0003**
C75E25	24.94±0.79	14.22±1.68	0.0004**

4.3.7. HUVEC Behaviour on Scaffolds

In the second part of the study, the effect of the HA-infiltrated scaffolds to induce neovascularisation was determined using HUVECs. The cell viability within the construct was investigated using alamarBlue™ for a week. A calibration curve (Figure 4.15) was also plotted for this cell type, and the slope was utilised for calculating relative cell numbers.

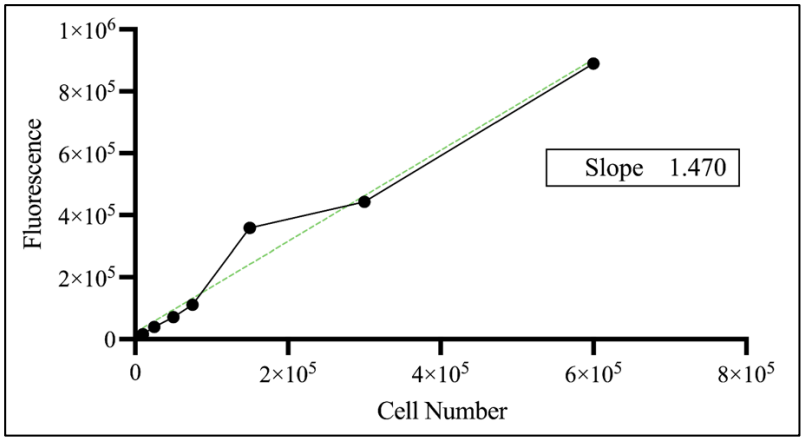


Figure 4.15. The calibration curve from alamarBlue™ assay of HUVECs.

The HUVEC proliferation on TCPS and 3D constructs is presented in Figure 4.16. The results indicated that the cell seeding procedure was successful. The viability was ~100% for 2D culture; however, the cell attachment was ~20% on the 3D scaffolds. A 4-times increased cell viability was seen on TCPS by D4, and cell number remained unchanged on D7 as the cells had already reached confluence. Although the initial cell numbers attached to the scaffold were

similar, the cell growth was significantly different between the constructs. For instance, HUVECs on C100 have adapted to the environment more quickly than any other construct; 3 times more cells were detected on D4, and these further increased on D7. For collagen-FEG composite scaffolds, the cellular adaptation was seen on D7 for C90E10 and C75E25 scaffolds, reaching a double number of living cells. Yet, the number of cells in C80E20 remained around $1x10^5$ throughout the experiment.

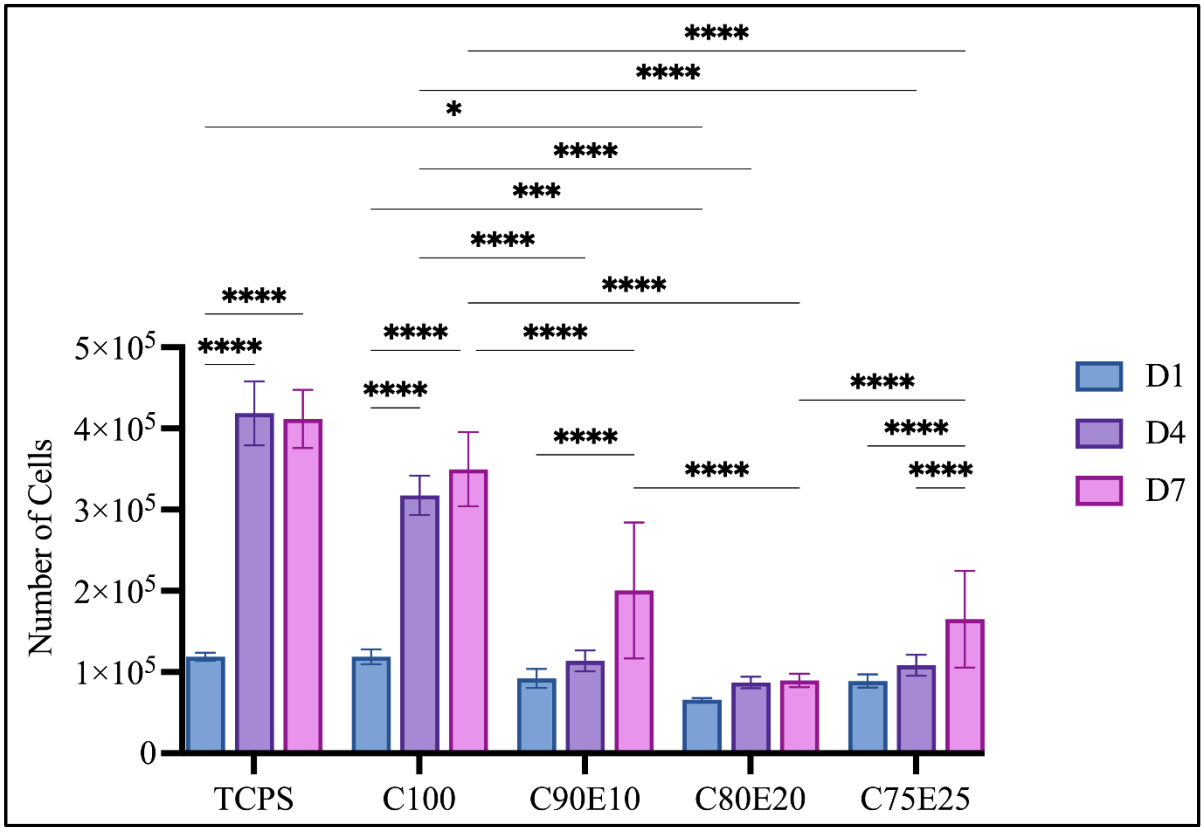


Figure 4.16. AlamarBlue™ cell viability analysis of HUVECs cultured on a monolayer (TCPS), C100, C90E10, C80E20 and C75E25 scaffolds for 1, 4 and 7 days. *p<0.05, **p<0.01, ***p<0.001, ****p<0.0001. Two-way ANOVA with Tukey's post-hoc test was used. Data represented the Mean±SD (N=3).

The effect of IM on cell attachment and proliferation was examined by SEM on D8, as seen in Figure 4.17. The images showed that significantly more cells existed in the scaffolds cultured with IM. A cell sheet was seen on C100 and C75E25 scaffolds cultured in IM, whereas fewer cells could be seen on C90E10 and C80E20 scaffolds. In areas with low numbers of cells, branching cells from one pore wall to another could be seen.

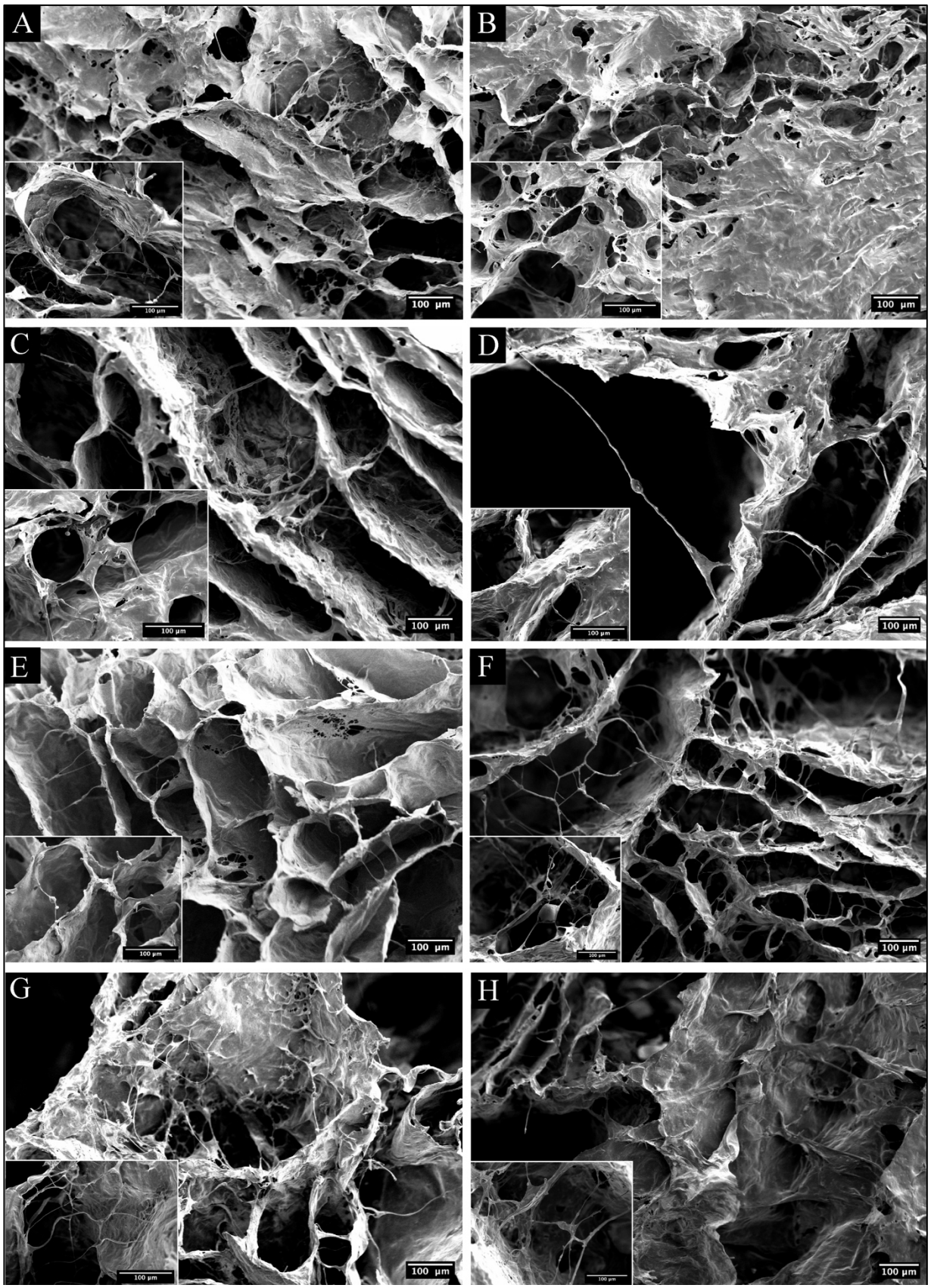


Figure 4.17. SEM images of HUVECs on C100 (A-B), C90E10 (C-D), C80E20 (E-F) and C75E25 (G-H) cultured with (right) and without (left) IM. Mag.:100X with 200X insets. Scale Bar: 100 µm.

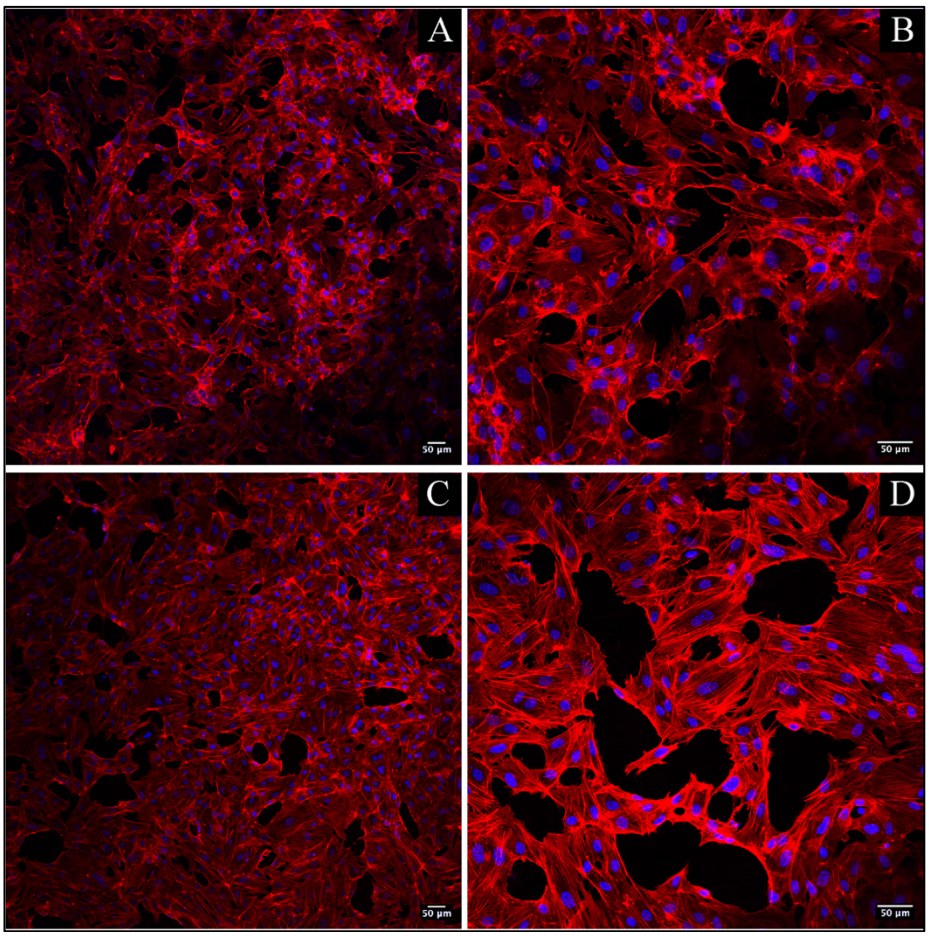


Figure 4.18. Phalloidin-DAPI staining of HUVECs on TCPS cultured with (A-B) and without (C-D) IM. Phalloidin: red, DAPI: blue. 10X (left), 20X (right). Scale Bar: 50 µm.

Actin filaments and nuclei were stained with Phalloidin-DAPI and imaged by confocal microscopy, as shown in Figure 4.18-20. The images from HUVECs on TCPS indicated randomly oriented actin filaments throughout the surface regardless of media. However, it was observed that the cells became enlarged and more elongated in the presence of IM. The staining on scaffolds revealed that the cell distribution was more even on C100 and C75E25 scaffolds regardless of culture medium (Figures 4.19 and 4.20). The cell enlargement could not be assessed in 3D as the structure made it impossible to see all actin filaments of a single cell in one focal plane. Also, as cells in 3D spread by clinging to each other along the pore walls of the scaffold, the ends of the filaments of a single cell were hard to detect. However, Phalloidin-DAPI staining confirmed that the HUVEC attachment and proliferation were feasible on HA-infiltrated scaffolds.

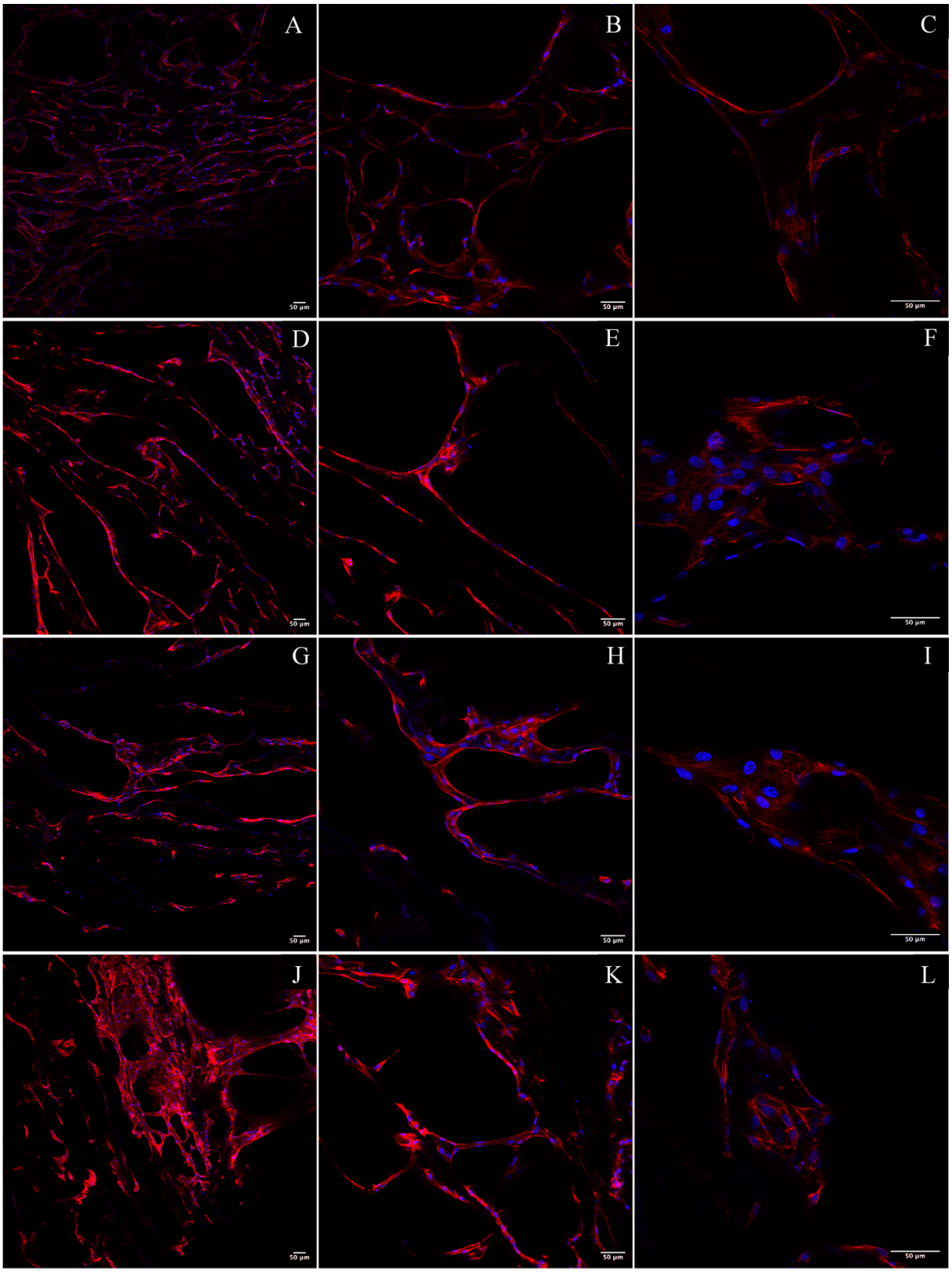


Figure 4.19. Phalloidin DAPI staining of HUVECs on C100 (A-C), C90E10 (D-F), C80E20 (G-I) and C75E25 (J-L) cultured without IM. Phalloidin: red, DAPI: blue. 10X (left), 20X (middle) and 40X (right). Scale Bar: 50 µm.

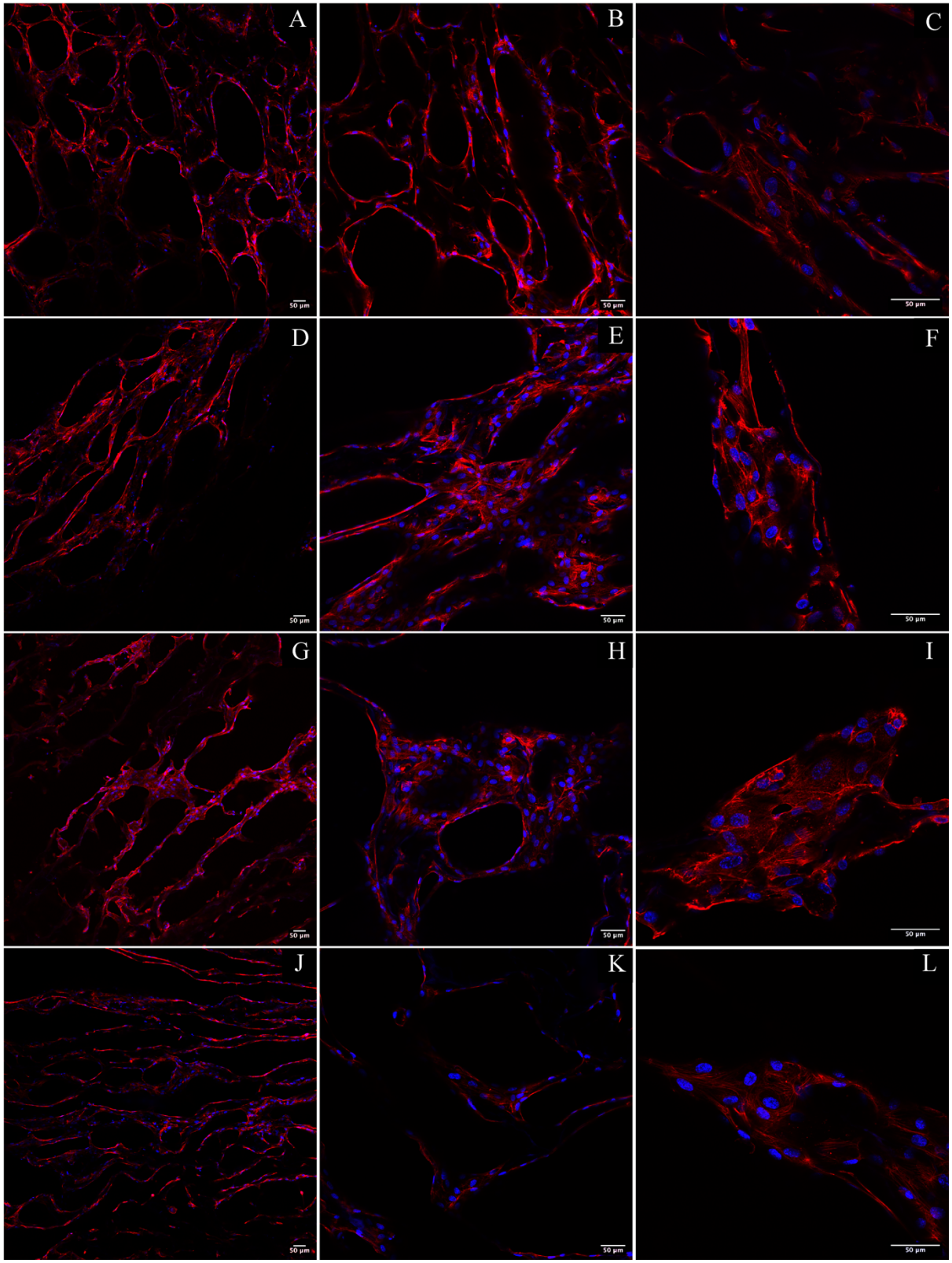


Figure 4.20. Phalloidin DAPI staining of HUVECs on C100 (A-C), C90E10 (D-F), C80E20 (G-I) and C75E25 (J-L) cultured with IM. Phalloidin: red, DAPI: blue. 10X (left), 20X (middle) and 40X (right). Scale Bar: 50 µm.

4.3.8. Gene Expression for HUVEC

Endothelial cell-specific markers were used in RT-PCR to see if any scaffold contribution on these markers has formed. The relative fold change in CD31, CD105, VEGFR2 and ANG2 expression are shown in Figure 4.21 for HUVECs cultured with or without IM. The induction significantly upregulated the CD31 and VEGFR2 expression for those collagen-FEG composite scaffolds by ~2-fold compared with C100. A similar pattern was also found in the genes of interest for HUVECs cultured without IM. No significant difference was observed for CD105 and ANG2 expression for the cells cultured in the IM. However, they significantly upregulated as FEG increased for cells without IM. Particularly, ~3-fold upregulation in the ANG2 gene expression was seen as more collagen was substituted with FEG.

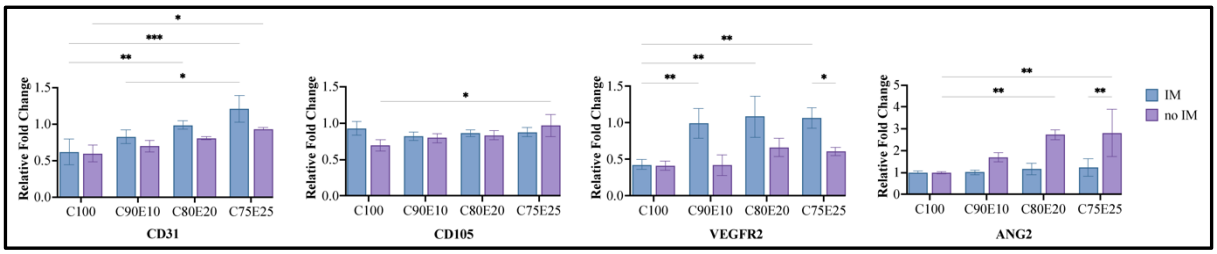


Figure 4.21. Endothelial gene expression on HUVEC-seeded scaffolds (A) with and (B) without IM. Two-way ANOVA with Tukey's post-hoc test was used. Data represented the Mean±SD and was normalised to monolayer cells cultured in the same condition. *p<0.05, **p<0.01, ***p<0.001 (N=3).

4.4. Discussion

4.4.1. hiPSC Viability and Proliferation

Several physical, biochemical, and biomechanical characteristics influence a scaffold's bioactivity and affect the behaviour of adhered cells. In addition, cell confluence affects cell behaviour. In a previous study from our group using porous collagen-FEG composite scaffolds, the hiPSCs were differentiated as a monolayer before being seeded on scaffolds, which resulted in low adherence (12). Here, we aimed to overcome this by seeding undifferentiated hiPSCs on scaffolds and allowing them to proliferate before inducing differentiation. However, optimising the cell seeding density to allow better cellular attachment was challenging. In our

first trial, non-coated scaffolds were utilised and showed poor cell adhesion. Therefore, a supportive coating agent was necessary. Several matrix proteins, including laminin, vitronectin, and fibronectin, can support stem cell growth. The two coating agents tested here were Matrigel and VTN. The alamarBlue assay was used to determine cell adherence in monolayer or on scaffolds with no coating or coated with GFR Matrigel or VTN (Figure 4.5). Analysis of the monolayer indicated that the efficiency of VTN for cell adherence was significantly lower than Matrigel. A previous study found a similar result comparing coating agents for the IMR90 cell line (13), and the VTN efficacy was shown in other iPSCs and embryonic stem cells (14, 15). This could be tolerable, as more than 80% of cells seemed to be adherent successfully using VTN. It was also evident that the Matrigel coating resulted in more efficient adhesion on scaffolds but at a significantly lower level than in the monolayer. This could be due to the porous structure causing the cells to flow out before attaching properly. However, although Matrigel is frequently used in monolayer culture, there were concerns with using Matrigel here as it contains growth factors which may conflict with the direct effect of the scaffold composition. Because feeder-free VTN is a polypeptide with Arg-Gly-Asp (RGD) sites (16) for cellular attachment, this study used it as the best option for effective coating.

The second part of optimisation covered the efficient cell seeding number. All experiments were initiated with 500.000 cells/well/scaffold; however, the number of cells attached was nearly half that seen with Matrigel. The cell seeding density was doubled, which resulted in a better cell attachment by more than 2-fold for the scaffolds. Therefore, the optimum cell seeding density was determined as $1x10^6$ cells/scaffold throughout the study.

Porosity, pore size, pore interconnectivity, and the presence of cell binding sites are some of the key physical features of a scaffold. While integrins like $\alpha_1\beta_1$ and $\alpha_2\beta_1$ mediate cellular attachment through collagen's RGD peptides (17), elastin possesses elastin-binding protein (EBP) complexes that serve as cell receptors (18). The results of the cell attachment

experiments showed that the combination of binding sites in the collagen-FEG composite scaffolds resulted in improved cellular adhesion.

Looking at the fold change in cell numbers, the proliferation rate seemed to slow down in all scaffolds, implying that the cells were getting confluent. SEM images from D21 showed that a cell sheet covered areas of the scaffold surface, especially on the C100 and C75E25 scaffolds. According to absorbance from the alamarBlue assay, the cell number after 3 weeks was around $2x10^5$ cells/scaffold. However, it is likely that the cell number was higher as it was difficult to ensure the full collection of the alamarBlue reagent from the well without disturbing the cells on the scaffold. The bright pink colour seemed to be brighter within the scaffold, suggesting that during the assay, more than $3x10^5$ cells may be present even after 14 days (Figure 4.22, red arrow). Therefore, the assay should not be viewed as a direct indicator of cell number but rather as an approximation that shows the growth trend within each scaffold.

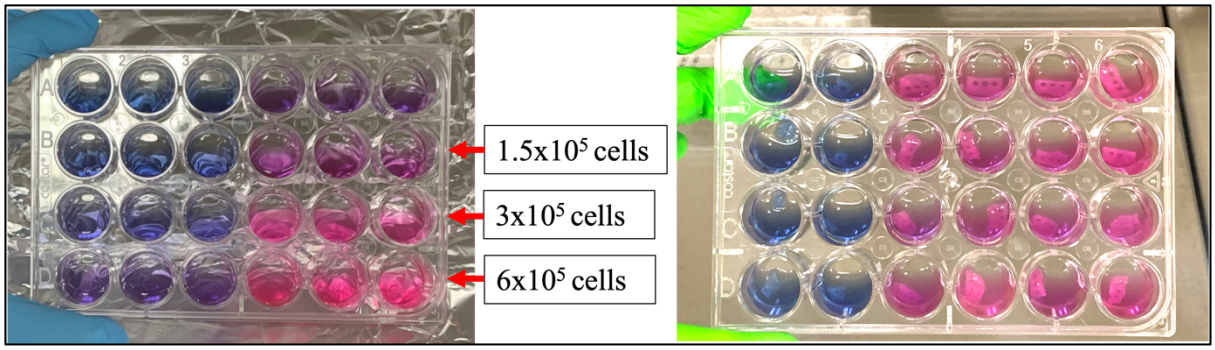


Figure 4.22. Cell number validation by colour change. The image on the left shows the change in colour based on the number of cells seeded on a monolayer. The right image shows the colour change on scaffolds after 14 days of culture (Blue: acellular control, Pink: Cellular sample). The black arrows on the right indicate that the scaffolds turned pink.

One of the aims of this study was to create a platform for cardiac differentiation without requiring any small molecule stimuli or genetic alteration, thereby lowering total cost. We altered the monolayer-based, small molecule strategy outlined elsewhere (9) to culture in 3D without small molecules. For long-term culture of hiPSCs, we switched from mTeSR1 medium to the less complex TeSR-E8 formulation and from Matrigel to the less expensive and more defined extracellular matrix, VTN. Moreover, we supported cell expansion by providing a

larger space in the 3D multicomponent scaffolds. In general, a time-dependent growth curve was seen in all scaffold types, supported by collagen and FEG. Considering the SEM results, it was decided that the 21-day culture period was ideal for initiating differentiation studies.

4.4.2. Change in Pluripotency

The maintenance of pluripotency in culture is highly controlled by the function of the gene regulatory network (GRN) that involves three core transcription factors: SOX2, OCT4 and NANOG. They are believed to be at the centre of a GRN that develops and sustains the pluripotent state, although other transcription factors are involved. This study used OCT4 and NANOG from this trio as the most extensively studied genes to assess the change in the pluripotency of hiPSC upon long-term culture.

iPSCs are generated by the over-expression of key transcription factors, including OCT4, SOX2 and NANOG. OCT4 is a homeobox-containing factor, whereas SOX2 is a high-mobility group protein that regulates DNA-dependent processes such as transcription, replication, and recombination (19). These two genes are critical factors for maintaining self-renewal (20). NANOG is expressed in the early embryo and is a master regulator of cell self-renewal. In the genome, OCT4 and SOX2 interact to regulate their own transcription as well as that of NANOG. The OCT4 is more critical for a cell's fate because, while low levels of OCT4 cause differentiation into trophectoderm and loss of pluripotency, high levels induce differentiation into primitive endoderm-like cells. In general, OCT4 positively regulates NANOG expression: if OCT4 expression reduces, so does NANOG. Surprisingly, we saw in the IMR90 cell line that OCT4 was downregulated over time, but NANOG expression was unchanged, whereas in the M180 cell line, there was no change in OCT4 expression, but we saw downregulation of NANOG over time. It is known that retention of epigenetic markers can affect the expression of OCT4 and NANOG and routes of differentiation (21). The IMR90 line was derived from foetal lung fibroblasts, whereas the M180 line was derived from adult myoblasts, which may

account for the difference in the behaviour of the pluripotency genes. In the M180 cells, NANOG expression increased in collagen-FEG composites at 7 days compared with the C100 composites, although this difference was lost after 21 days.

Nevertheless, the relatively small changes in gene expression seen suggest that the cells remained largely pluripotent over three weeks of culture on the scaffolds.

4.4.3. Cardiac Differentiation

Cardiac differentiation was evaluated for the cells cultured with or without DM by RT-PCR and ICC. The expression of MYL7, MYH6 and TNNT2 was measured to assess the onset of cardiac differentiation. MYL7 gene induces myosin light chain (MLC) expression in early-stage CMs, which switches to MYL2 as CMs mature (22). MYH6 encodes α-myosin-heavy chain (α-MHC) in the developing human ventricle and in the adult atrium. TNNT2 encodes the protein called cardiac muscle troponin T, found solely in the cardiac muscle. During CM maturation, changes in the expression of these genes have been shown to be time-dependent and can be used to assess the stage of cardiac differentiation (22). Expression of MYL7 and MYH6 was significantly higher when cells were cultured with DM, as expected, but cells on scaffolds did not differentiate to the same extent as those in a monolayer. Nevertheless, when cells were cultured without DM, there was an increase in expression of MYL7 over that seen in undifferentiated cells in a monolayer, and this increase was highest in cells on C75E25 scaffolds. It may also be that culture on the more elastic scaffolds promoted differentiation, as there was a small decrease in NANOG expression in the IMR90 cells on the C7E25 scaffold over 21 days. When DM was introduced, a more significant fold change was observed in all scaffolds, and the cells from C80E20 exhibited significantly higher MYL7 expression than C75E25 scaffolds. An increase in MYH6 expression was also seen in cells on the composite scaffolds, compared to C100, although there was no difference in expression between the

composites. Therefore, the 3D culture method could be a better representative of understanding the spatial cell-cell interactions on cellular fate and elucidating molecular mechanisms.

We aimed to assess cardiomyocyte differentiation using ICC; however, the 3D structure obscured the visualisation of cell structure and was confounded by non-specific binding to the scaffold material. In this case, the degree of maturation could only be assessed by RT-PCR. The present study was limited to a single time point to evaluate the change in gene expression. Early studies concluded that a degree of maturation could be achieved through a prolonged culture (23, 24), and the scaffold would prompt maturation (23). However, this study focuses on showing the contribution of the scaffold's content on CM differentiation, not the maturation, which would require a long-term culture of more than 38 days. Successful proliferation and differentiation, the main objective of this study, were achieved, but the development of cheaper cell culture media and components will undoubtedly increase the use of the culture method we established.

4.4.4. ECM Production

The ability of ECM molecules to interact and bind with each other is crucial for the function and integrity of the matrix. After myocardial infarction (MI), as well as the formation of new CMs to restore the infarcted region, but scar tissue also needs to be remodelled. The cardiac ECM comprises organised fibrous protein structures, mainly collagen and elastin, and other membrane proteins (25). It maintains the alignment of the CMs and assists in conducting electrical activity over the heart, forming a supportive network, and translating single CM contractility into a ventricular syncytium. Transmembrane integrins link the cardiac ECM to the contractile cytoskeleton of the CMs and provide the structural and mechanical linkage between the two (26). Therefore, determining the scaffold effect on the production of such ECM proteins for remodelling is crucial. Here, the study analysed the contribution of scaffolds to ECM synthesis by the CMs using RT-PCR. It is believed that the scaffold's chemical

structure and content would contribute more to the new ECM formation (27). As the scaffolds were composed of collagen type I, elastin and HA, the genes producing these were of interest: COL1A1, ELA, and HAS-2. In cells without DM, ELA expression increased with FEG content in the scaffolds, but this difference was not seen in the DM-cultured cells. COL1A1 expression decreased with differentiation in monolayer cells but increased in cells on C100 and C75E25. In contrast, HA production became more significant after DM. HAS-2 was upregulated in monolayer cells and to a greater extent (albeit not significantly) in cells on all scaffolds. In natural ECM, GAGs like HA can be found both alone and coupled to core proteins to form proteoglycans (28). Thus, GAGs can enhance and have an impact on protein functionality. As mechanical analysis also showed a positive correlation between FEG and HA (Chapter 3), it is thought their mutual companionship may support the new ECM synthesis more than C100-HA scaffolds. In cardiac ECM, elastin oversees recoil and prevents the myocardium from progressive dilation (29). The precise role of elastin in mechanical behaviour is uncertain, yet elasticity is reduced during MI, contributing to the thinning and growth of the infarcted area. For this reason, it has been hypothesised that higher elastin content may aid in MI recovery. This study also concludes that FEG is an essential component of the scaffold design, and its contribution is even more evident when collagen and HA are present.

4.4.5. Mechanical Properties

As previously discussed, a scaffold's physicochemical structure and stiffness can determine cell fate. But also, the presence of cells producing ECM can reshape the mechanical properties of the scaffold (30). Here, cellular tensile testing aimed to understand the role of cells and ECM in the scaffold’s mechanics.

As expected, the presence of the cells increased the stiffness of the scaffolds in collagen-FEG composites. What was unexpected was that this was not the case in collagen scaffolds. We believed this resulted from faster interaction-related (media-scaffold or cell-scaffold)

degradation in C100 compared to composites, as FEG prevented the interaction with surroundings and preserved structural integrity. This was also supported by early enzymatic degradation characteristics of C100 scaffolds (Section 3.3.5.2) as well as improved strain-to-failure, although this was significantly lower than in the acellular scaffolds (Table 4.2).

Unfortunately, cardiomyocyte contraction could not be seen in the scaffolds after differentiation. This could be either due to low cell-to-cell interactions resulting from high porosity or the scaffolds being too rigid to allow cell contraction. The cytoskeleton organisation of a CM is highly controlled by substrate stiffness, and optimum stiffness can determine the myocyte contractility (Section 1.5) (31). A construct with Young's modulus of ~10 kPa can promote contraction in most cells adhered to it. Considering the designed scaffolds had an E_T in the MPa scale, they may not be compatible with cardiac contractility. However, when bending properties were tested by self-deflection in the presence of cells, the scaffold's stiffness (lower than that of acellular scaffolds) decreased as FEG content increased in the construct, suggesting that FEG can be a better regulator of contractility once cells are mature. Bending stiffness was considerably lower than tensile stiffness; however, the characterisation of cell response to the substrate stiffness may not be simple as elastic moduli of the material measured under shear or uniaxial deformation because cells exert both tangential and vertical stresses at their attached site to the material. These suggest that the contraction of the scaffold is tied to its distinct mechanical properties, size and accompanying biological response.

4.4.6. Support for Endothelisation

HUVECs have been extensively used to characterise scaffolds' impact on neovascularisation. These cells need to anchor to ECM for migration as cell migration promotes sprouting from the existing vascular network. Several interstitial and provisional ECM elements, seen during sprouting angiogenesis, including collagen type I and fibrin, can facilitate chemotactic migration (32). 3D interstitial collagen type I induces ECs to undergo noticeable shape changes

that closely resemble the creation of precapillary cords seen during adult angiogenesis. The cells partially retract and display a spindle-shaped morphology within hours of adding collagen type I to confluent EC cultures. At the same time, the cells realign to form solid cords arranged in a polygonal pattern, as seen in Figure 4.23. One can notice that this appearance resembles the morphology of these cells on the porous scaffolds (Figures 4.19 and 4.20). SEM also showed cells branching from pore to pore, suggesting that sprouting had occurred and that the porosity of the scaffold would also support vasculature.

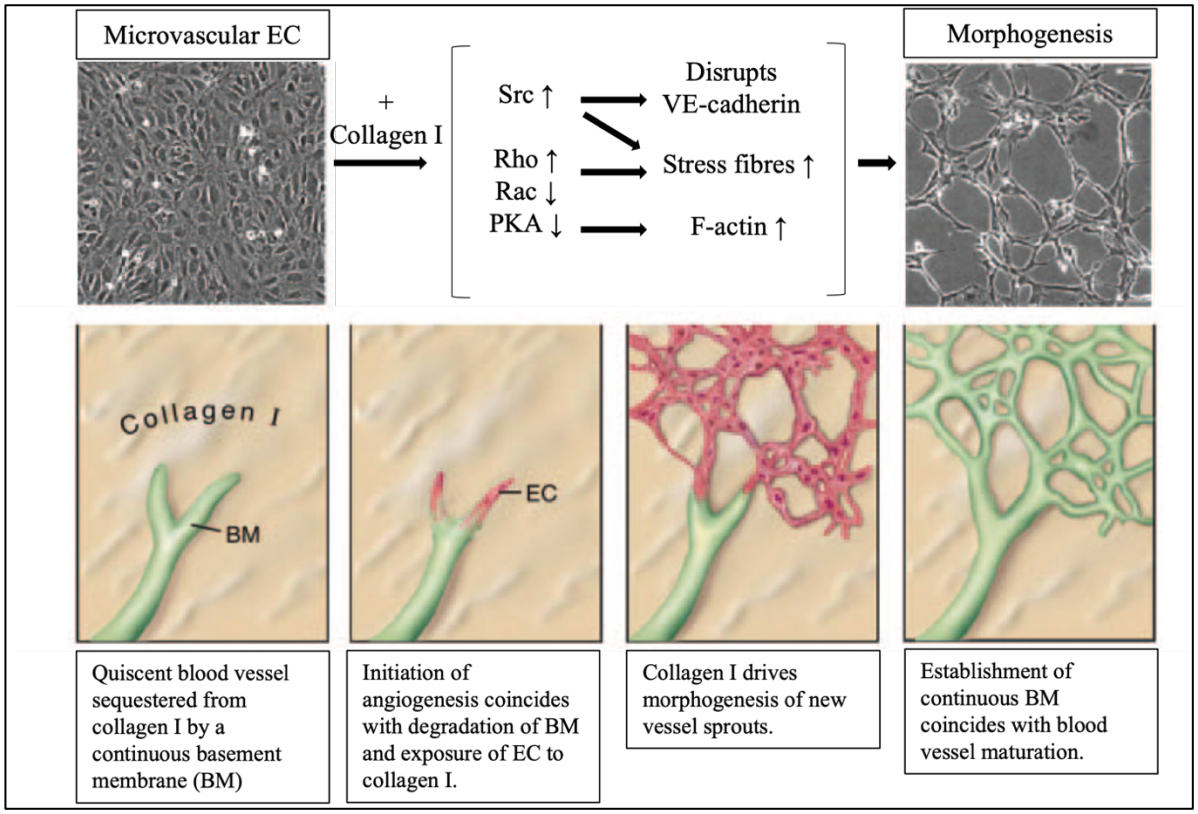


Figure 4.23. Collagen type I signalling in ECs forming capillary morphogenesis *in vitro*. Through integrins, collagen type I activates Src and Rho and suppresses Rac and protein kinase A (PKA). Actin stress fibres are induced, VE-cadherin is broken down, and precapillary cords are created (top). Basement membrane breakdown and the exposure of activated and proliferating ECs to collagen type I trigger the morphogenesis of new capillary sprouts (bottom). Adapted from (32).

EC viability has been reportedly supported by both collagen type I and VTN by their distinct integrins ($\alpha_1\beta_1$ and $\alpha_2\beta_1$ for collagen type I; $\alpha_v\beta_3$ and $\alpha_v\beta_5$ for VTN) (33). The same study also found that VTN significantly improved viability on 3D collagen type I gel and coating with

mixtures of collagen type I and VTN were most successful at promoting viability. In the current study, the scaffolds were also coated with VTN to encourage cell adherence and proliferation. During sprouting, ECs in already-existing blood vessels break through the basement membrane and go into the connective tissue rich in interstitial collagens, where they can multiply. Therefore, the higher proliferation rate of those cultured on C100 scaffolds compared to composites could be due to more collagen type I present in these constructs.

SEM and phalloidin-DAPI staining examined HUVEC attachment and proliferation. Phalloidin binds to F-actinin to stabilise by preventing actin fibres' depolymerisation. Its specificity to actin fibres makes it a great candidate to visualise cell behaviour under a microscope. On the other hand, SEM will provide more information about the interaction between scaffold and cells. Here, we visualised the cells' actin fibres in 2D and 3D. In 2D, cells were randomly distributed and interacted with each other. The cells enlarged after induction, possibly due to more ECM production. However, even after the direct induction, there was no capillary-like morphogenesis. This could result from the absence of a proper surface (here, it is a glass cover), such as collagen. In addition, the number of cells has been found to be a critical parameter to achieve vasculature; fewer cells form a better capillary-like structure. When the HUVECs adhered to the scaffolds, the cells seemed less confluent and bonded to one another. SEM also showed that cell adherence occurred within the larger pores, suggesting that the 3D structure was favourable for these cells. It is believed that this could contribute more to capillary-like morphogenesis in the way the cells are known to behave on collagen-coated surfaces (Figure 4.23). The presence of collagen type I in scaffold design could also hasten the process.

One of the main goals of this study was to understand the effect of scaffolds on promoting vascularisation. Therefore, we analysed several angiogenic and endothelial markers using RT-PCR. CD31 and CD105 would indicate endothelial growth, whereas VEGFR2 and ANG2

would show angiogenesis. VEGFR2 expression increased with induction in cells on all scaffolds except C100, suggesting that FEG may encourage angiogenesis. This may have been promoted as IM containing VEGF and FBS was chosen, with the hope that this would support angiogenesis. Few other changes were seen with induction, apart from a significant decrease in ANG2 expression in cells on the C75E25 scaffold. A gradual increase in CD31 expression with FEG content was seen regardless of media content. CD105 expression was not affected by induction or scaffold composition, apart from a small increase in cells without IM on C75E25 scaffolds compared to those on C100 scaffolds.

Overall, these findings showed that the combination of collagen with FEG may enhance its compatibility with angiogenesis.

4.5. Summary

This chapter aimed to characterise iPSCs viability, differentiation into CMs, HUVECs proliferation, and neo-endothelisation on HA-infiltrated collagen and collagen-FEG composite scaffolds. The main findings include the following:

- Our scaffold design is feasible to use in hiPSC maintenance and growth for the long term. The scaffold design can influence the state of pluripotency, yet this seemed to be cell-type-dependent.
- Successful cardiac differentiation on scaffolds has been established, and native ECM production was supported by scaffold content. The combination with advanced CM maturation techniques would expand its use in cardiac tissue engineering.
- Mechanical studies showed the rigidity of scaffolds over native cardiac tissue. The FEG significantly reduced the substrate stiffness to which the cells respond, suggesting that it can also mediate contractility when cells are mature.

- The collagen-FEG composite scaffold is a suitable alternative to promote cell adhesion and endothelisation. The porous structure and content of the scaffolds were found to be more encouraging in supporting angiogenesis.

References

1. Yu J, Vodyanik MA, Smuga-Otto K, Antosiewicz-Bourget J, Frane JL, Tian S, et al. Induced pluripotent stem cell lines derived from human somatic cells. science. 2007;318(5858):1917-20.

2. Braam SR, Zeinstra L, Litjens S, Ward-van Oostwaard D, van den Brink S, van Laake L, et al. Recombinant vitronectin is a functionally defined substrate that supports human embryonic stem cell self-renewal via alphavbeta5 integrin. Stem Cells. 2008;26(9):2257-65.

3. Rampersad SN. Multiple applications of Alamar Blue as an indicator of metabolic function and cellular health in cell viability bioassays. Sensors (Basel). 2012;12(9):12347-60.

4. Sousa Fialho MdL, Purnama U, Dennis KM, Montes Aparicio CN, Castro-Guarda M, Massourides E, et al. Activation of HIF1α rescues the hypoxic response and reverses metabolic dysfunction in the diabetic heart. Diabetes. 2021;70(11):2518-31.

5. Hayat M. Glutaraldehyde: role in electron microscopy. Micron and Microscopica Acta. 1986;17(2):115-35.

6. Cooper JA. Effects of cytochalasin and phalloidin on actin. The Journal of Cell Biology. 1987;105:1473 - 8.

7. Kapuscinski J. DAPI: a DNA-specific fluorescent probe. Biotech Histochem. 1995;70(5):220-33.

8. Lian X, Hsiao C, Wilson G, Zhu K, Hazeltine LB, Azarin SM, et al. Robust cardiomyocyte differentiation from human pluripotent stem cells via temporal modulation of canonical Wnt signaling. Proc Natl Acad Sci U S A. 2012;109(27):E1848-57.

9. Lian X, Zhang J, Azarin SM, Zhu K, Hazeltine LB, Bao X, et al. Directed cardiomyocyte differentiation from human pluripotent stem cells by modulating Wnt/β-catenin signaling under fully defined conditions. Nature Protocols. 2013;8(1):162-75.

10. Burridge PW, Holmström A, Wu JC. Chemically Defined Culture and Cardiomyocyte Differentiation of Human Pluripotent Stem Cells. Curr Protoc Hum Genet. 2015;87:21.3.1-.3.15.

11. Burridge PW, Matsa E, Shukla P, Lin ZC, Churko JM, Ebert AD, et al. Chemically defined generation of human cardiomyocytes. Nature Methods. 2014;11(8):855-60.

12. Iftekhar S. Isolation of Fibrillar Elastin Gel (FEG) and its application in heart valve tissue engineering: University of Oxford; 2020.

13. Rowland TJ, Miller LM, Blaschke AJ, Doss EL, Bonham AJ, Hikita ST, et al. Roles of integrins in human induced pluripotent stem cell growth on Matrigel and vitronectin. Stem cells and development. 2010;19(8):1231-40.

14. Chen G, Gulbranson DR, Hou Z, Bolin JM, Ruotti V, Probasco MD, et al. Chemically defined conditions for human iPSC derivation and culture. Nature methods. 2011;8(5):424-9.

15. Prowse AB, Doran MR, Cooper-White JJ, Chong F, Munro TP, Fitzpatrick J, et al. Long term culture of human embryonic stem cells on recombinant vitronectin in ascorbate free media. Biomaterials. 2010;31(32):8281-8.

16. Su Y-C, Riesbeck K. Vitronectin. The Complement FactsBook: Elsevier; 2018. p. 351-60.

17. Terzi A, Storelli E, Bettini S, Sibillano T, Altamura D, Salvatore L, et al. Effects of processing on structural, mechanical and biological properties of collagen-based substrates for regenerative medicine. Sci Rep. 2018;8(1):1429.

18. Robert L. Cell-elastin interaction and signaling. Pathol Biol (Paris). 2005;53(7):399-404.

19. Kalmar T, Lim C, Hayward P, Munoz-Descalzo S, Nichols J, Garcia-Ojalvo J, et al. Regulated fluctuations in nanog expression mediate cell fate decisions in embryonic stem cells. PLoS biology. 2009;7(7):e1000149.

20. Kashyap V, Rezende NC, Scotland KB, Shaffer SM, Persson JL, Gudas LJ, et al. Regulation of stem cell pluripotency and differentiation involves a mutual regulatory circuit of the NANOG, OCT4, and SOX2 pluripotency transcription factors with polycomb repressive complexes and stem cell microRNAs. Stem Cells Dev. 2009;18(7):1093-108.

21. Kim K, Doi A, Wen B, Ng K, Zhao R, Cahan P, et al. Epigenetic memory in induced pluripotent stem cells. Nature. 2010;467(7313):285-90.

22. Guo Y, Pu WT. Cardiomyocyte maturation: new phase in development. Circulation research. 2020;126(8):1086-106.

23. Lopez C. Metabolic maturation of induced pluripotent stem cell-derived cardiomyocytes: University of Oxford; 2018.

24. Lundy SD, Zhu W-Z, Regnier M, Laflamme MA. Structural and functional maturation of cardiomyocytes derived from human pluripotent stem cells. Stem cells and development. 2013;22(14):1991-2002.

25. Bax NA, van Marion MH, Shah B, Goumans M-J, Bouten CV, van der Schaft DW. Matrix production and remodeling capacity of cardiomyocyte progenitor cells during in vitro differentiation. Journal of molecular and cellular cardiology. 2012;53(4):497-508.

26. Ross RS, Borg TK. Integrins and the myocardium. Circulation research. 2001;88(11):1112-9.

27. Brown BN, Badylak SF. Extracellular matrix as an inductive scaffold for functional tissue reconstruction. Translational Research. 2014;163(4):268-85.

28. Rienks M, Papageorgiou A-P, Frangogiannis NG, Heymans S. Myocardial extracellular matrix: an ever-changing and diverse entity. Circulation research. 2014;114(5):872-88.

29. Mizuno T, Yau TM, Weisel RD, Kiani CG, Li RK. Elastin stabilizes an infarct and preserves ventricular function. Circulation. 2005;112(9 Suppl):I81-8.

30. Frantz C, Stewart KM, Weaver VM. The extracellular matrix at a glance. J Cell Sci. 2010;123(Pt 24):4195-200.

31. Discher DE, Janmey P, Wang Y-l. Tissue cells feel and respond to the stiffness of their substrate. Science. 2005;310(5751):1139-43.

32. Davis GE, Senger DR. Endothelial extracellular matrix: biosynthesis, remodeling, and functions during vascular morphogenesis and neovessel stabilization. Circulation research. 2005;97(11):1093-107.

33. Perruzzi CA, de Fougerolles AR, Koteliansky VE, Whelan MC, Westlin WF, Senger DR. Functional overlap and cooperativity among alphav and beta1 integrin subfamilies during skin angiogenesis. J Invest Dermatol. 2003;120(6):1100-9.



SCAFFOLD IMPLANTATION

5. SCAFFOLD IMPLANTATION

5.1. Introduction

This chapter will address the implantation of C100 and C75E25 scaffolds *in vivo* to evaluate biocompatibility with native tissue. Miniature acellular scaffolds were implanted into rats subcutaneously. After one or two weeks they were removed to determine scaffold adherence, host cell migration, tissue formation, and angiogenesis using histology. Imaging was performed under the light microscope, and images were assessed to characterise inflammation, new ECM deposition and vascularisation.

5.2. Materials and Methods

5.2.1. Scaffold Preparation and Sterilisation

Non-crosslinked, crosslinked, and HA-infiltrated C100 and C75E25 scaffolds were used for *in vivo* implantation as they gave the best results in mechanical studies, the support of cell adherence, new ECM formation and differentiation. Rectangular scaffolds were resized as described in Table 3.1, placed in 50 mL falcon tubes, and sterilised in absolute EtOH at +4°C for 24 hrs by two washes lasting 6 hrs and one wash for 12 hrs consequentially, ensuring the EtOH was refreshed. They were then rinsed with DPBS twice and transferred into DPBS containing 1X penicillin-streptomycin containers to store at +4°C for 24 hrs. Sterile scaffolds were transferred to a 24-well plate with DPBS having 1X penicillin-streptomycin for easy handling during surgery.

5.2.2. Animals and Surgery

Animal work was carried out under Protocol 5 of the Home Office Project Licence number PP9434487, approved by the University of Oxford ethical review process. All experimental procedures were carried out by Prof Carolyn Carr (Personal licence number ID0AB9EDC). Wild-type Sprague-Dawley male rats (6-8 weeks old) weighing 250-300 g (N=12 rats for each group) were purchased from Charles River Labs UK. All animals were kept at stable room

temperature (±22°C) and humidity (~52%). They were fed a standard chow diet under a controlled 12-hour light/dark cycle. The rats were anaesthetised by inhaling 2% Isoflurane (Halocarbon Life Sciences, USA) in oxygen. The rat back hairs were shaved with the underlying skin cleaned and sterilised with 1% disinfectant spray (Anistel, UK) and pre-injection swabs containing 70% alcohol (Medisave, UK). Animals were then placed on a heated plate, and the paws were placed on electrodes to monitor the ECG (MouseMonitor, Indus Instruments UK). The animals were treated with 0.2 µL/g MetaCam (Boehringer Ingelheim, Germany), depending on animal weight, by subcutaneous injection at the start of the surgery. All surgical procedures were performed using aseptic techniques. To implant the scaffolds, a transverse incision of ~2 cm was cut on the dorsal section of each rat using a sterile surgical blade. Connective tissue was dissected to create a subcutaneous pocket on the left and right. According to the respective groups described in Figure 5.1, two acellular scaffolds were separately placed into the two pockets without suturing. The incisions were then sutured using either Ethicon 5-0 vicryl with a 16 mm compound curve reverse cutting needle (45 cm) (Johnsons & Johnsons Surgical Technologies, Belgium). Each rat was held in a recovery cage until it recovered and then returned to its cage mates in a cage supplied with jelly containing MetaCam and mash. All animals were then carefully monitored and weighed for the following three days by Prof Carr and Mrs Mala Gunadasa-Rohling.

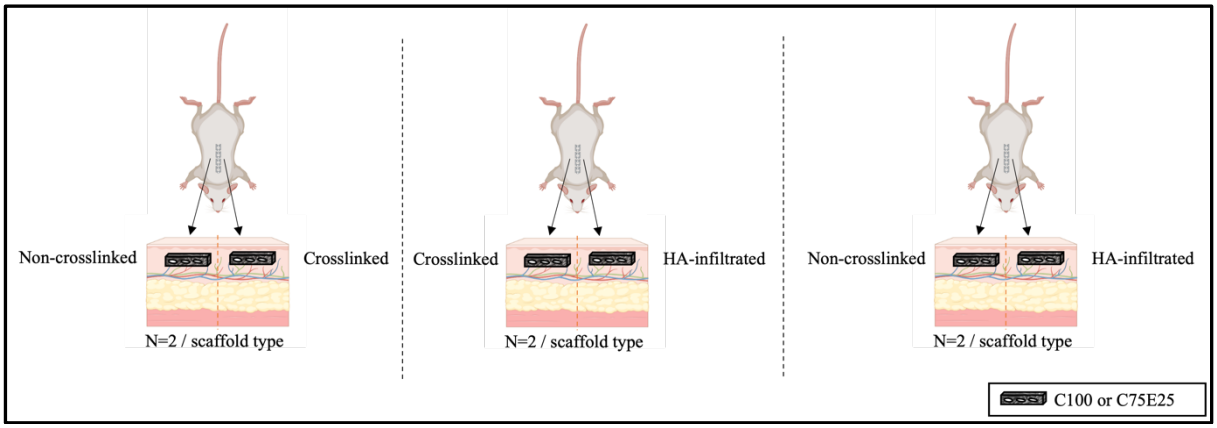


Figure 5.1. The study design of scaffold implantation. The rats were classified into three groups with different conditions of C100 and C75E25 scaffolds; 2 rats for each replicate produced 12 specimens per week (N=4).

5.2.3. Animal Care and Tissue Fixation

Rats were sacrificed at the end of each time point (1- or 2-week), and the skin part where the scaffolds were implanted was harvested together with the surrounding tissue and scaffold. The tissue samples were then transferred into 10% formalin (Sigma Aldrich, UK) to fix for 6 hrs at room temperature. The fixed tissues were immersed in 30% sucrose solution (Sigma Aldrich, UK) prepared in PBS (pH: 7.4) and stored at +4°C overnight.

5.2.4. Paraffin Embedding and Sectioning

The Mommersteeg Group in DPAG supplied all paraffin embedding and sectioning facilities. The fixed samples were transferred to 10 mL glass vials, rinsed with PBS, and then dehydrated by EtOH series (70, 80, 90, 96, 100, 100%) for 1 hr each at room temperature on a shaker. The dehydrated samples were transferred into Butanol-1 (Sigma Aldrich, UK) containers and left for shaking overnight at +4°C. The solution was changed to paraffin (Sigma Aldrich, UK) and incubated in Hybaid Shake 'n' Stack oven (Thermo Fisher Scientific, UK) at 65°C for 1.5 hrs by refreshing thrice. The samples were stored in paraffin solution for another 24 hrs at 65°C and embedded in paraffin-containing cassettes for 24 hrs. The specimens were ready to be sectioned the next day.

The paraffin blocks were sectioned by Epredia™ HM 325 rotary microtome (Fisher Scientific, UK) using MX35 ultra microtome blades (Thermo Scientific, UK). A series of sections was taken as 10 µm on positively charged slides (VWR, UK). Distilled water was added by pipetting to smoothen and sucked by a vacuum pump before mounting the sections on a slide drying bench (Electrothermal, Keison Products, UK) at 37°C for 2-3 mins. The slides were then left in a 37°C oven for overnight drying. Dry sections were ready for staining the next day.

5.2.5. Histology Staining

Haematoxylin and Eosin (H&E), Elastica van Gieson (EVG) and Alcian Blue (AB) staining protocols were performed in the Department of Materials. The slides were placed in glass jars containing Xylene (VWR, UK) for 15 mins, and the solution was refreshed for 10 mins. The hydration and H&E staining were performed as mentioned in Section 2.2.3.1. EVG and AB staining was conducted as described in Sections 2.2.3.2 and 2.2.3.3, respectively. After dehydration, slides were incubated in Xylene solution for 1 min and refreshed for another minute. The slides were cleared with Histo-Clear II (National Diagnostics, Scientific Laboratory Supplies, UK) for 1 min, and DPX (Thermo Scientific, UK) was used for mounting.

5.2.6. Light Microscopy Imaging

The brightfield images were taken using Axio Observer inverted microscope (Zeiss, Germany) provided by Biomaterial Application and Research Centre in ACU, Türkiye. To image the whole sample, the tiles tool was acquired to stitch into larger mosaics where the area was adjusted as required.

The ECM deposition within the scaffold was calculated using ImageJ software's colour deconvolution feature for H&E, separating the haematoxylin and eosin components. The total area of the scaffold was determined from the original picture. The collagen from scaffolds was masked using the threshold tool in ImageJ, allowing the quantify the ECM collagen only. Eosin corresponding to ECM content measured from the scaffold area (A_{eosin}) was proportioned to the full size of the scaffold ($A_{scaffold}$) to obtain a percentage using Equation 5.1.

$$\text{ECM \%} = \frac{A_{eosin}}{A_{scaffold}} \times 100$$

(Equation 5.1)

The cell migration was also calculated from the haematoxylin-stained area of the scaffold ($A_{haematoxylin}$) proportioned to $A_{scaffold}$ using Equation 5.2.

$$\text{Cell Migration \%} = \frac{A_{haematoxylin}}{A_{scaffold}} \times 100$$

(Equation 5.2)

Statistical analyses were performed using two-way ANOVA with Tukey's HSD post-hoc test. $p<0.05$ was found statistically significant. The significance was indicated for multiple comparisons where the difference between the same condition at different time points or between the different conditions at the same time point.

5.3. Results

5.3.1. Animal Care and Surgery

Figure 5.2 represents the procedure followed throughout *in vivo* experiments. In a pilot study, implantation was first tried with and without suturing scaffolds, which showed no significant effect on scaffold adherence. Therefore, surgeries with no sutures were operated on for the experimental group. There was an apparent recovery in the suture area and hair growth after 1 week of operation (Figure 5.2C). No swelling or evidence of inflammation was observed for any of the animals. The change in body weight in the first three days was given in Appendix F, indicating that the rats were healthy. All animals were carefully monitored for one or two weeks and sacrificed to collect scaffolds. It was found that all implanted scaffolds adhered to the native tissue, and some even were surrounded by capillary vessels (Figure 5.2D).

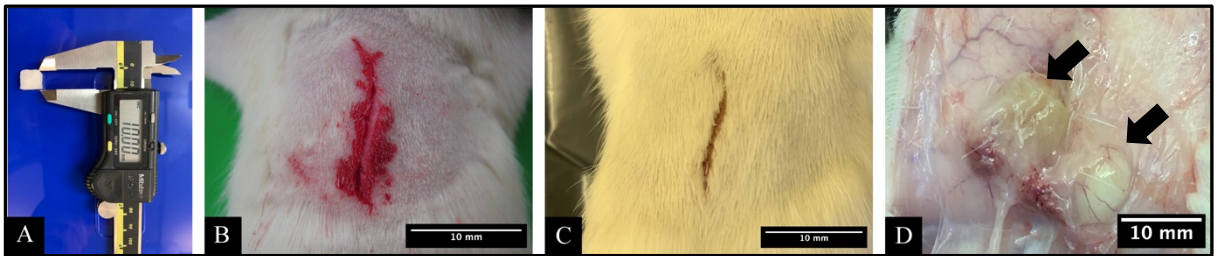


Figure 5.2. The process of scaffold implantation on rats. (A) The implanted scaffold. (B) The suture area after the scaffold was implanted. (C) The recovery of the suture area after a week. (D) The implanted scaffolds (black arrow) under the skin.

5.3.2. ECM Deposition and Cell Migration

Figures 5.3-5.5 show how implanted scaffolds appear in their entirety. Unfortunately, it was not possible to do immunohistochemistry on these samples, due to time constraints. However, there was no evidence of an immune response in the surrounding dermis tissue, and active cell migration within all scaffolds was observed. This was concomitant with the deposition of collagen ECM. Clearly, non-crosslinked scaffolds had more ECM deposition than crosslinked and HA-infiltrated scaffolds. In the C100 and C75E25 non-crosslinked scaffolds, the ECM covering the scaffold region grew by 44 and 68%, respectively, between 1 and 2 weeks. Although there was a significant increase in ECM coverage within the same group, there was no significant difference between C100 and C75E25 scaffolds. After one week, the crosslinked scaffolds showed the least ECM deposition, although this was not significant, but after two weeks, their ECM content grew to match that of the HA-infiltrated group at ~40% coverage 2 weeks post-implantation.

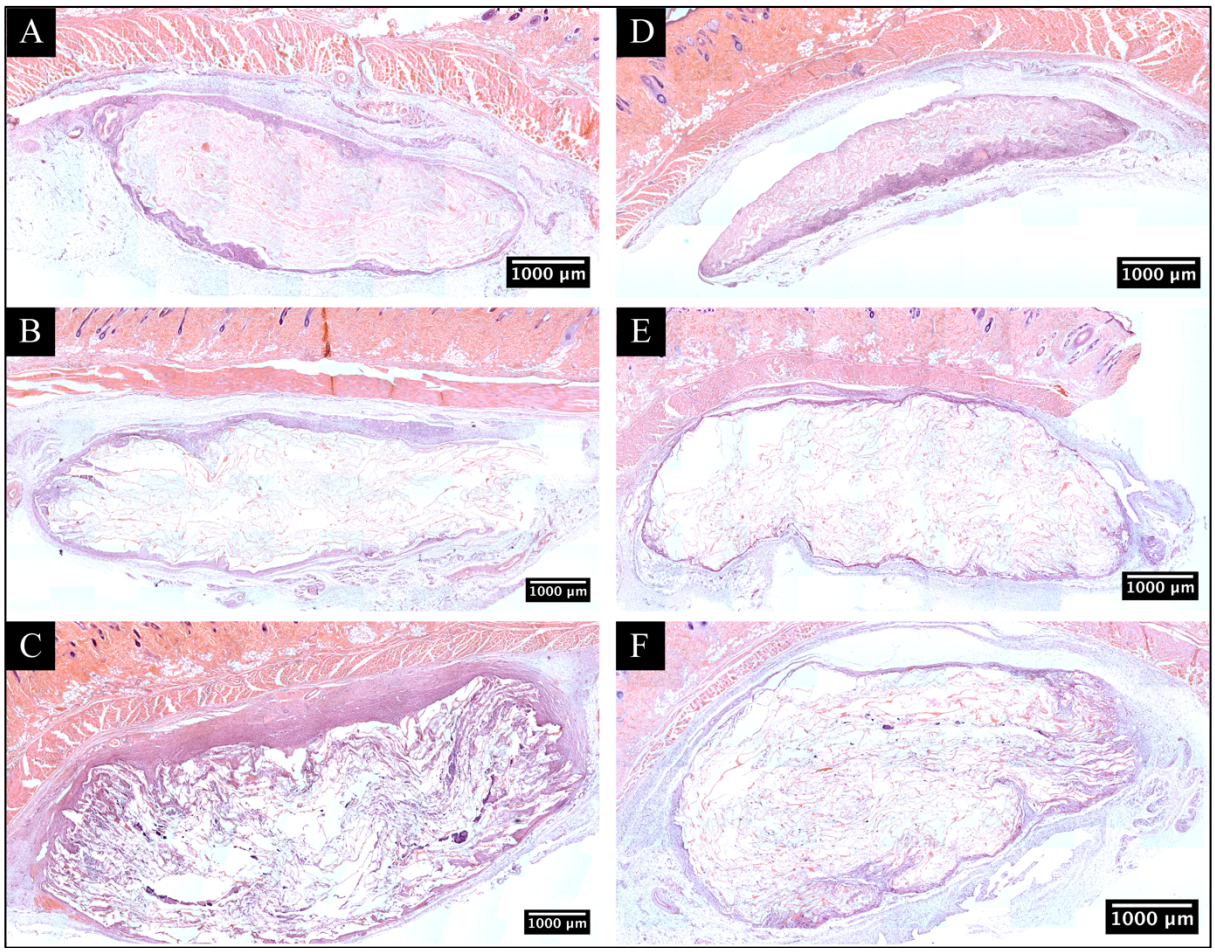


Figure 5.3. Representative H&E images from implanted scaffolds of C100 (A-C) and C75E25 (D-F) after one week. (A&D), (B&E) and (C&F) indicate non-crosslinked, crosslinked and HA-infiltrated scaffolds, respectively.

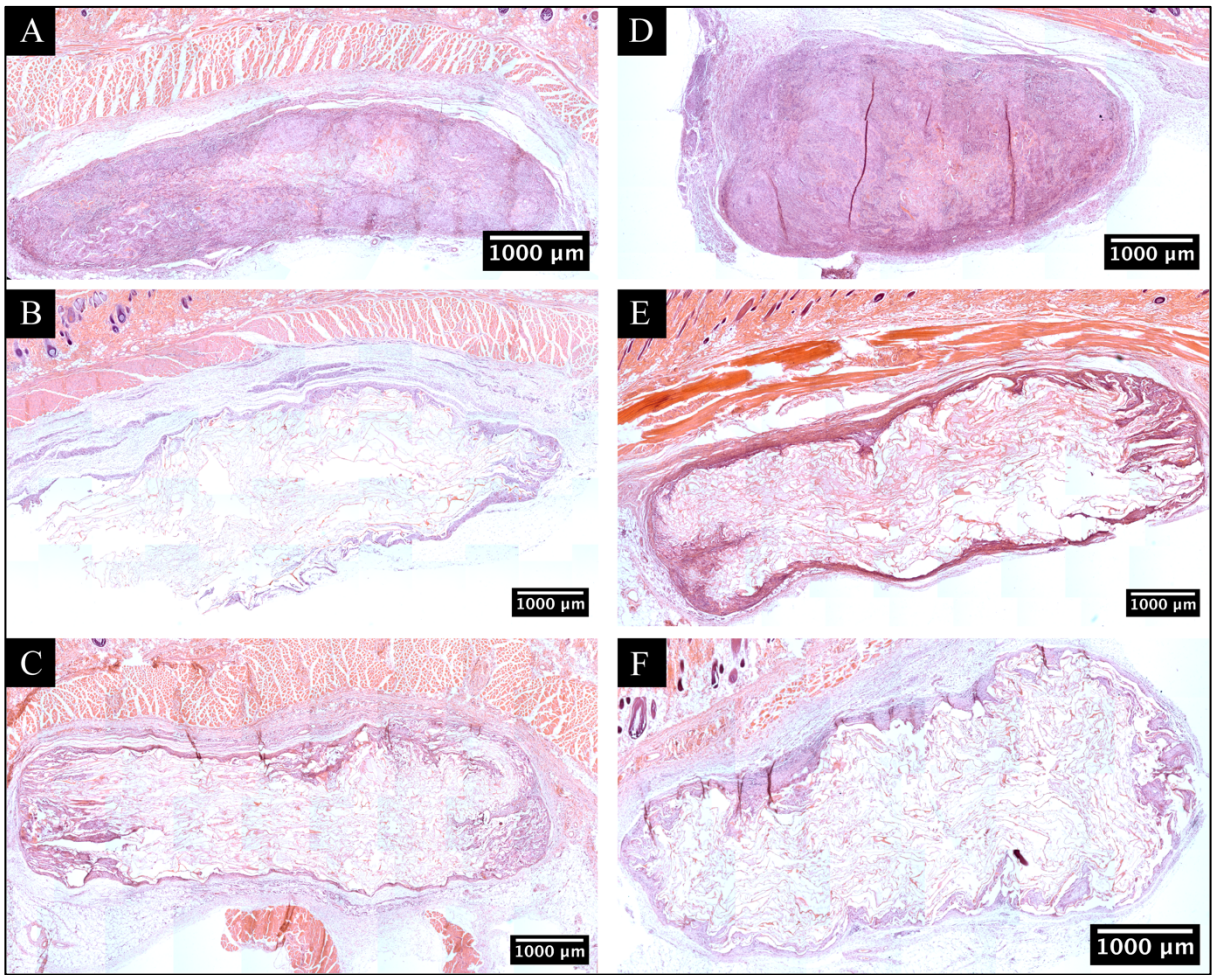


Figure 5.4. Representative H&E images from implanted scaffolds of C100 (A-C) and C75E25 (D-F) after two weeks. (A&D), (B&E) and (C&F) indicate non-crosslinked, crosslinked and HA-infiltrated scaffolds, respectively.

The channels inside the scaffold could not be seen because they were compressed by external pressure. But when it could, as in Figure 5.5, the perforations allowed a quicker construction of the ECM, beginning with the inner scaffold.

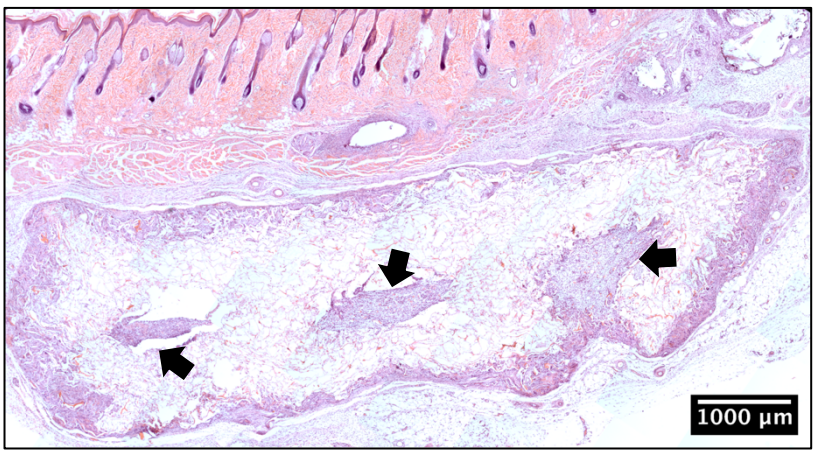


Figure 5.5. H&E image showing the channels of the scaffold indicated by black arrows.

H&E staining was used to calculate the amount of ECM present in the scaffolds (Figure 5.6) and the surface area occupied by host cells (Figure 5.7).

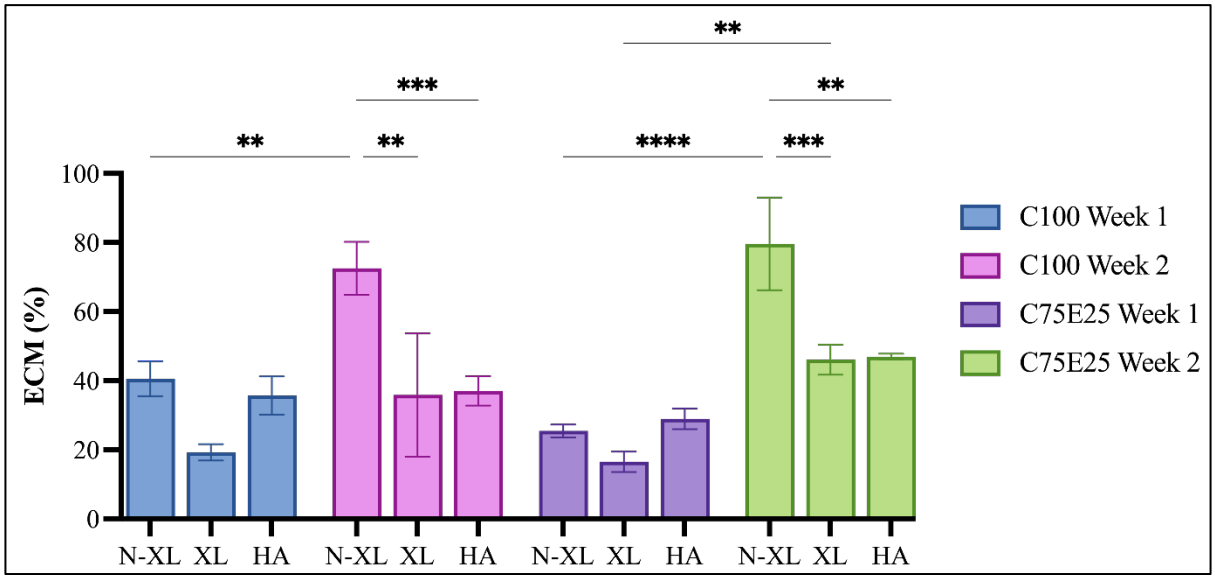


Figure 5.6. ECM deposition in C100 and C75E25 scaffolds at different conditions and time points. Two-way ANOVA with Tukey's HSD post-hoc test was used for multiple comparisons. ** p<0.01, ***p<0.001, ****p<0.0001.

Host cell migration was quantified by the area covered by the staining of nuclei. The results indicated that the largest migration was in C75E25 non-crosslinked group at week 2 by ~60% coverage. After two weeks, cell migration increased in all C75E25 scaffolds but only significantly in non-crosslinked scaffolds. Cell number in C100 scaffolds did not significantly differ between conditions and time points.

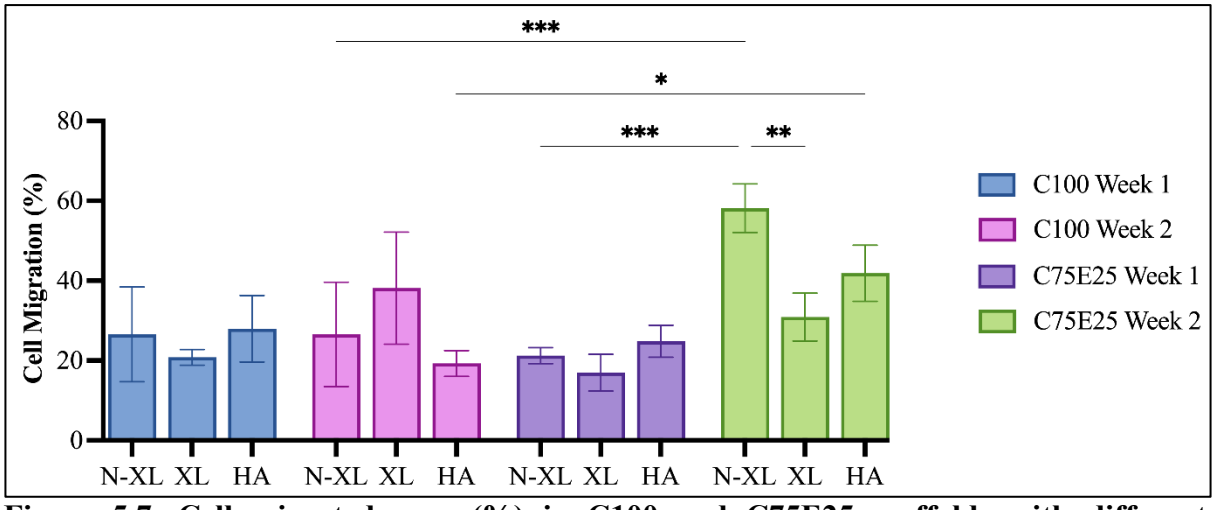


Figure 5.7. Cell migrated area (%) in C100 and C75E25 scaffolds with different conditions and time points. Two-way ANOVA with Tukey's HSD post-hoc test was used for multiple comparisons. *p<0.05, ** p<0.01, ***p<0.001.

Figures 5.8-11 represent the closer view of H&E-stained scaffolds where black arrows indicate the scaffold lines. Here, the host ECM has stained bright pink, while the scaffold structure was an orange shade. Both cell infiltration and ECM deposition could be seen in all groups, implying that the porous structure enabled easy diffusion. Additionally, each scaffold exhibited a good attachment side with the host tissue. No visible degradation was observed in crosslinked or HA-infiltrated groups after 2 weeks. It was possible to see the inner scaffold for C100 non-crosslinked group 2 weeks post-implantation (Figures 5.10A&D) but this was less clear in C75E25 (Figures 5.11A&D), suggesting that more of the C75E25 scaffold had degraded.

The presence of capillary vessels within the scaffolds was also examined by H&E staining. The vessels indicated by white arrows could be seen in every scaffold type. More capillaries were observed in non-crosslinked groups; however, this was not quantified in this study.

According to H&E staining, the compatibility of scaffolds was determined as follows:

$$\text{C100: N-XL} > \text{XL} \approx \text{HA}$$

$$\text{C75E25: N-XL} > \text{HA} \approx \text{XL}$$

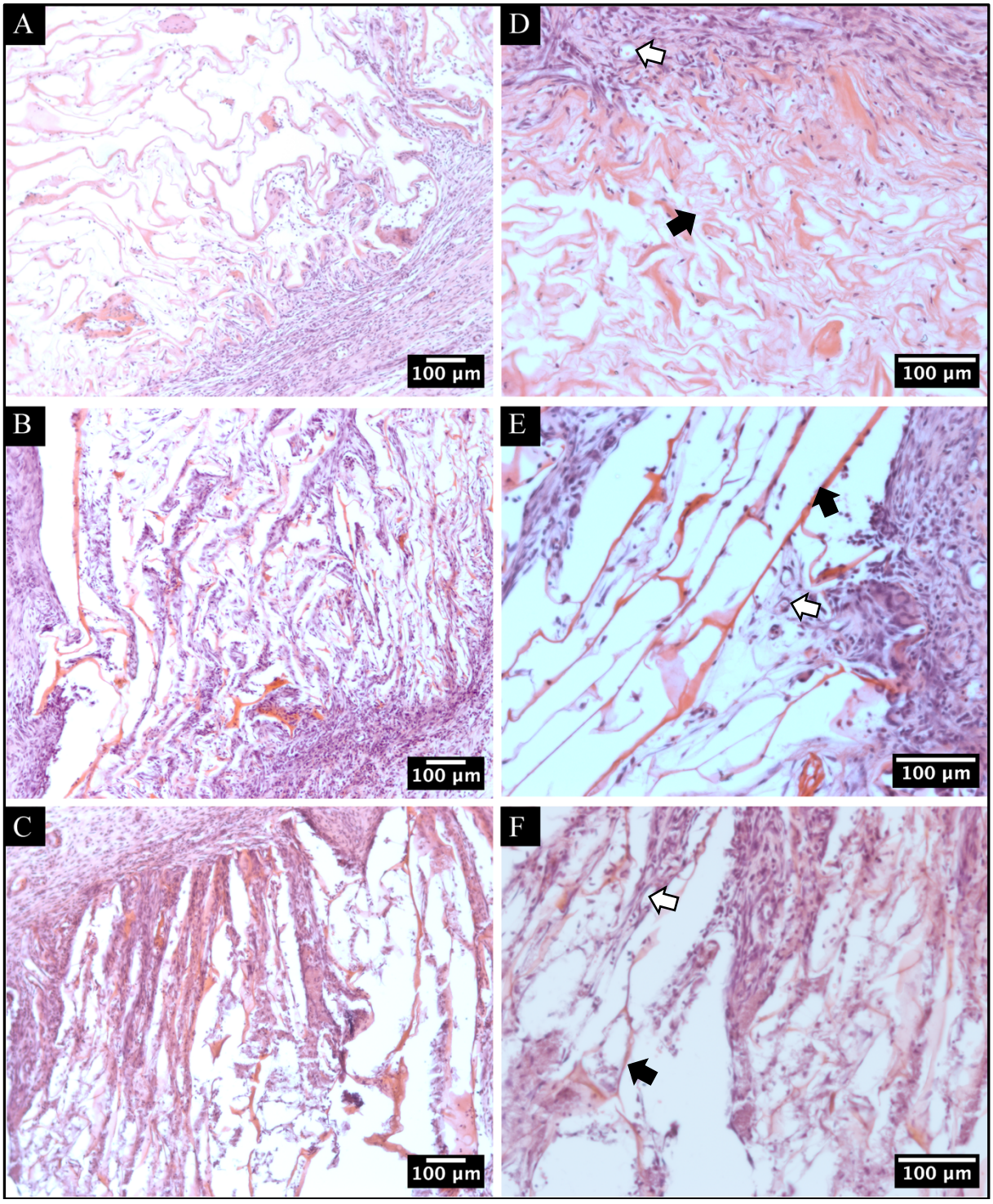


Figure 5.8. The close look of H&E images for the C100 (A&D) non-crosslinked, (B&E) crosslinked, and (C&F) HA-infiltrated scaffold at week 1. (A-C) and (D-F) were imaged at 10X and 20X, respectively. Bright pink: ECM; purple: Nuclei. The black and white arrows indicate the scaffold lines and capillary vessels, respectively.

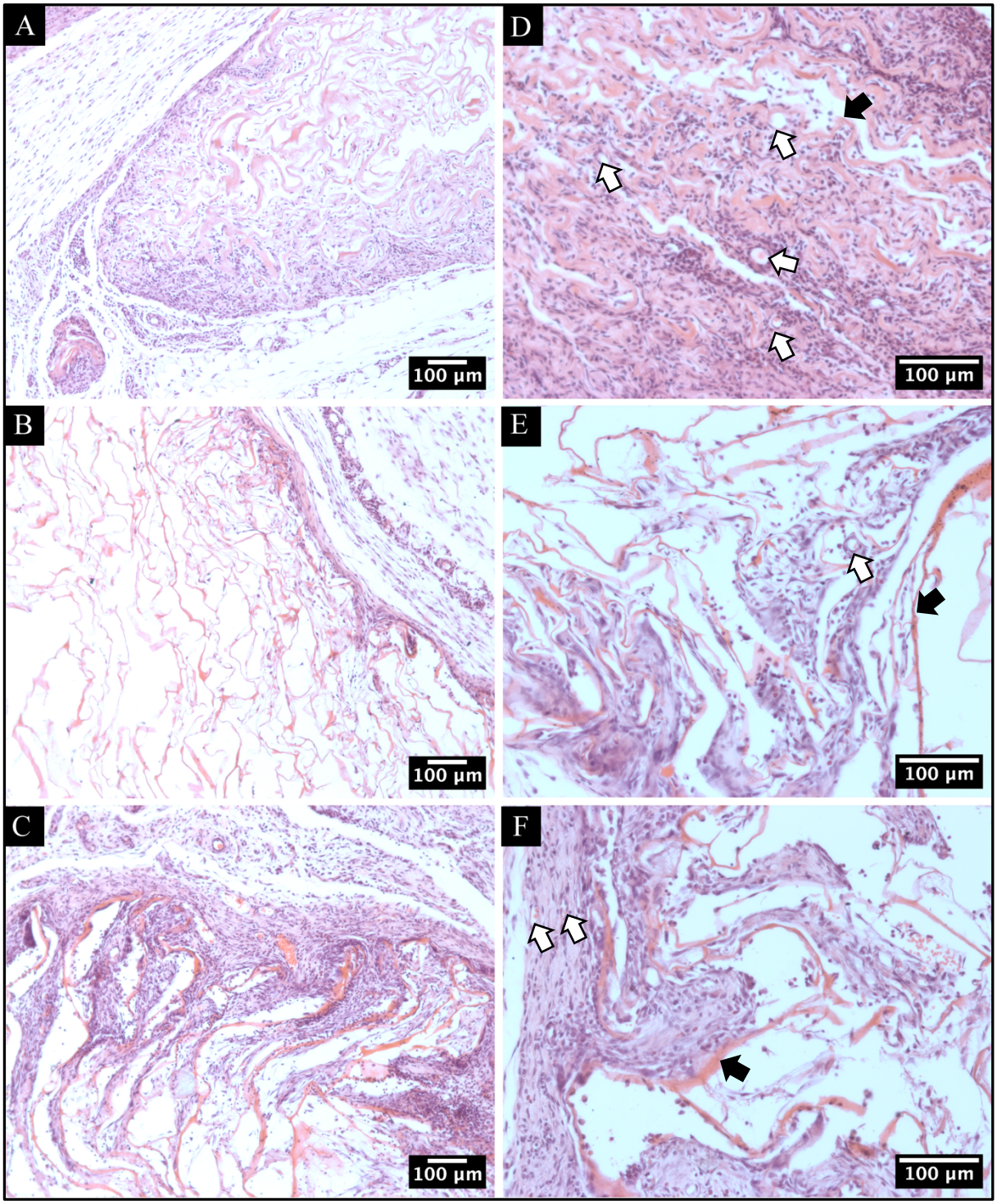


Figure 5.9. The close look of H&E images for the C75E25 (A&D) non-crosslinked, (B&E) crosslinked, and (C&F) HA-infiltrated scaffold at week 1. (A-C) and (D-F) were imaged at 10X and 20X, respectively. Bright pink: ECM; purple: Nuclei. The black and white arrows indicate the scaffold lines and capillary vessels, respectively.

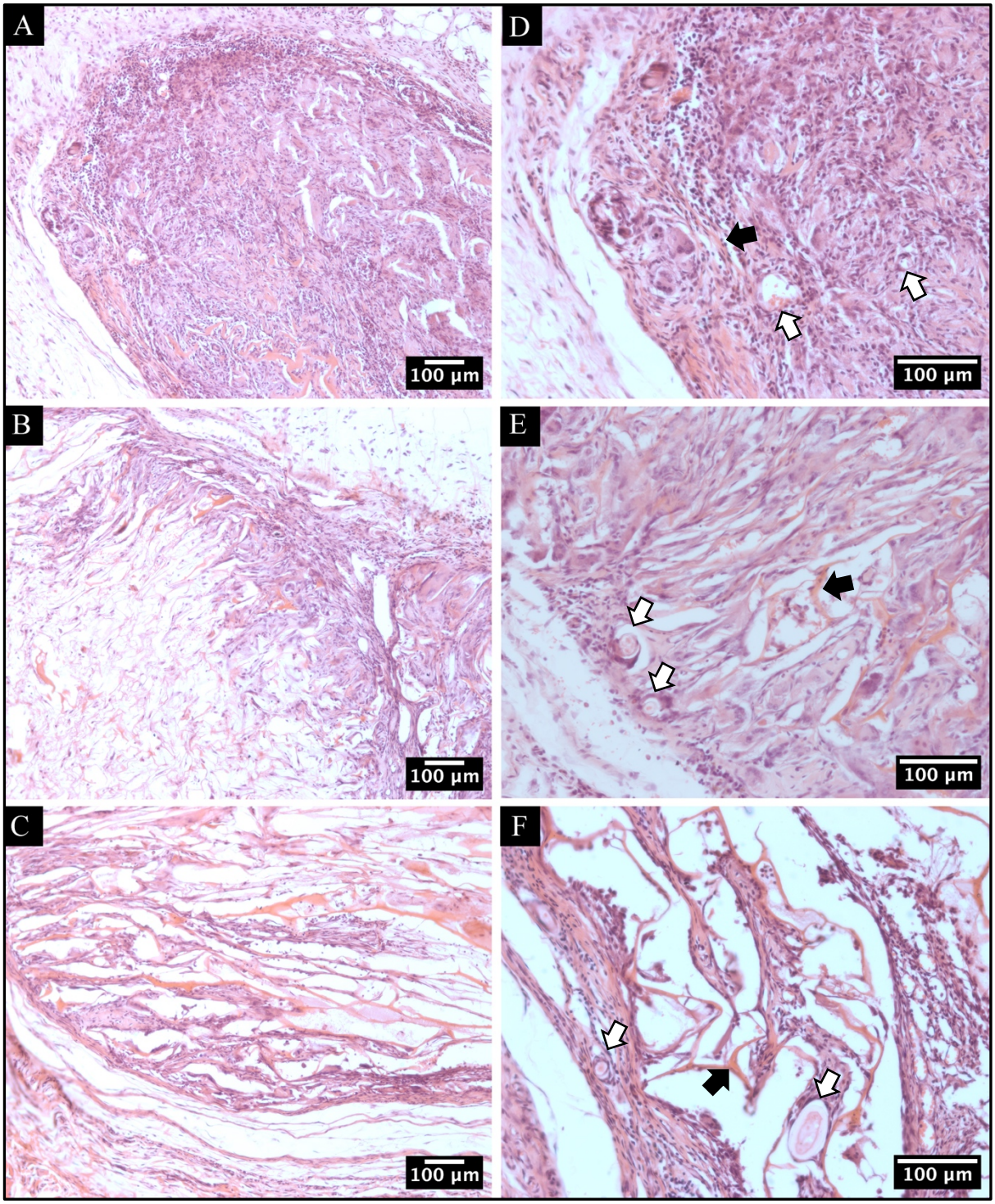


Figure 5.10. The close look of H&E images for the C100 (A&D) non-crosslinked, (B&E) crosslinked, and (C&F) HA-infiltrated scaffold at week 2. (A-C) and (D-F) were imaged at 10X and 20X, respectively. Bright pink: ECM; purple: Nuclei. The black and white arrows indicate the scaffold lines and capillary vessels, respectively.

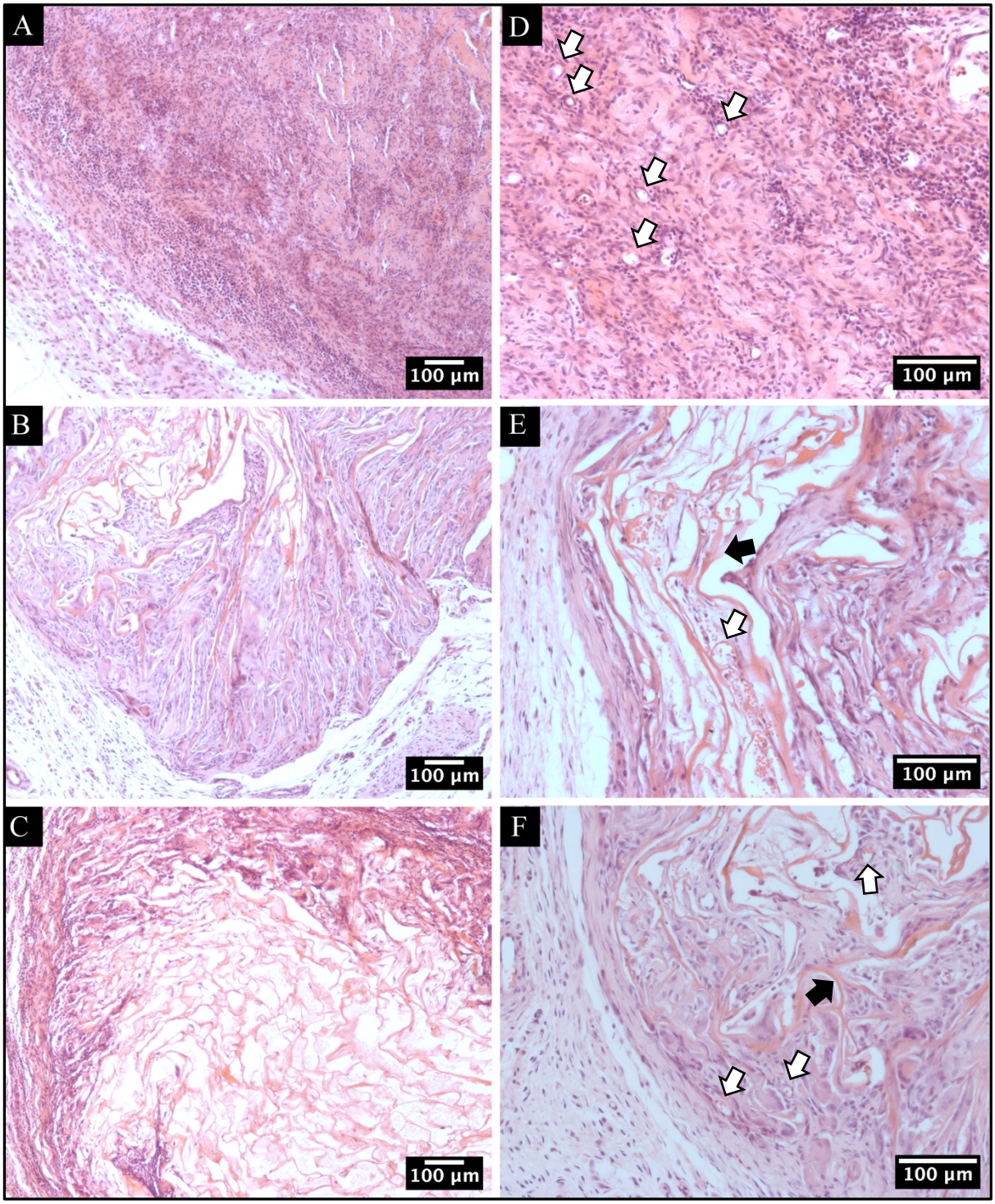


Figure 5.11. The close look of H&E images for the C75E25 (A&D) non-crosslinked, (B&E) crosslinked, and (C&F) HA-infiltrated scaffold at week 2. (A-C) and (D-F) were imaged at 10X and 20X, respectively. Bright pink: ECM; purple: Nuclei. The black and white arrows indicate the scaffold lines and capillary vessels, respectively.

5.3.3. Elastica van Gieson

EVG was mainly used to stain elastic fibres within the construct and the surrounding tissue. Figures 5.12-15 represent the EVG-stained sections of C100 and C75E25 scaffolds at different conditions and time points. It was found that the C100 scaffolds had no elastic fibre content but did contain collagen (yellow arrow). There was also no evidence of ECM elastin. As expected, C75E25 scaffolds had black thread-like structures within the scaffold (Figures 5.13&15), proving that elastin was incorporated. Sections of collagen-FEG composite scaffolds showed that the elastin spheres from the FEG were still present 2 weeks after implantation in rats (Figure 5.15). Within the non-crosslinked scaffolds, elastin spheres (black arrow) were quite large (Figures 5.13&15), where more intense elastic regions were seen in week 2. The surrounding tissue primarily represented the ECM collagen with no clear elastic fibre form.

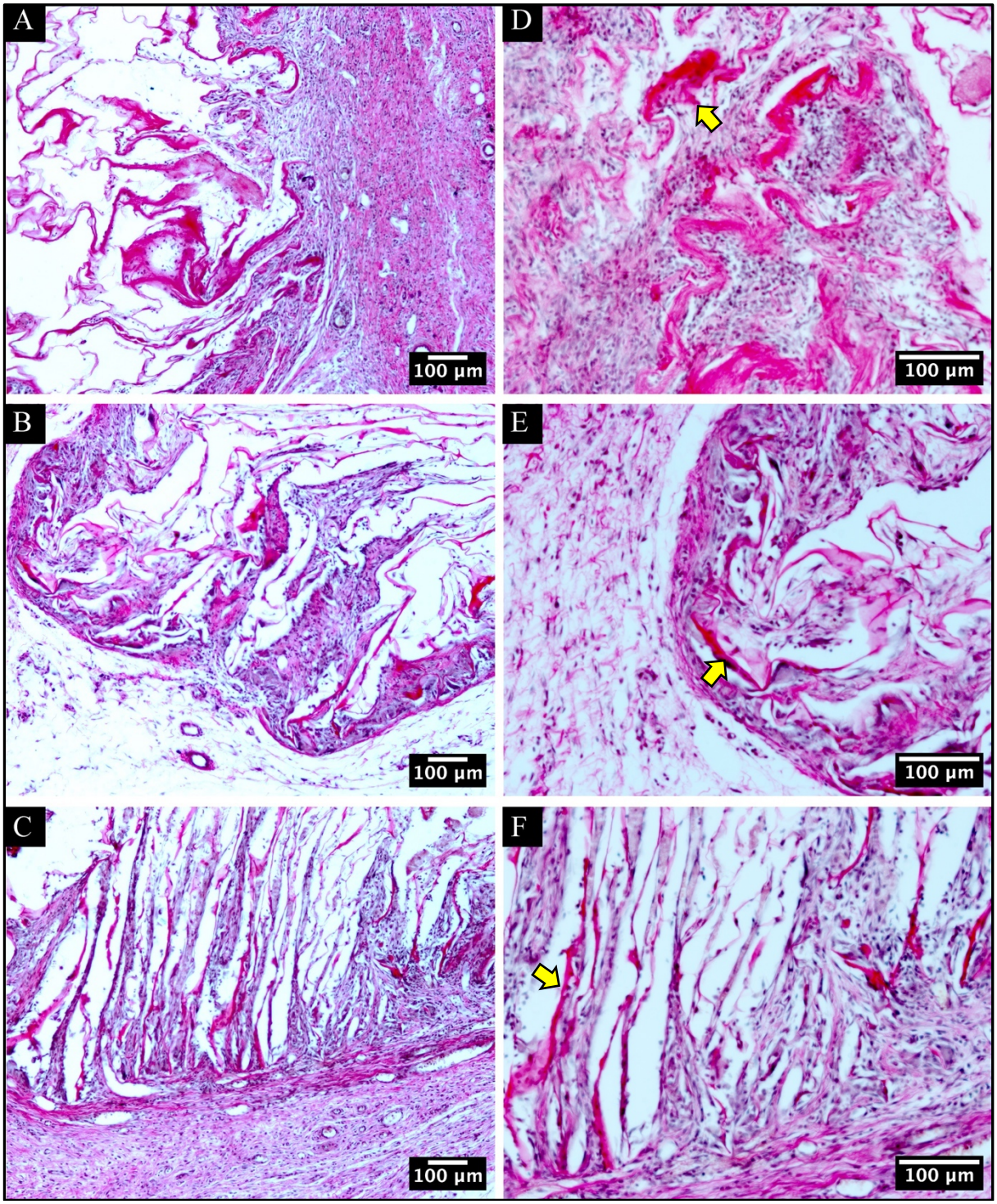


Figure 5.12. EVG images for the C100 (A&D) non-crosslinked, (B&E) crosslinked, and (C&F) HA-infiltrated scaffold at week 1. (A-C) and (D-F) were imaged at 10X and 20X, respectively. Black: Elastin, dark pink/ red: Scaffold collagen, light pink: ECM collagen, black dots: Nuclei. The yellow arrows indicate the collagen fibres of the scaffold.

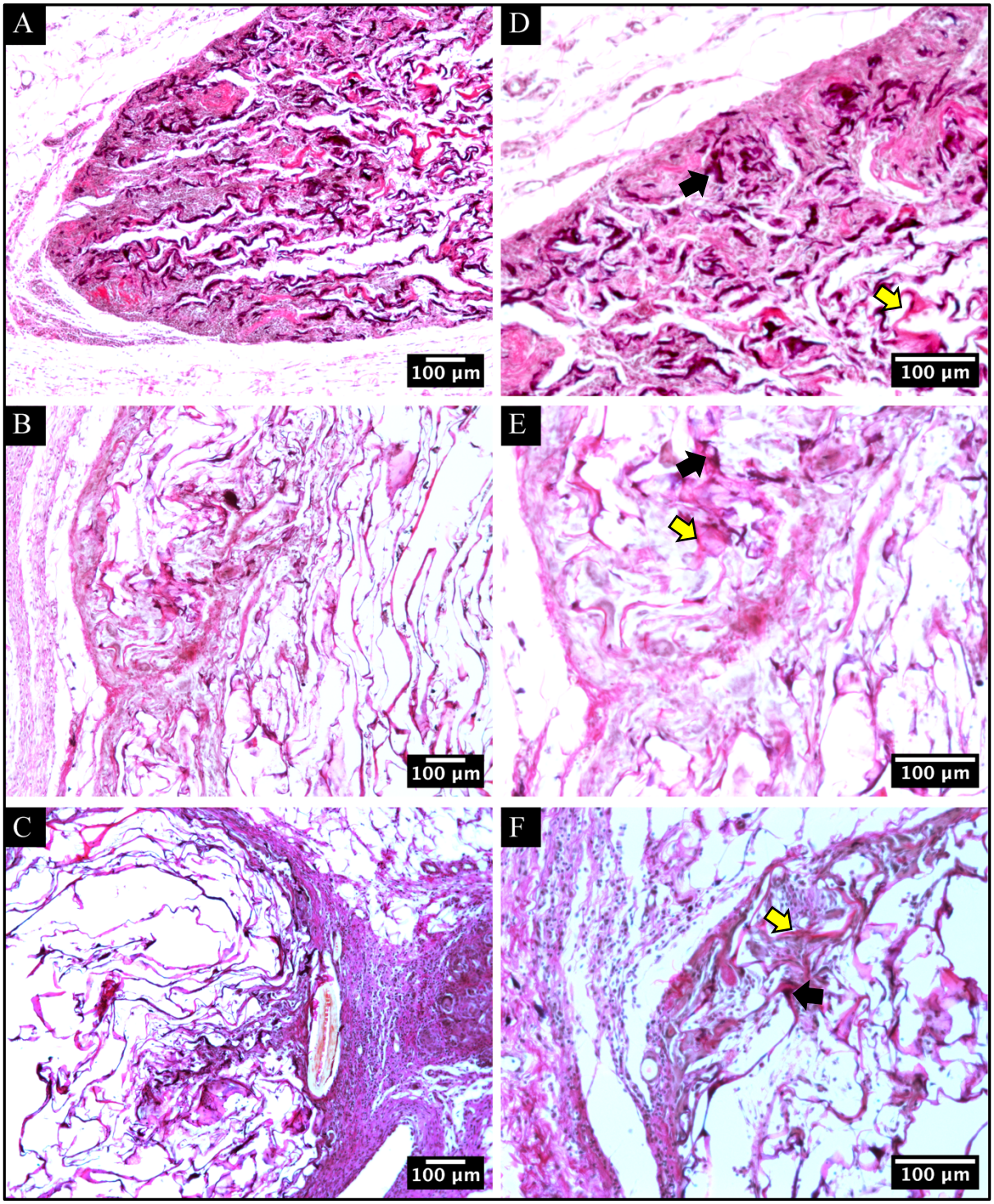


Figure 5.13. EVG images for the C75E25 (A&D) non-crosslinked, (B&E) crosslinked, and (C&F) HA-infiltrated scaffold at week 1. (A-C) and (D-F) were imaged at 10X and 20X, respectively. Black: Elastin, dark pink/ red: Scaffold collagen, light pink: ECM collagen, black dots: Nuclei. The black and yellow arrows indicate elastic and collagen fibres within the scaffold, respectively.

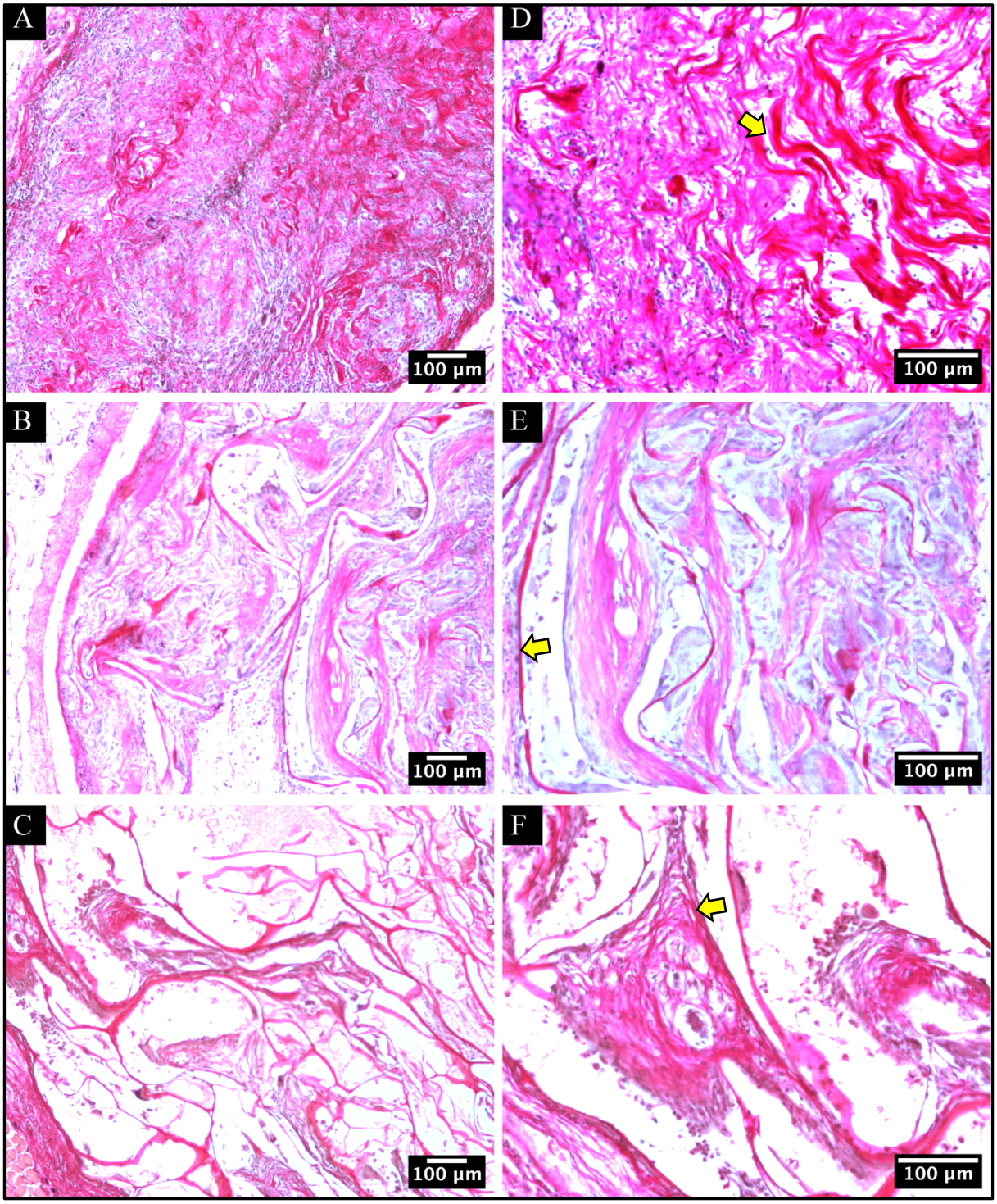


Figure 5.14. EVG images for the C100 (A&D) non-crosslinked, (B&E) crosslinked, and (C&F) HA-infiltrated scaffold at week 2. (A-C) and (D-F) were imaged at 10X and 20X, respectively. Black: Elastin, dark pink/ red: Scaffold collagen, light pink: ECM collagen, black dots: Nuclei. The yellow arrows indicate the collagen fibres of the scaffold.

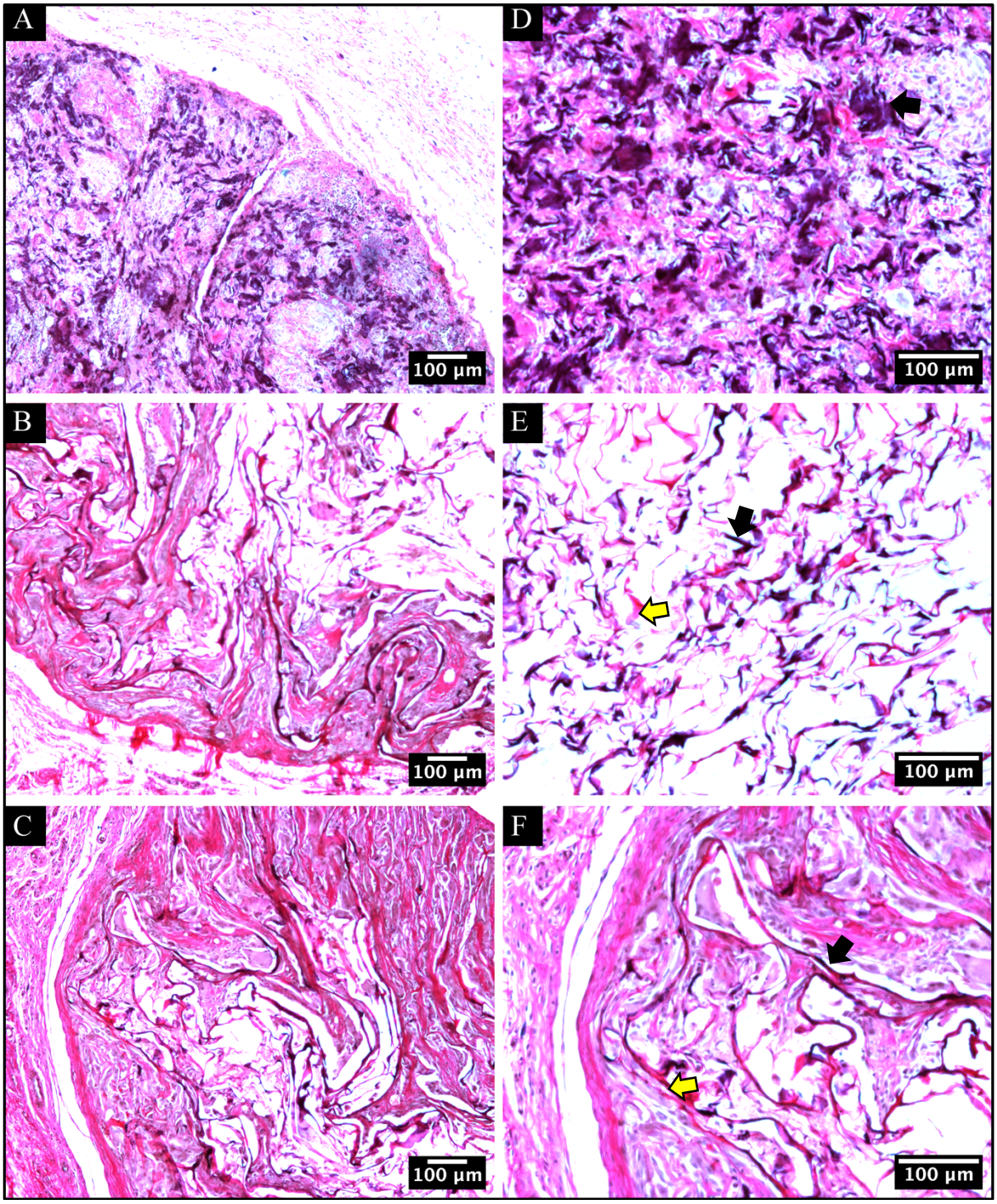


Figure 5.15. EVG images for the C75E25 (A&D) non-crosslinked, (B&E) crosslinked, and (C&F) HA-infiltrated scaffold at week 2. (A-C) and (D-F) were imaged at 10X and 20X, respectively. Black: Elastin, dark pink/ red: Scaffold collagen, light pink: ECM collagen, black dots: Nuclei. The black and yellow arrows indicate elastic and collagen fibres within the scaffold, respectively.

5.3.4. Alcian Blue

AB was utilised to stain acidic GAGs, including hyaluronic acid, in both tissue and scaffold, as shown in Figures 5.16-19. GAGs within ECM were detected in some regions, particularly in HA-infiltrated scaffolds (C and F in all figures). GAGs from ECM became more apparent in the non-crosslinked scaffold as the ECM deposition was more in this type.

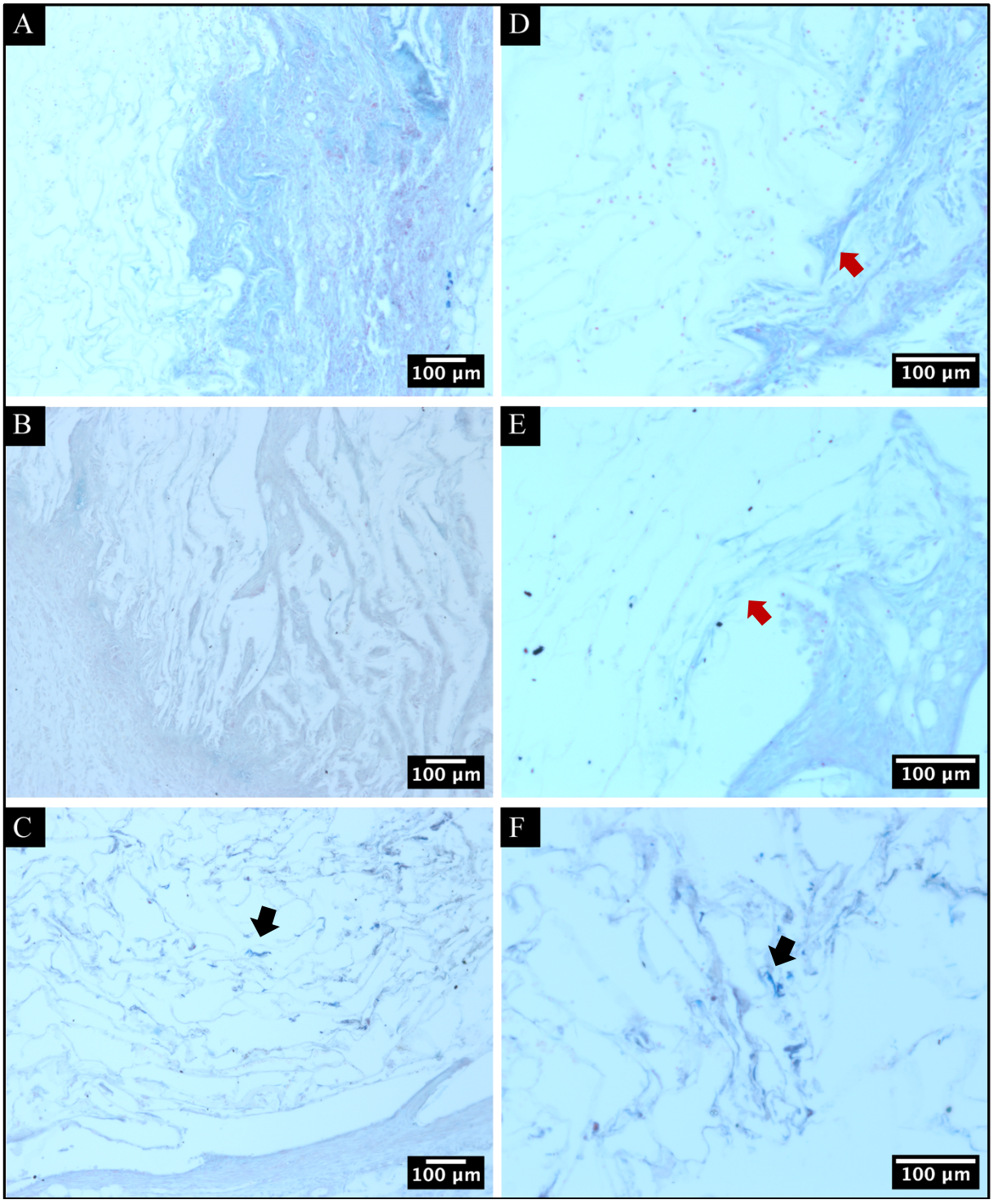


Figure 5.16. AB images for the C100 (A&D) non-crosslinked, (B&E) crosslinked, and (C&F) HA-infiltrated scaffold at week 1. (A-C) and (D-F) were imaged at 10X and 20X, respectively. Dark blue: GAGs; red: Nuclei. The black and red arrows indicate HA in the scaffold and GAGs in ECM, respectively.

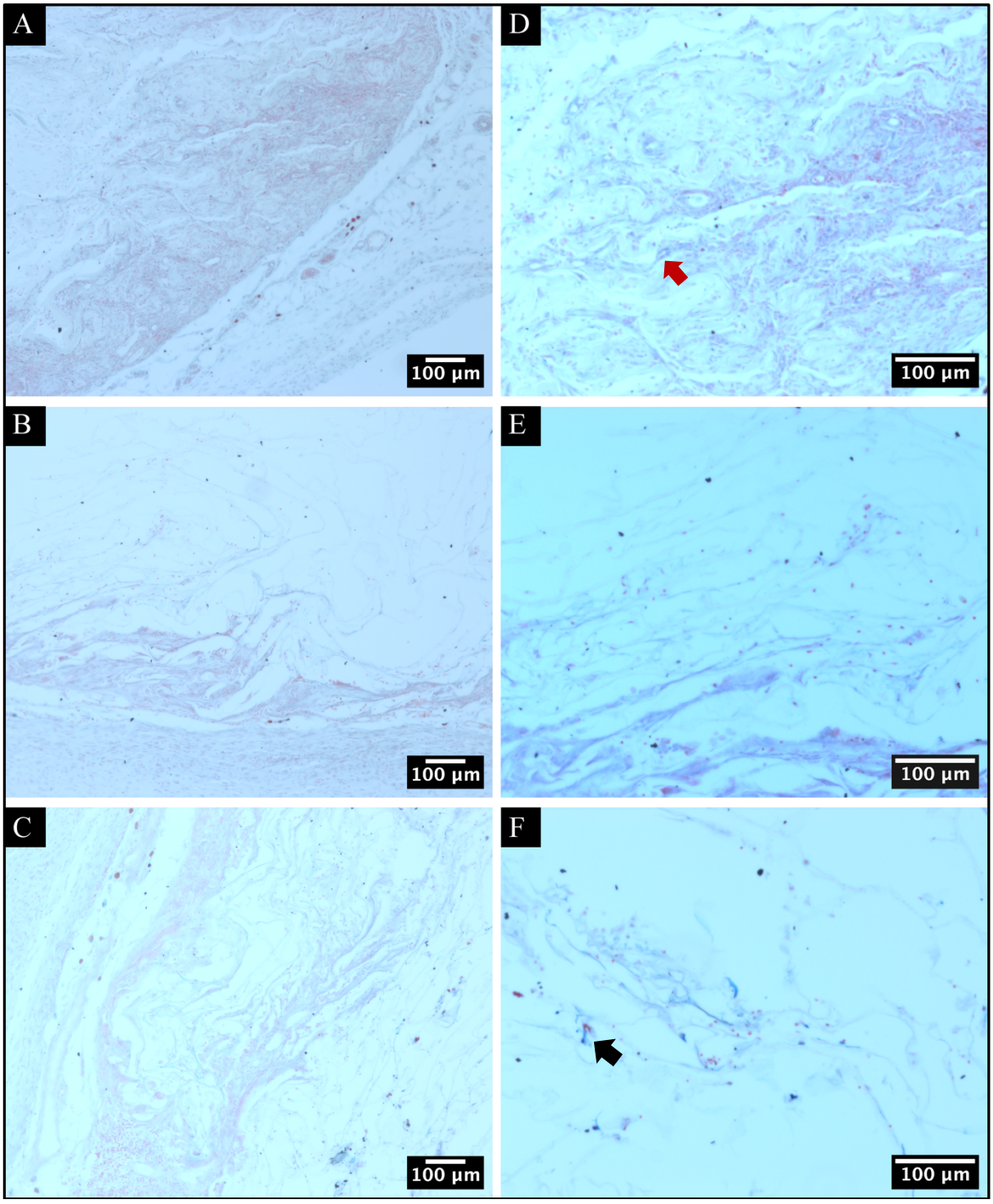


Figure 5.17. AB images for the C75E25 (A&D) non-crosslinked, (B&E) crosslinked, and (C&F) HA-infiltrated scaffold at week 1. (A-C) and (D-F) were imaged at 10X and 20X, respectively. Dark blue: GAGs; red: Nuclei. The black and red arrows indicate HA in the scaffold and GAGs in ECM, respectively.

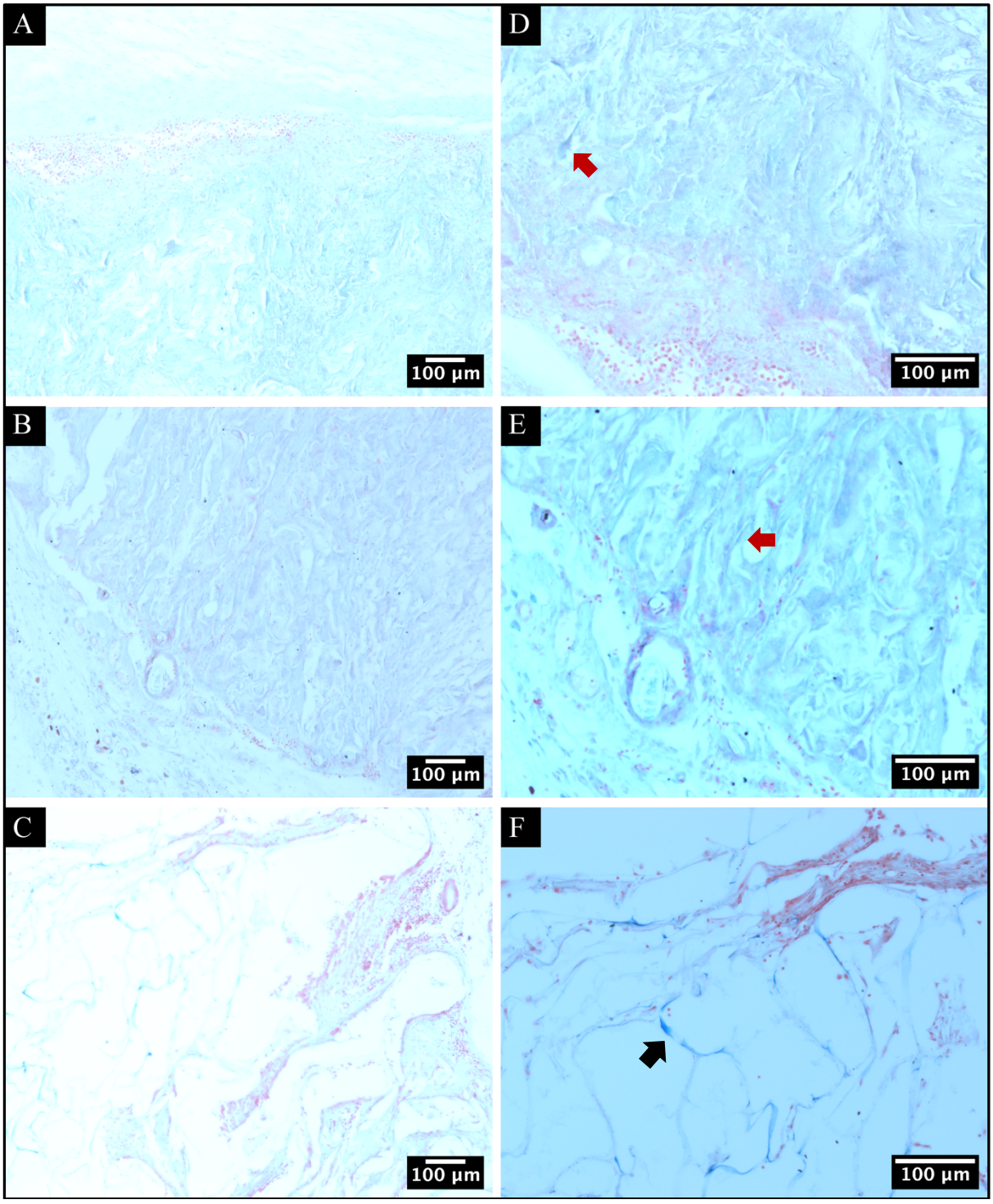


Figure 5.18. AB images for the C100 (A&D) non-crosslinked, (B&E) crosslinked, and (C&F) HA-infiltrated scaffold at week 1. (A-C) and (D-F) were imaged at 10X and 20X, respectively. Dark blue: GAGs; red: Nuclei. The black and red arrows indicate HA in the scaffold and GAGs in ECM, respectively.

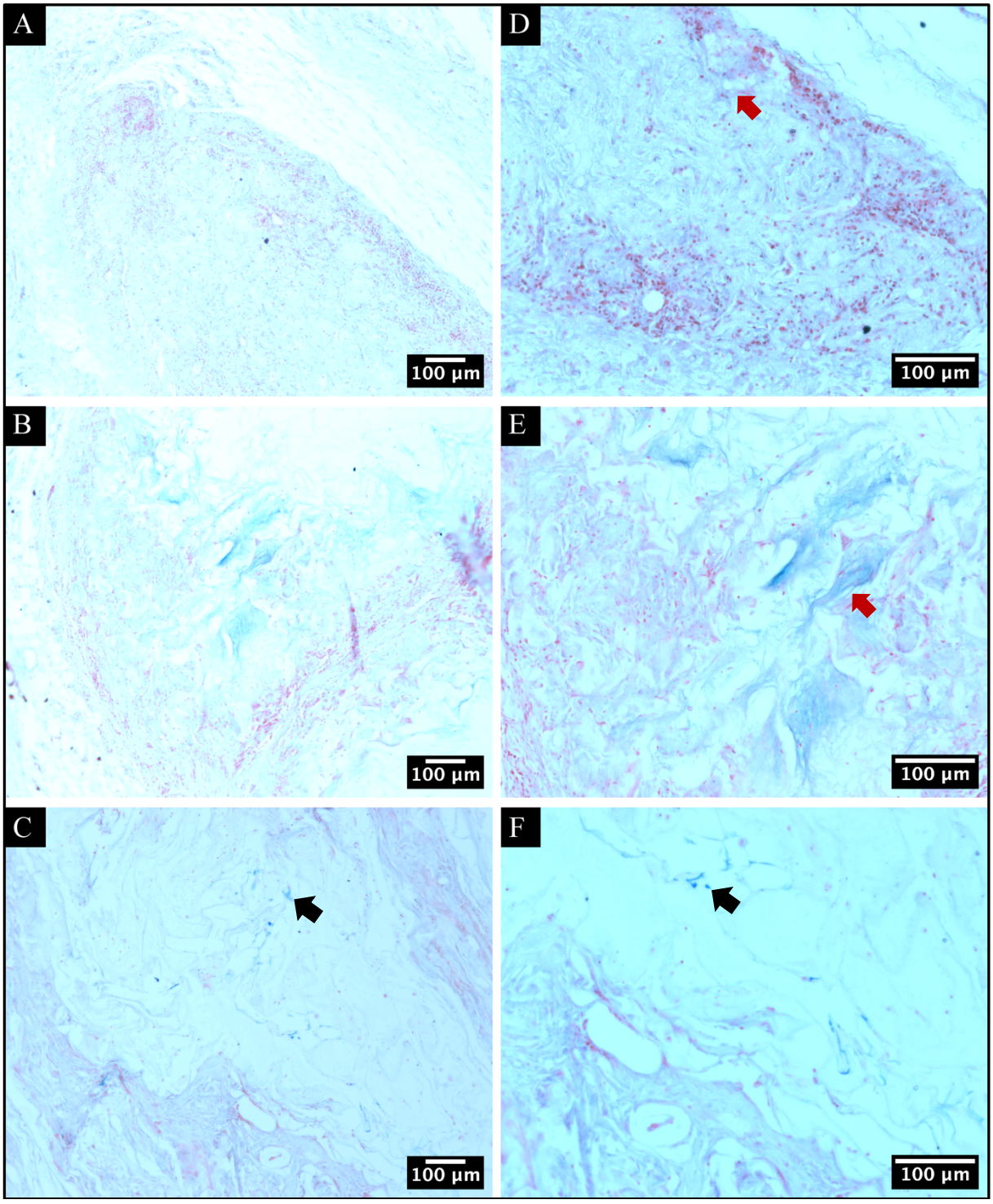


Figure 5.19. AB images for the C75E25 (A&D) non-crosslinked, (B&E) crosslinked, and (C&F) HA-infiltrated scaffold at week 2. (A-C) and (D-F) were imaged at 10X and 20X, respectively. Dark blue: GAGs; red: Nuclei. The black and red arrows indicate HA in the scaffold and GAGs in ECM, respectively.

5.4. Discussion

Biocompatibility is the most crucial requirement for a biomaterial to succeed in biomedical applications. A scaffold's biomaterial should not be immunotoxic, carcinogenic, or harmful to living tissue. For instance, the crosslinking can increase the scaffold's resilience against biodegradation (Chapter 3), but it may also result in encapsulation preventing cell infiltration and scaffold degradation (1). Various studies assess the biocompatibility of material to mimic native tissue, some assessing it by subcutaneous implantation (2-4). This study focuses on how scaffolds support cell migration and new ECM formation without inducing immunogenicity, and neovascularisation. To this end, acellular collagen or collagen-FEG composite scaffolds were subcutaneously implanted within immunocompetent rats to establish their biocompatibility. The histological and morphological investigation of the subcutaneous tissue around the implanted scaffolds revealed no apparent adverse inflammatory reaction, although time constraints meant that we could not confirm the types of cells which infiltrated the scaffold. Studies in a range of acellular ECM scaffolds have shown that the early infiltrating cells are leucocytes and mononuclear cells. Over time, there is neovascularisation and deposition of host ECM, followed by infiltration by parenchymal cells such as fibroblasts (1). There was also no evidence of scaffold encapsulation in the study, which is one of the major advantages of these scaffolds.

Another critical factor in biocompatibility is degradation which occurs when the scaffold degrades or is incorporated into the host tissue. The accumulation of host cells within an implanted acellular scaffold has been suggested as a potential cause of scaffold degradation (5). The idea was that the biomaterial quickly broke down and was replaced by host tissue. Here, non-crosslinked scaffolds exhibited faster cellular invasion and ECM deposition, implying that they were degraded. The degradation started even 1-week post-implantation, and the scaffolds became indistinguishable at week 2. In contrast to another work examining the

time-dependent breakdown of subcutaneously implanted-collagen scaffolds (6), our findings demonstrated faster cellular degradation. Although ECM deposition was significantly lower in crosslinked and HA-infiltrated scaffolds than in non-crosslinked scaffolds, the sign of cellular migration from the edges of the scaffold suggested that an extended implantation period could result in full ECM coverage and degradation.

The surface morphology and topographical structure of the implanted scaffold are effective in the interactions between cells and the scaffold by mediating the accumulation of inflammatory cells and the tissue response. The porous architecture efficiently facilitated the transfer of nutrients throughout the scaffold, supporting cell migration. Here, the number of cells migrating into the scaffold was higher in collagen-FEG composites compared to collagen scaffolds, indicating that FEG attracted cells more. Ideally, the cellular inflammatory response could be further confirmed by immunohistochemistry (IHC) using rat CD45 antibody, a well-known marker of leukocytes (7). Macrophages are also extensively used in characterising tissue remodelling from weeks to months. During wound healing, macrophages initially take on the proinflammatory phenotype known as "M1," secreting proinflammatory cytokines for the acute phase response, before switching to the tissue-repairing phenotype known as "M2," which are responsible for secreting new matrix and attracting migrating MSCs. The balance between M1 and M2 could indicate the level of tissue repair and be determined by macrophage-specific markers such as CD68, CCR7 and CD206 (8).

One of our objectives was to identify FEG-originated elastic fibres and see if elastogenesis occurred within the construct. The results demonstrated that the FEG was successfully incorporated into the construct, which was previously confirmed by FT-IR in Chapter 3. The striking point was that the non-crosslinked group exhibited more elastic fibre accumulated at certain regions than crosslinked and HA-infiltrated groups, even though they all had the same ratio of FEG. Crosslinked and HA-infiltrated collagen-FEG composites could still be detected

2 weeks post-implantation and may thus accomplish their biological effect over a longer period. The reason why non-crosslinked composites had more elastin thread-like fibres could be because the soluble FEG attracted more ECM elastin to itself by regulating neovascularisation. Soluble elastin can start a chain reaction that leads to angiogenesis and tissue remodelling. A study concluded that k-elastin, produced by treating elastin with potassium hydroxide, stimulated angiogenesis by encouraging cell migration and tubulogenesis in the human vascular ECs (9). Another study also suggested that the solubilised form of elastin could facilitate *in vivo* angiogenesis and new ECM formation better than the insoluble form (10). Although H&E staining showed the formation of blood vessels in the scaffolds, there was no direct proof of the host's elastic fibres in the current study. Potentially, elastogenesis formed in scaffolds could be determined using elastin or fibrillin-specific antibodies (10).

One of the most crucial elements of the ECM is the linear polysaccharide HA. Studies have shown that HA controls cellular differentiation, migration, angiogenesis, and the inflammatory response (11, 12). Due to its widespread distribution in vertebrate tissues, high biocompatibility, and non-toxic degradation products, HA has emerged as a hot topic in tissue engineering. Here, our goal was to see whether the inclusion of HA resulted in tissue remodelling by attracting more ECM deposition within the scaffolds. The presence of HA was imaged by AB staining, showing both scaffold-originated HA and ECM GAGs. We did not see any significant difference in ECM deposition or cell infiltration in scaffolds incorporating HA compared to the crosslinked scaffolds, although there was a slight increase in ECM deposition and cell infiltration at 1-week. Since both scaffolds are crosslinked, it may be that HA helped reduce the adverse effects of crosslinking and may contribute long term tissue remodelling. As aforementioned, the interaction of FEG with HA is stronger than that of collagen-HA, which could also be explained by the cell migration semi-quantitative analysis, indicating cell migration over time was more significant towards collagen-FEG-HA composites rather than

collagen-HA ones. Yet, the non-crosslinked scaffolds had better ECM deposition as it is highly related to crosslinking agents which are usually introduced into the molecular structure of biological implants to control their degradation rate and improve their mechanical stability (Chapter 3). However, such crosslinking procedures have some consequences including cytotoxicity, calcification, and foreign body response (13). Studies also showed that crosslinking could delay ECM deposition and host cell infiltration, and it is highly EDC-concentration-dependent (14). Chapter 3 also explained that the carboxylate group of glucuronic acid in HA enables very easy crosslinking and chemical modification of HA to produce scaffolds. The resulting HA-based scaffolds, however, bear little resemblance to the actual structure and presentation of HA found in the body. The affinity of CD44 (membrane protein) for HA determines the activity of HA. This affinity, in turn, is determined by the molecule's concentration and molecular weight, as well as by glycosylation of extracellular domains and/or phosphorylation of serine residues (15). A more natural, physiologically realistic presentation of the HA may provide additional insight into the impacts of HA-based scaffolds to improve tissue healing (16). As non-crosslinked and HA-infiltrated scaffolds are not directly comparable, methods blending HA into the scaffolds without crosslinkers (17) would be ideal for yield applications across tissue engineering and regenerative.

5.5. Summary

This chapter focused on the *in vivo* biocompatibility of C100 and C75E25 scaffolds as they were found to be more promising both mechanically and *in vitro* cell studies. Images of implanted scaffolds were utilised to assess ECM deposition, cell migration, neovascularisation, and the confirmation of elastic fibre and HA within the scaffolds. The main findings are the following:

- Our results demonstrate that designed scaffolds are biocompatible and exhibit promising potential as an implant.

- The solubilised FEG facilitates *in vivo* ECM deposition and angiogenesis better than collagen scaffolds.
- Crosslinking affects the scaffold's ability to induce cell migration and tissue growth in the short term. However, these effects can be improved by HA infiltration.

References

1. Badylak SF, editor The extracellular matrix as a scaffold for tissue reconstruction. Seminars in cell & developmental biology; 2002: Elsevier.

2. Fredriksson C, Hedhammar M, Feinstein R, Nordling K, Kratz G, Johansson J, et al. Tissue response to subcutaneously implanted recombinant spider silk: an in vivo study. Materials. 2009;2(4):1908-22.

3. Jaiswal AK, Dhumal RV, Bellare JR, Vanage GR. In vivo biocompatibility evaluation of electrospun composite scaffolds by subcutaneous implantation in rat. Drug delivery and translational research. 2013;3:504-17.

4. Khorramirouz R, Go JL, Noble C, Jana S, Maxson E, Lerman A, et al. A novel surgical technique for a rat subcutaneous implantation of a tissue engineered scaffold. Acta histochemica. 2018;120(3):282-91.

5. Badylak S, Kropp B, McPherson T, Liang H, Snyder P. Small intestinal submucosa: a rapidly resorbed bioscaffold for augmentation cystoplasty in a dog model. Tissue engineering. 1998;4(4):379-87.

6. Chan EC, Kuo S-M, Kong AM, Morrison WA, Dusting GJ, Mitchell GM, et al. Three dimensional collagen scaffold promotes intrinsic vascularisation for tissue engineering applications. PloS one. 2016;11(2):e0149799.

7. Modulevsky DJ, Cuerrier CM, Pelling AE. Biocompatibility of subcutaneously implanted plant-derived cellulose biomaterials. PloS one. 2016;11(6):e0157894.

8. Brown BN, Londono R, Tottey S, Zhang L, Kukla KA, Wolf MT, et al. Macrophage phenotype as a predictor of constructive remodeling following the implantation of biologically derived surgical mesh materials. Acta Biomater. 2012;8(3):978-87.

9. Robinet A, Fahem A, Cauchard JH, Huet E, Vincent L, Lorimier S, et al. Elastin-derived peptides enhance angiogenesis by promoting endothelial cell migration and tubulogenesis through upregulation of MT1-MMP. J Cell Sci. 2005;118(Pt 2):343-56.

10. Daamen WF, Nillesen ST, Wismans RG, Reinhardt DP, Hafmans T, Veerkamp JH, et al. A biomaterial composed of collagen and solubilized elastin enhances angiogenesis and elastic fiber formation without calcification. Tissue Engineering Part A. 2008;14(3):349-60.

11. Pardue EL, Ibrahim S, Ramamurthi A. Role of hyaluronan in angiogenesis and its utility to angiogenic tissue engineering. Organogenesis. 2008;4(4):203-14.

12. Silva LP, Pirraco RP, Santos TC, Novoa-Carballal R, Cerqueira MT, Reis RL, et al. Neovascularization Induced by the Hyaluronic Acid-Based Spongy-Like Hydrogels Degradation Products. ACS Appl Mater Interfaces. 2016;8(49):33464-74.

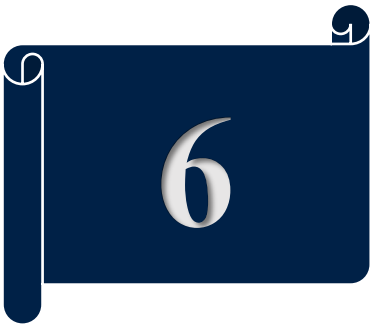
13. Delgado LM, Bayon Y, Pandit A, Zeugolis DI. To cross-link or not to cross-link? Cross-linking associated foreign body response of collagen-based devices. Tissue Eng Part B Rev. 2015;21(3):298-313.

14. Burugapalli K, Chan JC, Kelly JL, Pandit AS. Efficacy of crosslinking on tailoring in vivo biodegradability of fibro-porous decellularized extracellular matrix and restoration of native tissue structure: a quantitative study using stereology methods. Macromol Biosci. 2014;14(2):244-56.

15. Skelton TP, Zeng C, Nocks A, Stamenkovic I. Glycosylation provides both stimulatory and inhibitory effects on cell surface and soluble CD44 binding to hyaluronan. J Cell Biol. 1998;140(2):431-46.

16. Abatangelo G, Vindigni V, Avruscio G, Pandis L, Brun P. Hyaluronic Acid: Redefining Its Role. Cells. 2020;9(7).

17. Kotla NG, Mohd Isa IL, Larranaga A, Maddiboyina B, Swamy SK, Sivaraman G, et al. Hyaluronic Acid-Based Bioconjugate Systems, Scaffolds, and Their Therapeutic Potential. Adv Healthc Mater. 2023:e2203104.



THESIS SUMMARY AND FUTURE WORK

6. THESIS SUMMARY AND FUTURE WORK

6.1. Thesis Summary

Cardiac tissue engineering (CTE) aims to improve cardiac function by combining diverse scaffolds, cell sources, and pharmacological stimuli to alleviate injury and accelerate regeneration. Vascularisation is also required to prevent tissue rejection and to shorten the time it takes for a native capillary-like network to grow across the scaffold *in vivo*. However, it is very difficult for a structure that imitates the natural tissue to have both the original composition and natural mechanical properties and to support the formation of new blood vessels while being biocompatible. Here, the study aimed to create a composite porous scaffold made of collagen type I, fibrillar elastin gel (FEG), and hyaluronic acid (HA) on which to culture human induced pluripotent stem cells (hiPSCs)-derived cardiomyocytes (hiPSC-CMs) and human umbilical vein endothelial cells (HUVECs). To our knowledge, this is the first study using these three polymers in a scaffold design on which hiPSCs are cultured and differentiated into hiPSC-CMs.

First, we began with a study of native porcine heart tissue that we aimed to mimic. Chapter 2 investigated the histological and mechanical characterisation of hearts so that we could see if scaffolds reflected native mechanical properties. The results showed that most of the cardiac extracellular matrix (ECM) is made up of collagen, where the fibre orientation varied. Although elastic fibres were hard to locate, acidic glycosaminoglycans (GAGs), including HA, were defined along the axis of the collagen fibres by Alcian Blue (AB) staining. Mechanical testing revealed that fibre orientation is a critical value in stiffness which is mainly regulated by elastic and collagen fibres.

Chapter 3 studied either collagen or collagen-FEG composite scaffolds with the infiltration of HA. Because of the high porosity and strong interconnectivity of the scaffolds, freeze-casting was chosen as the method for fabrication. Infrared spectroscopy and scanning electron

microscopy (SEM) revealed the successful manufacturing of collagen-FEG composites and HA-infiltrated variants with high porosities (>97%). This polymer composition interacted with the solvent better after mixing for an extended period of time at a lower temperature (+4°C) and pH (2.7) that was below the isoelectric point of both collagen and FEG. Further characterisation studies indicated that FEG dominates the swelling properties of composites in a concentration-dependent manner. However, FEG exhibited a lower affinity to crosslinking, possibly due to physical interaction between collagen and FEG, which also affected the structural integrity of composites during degradation studies. FEG and HA infiltration considerably influenced the mechanical characteristics of composite scaffolds. The FEG dominated the compressive and tensile properties, but the HA had a strong influence on the bending properties in the hydrated state.

The *in vitro* cellular response of hiPSC-CMs was studied in Chapter 4. HA-infiltrated collagen or collagen-FEG composite scaffolds were used for cell attachment and viability. The results showed that our scaffold design is biocompatible for long-term hiPSC maintenance and growth according to the alamarBlue assay. The scaffold combination could also modulate the state of pluripotency, depending on cell origin, as shown in the real-time polymerase chain reaction (RT-PCR). We established an hiPSCs culture and differentiation protocol on 3D scaffolds and analysed its efficiency by RT-PCR and immunocytochemistry (ICC). We found that differentiation upregulated cardiac genes but to a lesser extent than in cells differentiated in 2D. We found that the scaffold substance mainly regulated the ECM deposition. *In vitro* evaluation of HUVECs on the scaffolds showed that collagen is a key factor in cell migration, and its combination with FEG can be valuable for promoting cell adhesion and angiogenesis.

Chapter 5 studied *in vivo* biocompatibility of acellular C100 and C75E25 scaffolds in rats. These scaffolds showed distinctive characteristics mechanically and *in vitro* and thus were chosen as valuable candidates for tissue implants. Histology staining of haematoxylin and eosin

(H&E), Elastica van Gieson (EVG) and AB were used to assess ECM deposition, cell migration, neovascularisation, and elastic fibre and HA confirmation within the scaffolds. EVG and AB proved the incorporation of FEG and HA, respectively. The results indicated the biocompatibility of all scaffolds, where each composition contributed differently. Semi-quantitative analysis of H&E images demonstrated that non-crosslinked scaffolds deposited ECM faster than those crosslinked and HA-infiltrated scaffolds. None of the samples exhibited encapsulation by the host tissue, which was advantageous for the study. The presence of FEG regulated ECM deposition and new capillary vessel formation better than collagen scaffolds, although this was not quantified.

6.2. Future Work

Here, we have manufactured a new type of scaffold using commercialised collagen type I and a new form of soluble elastin, FEG, further incorporating HA. A better polymeric interaction between collagen and FEG was achieved, and a strong physical relationship between FEG and HA was demonstrated in this study. Both *in vitro* and *in vivo* analyses showed the biocompatibility of scaffolds, yet they need further improvement and characterisation. In terms of scaffolds for CTE, future studies could employ a bottom-up strategy using FEG's self-assembly ability to create scaffolds with improved cellular interactions by higher control of mechanical properties. Also, the infiltration of HA without crosslinkers would be an ideal approach to increase cellular activity and the better resemblance of mechanical properties in native cardiac.

The covid-19 pandemic has extensively disrupted the current study for almost a year, which limited certain aspects of the study. For instance, cardiac maturation and contractile motion could not be addressed in this study, as these are fundamental for cardiomyocyte (CMs) characterisation and require a longer culture period. The protocol of iPSC culture and differentiation to CMs on 3D could potentially be optimised with different small molecules

and cheaper and more controllable methods to be used extensively in CTE. Although we examined the feasibility of scaffolds in cellular response by hiPSC-CMs and HUVECs, there are various types of cells (cardiac fibroblasts, smooth muscle cells etc.) contributing to cardiac remodelling (Section 1.2), and how they could contribute to cardiac regeneration when combined with our design can also be addressed in future.

Our *in vivo* results exhibited potential for these scaffolds to be used in CTE regarding biocompatibility and endothelial growth. Although there was no sign of scar tissue formation, the type of cells that migrated to the scaffolds should be characterised to understand the inflammatory response comprehensively. Another drawback of this study was the short-term implantation because crosslinked and HA-infiltrated scaffolds could not be deposited by host ECM entirely as in non-crosslinked scaffolds. This precluded the quantitative analysis of capillary vessels from understanding the extent of endothelialisation regarding scaffold type. Therefore, a longer implantation period of these scaffolds would be beneficial.

APPENDICES

Appendix A: General Consumables

Reagent	Manufacturer	Cat. No
Collagen from bovine Achilles tendon	Sigma	C9879
Elastin from bovine neck ligament	Sigma	E1625-10G
Sodium hyaluronate, 95%	Acros Organics	251770050
Distilled water	Department Stores	
Hydrochloric acid	Merck	30721-2.5-M
Ethanol absolute	Sigma Aldrich	32221-2.5L-M
Sodium chloride	FluoroChem	094554
Sodium hydroxide (NaOH)	MP Biomedicals	153495
Acetic acid, glacial	Fisher Chemical	A/0360/PB15
Oxalic Acid	Sigma Aldrich	658537-100G
Phosphate buffer saline (tablets)	Sigma	P4417-100TAB
EDC Hydrochloride	FluoroChem	024810
N-hydroxysuccinimide (NHS)	Sigma-Aldrich	130672-100G
Adipic acid dihydrazide	Sigma-Aldrich	A0638-100G
Elastase from porcine pancreas	Sigma-Aldrich	E1250-50MG
Collagenase from *Clostridium histolytium*	Sigma-Aldrich	C0130-500MG
Hyaluronidase from bovine testes Type I-S, lyophilized powder	Sigma-Aldrich	H3506-100MG
Dialysis tubing cellulose membrane	Sigma-Aldrich	D9652-100FT
Tris(hydroxymethyl)amino methane	Sigma-Aldrich	252859-100G
TES free acid	Sigma-Aldrich	T1375-25G
Calcium chloride	Sigma-Aldrich	C1016-100G

Appendix B: *In vivo* & Histology Staining Consumables

Reagent	Manufacturer	Cat. No
DPX Mounting Media	Thermo Scientific	LAMB/DPX
Entellan	DPAG Histology Lab	
SuperFrost® Plus	Thermo Scientific	J1800AMNZ
SuperFrost® Plus	VWR	631-0108
Histo-Clear	National Diagnostics	HS-200
Sodium Azide	Sigma	S2002-5G
Hematoxylin solution according to Mayer	Sigma	51276-500ML
Eosin Y Solution 1% alcoholic for microscopy	Sigma-Aldrich	1.17081.1000
Hematoxylin Hydrate	MP Fisher Scientific	0210192205
Elastica van Gieson staining kit	Merck	1.15974.0002
Neutral Red Solution (1:300)	MP Biomedicals	1691149
Alcian Blue Solution 1%, 3% acetic acid	Merck	B8438
Isoflurane, USP	Halocarbon Life Sciences	26675-46-7
Surface disinfectant spray	Anistel	TR295
Pre-injection swaps (70% Alcohol)	Medisave	MS100
MetaCam	Boehringer Ingelheim	601304-08
Ethicon 16 mm	Johnsons & Johnsons Surgical Technologies	W9436
Paraplast Plus®	Sigma	P3683-1KG
OCT Compound	Tissue Tek	4583
Sucrose	Sigma	S0389-500G
1-Butanol, minimum 99%	Sigma	BT105
Xylene	VWR	305756G
MX35 ULTRA Microtome Blade	Thermo Scientific	3053835
Formalin Solution, 10% Neutral Buffered	Sigma Aldrich	HT501128-4L

Appendix C: *In vitro* Consumables

Reagent	Manufacturer	Cat. No
TeSR™-E8™ Basal Medium	StemCell Technologies	#05991
TeSR™-E8™ 25X Supplement	StemCell Technologies	#05992
GFR Matrigel	Corning	354230
ROCK Inhibitor (Y-27632)	Merck	SCM075
Dulbecco's Phosphate Buffered Saline	Sigma-Aldrich	D8537
Dulbecco's Phosphate Buffered Saline with Magnesium and Calcium	Thermo Fisher Scientific	14040-083
ReLeSR™	StemCell Technologies	#05872
CryoStor® CS10	StemCell Technologies	#07930
RPMI 1640 (1X)	Gibco	11875-093
RPMI 1640 (1X)	Gibco	21875-074
RPMI	Gibco	11879-020
DMEM/F-12 (1:1) (1X)	Gibco	11320-074
B-27® Minus Insulin (50X)	Gibco	A18956-01
B-27® Supplement (50X)	Gibco	17504-044
CHIR 99021	Tocris Bioscience	4423
Wnt-C59	Tocris Bioscience	5148
Vitronectin XF™	StemCell Technologies	#07180
Cell Adhere Dilution Buffer	StemCell Technologies	#07183
Clonetics® EGM™-Plus	Lonza	CC-5036
Clonetics® EGM™-Plus SingleQuots®	Lonza	CC-4542
Clonetics® EGM™-2 SingleQuots®	Lonza	CC-4176
Clonetics® ReagentPack™	Lonza	CC-5034
Trypsin/EDTA	Lonza	CC-5012
TNS	Lonza	CC-5002
HEPES-BSS	Lonza	CC-5022
AlamarBlue™ Call Viability Reagent	Invitrogen	DAL1025
Glycerol	Sigma Aldrich	G9012-100ML
Countess™ cell counting chamber slide	Thermo Fisher	C10312
Glycine	Sigma-Aldrich	G8898-500G
Bovine Serum Albumin (BSA)	Sigma-Aldrich	A9418
Dimethyl Sulfoxide (DMSO)	ChemCruz	SC-358801
Fetal Bovine Serum (FBS), qualified, heat inactivated,	Thermo Fisher	10500
Triton® X-100, molecular biology	MP Biomedicals	194854
Glutaraldehyde (ca 50% in water, ca. 5.6 mol/L)	Fluorochem	111-30-8
Paraformaldehyde	Sigma Aldrich	16005-1KG-R
Sodium cacodylate trihydrate	Sigma	C0250-25G
RNeasy Mini Kit	Qiagen	74104
RNaseZap™ RNase Decontamination Solution	Invitrogen	AM9780
Trizol reagent	Ambion	15596026
High-Capacity cDNA Reverse Transcription Kit	Applied Biosystems	4368814
Power SYBR® Green PCR Master Mix	Applied Biosystems	4367659

MicroAmp™ Optical Adhesive Film	Applied Biosystems
PCR-Cooler	Eppendorf

Appendix D: RT-PCR Primers* List

Gene	Sequence	Annealing Temperature	Category
β-ACTIN	F: GCTGTGCTACGTCGCCCTG R: GGAGGAGCTGGAAGCAGCC	56/60ºC	Housekeeping
UBC	F: TTTCCCAGCAAAGATCAACC R: CCTGGTGCTCCGTCTTAGAG	58/60/62ºC	Housekeeping
OCT4	F: CAGTGCCCGAAACCCACAC R: GGAGACCCAGCAGCCTCAAA	62ºC	Pluripotency
NANOG	F: CAGAAGGCCTCAGCACCTAC R: ATTGTTCCAGGTCTGGTTGC	62ºC	Pluripotency
MYL7	F: GGAGTTCAAAGAAGCCTTCAGC R: GTCCCATTGAGCTTCTCCCC	60ºC	Cardiac
MYH6	F: TCCTGCGGCCCAGATTCTTC R: TCTTCCTTGTCATCGGGCAC	58ºC	Cardiac
TNNT2	F: GACAGAGCGGAAAAGTGGGA R: CTCCTTGGCCTTCTCCCTC	60ºC	Cardiac
COL1A1	F: GGACACAGAGGTTTCAGTGGT R: GCACCATCATTTCCACGAGC	60ºC	ECM
ELA	F: CTGGAATTGGAGGCATCG R: TCCTGGGACACCAACTAC	58ºC	ECM
HAS-2	F: AGCCTTCAGAGCACTGGGACGA R: ACAGATGAGGCTGGGTCAAGCA	58ºC	ECM
CD31	F: AACCCACTCCCCGACCTAGA R: CCAGACACCATTCCAAAACC	60ºC	Endothelial
CD105	F: GCCAGCATTGTCTCACTT R: GGCACACTTTGTCTGGAT	60ºC	Endothelial function
VEGFR	F: GGGAAAGCATCGAAGTCTC R: CTCTGCGGATAGTGAGGTT	56ºC	Angiogenesis
ANG2	F: TGCCACGGTGAATAATTCAG R: TTCTTCTTTAGCAACAGTGGG	56ºC	Angiogenesis

*All primers were purchased from Sigma-Aldrich.

Appendix E: Staining Reagents

Reagent	Manufacturer	Cat. No	Host	Working Dilution /Concentration
Phalloidin-TRITC	Sigma-Aldrich	P1951	*Amanita phalloides*	1:200
DAPI	Life Technologies	D1306		1:5000
Anti-α-Actinin (Sarcomeric)	Sigma-Aldrich	A7811	Mouse (Monoclonal)	1:500
Anti-Cardiac Troponin T	Abcam	ab8295	Mouse (Monoclonal)	2 μg/mL
Alexa Fluor 488	Invitrogen	A-21202	Donkey anti-mouse	1:200
Alexa Fluor 594	Invitrogen	A-21203	Donkey anti-mouse	4 μg/mL

Appendix F: Animal Study Design

	Animal ID	Cage ID	Type of Scaffold		Body Weight (g)		
			Left	Right	Day 0	Day 1	Day 2
1-week	1	551756	C100 Non-XL	C100 XL	260	268	272
	2	551756	C100 Non-XL	C100 XL	255	261	267
	3	551756	C100 XL	C100 HA	282	284	299
	0	551756	C100 XL	C100 HA	272	280	294
	1	551757	C100 HA	C100 Non-XL	263	266	279
	2	551757	C100 HA	C100 Non-XL	276	280	289
	3	551757	C75E25 Non-XL	C75E25 XL	246	252	264
	0	551757	C75E25 Non-XL	C75E25 XL	250	257	267
	1	551758	C75E25 XL	C75E25 HA	259	267	276
	2	551758	C75E25 XL	C75E25 HA	283	289	300
	3	551758	C75E25 HA	C75E25 Non-XL	243	257	262
	0	551758	C75E25 HA	C75E25 Non-XL	244	255	262
2-week	1	556106	C100 Non-XL	C100 XL	228	233	243
	2	556106	C100 Non-XL	C100 XL	225	228	234
	3	556106	C100 XL	C100 HA	213	216	230
	0	556106	C100 XL	C100 HA	214	221	232
	1	556107	C100 HA	C100 Non-XL	221	226	237
	2	556107	C100 HA	C100 Non-XL	223	228	239
	3	556107	C75E25 Non-XL	C75E25 XL	223	230	240
	0	556107	C75E25 Non-XL	C75E25 XL	215	216	228
	1	556108	C75E25 XL	C75E25 HA	226	232	235
	2	556108	C75E25 XL	C75E25 HA	214	224	233
	3	556108	C75E25 HA	C75E25 Non-XL	228	234	241
	0	556108	C75E25 HA	C75E25 Non-XL	232	242	246